Phenomenological modelling of particulate emissions in direct injection spark ignition engines for driving cycle simulations.

Phänomenologische Modellierung von Partikelemissionen direkteinspritzender Ottomotoren für die Fahrzyklussimulation.

Zur Erlangung des akademischen Grades Doktor-Ingenieur (Dr.-Ing.)
genehmigte Dissertation von Stefan Frommater, M.Sc. aus Plauen/Vogtl.
Tag der Einreichung: 28.03.2018, Tag der Prüfung: 13.6.2018
Darmstadt 2018 — D 17

1. Gutachten: Prof. Dr.-Ing. Christian Hasse
2. Gutachten: Prof. Dr. techn. Christian Beidl

TECHNISCHE UNIVERSITÄT DARMSTADT

Fachbereich Maschinenbau
Simulation reaktiver Thermo-Fluid Systeme

Phenomenological modelling of particulate emissions in direct injection spark ignition engines for driving cycle simulations.
Phänomenologische Modellierung von Partikelemissionen direkteinspritzender Ottomotoren für die Fahrzyklussimulation.

Genehmigte Dissertation von Stefan Frommater, M.Sc. aus Plauen/Vogtl.

1. Gutachten: Prof. Dr.-Ing. Christian Hasse
2. Gutachten: Prof. Dr. techn. Christian Beidl

Tag der Einreichung: 28.03.2018
Tag der Prüfung: 13.6.2018

Jahr der Veröffentlichung der Dissertation auf TUprints: 2018

Darmstadt 2018 — D 17

Vorwort

Die vorliegende Arbeit entstand während meiner Tätigkeit als Doktorand und Mitarbeiter der BMW Group in der Abteilung „Entwicklung Ottomotor - Emissionskonzepte“ in den Jahren 2014 bis 2017.

Bei Herrn Prof. Dr.-Ing. Christian Hasse bedanke ich mich dafür, mir die Bearbeitung dieses Themas ermöglicht zu haben. Herrn Prof. Dr. techn. Christian Beidl danke ich für sein Interesse an der Arbeit und die Bereitschaft, diese als Zweitgutachter zu betreuen.

Des Weiteren danke ich Herrn Manfred Schleich und Herrn Dr.-Ing. Bodo Durst dafür, die Arbeit bei ihnen in der Abteilung anfertigen zu dürfen. Insbesondere danke ich ihnen für die stetige Unterstützung und den Freiraum, den sie mir zur Gestaltung der Arbeit gegeben haben. Ich danke ebenfalls meinen Kolleginnen und Kollegen bei der BMW Group für das immer angenehme und produktive Arbeitsumfeld.

Ein besonderer Dank gilt Herrn Dr.-Ing. Jens Neumann, der mich während der gesamten Zeit mit vollem Einsatz bei der Bearbeitung und Anfertigung der Arbeit unterstützt hat. Außerdem danke ich ihm dafür, dass er mir die Möglichkeit einer Industriepromotion erst gegeben hat.

Ich danke vor allem auch Tobias Hanisch, der im Rahmen seiner studentischen Abschlussarbeit bei mir einen großen Beitrag zu dieser Arbeit geleistet hat.

Der größte Dank gehört meiner Familie, auf deren uneingeschränkte Unterstützung ich mich immer verlassen kann und die während der Zeit der Entstehung dieser Arbeit immer verständnisvoll waren.

"Success is getting what you want. Happiness is wanting what you get."

(Dale Carnegie)

Abstract

In order to achieve local air purity, particulate emissions from gasoline engines are meanwhile subject to statutory regulations. Due to the increasing complexity of the test procedures, away from standardized driving cycles to the point of real driving emissions, an almost infinite number of characteristics of the driving profile is possible. Simulation methods can help to reduce engine-out particle emissions by means of engine design and application, particularly at an early stage of development and by transferring the results to different variants.

For this purpose, a new phenomenological simulation model is developed within this work that allows the determination of the particle raw emissions of gasoline engines based on physical principles. It is applicable both at stationary operating conditions and in transient driving cycles. Not only the particle number values are calculated, but also the particle mass and size distribution. This is achieved by the coupling of a 0D/1D engine process simulation, a new quasi-dimensional multi-zone model for the consideration of different soot particle formation causes and a stochastic soot model.

Particle emissions from injector deposits, inhomogeneous gaseous mixture preparation and remaining fuel wall film are taken into consideration, as they contribute to the overall emissions by a different proportion. The applied gas-phase boundary conditions of the multi-zone structure are based on these formation processes. In zones that arise from inhomogeneous mixture preparation, the reaction of the air-fuel mixture under sub-stoichiometric conditions is calculated, whereas pyrolysis reactions are considered in zones with remaining liquid fuel film. The calculation of the remaining injector film mass considers film formation and evaporation. The formation of liquid wall films is calculated by the coupling of a newly developed spray model, a spray-wall interaction model and an evaporation model. The - within the framework of this work developed - homogenization sub-model calculates the in-cylinder mixing process over time by considering charge motion, spray-charge interaction and mixing time, enabling the estimation of the statistical equivalence ratio distribution function. The creation of the final simulation framework is accompanied by an engine measurement program and additional 3D-CFD simulations to evaluate the different sub-models.

Due to its physically based structure, the model can take into account changes in thermodynamic boundary conditions and engine actuator settings after an engine-specific calibration at a couple of selected operating points. The final simulation framework is successfully evaluated by test bench measurements of the engine operating map, a variation of engine actuator settings and transient driving profiles. Thereby, the model can be applied in the future engine development in order to further reduce engine-emitted soot particle emissions.

Zusammenfassung

Zur Erhaltung der lokalen Luftreinheit sind Partikelemissionen auch bei Ottomotoren zunehmend Teil der gesetzlichen Regulierung von Abgasemissionen. Durch die steigende Komplexität der Testverfahren - von standardisierten Fahrzyklen hin zu Emissionen realer Straßenfahrten - entwickelt sich eine nahezu unbegrenzte Anzahl von möglichen Fahrfällen und Streckenkombinationen. Simulationsmethoden können bereits früh im Entwicklungsprozess bei der Reduktion von Partikelrohemissionen unterstützen, etwa durch Optimierung von Konstruktion und Motorapplikation sowie durch Bewertung verschiedener Motorzustände und Fahrfälle.

Im Rahmen der vorliegenden Arbeit wird ein neues phänomenologisches Simulationsmodell entwickelt, mit dessen Hilfe die Partikelrohemissionen von Ottomotoren basierend auf physikalischen Grundprinzipien berechnet werden. Das Modell ist sowohl für quasi-stationäre Motorbetriebspunkte als auch für transiente Fahrprofile anwendbar. Zusätzlich zu den Partikelanzahlemissionen sind auch Partikelmasse und -größenverteilung bestimmbar. Dies erfolgt durch die Kopplung einer 0D/1D Motorprozesssimulation mit einem neuentwickelten quasi-dimensionalen Mehrzonenmodell, welches wesentliche innermotorische Rußpartikelquellen berücksichtigt, und einem stochastischen Rußmodell.
Es werden Partikelemissionen von Kraftstoffablagerungen am Injektor, inhomogener Gemischaufbereitung und verbleibendem Kraftstofffilm an den Brennraumwänden berücksichtigt, da diese, abhängig vom Betriebszustand, einen variablen Anteil an den Gesamtemissionen aufweisen. Die im Mehrzonenmodell aufgeprägten Randbedingungen der Gasphasenkinetik basieren auf diesen Entstehungsorten. In Zonen mit unzureichender Gemischhomogenisierung erfolgt die Berechnung einer Reaktion des Kraftstoff-Luft Gemisches bei unterstöchiometrischen Bedingungen, während in Zonen mit verbleibendem Kraftstofffilm Pyrolysereaktionen betrachtet werden.
Die Bestimmung der verbleibenden Kraftstoffmasse bezieht Filmbildung und -verdampfung ein. Die Berechnung von Kraftstofffilmen an den Brennraumwänden erfolgt durch die Kopplung eines neu entwickelten Spraymodells mit Modellen zur Spray-Wand Interaktion und Filmverdampfung. Das Homogenisierungsmodell berechnet zeitlich aufgelöst den Gemischbildungsprozess im Brennraum unter Berücksichtigung von Ladungsbewegung, Spray-Gemisch Interaktion und Mischungszeit und ermöglicht die Bestimmung der statistischen Verteilung des Verbrennungsluftverhältnisses.
Die Entwicklung der Simulationsmethodik wird begleitet von Motorprüfstandsmessungen und 3D-CFD Simulationen zur Parametrierung und Evaluation der einzelnen Submodelle. Aufgrund der physikalisch basierten Struktur ist das Modell nach einer motorspezifischen Parametrierung an einigen ausgewählten Betriebspunkten in der Lage, Änderungen von thermodynamischen Randbedingungen und der Aktuatorik zu berücksichtigen.

Die Evaluation der finalen Simulationsumgebung erfolgt mittels Messungen des Motorkennfeldes, einer Variation verschiedener Motorapplikationseinstellungen und thermischer Randbedingungen sowie transienten Fahrprofilen. Basierend auf den Ergebnissen der Arbeit wird eine Anwendung der Simulationsmethodik bei Motorentwicklungen zur weiteren Verringerung der Partikelrohemissionen ermöglicht.

Contents

List of Figures

List of Tables

Nomenclature

Abbreviation

Symbol	*Meaning*	*Unit*
a/bTDCf	after/before top dead centre firing	—
amu	atmospheric mass unit	—
BDC	bottom dead centre	—
CA	crank angle	°
CPC	condensation particle counter system	—
DISI	direct injection, spark ignition engine	—
DSMC	direct simulation Monte-Carlo algorithm	—
ECT	engine crank train	—
ECU	engine control unit	—
EOI	end of injection	—
EQR	equivalence ratio	—
GPF	gasoline particulate filter	—
HACA	hydrogen abstraction, carbon addition	—
HCCI	homogeneous charge compression ignition	—
IMAP	intake manifold pressure	bar
IMEP	indicated mean effective pressure	bar
IVC	inlet valve closing	—
LIF	laser-induced fluorescence	—
MOMIC	method of moments with interpolative closure	—
ODE	ordinary differential equation	—
PAH	polycyclic aromatic hydrocarbons	—
PFI	port fuel injection	—
PM	particle mass	—
PN	particle number	—
PSD	particle size distribution	—
PSR	perfectly stirred reactor	—
QD	quasi-dimensional	—
QMOM	quadrature method of moments	—
SOC	start of combustion	—
SOI	start of injection	—
SRM	stochastic reactor model	—
TEM	transmission electron microscopy	—
WLTP	Worldwide Harmonized Light Duty Test Procedure	—

Greek Letters

Symbol	*Meaning*	*Unit*
α	active particle surface area	—
α	heat transfer coefficient	$\mathrm{W/m^2\,K}$
α_{dry}	dry fraction of liquid film area due to boiling	—
β_1, β_2	model parameter of film boiling model	—

$\dot{\omega}$	chemical reaction rate	$\mathrm{mol/m^3 s}$
η	collision efficiency	—
λ	air-fuel ratio	—
λ	thermal conductivity	$\mathrm{W/m\,K}$
μ	dynamic viscosity	Pa s
ν	kinematic viscosity	$\mathrm{m^2/s}$
ω	Pitzer acentric factor (0.304 for iso-octane)	—
ϕ	equivalence ratio	—
ρ	density	$\mathrm{kg/m^2}$
σ	standard deviation	—
σ	surface tension	$\mathrm{N/m}$
σ_{lv}	surface tension between liquid and vapour phase	$\mathrm{N/m}$
τ	dimensionless time	—
Θ	crank angle	$^\circ$

Latin Symbols

Symbol	*Meaning*	*Unit*
$\bar{x}$	mean value	—
ΔH_v	Latent heat of vaporisation	$\mathrm{J/kg}$
Δm_{st}	injected mass per injection step	kg
Δt_{imp}	time between spray injection and impingement	s
Δt_{st}	injection step duration	s
$\dot{m}$	mass flow rate	$\mathrm{kg/s}$
$\dot{m}_p$	particle mass stream	$\mathrm{mg/s}$
$\dot{N}$	particle number stream	$\mathrm{\#/s}$
$\dot{Q}_d$	heat flow rate	W
$\dot{q}_{wl}$	heat flux from wall to liquid in direct contact	$\mathrm{W/m^2}$
$\dot{q}_{wvl}$	heat flux from wall to liquid through the vapour layer	$\mathrm{W/m^2}$
Sh	Sherwood number	—
$\overline{m}_d$	average single droplet mass	kg
$\vec{d}_{\mathrm{I}}$	unit injection direction vector	—
$\vec{x}_{\mathrm{I}}$	injector position	m
A	area	$\mathrm{m^2}$
A_{dry}	dry surface area due to boiling	$\mathrm{m^2}$
A_{wet}	total wetted area in the absence of boiling	$\mathrm{m^2}$
a_i, b_i, c_i	model coefficients for the calibration	—
B	bore diameter	m
B_m	Spalding mass transfer number	—
c	concentration	$\mathrm{mol/cm^3}$
c_m	mean piston velocity	$\mathrm{m/s}$
c_v	coefficient of variation	—
c_D	drag coefficient	—
C_{lld}	length density of the liquid film's contact lines	$\mathrm{m/m^2}$
$c_{p,m}$	molar heat capacity	$\mathrm{J/mol\,K}$
c_p	specific heat capacity	$\mathrm{J/kg\,K}$
D	binary diffusion coefficient between fuel and ambient gas	$\mathrm{m^2/s}$
d	diameter	m
d	distance	m
d_{32}, SMD	Sauter mean diameter	m

E	chemical activation energy	$^{J}/_{mol}$
E	homogeneity index	—
f_D	drag modifying factor	—
f_V	vaporisation modifying factor	—
F_D	drag force	N
f_h	wall film thickness modifying factor	—
h	film thickness	m
k_B	Boltzmann constant	$^{J}/_{K}$
k_{clld}	dimensionless function of length density of contact lines	—
$k_{tr,sf,fm}$	coagulation kernel	$^{m^3}/_{s}$
Kn	Knudsen number	—
L_{ch}	characteristic length	m
L_{St}	stoichiometric air ratio	—
M	molar mass	$^{kg}/_{mol}$
m	mass	kg
m_d	particle mass density	$^{mg}/_{cm^3}$
m_k,M_k	k-th moment of the particle distribution	—
$m_{d,i}$	injected mass per injection step, nozzle hole and diameter class	kg
n	engine speed	rpm
n	number	—
$N_{classes}$	number of diameter classes	—
N_{holes}	number of injector holes	—
N_{st}	number of injection steps	—
N_A	Avogadro number	1 mol
N_d	particle number density	$^{\#}/_{cm^3}$
n_p	absolute number of particles	#
$N_{d,st}$	number of droplets per injection step	—
$N_{d,i}$	number of droplets per injection step, injector hole and diameter class	—
p	pressure	Pa
p_v	vapour pressure	Pa
Pr	Prandtl number	—
R	universal gas constant	$^{J}/_{mol\ K}$
R_{incept}	soot inception rate	$^{\#}/_{m^3 s}$
Re	Reynolds number	—
S	penetration depth	m
s	stroke	m
Sc	Schmidt number	—
T	temperature	K
t	time	s
T_L	Leidenfrost temperature	K
T_N	Nukiyama temperature	K
T_{**}	dimensionless wall temperature for liquid length density of contact lines	—
T_*	dimensionless wall temperature for dry fraction	—
T_b	atmospheric boiling point	K
u	velocity	$^{m}/_{s}$
V	volume	m^3
V_m	molar volume	$^{m^3}/_{mol}$
Var	variance	—
w	weighting factor	—

We	Weber number	–
X	molar fraction	–
x, y, z	cartesian coordinates	m
Y	mass fraction	–
Z	error value of objective function	–
L_0/h_0	ratio of characteristic length to film thickness	–
Z	error value for optimization function	–

Superscripts

Symbol	*Meaning*	*Unit*
0	ideal gas state	–
PL	Leidenfrost point	–
PN	Nukiyama point	–
l	liquid state	–
mod	modified	–

Subscripts

Symbol	*Meaning*	*Unit*
∞	ambient state	–
inj	injection	–
lin	liner	–
max	maximum	–
min	minimum	–
pis	piston	–
ref	reference	–
vap	vaporisation	–
wf	wall film	–
a	air	–
b	value at the atmospheric boiling point	–
c	critical	–
f	fuel	–
g	gas	–
l	liquid	–
r	reduced	–
sat	saturation	–
v	vapour	–
m	molar	–
ad	adiabatic	–
b	burned	–
chem	chemical	–
corr	correction	–
cyl	cylinder	–
d	droplet	–
dep	deposited	–
EGR	exhaust gas recirculation (residual gas)	–
evap	evaporation	–
exh	exhaust	–
H	homogeneity	–

ign	ignition	–
imp	impingement	–
incr	increment	–
inj	injection	–
mix	mixing	–
noz	nozzle	–
P	particle	–
p	piston	–
ref	reference	–
stoch	stochastic	–
ub	unburned	–
w	wall	–
wf	wall film	–

1 Introduction

In order to meet the ambitious global climate targets and to achieve local air purity, a continuous reduction of the permissible pollutant emissions is required from vehicles that are powered by internal combustion engines. In addition to alternative mobility concepts and the electrification of the power train, it is still purposeful to max out the existing potentials of combustion engines. This especially includes the further development of efficient turbo-charged, direct-injection gasoline engines.

Besides gaseous species (such as nitrogen oxides, unburned hydrocarbons, carbon monoxide and dioxide), particulate emissions from gasoline engines are meanwhile subject to statutory regulations. In addition to the reduction of the permissible limits, differentiations of the legislative process in the various markets are also growing. Due to the increasing complexity of the test procedures, away from standardized driving cycles to the point of real driving emissions, almost any number of characteristics of the driving profile is possible. This especially takes the complete power and speed spectrum of the engines into account. Moreover, altered driving conditions, such as an high proportion of cold starts needs to be considered due to the engine hybridization.

These increasing external demands are additionally superimposed by the wide variety of vehicle and engine variants that are offered by the manufacturers. All these requirements lead to a great complexity in the development of gasoline engines.

In order to reduce costs and experimental efforts while at the same time meeting the legal requirements regarding exhaust emissions, simulation methods are an important way to improve the development process. These methods can help to evaluate and optimize the effects caused by different driving profiles, application influences and engine conditions. This allows the reduction of engine-out particle emissions by means of engine design and application, particularly at an early stage of development and by transferring the results to different variants.

Therefore, the aim of this work is to investigate the simulative determination of particulate emissions of gasoline engines. For this purpose, a new phenomenological simulation model is developed within the framework of the work that allows the determination of the particle raw emissions based on physical principles. It is applicable both in stationary operating points and in transient driving cycles. Not only the particle number values are calculated, but also the particle mass and size distribution is investigated. This is particularly necessary due to new technologies, such as the gasoline particulate filter (GPF), which place additional requirements on the simulation of the raw emissions. For example, the filtration efficiency can be taken into account depending on the particle size and the filter loading can be determined over time. Within the scope of modelling, it is necessary to reduce the computation time of the simulation to such an extent that an application is possible in transient driving profiles with several thousand working cycles. This is achieved by the coupling of a 0D/1D engine process simulation, a quasi-dimensional multi-zone model for the consideration of different soot particle formation causes and a stochastic soot model.

To develop the simulation model, it is also necessary to investigate the points of origin of soot particles and to assess the individual contributions to the total emissions, which is done by an additional measuring program and by an extensive literature study. Within the scope of this work, this leads to the development of sub-models that include the formation of soot particles from injector film deposits, inhomogeneous mixture preparation and remaining wall film mass.

Briefly summarized, the structure of this work is as follows:

- Chapter 2 describes the basic principles for particle formation and simulation by summarizing the essential literary sources. This includes the explanation of the fundamental formation processes as well as the causes of soot particle in gasoline engines. Additionally, the individual sources are evaluated according to their influence on the total emissions in driving cycles. An overview of already existing simulation methods is presented and an estimation of the usability is made with regard to the prior described requirements. Based on the state of the art technologies, a new basic methodology is then defined.
- The resulting model concept and structure is described in detail in Chapter 3. A physically based modelling is carried out by using a multi-zone approach. The multi-zone approach is further explained regarding the calculation of the gas-phase kinetics and the particle formation process. Within this chapter, the applied software tools and programming languages are also presented. Furthermore, a validation strategy is presented that is based on the encapsulation of the different model components.
- The subsequent chapters include the description and inclusion of the individual sub-models and thus have a similar structure. After presenting the sub-models for injector film and pyrolysis (Chapter 4), mixture homogenization (Chapter 5) and the calculation of remaining wall film mass (Chapter 6), the parametrization strategy is explained for each model part. Thereafter the results are compared to engine-out measurement data and evaluated for accuracy. Finally, a comprehensive analysis of the simulation process enables a conclusions to be drawn about the sensitivities of the individual model parameters and an evaluation of the achieved model quality.
- In Chapter 7 the evaluation of the overall model is performed for stationary engine conditions and during different driving cycles. This not only includes the assessment of sensitivities and emission results, but also an examination of the error chain within the simulation process.
- Finally, a summary of the thesis work is given and further research fields are outlined in Chapter 8.

2 Theoretical Background

2.1 Fundamentals of Particle Formation

2.1.1 Formation Process Theory

According to Tree et al. [180], the term “particle” is generally defined as the material that is collected when exhaust gases pass through a filter. It is a combination of soot and liquid- or solid-phase materials and can be separated into a soluble and insoluble fraction. Soot in particular is a combination of carbon and hydrogen atoms at a ratio of about eight to one [180]. In the context of this work, the term particles is used as a superordinate and means soot particles, unless otherwise explained.

In general, soot is formed in fuel-rich regions at higher temperatures by the nucleation of unburned fuel from a gaseous phase to a solid phase [180]. The density of soot is reported to be approximately $\rho_{\text{soot}} \approx 1.8$ g/cm^3, which corresponds to the density of graphite [34, 180]. In the literature, there is considerable agreement about the processes that are included during the soot formation. The six processes that are commonly identified are: fuel pyrolysis, particle nucleation, coalescence (coagulation), surface growth, agglomeration and oxidation [107, 152, 180, 181]. It is of special interest that, according to Lahaye [107], soot is always produced from the gas phase regardless of the original material. Whereas the pyrolysis occurs in the gas phase, the nucleation process forms the transfer to the solid phase. The growth processes take place in the solid phase and the oxidation transfers parts of the soot back into the gas phase. Once the carbon has been oxidized to CO, it will not form a soot particle again [180].

The structure of the resulting particles is affected in different ways by the specific processes. This is especially of interest when the number and mass density or the size is chosen to describe the morphology of the particles. In Tab. 2.1, a rough general overview about the influences of the different formation processes on these properties is presented for fuel-rich laminar premixed flames.

Tab. 2.1.: Influence of particle formation processes on particle number and mass density and size.

	number	mass	size
nucleation	↑↑	↑	-
coagulation/agglomeration	↓↓	-	↑
surface growth	-	↑↑	↑
oxidation	-	↓	↓

The initial particle number set is formed by the nucleation process, but only about 10 % of the final soot mass [107]. Due to coagulation processes, the number density decreases and the particle size increases at a constant mass [71, 152]. The mass and size of the particles increase at constant particle number density by surface growth reactions [71, 152]. By oxidation processes, the particle size and mass decreases [107, 152]. The effect of the oxidation of the smallest particles (burnout) was found not to be important by investigations of Balthasar and Kraft [16] on laminar premixed flames. An overview of the included processes focussed on reaction time and magnitude of the size is presented schematically in Fig. 2.1.

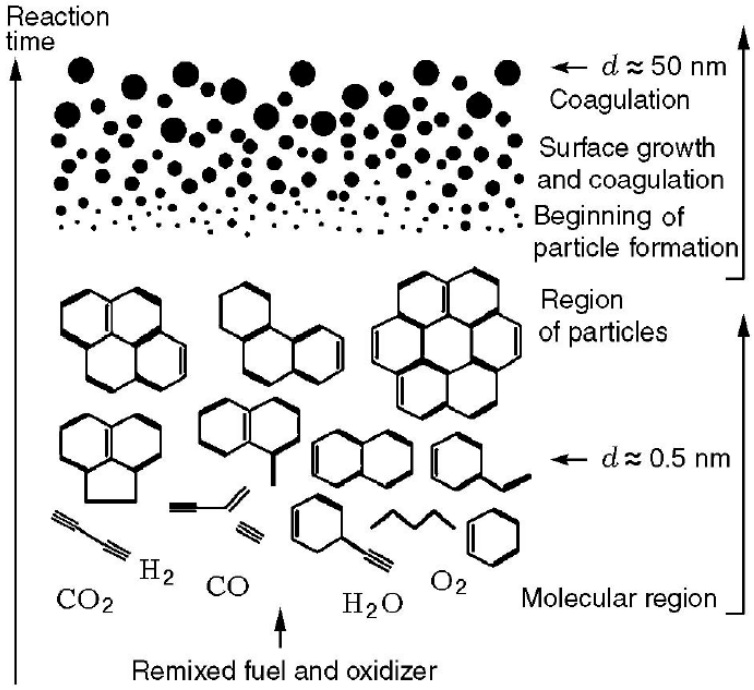

Fig. 2.1.: Schematic presentation of particle formation process for homogeneous mixture of fuel and oxidizer [115] (acc. to Bockhorn [25]).

The formation process depends mainly on the mixture composition, the temperature and the pressure. Especially the carbon to oxygen (C/O) ratio is crucial for the particle processes to begin. The required threshold at which the C/O value has to fall below is not constant but changes with temperature and pressure [79, 115]. Studies of laminar and turbulent flames showed that this threshold only slightly changes with pressure [119]. Values of required C/O ratios for different mixture types are summarized by Mansurov [115] for burner flames.

It is reported that the most dominant physical characteristic that affects the soot formation processes is the temperature [71, 180]. A minimum temperature is required for the kinetic rates to be fast enough for soot formation. Glassman [71] summarizes that different studies come to the conclusion that a minimum temperature of $T_{\text{min}} \approx 1300\,\text{K} \ldots 1600\,\text{K}$ is required. At higher temperatures, the formation rate increases first, but decreases after reaching a maximum rate for premixed flames (maximum at about $T \approx 1500\,\text{K} \ldots 1700\,\text{K}$ for well stirred reactors [162]). This effect occurs because the increase of the oxidative rates at higher temperatures is faster than the increase of the formation rates [71]. In diffusion flames, the soot formation increases monotonically with increasing temperature [71, 180]. Investigations on laboratory flames also identified a significant increase of soot formation at higher pressures for premixed flames [79, 82].

Subsequently, a more detailed analysis on the processes in the gas and solid phase is presented. However, the explanations do not claim to include all processes and pathways in the formation of soot. Rather, they are concentrated on the later use in the context of gasoline combustion engine simulations. For further information, the reader is referred to in-depth reviews by Tree and Svensson [180], Smith [167], Glassman [71], Homann [99], Palmer and Cullis [142] and Haynes and Wagner [82].

2.1.2 Gas Phase Reaction Kinetics

Fuel Pyrolysis

In a first step towards primary soot particles, the fuel undergoes either pure or oxidative pyrolysis, regardless of flame and fuel type [71]. By a definition of Tree et al. [180], pyrolysis is the process of organic compounds, such as fuels, altering their molecular structure in the presence of high temperature without significant oxidation ("pure" pyrolysis if no oxygen is present). This process also takes place if some oxygen species are present ("oxidative" pyrolysis), as it is typically the case for fuel-rich premixed flames. Fuel pyrolysis is mainly a function of temperature and concentration [180].

The resulting products of pyrolysis processes are mainly small hydrocarbons, such as alkane (methane - CH_4,), alkene (ethylene - C_2H_4, propene - C_3H_6), alkyne (acetylene - C_2H_2) or polyacetylenes ($(C_2H_2)_n$) [82, 180]. In terms of oxidative pyrolysis, additional products are CO_2, H_2O and CO, as it is known from complete stoichiometric combustion. In premixed flames, oxidation and pyrolysis processes occur at the same time, whereas in diffusion flames no oxygen is present in the pyrolysis region [180]. Concerning the pyrolysis process, Glassman [71] mentions that (in case of non-aromatic fuels) the original fuel structure plays no role in a fuel's relative tendency to soot in premixed flames because all fuels pyrolyze to acetylene. The tendency to form soot correlates with the number of C–C bonds in the fuel and the C/H ratio.

Aromatic Ring Formation

If the initial fuel is non-aromatic, the pyrolysis products undergo cyclization to create the first aromatic ring, which is benzene (C_6H_6). In this case, the formation of aromatic radicals is a rate-determining step in the kinetics of the formation of soot precursors [107]. According to Richter and Howard [152], different reactions that involve stable species and pathways that include at least one radical have been assessed. They summarize that the radical pathways have been shown to be more important. Some example pathways are presented in the following:

- The direct polymerization of acetylene (C_2H_2) [21, 152].
- The addition of acetylene onto cyclobutadiene (C_4H_3) or 1-Butyn-3-yl (C_4H_5) radicals [187].
- The self-recombination of propargyl radicals (C_3H_3) [180] or the reaction of propargyl radicals with allyl radicals ($a-C_3H_5$) [128].

After the first aromatic ring structure is created, the growth to even larger molecules, called "polycyclic aromatic hydrocarbons" (PAH), also includes a number of different pathways. These processes are assumed to be similar for all fuels [180]. An overview of the different processes is given by Blanquart et al. [24] and summarized in the following:

- Additional aromatic rings are formed by addition of two acetylene molecules. This is called the H-abstraction/C_2H_2-addition (HACA) reaction sequence [66].
- By the reaction with propargyl radicals, benzyl radicals can form naphthalene ($C_{10}H_8$) [41].
- The addition of vinylacetylene (C_4H_4) on an aromatic radical, followed by direct cyclization [4, 188].

- The recombination of cyclopentadienyl radicals (C_5H_5) to form naphthalene and the reaction of cyclopentadienyl and indenyl (C_9H_8) radicals to form Phenanthrene ($C_{14}H_{10}$) [41, 152].

A recent study on the formation mechanism of PAHs beyond the second aromatic ring - which is naphtalene ($C_{10}H_8$) - was also published by Kislov et al. [101]. A schematic overview of the pyrolysis and cyclization processes is shown in Fig. 2.2.

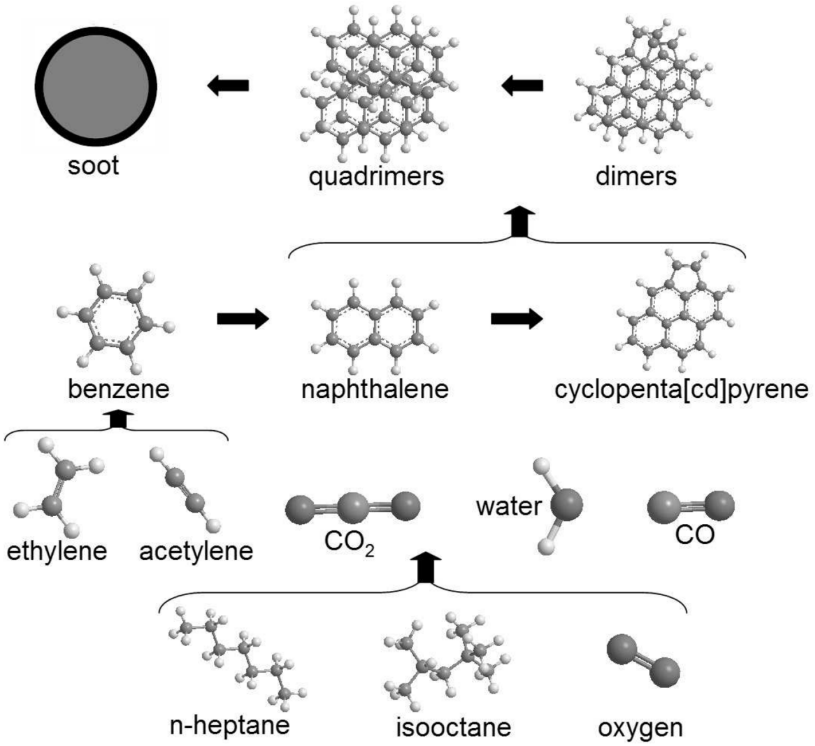

Fig. 2.2.: Schematic presentation of main pathways in the gas phase from fuel compontents to formation of first soot particles [23].

According to the above described reaction pathways, the influence of different types of fuel can be estimated on a chemical basis. If there is additional oxygen bound in the structure (e.g. ethanol (C_2H_5OH)), the oxidation rates increase and dominate the pyrolysis rates. Aromatic components in the fuel (such as benzene or toluene (C_7H_8)) are more prone to form soot than alkanes like n-heptane or iso-octane [24]. This is mainly because these fuels can bypass the formation of the first aromatic rings [6, 152]. The soot formation rate increases from paraffin to mono- and di-olefins, benzenes and naphthalenes in the fuel [152]. However, the molecular structure of the fuel only influences the early growth processes [107].

Reaction Mechanism

In order to calculate the gas phase kinetics, it is essential to create an appropriate reaction mechanism. In the literature, a number of reaction mechanisms exist with regard to soot formation processes, e.g. the well known ABF mechanism [9]. These mechanisms are often limited to fuels with a small number of hydrocarbons (C_1 or C_2 species). In the context of combustion engine soot formation, more complex fuels need to be considered. However, the exact composition and the properties of engine fuels are generally not completely known. Instead, they are typically represented by surrogates. More complex reaction mechanisms include surrogate fuels like iso-octane or n-heptane and

aromatic species like benzene and toluene (e.g. Blanquart et al. [24], Narayanaswamy et al. [135] and Marchal et al. [116]).

In the current work, the detailed reaction mechanism of Blanquart et al. [24] is used. The mechanism contains 149 species and 1651 reactions and was validated against experimental data of laminar premixed and counterflow diffusion flames in order to assess the ability of the mechanism to predict soot precursor formation. In the following, an overview of the mechanism components that enables the simulation of fuel surrogates is presented briefly. However, various adaptions were implemented by the authors. Detailed information about the included reactions and kinetic parameters can be found in the publications of Blanquart et al. [23, 24].

- The widely used GRI-MECH 3.0 [165] mechanism is the base to model reactions of C_2 species like acetylene or ethylene. It is complemented by the mechanism of Eiteneer and Frenklach [58] and Davis et al. [43]. This enables the calculation of C_3 species like propane (C_3H_8) and propene (C_3H_6).
- The C_4 chemistry is taken from Hidaka et al. [83] and Laskin et al. [108].
- The combustion of aromatic species has been derived from Djurisic [49] (benzene) and Oehlschlaeger et al. [140] (toluene).
- Finally, the mechanism of Curran et al. [37] and Curran et al. [38] was used for n-heptan combustion and iso-octane combustion, respectively. These mechanisms were reduced to remove the low temperature chemistry which is not relevant in the context of particulate emissions.

The mechanism has been validated against ignition delay times and laminar burning velocities over a large range of equivalence ratios and pressures [24]. The mechanism includes the pyrolysis processes of the fuel components, the aromatic ring formation and the growth up to pyrene ($C_{16}H_{10}$). In Fig. 2.3, the main pathways of the mechanism towards the first aromatic ring are presented for a premixed iso-octane or n-heptane flame with an equivalence ratio of $\phi = 1.9$.

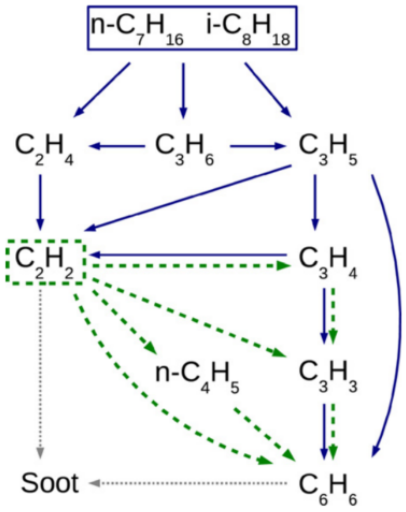

Fig. 2.3.: Schematic presentation of main pathways towards the first aromatic ring formation (benzene) for a rich premixed iso-octane or n-heptane flame (solid lines) and for an acetylene flame (dashed lines) [24].

2.1.3 Formation and Growth of Soot Particles

Nucleation

One of the most complex steps in the particle formation process is the transfer from the molecular (gas-phase) to the particulate (solid-phase) system. This process is called nucleation or soot particle inception [180].

The chemical details of the formation of nascent soot particles is still subject of scientific researches. According to Richter and Howard [152], this is mainly caused by experimental difficulties. Identifying species on a molecular basis during the soot formation process is only possible up to about 300 amu by gas chromatography (for comparison: one pyrene molecule has approx. 200 amu). The observation of particles is limited to diameters above 1.5 nm by electron microscopy.

Based on a recapitulation of Lahaye [107], three routes have been proposed to the formation of carbon particles: (1) polyacetylene, (2) polyaromatic hydrocarbons (PAH) and (3) carbon vapour resulting from dehydrogenation of hydrocarbon molecules. The author comes to the conclusion that PAH are the precursors of carbon nuclei. This is based on investigations of methane diffusion flames, where the PAH profiles sharply decrease at the inception of soot. This conclusion is also affirmed by other authors, e.g. Frenklach and Wang [66], Richter and Howard [152] and Kazakov et al.[94]. Other hypothesis about the soot nucleation process are also summarized by Richter and Howard [152].

Frenklach and Wang [66] state that molecular reactions alone cannot explain the formation of soot, because the initial soot particles are much larger than the measured PAH molecules. Instead, the PAH molecules grow by coagulation. In the literature, the inception of soot by the four-ring PAH pyrene ($C_{16}H_{10}$) is commonly prevalent [9, 24]. Investigations of Yoshihara et al. [197] showed that the complete disregard of PAH growth to molecules that are larger than pyrene results in an error of factor two in the nucleation rate.

Surface Growth

The particle nuclei still contain large amounts of hydrogen at the point of their formation [180]. The surface growth processes are again characterized by the HACA reactions, i.e. the addition of acetylene and the abstraction of hydrogen [71, 107, 180]. Besides the addition of acetylene, the addition of PAH and PAH radicals on the soot surface is also a growth process (often referred to as condensation) that is discussed in the literature [152]. The surface reaction process is the main factor for particle mass increase. Therefore, the residence time of this process has a great influence on the total soot mass or soot volume fraction [180]. Based on surface aging effects and the reduction of hydrocarbon, the surface growth reactions declines with the extent of particle growth [65].

Coagulation and Agglomeration

The size of the primary soot particles also increases by coagulation processes between two particles. Initially, there is a complete coalescence of the particles that leads to the formation of spherical structures [65]. The mathematical treatment of this process is typically captured by the Smoluchowski equation which was developed in the field of aerosol dynamics [168].

$$\frac{d}{dt}n(x) = \sum_{y=1}^{x-1}\beta(x-y,y)n(x-y)n(y) - \sum_{y=1}^{\infty}\beta(x,y)n(x)n(y) \tag{2.1}$$

This equation describes the number density $n(x)$ of two coagulating particles x and y over time. The coagulation kernel $\beta(x,y)$ depends on the flow regime that is typically defined by the Knudsen number.

The coagulation process is limited to particle sizes of about $20-70$ nm, as it is summarized by Tree et al. [180]. It is an irreversible process. The coagulation rate mainly affects the total number density of the particles. Based on surface ageing and increased viscosity, larger particles do not coagulate any more but stick together, building aggregate structures [65]. These structures are not supposed to be spherical any more, but are forming a random structure of sticking spherical particles. This is exemplarily shown in Fig. 2.4.

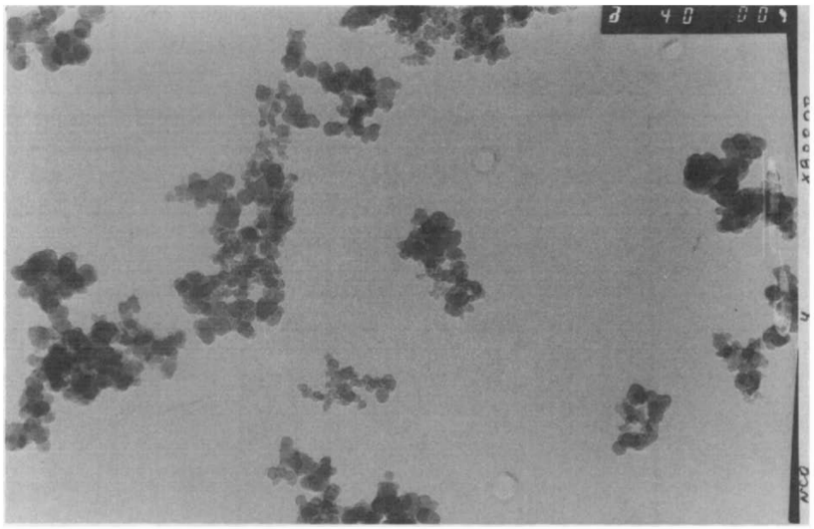

Fig. 2.4.: Micrograph of soot aggregates [107].

Oxidation

Oxidation processes not only occur during fuel pyrolysis and PAH formation in the gas-phase, but also in the solid particle regime. The particle mass is reduced by the formation of CO and CO_2 with OH, O and O_2 [107]. The largest contributor is OH under fuel-rich conditions and O_2 under fuel-lean conditions [152]. The oxidation process by OH is quite reactive and oxidizes the particle surface uniformly, keeping the particles stable and reducing the mass [107]. Oxidation with O_2 occurs only at specific positions of the particle, resulting in increased porosity and finally leads to a breakup of the aggregate structure, but without much loss in mass [107].

Summarizing, the soot formation, growth and oxidation processes occur simultaneously and are closely connected to the processes including large PAH molecules, especially for nascent soot particles. The sum of all explained processes significantly influences the particle number density, the particle mass and the shape of the corresponding solid particles. A schematic and simplified overview of the particle formation process with the assumption of pyrene nucleation and surface growth by pyrene and acetylene is shown in Fig. 2.5.

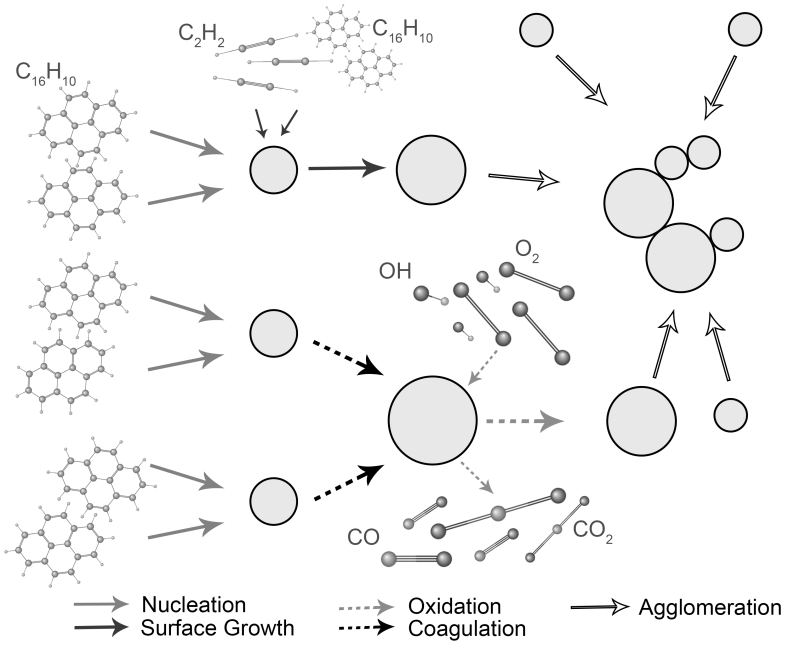

Fig. 2.5.: Schematic and simplified presentation of particle formation, growth and oxidation process. Nucleation by pyrene coagulation, surface growth by acetylene and pyrene addition.

2.2 Sources of Particulate Emissions in DISI Engines

2.2.1 Liquid Fuel Films

In Section 2.1.1, it is already mentioned that soot is formed in fuel-rich regions at higher temperatures. This fundamental formation process is also applicable in the context of direct-injection, spark-ignition (DISI) engines. The difficulty is to identify where the particle emissions originate during engine operation. A number of investigations is available in the literature that apply exhaust gas measurement or optical analysis to DISI engines (e.g. Maricq et al. [118, 173], Stevens and Steeper [174], Warey et al. [189], Sabathil et al. [156], Ketterer and Cheng [98], Bonatesta et al. [26], Dagefoerde et al. [39] and Miklautschitsch et al. [125]).

There is a broad agreement in the literature that particle emissions in DISI engines originate to a great extend from liquid wall films that are caused by fuel impingement [26, 36, 98, 125, 174, 189]. This is mainly concluded from optical investigations of the combustion process, where soot particles are visible as emitted bright yellow light [156, 174]. In Fig. 2.6, different engine parts are shown that have been identified to emit soot particles from liquid film [125]. This includes the piston (a), the liner (b,c) and the injector tip (c).

Stevens and Steeper [174] investigated the fuel film creation and evaporation in an optical DISI engine. They conclude that particle emissions result from remaining fuel on the piston surface during premixed combustion, which is in agreement to investigations of Warey et al. [189]. The liquid film is visualized with a laser-induced fluorescence (LIF) imaging technique. In Fig. 2.7, the remaining film on the surface of an optical piston is presented at ignition time for different injection time angles. It is clearly visible that early and late injections cause liquid films that remain until start of combustion. For mid-range injection times, liquid deposits are slightly visible. They are formed at the injector tip and the edges of the inlet valves [174]. This also correlates with the investigations of Miklautschitsch et al. [125], where injector tip film is named to be a main source of soot particles. The risk of inlet valve wetting strongly depends on injector position, spray targeting and valve control technology.

(a) (b) (c) (d)

Fig. 2.6.: Optical analysis of soot formation by remaining fuel films in DISI engines. Emissions from piston impingement (a), liner impingement (b,c) and injector film (d) [125].

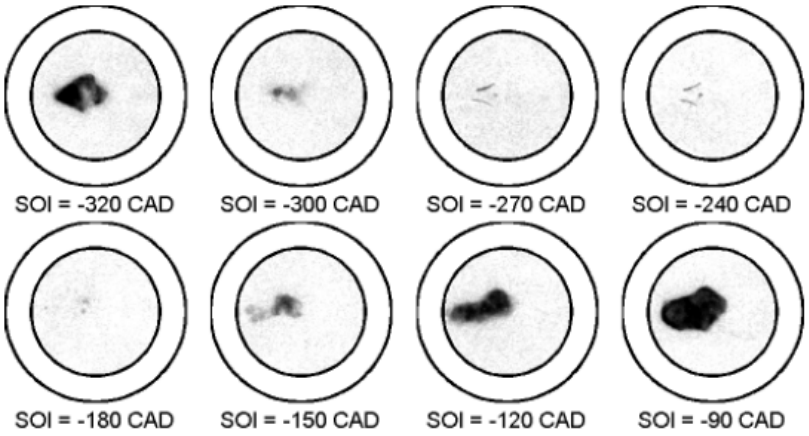

Fig. 2.7.: Optical analysis of fuel film at ignition time (−30°CA bTDCf) for different start of injection (SOI) times [174].

In the literature, different physical explanations are presented for the processes that arise from liquid wall films during combustion. Because of the bright yellow light, some of the publication denote the effect as “pool fire” that is caused by a diffusion flame [125, 174]. However, based on their recent studies on a gasoline-fuelled DISI engine, Ketterer et al. [98] mention that there is not enough oxygen available for a diffusion flame (considering a global stoichiometric fuel-air ratio) and that soot is produced by a nearly oxygen free (“pure”) pyrolysis process and the visible light is caused by radiation of the hot soot particles. This is also confirmed by experiments with different equivalence ratio values. The amount of liquid fuel was fixed to global lean conditions. By an injection of gaseous propane, the fuel equivalence ratio was then increased without affecting wall fuel film formation [98]. No significant jump has been observed as the charge equivalence ratio changed from rich to lean, which would have been expected for a diffusion flame. Optical measurements with flood laser elastic scattering images also confirm that the luminosity is primarily due to incandescent particles [174]. This is of special interest for the modelling strategy of liquid film induced soot emissions (see also Chapter 4 for further explanation).

Optical investigations and exhaust emission measurements show that engine actuator settings, thermodynamic boundary conditions, engine geometry and injection strategy have a strong impact on the resulting wall-film-induced particle emissions. In the following, an incomplete list of conditions is presented that affect the remaining liquid film:

- The engine load and speed affects the total injection duration, the injected fuel mass and the available evaporation time [26, 118].

- An increased rail pressure improves the spray evaporation because of reduced droplet diameters, leading to reduced wall impingement [125].
- Under cold start conditions, the wall temperatures are too low to evaporate the impinged fuel until start of ignition [98, 125].
- The geometrical properties of the injector tip and deposits on injector and combustion chamber walls lead to different fuel film formation and evaporation rates [88, 125, 186, 198].
- The location of the piston and liner with respect to the injector and the remaining evaporation time, which is mainly depending on the engine geometry and injection time, also affects the remaining liquid film mass [7, 26, 156, 174].
- Wall-guided spray positioning increases the created fuel films compared to spray-guided systems [36, 125].

In Fig. 2.8, a correlation between injection time and particle number emissions is presented for a wall-guided DISI engine at cold fast idle conditions (engine crank train temperature of 20°C, 1200 rpm, 2 bar IMEP) [98]. Considering the piston position and the spray penetration, the increased emissions in set (A) and (D) can be explained by an intensified wetting of the piston and the cylinder head (verified by 3D-CFD results) [98]. In set (B) and (C), the spray also impinges the walls but is partly evaporated before impingement. This leads to a reduced total wall film mass that evaporates until start of combustion [98].

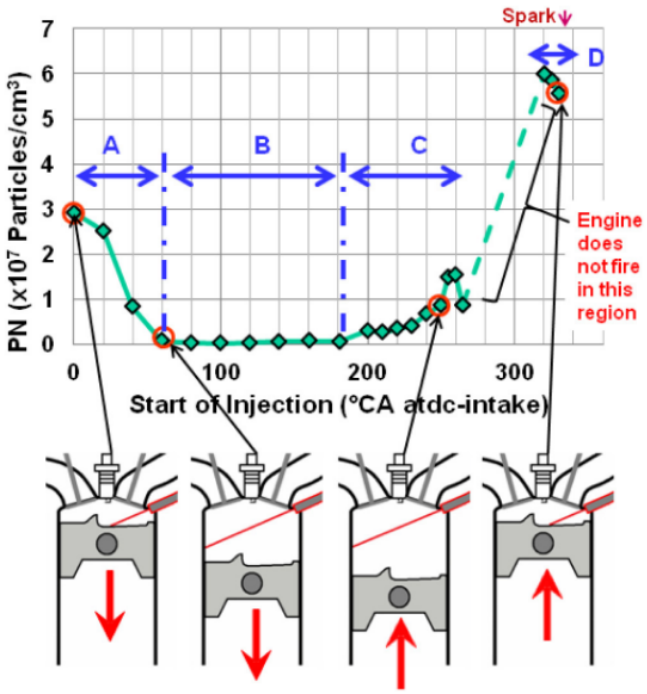

Fig. 2.8.: Influence of injection time on particle emission for wall-guided DISI engine. Cold fast idle (1200 rpm, 2 bar IMEP) at engine crank train temperature of 20°C [98].

Interestingly, the soot particles that result from set (A) show a different morphology compared to particles from set (B). In Fig. 2.9(a), the particle size distribution is presented for the injection time variation that includes liquid wall films. A peak at particle diameters around 100 nm is clearly visible that is reduced by retarding the injection time [98]. In comparison, Fig. 2.9(b) shows the size distribution for particle emissions that are emitted by locally rich regions of the charge [98]. The resulting soot particles diameters have peak values at about 30 nm.

This behaviour was also observed by Barone et al. [18], who analysed the particle emissions regarding size distribution and morphology of the primary particles using transmission electron microscopy (TEM). They summarized that DISI particle morphology depends on injection time and is influenced by fuel impingement [18]. Retarding the injection time resulted in smaller solid particles compared to early injection values.

Sabathil et al. [156] also mention that particles from late injection do not seem to create enough mass to color a filter measurement system. With additional measurements of the size distribution function using a Cambustion DMS 500, they also recognize that piston wetting results in larger particles compared to late SOI values.

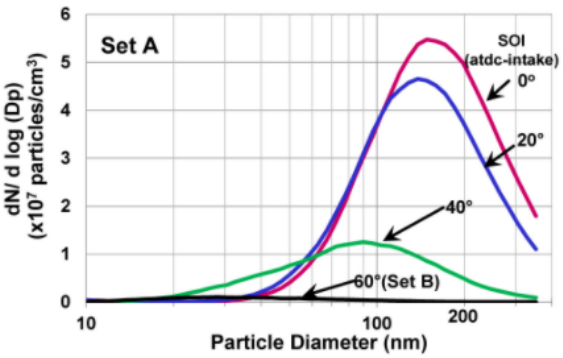

(a) Particle size spectrum for set (A) (early SOI time).

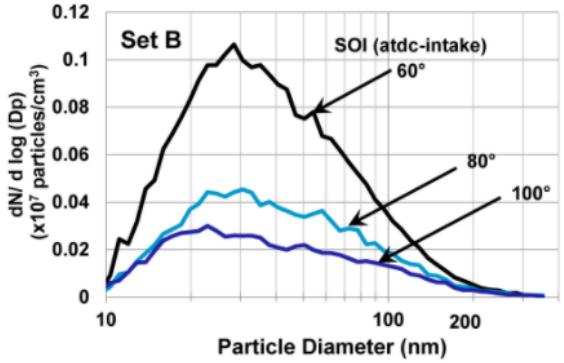

(b) Particle size spectrum for set (B) (moderate SOI time).

Fig. 2.9.: Particle size spectrum based on Fig. 2.8 [98].

2.2.2 Inhomogeneous Mixture Preparation

In addition to particle emissions caused by remaining liquid fuel, inhomogeneous mixture preparation of evaporated fuel and charge air has been identified in the literature to increase soot particle emissions of DISI engines [26, 79, 98, 118, 156, 198].

Sub-stoichiometric zones in the combustion chamber result in a fuel-rich premixed reaction process that enables the formation of soot precursors (see also Section 2.1). The identification of the local equivalence ratio in the combustion chamber can be achieved by accompanying 3D-CFD simulations or optical measurements. In Fig. 2.10, 3D-CFD results of the mixture homogeneity at start of combustion are presented for different values of SOI [98]. It is clearly visible that retarding the SOI leads to an inhomogeneous mixture with equivalence ratio values of about $\phi = 1.5$ due to a lack of time for mixture formation.

The variation of engine operating settings is a typical method to measure the influence on particle emissions caused by mixture inhomogeneity [88, 98, 156]. In Fig. 2.11, a sweep of the global equivalence ratio (Lambda=$1/\phi$) is presented by Sabathil et al. [156] that results in a significant increase of particle number emissions for global fuel-rich conditions. Fuel-rich conditions lead to an increased injection duration and reduced time for mixture formation in combination with an overall sub-stoichiometric mixture composition. This increases the chance that the soot formation threshold is locally exceeded (see also Section 2.1.1 for further explanation of the soot threshold).

However, the effects can hardly be separated due to the complexity of DISI mixture preparation. Increasing the injected fuel mass can also affect the injector-induced particle emissions or emissions

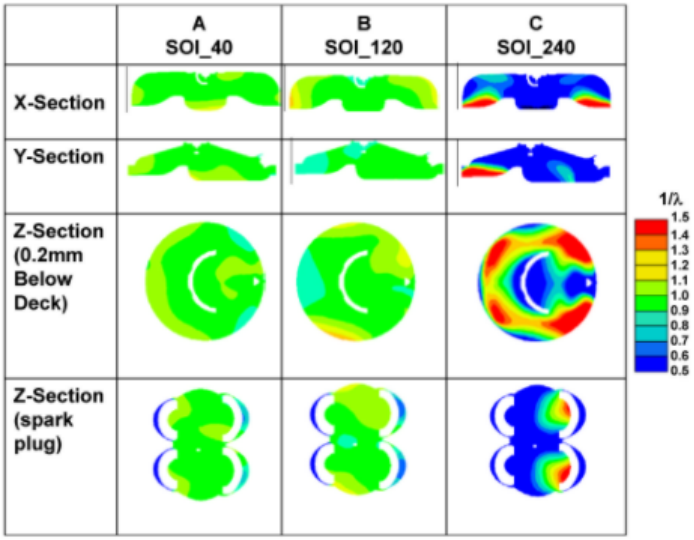

Fig. 2.10.: CFD simulations of fuel equivalence ratio $(1/\lambda)$ at 340° CA aTDC-intake for different SOI values. SOI also given in °CA aTDC-intake at an engine crank train temperature of 90°C [98].

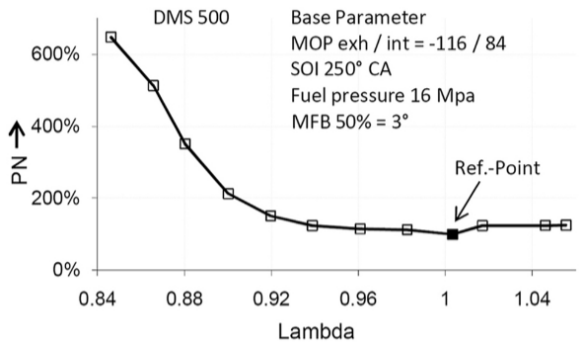

Fig. 2.11.: Measured particle number emissions for different air-fuel equivalence ratios $(1/\phi)$ [156].

caused by liquid wall film. Therefore, Hageman and Rothamer [79] investigated the sensitivity of particle emission on equivalence ratio with a port fuel injection strategy. This ensures that no particles are created by liquid fuel and that the mixture is completely homogeneous. In Fig. 2.12, the results of the equivalence ratio sweep with constant IMEP is presented for the particle number density and particle size distribution. The particle number value remains nearly constant until $\phi = 1.3$ and increases significantly with increasing equivalence ratio [79]. This seems to represent the threshold for the critical C/O ratio, which is C/O = 0.46. This is in agreement with the values that are described in Section 2.1.1. It is also visible that larger agglomerates are formed under globally rich conditions because no oxygen is available in the post flame region to reduce the particle size [79]. This differs from locally rich areas in globally stoichiometric DISI engine mode. Therefore, the results can not completely be transferred to a DISI engine, especially regarding particle mass and size.

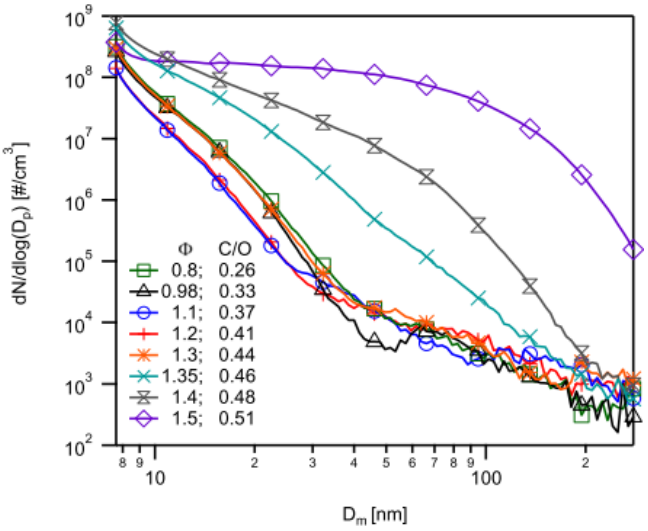

Fig. 2.12.: Measured particle size distribution for different EQR value at complete homogeneous conditions [79].

The presented investigations confirm that a homogeneous mixture has to be ensured to reduce the particle emission from locally rich areas in DISI engines. Therefore, the influence of engine actuator settings, engine geometry and operating conditions on the homogenization process is briefly explained in the following:

- The available mixing time is increased for an early start of injection time [88, 98, 156].
- An increasing engine speed or injected fuel mass decreases the available homogenization time [26, 118].
- Increased charge motion enables a better mixture homogenization, especially for the spray-guided mixing process [26, 36].
- A stratified operating mode increases the particle emissions from fuel-rich areas [118].
- The mixture formation also correlates with spray evaporation time, because the fuel droplets need to be evaporated before the mixing process starts [7].

The morphology of the created soot particles was also analysed in the literature by measuring the particle size distribution. As it is already explained in Section 2.2.1, the particles that result from wall films are supposed to be larger than particles from inhomogeneous mixture preparation. Especially particles caused by late injection time are smaller than for early injection time [18, 156]. In their investigations of particle emissions from DISI engines, Bonatesta et al. [26] conclude that the resulting

particles are very small at high engine speed and load, which is explained by a high fuel stratification combined with high exhaust gas temperatures. It is supposed that the high exhaust temperatures lead to higher oxidation rates in the exhaust gas [26]. Particle emissions of air-guided mixing strategies are smaller than spray-guided particle emissions, which is mainly explained by differences in wall film formation and homogenization [36]. Based on these conclusions, it is assumed that particle emissions of wall-guided injection are also larger than air-guided particles because of the higher tendency to wall film formation.

The formation of liquid wall film does also affect the mixture homogeneity. During the evaporation process, fuel-rich zones are created above the liquid wall film that may also react during combustion if there is time for further mixing [98]. In addition, large amount of liquid fuel films influence the global air-fuel equivalence ratio.

2.2.3 Additional Sources

Fuel Composition

In Section 2.1.2, the effect of fuel composition is already explained considering gas-phase kinetics. The fundamental particle formation process remains the same, but different reaction paths are dominant for different fuel components. Especially aromatic components (such as benzene) increase the formation rate of soot precursor molecules (e.g. pyrene). On the other hand, fuel-bound oxygen reduces the C/O ratio and increases the oxidation rate of the resulting particle emissions. These effects are also valid for particle emissions in an engine context, which is confirmed by several literature studies considering different fuels, such as toluene or ethanol [35, 98, 181, 186, 189]. A literature study on different investigations with various fuel compontents is also presented by Ueberall et al. [181].

However, not only the chemical properties affect the particle formation process in combustion engines, but also the evaporation properties are of special interest in direct injected engine processes. Adding ethanol can increase the particle emissions due to its higher latent heat of vaporization and leads to an increased mixture inhomogeneity [35]. In Fig. 2.13, different ethanol blends are compared for a cold (20°C) and warm (80°C) engine state by Chen et al. [35]. Increasing the ethanol content increases the particle number emissions over the whole size range, which is especially visible for cold engine conditions (dashed lines). This is explained by fuel spray characteristics rather than by the chemical structure of ethanol [35].

These correlations are also explained by Salenbauch et al. [158], who investigated the soot formation process in DISI engines with simulation and measurement methods. They state that increasing the ethanol content can decrease the soot formation in DISI engines because of the chemical bound oxygen, but it is required to optimize the mixing process because of the different evaporation properties [158].

In general, it is hardly possible to identify all fuel components, properties and the chemical composition to determine the influence on the injection and combustion of the fuel in an engine process. Therefore, a number of investigations were performed in the literature to identify a particle index for gasoline fuels [5, 109]. Additionally, Wang et al. [186] hypothecate that differences in particle emissions made by injection system are more important than differences by the composition of commercial fuels on the market. They describe that the PM index of 80 % of worldwide fuels is within the range of 1-2.2, which is below the influence of their study regarding the injection system [186].

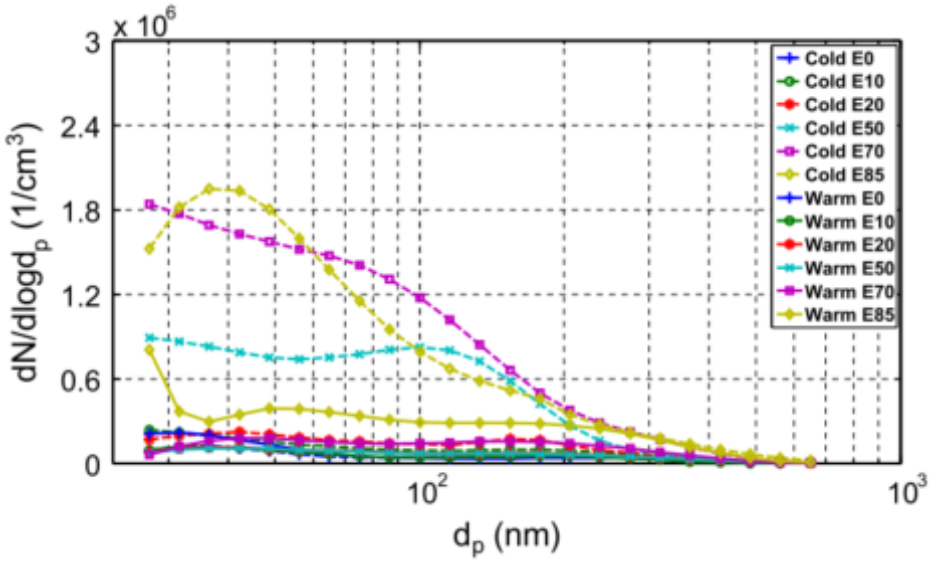

Fig. 2.13.: Particle size distribution of different gasoline/ethanol blends at cold (20°C) and warm (80°C) engine at 1500 rpm [35].

Lubricating Oil

Particle emissions that arise from lubricating engine oil are still not fully explored and part of current research [78]. The effect of engine oil on measured particle emissions is based on several correlations:

- Depending on the measuring system, volatile oil droplets can be recognized as particle emissions. These emissions are not part of the solid soot particles and are typically removed internally by the measuring system.
- Inorganic components in the oil can be emitted as solid particles [126]. These particles are mainly based on metal deposits in the oil.
- Liquid fuel can be bound in the oil, especially on the liner [78]. This fuel does not evaporate completely and undergoes a pyrolysis process during combustion.
- Comparable to liquid fuel films, the oil film that remains during combustion undergoes pyrolysis reactions and forms solid particles.

Hadler et al. [78] measured oil emissions and particle emissions in an DISI engine and identified correlations between increased oil and particle emission, especially for dynamic engine operation with different oil types.

To estimate the relevance of oil-related particle emissions, some investigations are available in the literature that remove mixture and fuel-related effects by changing the injection strategy or the injected fuel components. Hageman and Rothamer [79] investigated particle emissions for a port-fuel injection engine compared to a direct injection. They mention that changing the operating mode to port fuel injection (PFI) especially decreases particle emissions above 30 nm. The total reduction is not quantified by the authors. However, they mention that the remaining particle emissions may be mainly caused by unburned hydrocarbons of remaining fuel in the crevices [79]. Comparable results were also obtained by Maier et al. [12], who investigated particle emissions with methane and hydrogen fuels instead of gasoline. Methane is expected to reduce the particle emissions significantly and

hydrogen does not contribute to the soot formation process. the remaining particles then must arise from non fuel-related sources, such as oil, metal abrasion or inlet air [12]. The authors noted that very little particle emissions above 30 nm could be measured with both methane and hydrogen fuel. Using hydrogen fuel resulted in particle emissions that were reduced by about two order of magnitudes for particle sizes of about 25 nm (value is extracted from [12]). Particles smaller than 10 nm showed similar results for all testes fuels. The authors summarize that there is a fuel-independent amount of particle emission, but the fuel-related sources are dominant processes, especially at higher engine loads [12].

Spray Combustion

Besides the particle formation based on rich-premixed areas in the gas phase and fuel films on the walls, incomplete volatilized, liquid fuel droplets were also identified to create soot particle emissions [26, 198]. Incomplete evaporation leads to spray combustion that is comparable to the particle formation process in diesel engines, especially under stratified, globally lean conditions [118]. However, in a global homogeneous operating mode with single injection pulses, the injected fuel is expected to be completely evaporated until start of combustion. If the evaporation rate is reduced by an increased diameter of the fuel droplets or cold engine conditions, the spray is expected to impinge on the wall and to form a liquid fall film until start of combustion. Even under catalyst heating conditions with a secondary late injection, it is stated that the resulting particle emissions are formed due to liquid wall films on the piston rather than by spray combustion [88]. This is explained by the relative short distance between injector and piston. The characteristic of the spray droplets heavily depends on the applied rail pressure [125, 156].

Thermodynamic Properties

A sensitivity study under PFI conditions revealed that thermodynamic properties, such as in-cylinder pressure and temperature, also influence the resulting particle emissions [79]. This is plausible because of the underlying chemical formation and growth processes that are explained in Section 2.1. The temperature and pressure affect the reaction kinetics of the particle formation, growth and oxidation processes. The results of Hageman and Rothamer [79] are shown in Fig. 2.14 with respect to total particle number emissions for different global equivalence ratio values, air intake temperatures and cylinder pressures. Increasing the intake temperature and the cylinder pressure increases the total emissions.

Thermodynamic properties can also be affected by changing engine actuator settings, such as ignition time. This was experimentally investigated by Sabathil et al. [156], Maricq et al. [118], Drake et al. [52], Pei et al. [146] and Kayes and Hochgreb. [92]. They conclude that late ignition time reduces the particle emissions because of increased exhaust temperatures, leading to post reactions in the exhaust system. In addition, the increased temperatures increase HC oxidation rates and therefore decrease surface growth reactions of soot particles [92]. On the other hand, at stratified operation, advancing the ignition time increases the homogenization at the spark plug [52].

2.2.4 Weighting of Particle Emission Sources

The above described engine-specific particle sources do not contribute to the total emissions in equal share. It strongly depends on the engine type (e.g. port fuel or direct injection), the combustion process and the operating mode instead. Typically, the overall emissions are dominated by one or two

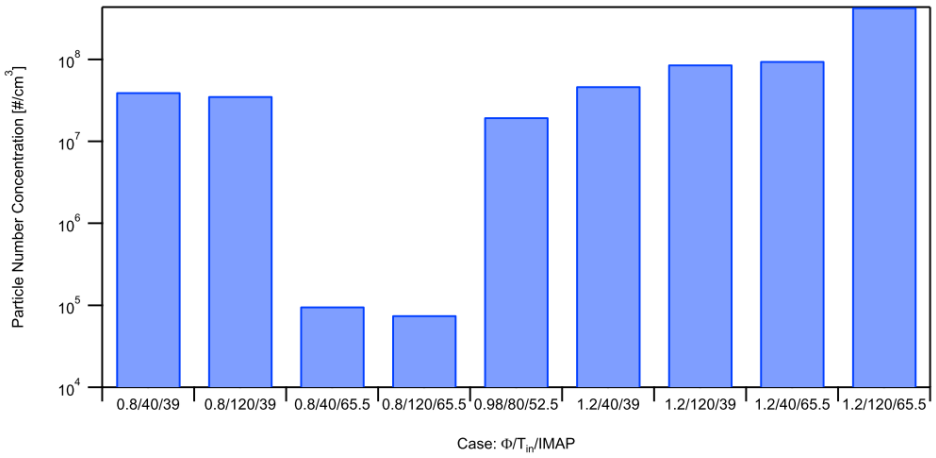

Fig. 2.14.: Influence of global equivalence ratio (ϕ), intake temperature (T_{in}) and intake manifold pressure (IMAP) on particle number emissions with PFI (complete homogenization) [79].

sources because the range of particle concentrations extend over several orders of magnitude. This is of special interest for modelling approaches that need to cover the most relevant particle source in stationary or transient operating mode. In the present work, a spray-guided DISI engine type with central injector position is investigated. The engine runs under global homogeneous operating conditions and includes a turbocharger and variable valve train. Therefore, the ranking of particle emissions sources is based on this engine type and explained in the following.

For stationary operating conditions, Sabathil et al. [156] identified the following engine parameters to be dominant in a DISI engine:

- **Global equivalence ratio**: The particle emissions increase with increased EQR value. This is mainly by increasing local rich mixture compositions. The increased injection duration also decreases the evaporation of injector tip film.
- **Injection time**: An Early injection time increases particle emissions caused by liquid wall films. A late injection time reduces the mixture homogenization and injector film evaporation.
- **Combustion Phasing**: There is a risk of increased particle emissions for early combustion phasing because of a reduced time for evaporation and mixture preparation and reduced exhaust temperatures.
- **Fuel pressure**: Low fuel pressure increases particle emissions because of reduced mixture preparation and increased injection duration. It also increases the risk of wall film creation because of increased fuel droplet sizes.
- **Coolant temperature**: Increased particle emissions occur at cold engine temperatures mainly by wall film formation.

These effects are also influenced by engine geometry and the applied spray targeting. More generalized, Zhao et al. [198] and Bonatesta et al. [26] identified relevant engine states in the (warm) engine operating map:

- **Low engine speed, high load**: There is a poor mixture preparation because of the reduced mixing time at low charge movement and turbulence. An increased injection duration decreases the available time for injector film evaporation.

- **Mid engine speed, mid load**: A reduced time for mixture preparation and injector film evaporation is available at moderate load.
- **High engine speed, high load**: The time for mixture preparation and injector film evaporation is also reduced. The risk of wall film formation is caused by early injection time values.

The increase of emissions as a function of engine load and speed was also confirmed by Maricq et al. [118]. According to Miklautschitsch et al. [125], the injector-induced emissions are dominant for engines that are calibrated to minimize inhomogeneous mixture preparation and wall film formation. Under cold operating conditions, these effects are further increased and liquid wall film also becomes more relevant.

The effects of stationary operating conditions can also be transferred to transient engine operation. This leads to a number of critical operating conditions:

- **Constant driving at moderate speed and load**: The particle emissions are mainly caused by injector tip film.
- **Cold engine start**: Depending on the catalyst heating strategy, a second injection can lead to particle emissions from spray combustion. Furthermore, the wall film formation is increased because of low engine temperatures.
- **High acceleration**: An increased load at different engine speeds leads to particle emissions, as it is already explained for stationary operating mode.
- **Acceleration after fuel cut-off**: This reduces the engine wall temperatures and leads to increased particle emissions from liquid wall films. Depending on the engine oil consumption, it also increases the risk of oil-induced particle emissions.
- **Global rich operating mode**: A globally rich air to fuel ratio during transient operation increases particle emissions according to a stationary operating mode.

Summarizing, under stationary and transient operating conditions, the risk of inhomogeneous mixture preparation, remaining liquid wall film and injector-tip-induced particle emissions are identified to be the main contributor to the overall emissions. They are superimposed by the chosen fuel type and thermodynamic properties. Spray combustion and oil-induced particle emissions are expected to be of minor interest for the relevant engine that is considered in the present work.

2.3 Classification and Overview of Simulation Techniques

Over the past decades, a large number of simulation models have been developed to calculate the soot formation process for different kinds of combustion processes, such as diffusion flames, premixed flames or in the context of internal combustion engines. It is hardly possible to extensively and chronologically describe the development of these models. For example, a comprehensive summary of Kennedy (1997) [97] already contains more than 30 pages. A more recent study was published by Omidvarborna et al. (2015) [141] and focusses on soot modelling regarding diesel combustion. Therefore, only some essential characteristics of the different levels of detail are explained below. A greater emphasis is placed on the explanation of available detailed models that are used in the context of gasoline engines.

Generally, the type of soot model is categorized by its level of detail in describing the underlying physical and chemical processes (further described in Section 2.1). The simplest types are the *empirical*

models that are typically related to gas turbines or combustion engines and that use empirical correlations to describe soot formation as a function of engine operating conditions [97]. They use experimental data and provide excellent agreement for a given set of operating conditions [141]. They are easy to implement and allow sensitivity analysis at low computational cost but cannot describe the underlying mechanisms of the soot formation process. They are thus only useful for testing previously established experiments under similar conditions [141] and they give no additional information about the soot morphology. A widely cited empirical model for diesel engines was proposed by Khan et al. [100], who assumed that the soot formation rate is only controlled by the soot inception rate. They calculated this inception rate as a function of pressure, equivalence ratio, temperature and a number of modelling parameters that were determined by comparing the results to diesel engine experiments. An improved correlation was proposed by Mehta and Das [121], including a seven parameter correlation for diesel engines that considered the spray mixing and swirl mixing rate among other engine specific parameters.

A simplified PAH and soot chemistry is taken into account by the *semi-empirical models*, leading to the development of rate equations for reactions of simple soot precursors (such as acetylene) and soot particles [97]. For example, the model of Smith [166] calculates the rate of particle nucleation and the size of a soot particle was assumed to be limited by the depletion of the growth species [97]. Other widely applied semi-empirical models were proposed by Tesner et al. [177] or Hiroyasu and Kadota [84]. More sophisticated semi-empirical methods also include rate equations for soot formation, growth and oxidation with simple models for these processes [97]. The disadvantage of these models is that they cannot be extended easily to different fuels or pressures because of their empirical inputs in the rate equations.

This leads to the set of *detailed-chemistry models* that include a high level of detail in the description of the PAH kinetics and soot formation processes [141]. Although these models have the highest requirements in terms of calculation effort, their application is becoming more feasible due to the increased speed of modern computers [93]. As a result, this type of model has become the state of the art choice in many modern applications. The gas-phase processes are described by detailed chemical mechanisms that contain hundreds of species and chemical reactions [141]. The interface between the gas-phase and soot is typically described by the interaction of aromatic species such as benzene, naphthalene or pyrene [22]. The three most common methods for the calculation of particle dynamics are the *method of moments*, the *sectional method* and the *particle tracking method*, described in the following.

Method of Moments

With the method of moments, the soot size distribution is described by calculating the transport equations of its moments [22]. To calculate the complete size distribution, an infinite number of moments is required. However, the required number of moments can be reduced when the shape of the distribution function is known a priori [22]. The advantage of this lumping technique is that it is computationally efficient since only a few equations are required to describe the change of the first moments [97].

The difficulty of this method is, that the equations for the moments are unclosed, which means that moments that are not directly solved are required to compute the source terms for the considered moments [132]. This leads to a number of approaches with different closure models. The most widely cited model, called *method of moments with interpolative closure* (MOMIC), was proposed and further developed by Frenklach and co-workers [64, 66, 123, 124]. With MOMIC, the equations for the moments are closed by logarithmic polynomial interpolation, leading to a numerically well-behaving and computationally efficient solution [132]. However, this method is not suitable for multivariate

distributions, which is why other models have been developed. These models can be summarized under the name *quadrature method of moments* (QMOM) [117, 120], where the size distribution is described by a series of delta functions and the moments are approximated by Gauss quadrature [132]. The direct quadrature method of moments can be used for multivariate distributions (DQMOM), but the calculation of the equations may be extremely ill-conditioned [132]. Therefore, it is a current field of research and a variety of different approximations are published to solve this area of conflict, such as the HMOM [132], EQMOM [31] CQMOM [30] or the recently proposed ECQMOM [158] methods.

Sectional Approach

In the sectional approach, the aerosol distribution function is divided into a finite number of groups with different sizes, each representing a set of particles [97]. Compared to the method of moments, this comes at a higher computational cost (depending on the number of sections) but accurate predictions of the size distribution function can be obtained [97, 132]. The sections are treated as "virtual" species with averaged properties and they can be easily coupled with the gas-phase chemistry [22]. This enables the calculation of the particle size distribution without a priori knowledge of the shape [22]. A number of publications are available using a sectional method to calculate the soot formation of laminar diffusion flames [42, 55] and laminar premixed flames [153, 157].

Particle Tracking Method

Probably the most complex technique to describe the particle formation process is tracking each particle individually or by a stochastic set of particles, which is also known as the *Monte-Carlo method*. In contrast to the sectional methods, the particles are not lumped by their properties but by their number, leading to an even higher degree of detail [22]. A direct simulation Monte-Carlo algorithm (DSMC) was proposed by Gillespie (1975) [70] to investigate the stochastic coalescence process in clouds. The main limitation of this method was the calculation time, which increased quadratically with the initial number of stochastic droplets. The groups of Eibeck and Wagner (2000) [57] and Goodson and Kraft (2002) [73] developed a more efficient method with orders of magnitude lower CPU times and thus enabled the extension to different problems that include population balance equations. Balthasar and Kraft (2003) [16] then combined the method with a detailed kinetic model to calculate the temporal development of the particle size distribution of laminar premixed acetylene flames. Further improvements of the method followed, such as the extension to higher pressures [145, 164], the direct coupling to the gas-phase chemistry [33] and an improved modelling of the PAH-particle interaction and aggregate formation [161]. The combination of good efficiency and a high level of detail makes this method also suitable for the calculation of combustion engine soot formation [60].

Modelling Soot Formation in Gasoline Engines

Compared to empirical or semi-empirical methods, much more effort is required to calculate the soot formation process in combustion engines with detailed-chemistry models. This is due to the additional necessity of calculating the thermodynamic properties in the combustion chamber and the mixture formation process. Therefore, modern soot models for gasoline combustion engines engines typically combine components for calculating the in-cylinder processes, the gas-phase kinetics and the particle dynamics. As a result, a comparatively small number of models is found in the literature dealing with gasoline engine soot formation.

Etheridge et al. [60] developed a method to calculate the soot mass, number density volume fraction and surface area of a DISI engine running in stratified operating mode. The engine process is described by a stochastic reactor model (SRM), which belongs to the group of Monte-Carlo methods. The cylinder charge is split into an ensemble of particles that represent the distribution of temperature, pressure and concentration of chemical species in the combustion chamber. Sub-models, such as a turbulent mixing model, stochastic heat transfer, piston movement and direct-injection model are also included. In addition, a flame propagation model has been added to enable SI simulation. The engine model needed to be calibrated to match an experimental pressure profile in homogeneous operating mode. Reaction kinetics were modelled by a reaction mechanism that contains 208 species and 1002 reactions. Soot formation was modelled based on a Monte-Carlo method [16, 73, 145]. The model was able to show the trend that the emissions increase at later injection times due to charge stratification. Within the publication, no additional information are given about the computational time of the simulation. However, in an earlier published work of a SRM for homogeneous charge compression ignition (HCCI) engines [175] the computational time of the engine model for one working cycle was mentioned to be between $30 - 705$ min, depending on the rate of down-sampling of the simulated properties.

Liang et al. [111] implemented the method of moments in the FORTÉ CFD Code to simulate a spray guided DISI engine under stratified conditions. The gas-phase mechanism contained of 230 species and 1740 reactions and the method of moments proposed by Frenklach [25] was used for particle tracking. The results showed the functionality of the method and were analysed qualitatively, but they were not compared to measured data.

Salenbauch et al. [159] combined an ANSYS CFX model for DISI engines and a tabulated calculation of the soot volume fraction. The soot model included a detailed gas-phase reaction mechanism for iso-octane and ethanol mixtures, soot nucleation by pyrene collision as well as surface growth by the HACA mechanism and pyrene condensation. The population balance equation was solved by the ECQMOM model. The method was capable to calculate the soot formation process in fuel-rich areas of the combustion chamber for different fuel compositions.

Jiao and Reitz [87] combined the KIVA CFD code with a semi-empirical soot model [86, 184] (based on the model of Hiroyasu [84]) to calculate soot emissions of DISI engines with special attention to wall-film-induced particle emissions and variable fuel types. The soot model was coupled with a chemistry mechanism that calculated PAH molecules up to pyrene and included equations for soot inception, surface growth, coagulation and oxidation. The model was able to calculate wall-film-induced pyrolysis reactions and soot formation under stratified conditions.

2.4 Closing Remarks

In this chapter, the fundamentals of particle formation were presented that determine the morphology of soot particles in fuel-rich combustion processes. Furthermore, the most relevant particle sources in modern gasoline engines were analysed and an overview of available simulation methods was given. This information is used to develop a simulation method which is intended to calculate the particulate emissions of DISI engines during driving cycles in terms of particle number, mass and size distribution.

The particle number, mass and size are influenced by different physical and chemical processes during formation. Depending on thermodynamic properties and the gas-phase composition, the resulting morphology and the size distribution varies. This leads to the necessity that the fundamental processes should be described with a high level of detail. Therefore, a detailed soot model and reaction mechanism are included in the current work. This principally leads to a conflict with the

requirement of calculating complex driving cycles. However, the Monte-Carlo method has already been applied to gasoline engines, generally shows a high efficiency regarding computational time and provides results with a high quality. This method is thus further used in the context of this work. Aside from this, the method of moments also plays an increasing role due to the ongoing development and can therefore be seen as an alternative to the chosen approach.

The investigations of soot sources in gasoline engines reveal that they contribute by a different proportion to the overall emissions, depending on the operating conditions. Due to the complexity of transient driving cycles, it is purposeful to consider all main causes that were mentioned. Empirical approaches, such as the mapping of stationary measured particle emissions to transient driving cycles are not capable to take the additional effects into account that occur during transient engine operation. They can also not provide the required quality of boundary and starting conditions for the soot formation models. By the authors knowledge, gasoline soot-formation processes have been simulated exclusively with detailed 3D-CFD or stochastic reactor models in the literature when combined to detailed reaction kinetics. This of cause is plausible due to the necessity of accurate input data for the soot models, but it obviously is in conflict with the computation time requirements of a driving cycle simulation.

Besides detailed 3D-CFD simulations and empirical models, phenomenological approaches become increasingly important. They correlate empirically observed phenomena in a way that is consistent with the fundamental theory, but without being directly derived from it [141]. Different processes are described by additional sub-models, using physical and chemical relations with an adjustable level of detail. These models are quite reliable, especially when the accuracy of the model parameters is low [141]. In the context of the current work, the engine parameters thus are simulated using a one-dimensional engine modelling tool with already included phenomenological combustion and turbulence approaches. The required chemical boundary conditions, which are not determined directly by the engine process simulation, require the development of new phenomenological sub-models that include mixture preparation, wall film formation and injector tip film. The model is not intended to meet the requirements of calculating soot emissions a priori. Rather, after an initial calibration (including 3D-CFD simulations and particle measurement information) it is supposed to be able to get reliable results even when the parameters in the system change significantly. It is therefore also important to examine the limits of the modelling technique in the context of this work.

By the authors knowledge, this is the first attempt of generating a model that combines a reduced engine process simulation with detailed chemical kinetics and soot formation methods to enable the computational efficient calculation of stationary and transient operating conditions of modern DISI engines. Detailed explanations about the model concept and structure are presented in the next chapter.

3 Model Concept and Structure

Preface for model concept and structure:
Parts of the presented modelling approach have been published previously at the conference VPC-Simulation and Test 2015 [67]. This includes the model process scheme, the application of a multi-zone approach for different particle emission sources in gasoline engines and the validation strategy.

3.1 Modelling Particle Emissions in an Engine Context

3.1.1 Physical Modelling Approach

Modelling the particle emissions of DISI engines requires the identification of areas in the combustion chamber that lead to fuel-rich combustion or pyrolysis processes. Not all effects are considered in the context of this work. However, the effects that were identified to contribute most to the total emissions are taken into consideration (see also Section 2.2.4). This includes effects at stationary operating points and in the context of transient driving cycles. A modelled physical event chain along the fuel path that leads to fuel-rich zones is presented in Fig. 3.1.

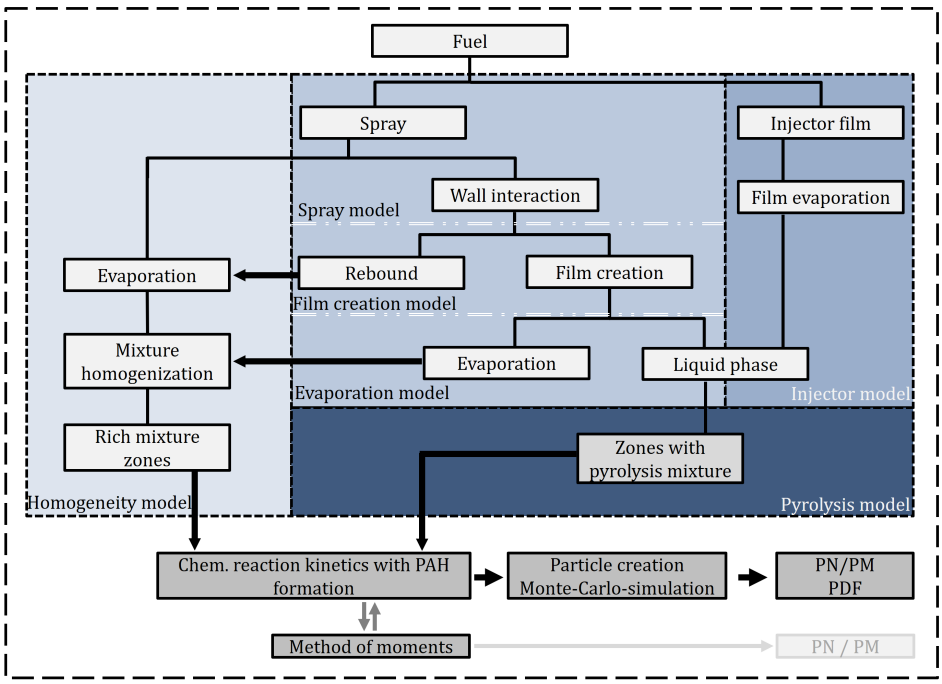

Fig. 3.1.: Physical modelling path of simulation framework from fuel injection to particle emission in exhaust system.

the modelling process is divided into three main paths:

1. Most of the injected fuel evaporates during load exchange and mixes up with the air/residual gas mixture. If this homogenization process is not completed until start of combustion, areas with sub-stoichiometric conditions remain in the gas-phase.

2. Depending on injection time and injected fuel mass, the spray can impinge the surrounding walls (especially liner or piston) and eventually builds up a fuel film. In case of an incomplete evaporation of the remaining film, pyrolysis processes occur due to the high temperatures in the burned zone and lead to particle formation processes.

3. Depending on the injector state and geometry, a part of the fuel remains at the injector tip and pre-stage after injection ends. An incomplete evaporation of this fuel also leads to a local area of particle formation.

The information of each path is not given locally resolved, but in terms of total mass fraction. This in summary forms a multi-zone approach that enables the calculation of local effects without a detailed resolution of the coordinates (named as “quasi-dimensional (QD)”). Each of the described paths is considered by one or more newly developed sub-models to identify the corresponding information of the zones that are required for gas-phase reaction kinetics. The mathematical description and further use of the zones is explained in the following sections. The sub-models are explained in detail in the following chapters.

Reaction mechanisms that consider the formation of polycyclic aromatic hydrocarbons, which are prerequisites for a particle formation, are already available (described in Section 2.1.2). These reaction mechanisms need information about species composition and thermodynamic properties, such as pressure and temperature profiles. The thermodynamic properties are considered by a complete engine process simulation, as it is further explained in Section 3.1.2. The selected reaction mechanism and the mathematical explanation of the reaction kinetics is presented in Section 3.2.

Solving the gas-phase reaction kinetics is the prerequisite for the calculation of the particle formation process in the solid phase. In the current work, the particle formation process is simulated by an inclusion of the Monte-Carlo tool SWEEP [144]. This enables the calculation of a complete stochastic particle ensemble and fulfils the demand of calculating particle number, mass and size distribution with an acceptable calculation time. Details about the implementation of the Monte-Carlo tool are presented in Section 3.3.1.

The connection between the gas-phase reaction kinetics and the solid-phase particle formation and growth processes is performed by the implementation of a method of moment, as it is further described in Section 3.2.3. This enables the consideration of species sink terms in the gas-phase caused by particle processes.

After calculating the information for each zone (initial conditions, reaction kinetics, particle formation), the zones are recombined to get the total result for one cylinder including particle number, mass and size distribution. A validation strategy is developed with measurements on an engine test bench to proof the concept of the model. More details about the measurement procedure are explained in Section 3.4.

In a first step, the simulation framework is created for stationary operating points, but can be easily extended to a simulation of driving cycles (further described in Section 7.3).

3.1.2 Software Coupling

The interactions of the engine process simulation, the gas-phase reaction kinetics and the particle formation process are realised by a complex simulation framework that consists of different software applications and programming languages to combine the specific advantages. This includes calculation time efforts, automation possibilities and usability in the industrial engine development process.

The main part is developed in MATLAB [178] and includes all sub-models and the coupling of the different model parts. A schematic presentation of the program interactions is shown in Fig. 3.2 and briefly explained in the following.

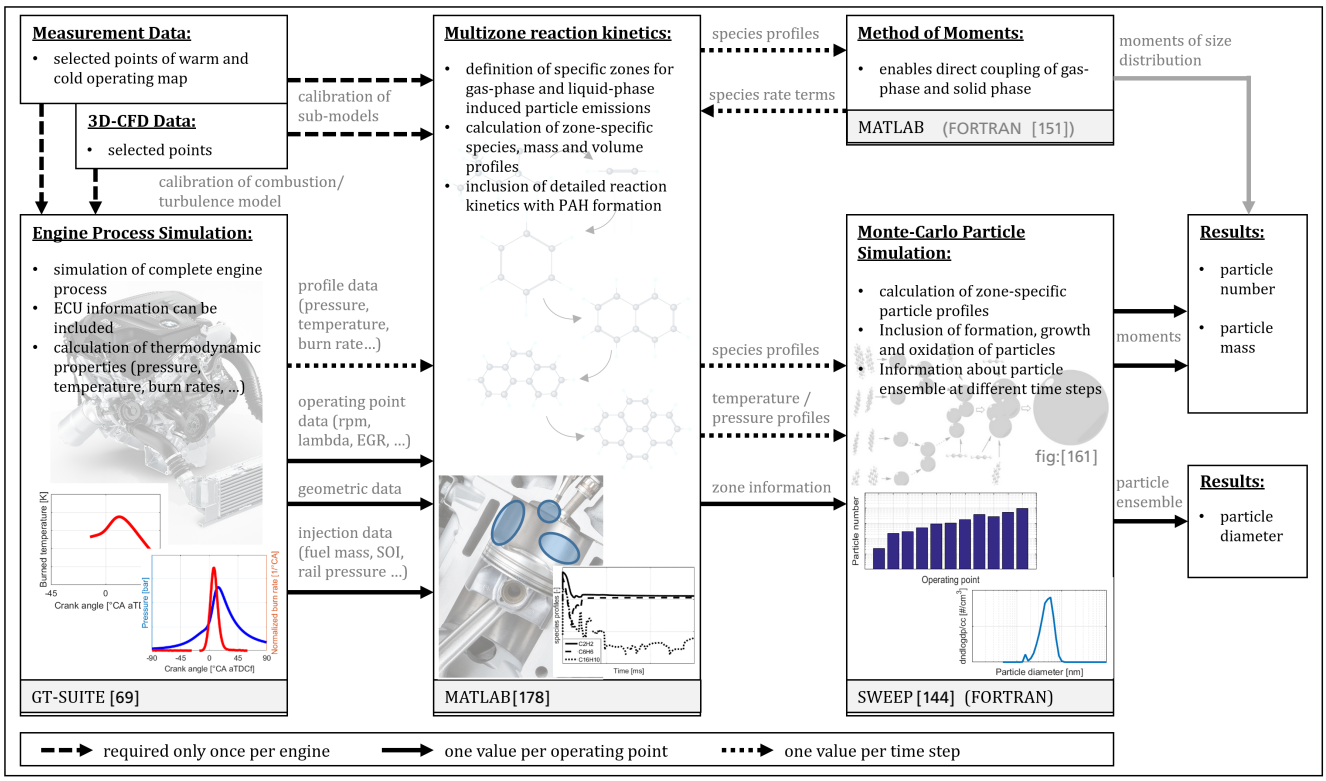

Fig. 3.2.: Process scheme of the complete simulation method with corresponding input and output data. Combination of different application tools and programming languages.

GT-SUITE

The engine process simulation is realised using the commercial software GT-SUITE [69]. The software allows the implementation of additional model components by Fortran user-routines. Simulating the complete engine process without additional measured information leads to the risk of a big error chain because the thermodynamic properties of the engine process simulation directly affect the processes of particle formation.

For this reason, the particle emission model development is performed with an reduced engine simulation model. The burn rate of the combustion process is calculated in combination with measured pressure profiles. The pressure sensors are applied in the intake and exhaust port and in the cylinder. In combination with a wall heat transfer model, the burn rate and the corresponding temperatures can be simulated to match the measured pressure profile. The gas load exchange is calculated to match the measured pressure profiles with the intake and exhaust pressure sensors. The engine model only consists of one cylinder and the corresponding inlet and exhaust pressure boundary conditions. This significantly reduces the dependency on the quality of the engine process simulation.

However, the application of the model to a transient operation requires the simulation of the complete engine. Besides the complete engine geometry, this includes an entrainment combustion model ([137]) that is updated with a quasi-dimensional turbulence model [75, 76]. The implementation of

these user-routines only requires a calibration based on a number of measurement points of the engine operating map and additional 3D-CFD simulations to estimate the turbulent kinetic energy.

The simulation results are stored and transferred to the MATLAB part of the model for each operating point. This includes crank angle resolved data and values that are constant for one operating point or that are constant for the engine type. A summary of the transferred data is shown in Tab. 3.1.

Tab. 3.1.: Transferred parameters from engine simulation process to multi-zone model for every operating point.

	Parameter
crank angle resolved data	cylinder pressure, cylinder volume, burned fuel fraction, unburned temperature, burned temperature, piston position
operating point data	engine speed, ignition time, global equivalence ratio, residual gas fraction, exhaust volume flow, exhaust open time, inlet closing time, average exhaust temperature, ignition delay, liner/piston/cylinder head temperature, average inlet temperature, average inlet pressure
injection data	injection time start, rail pressure, injected total fuel, fuel temperature
geometric data	bore/stroke, nr. of injection nozzles, nozzle diameter, nozzle directions, nr. of cylinders

MATLAB

The complete particle simulation structure and all sub-models are implemented in MATLAB [178]. This includes controlling the pre-processing (inclusion of engine simulation results), the handling of the multi-zone approach (see also Section 3.2) and post-processing (recombination of zones and calculation of final results). In addition, the required input data are sent to the particle simulation tool SWEEP and the zone-specific particle results are received from SWEEP. An overview of the transferred data between MATLAB and SWEEP is shown in Tab. 3.2.

In the context of this work, MATLAB offers the advantages of a number of built-in function to solve systems of stiff ordinary differential equations (especially to solve the species conservation equations). With the corresponding toolbox, MATLAB also offers functions for non-linear optimization tasks that are required for model parametrization.

Tab. 3.2.: Transferred parameters between MATLAB and SWEEP for each operating point.

	Parameter
MATLAB to SWEEP	species profiles, zone temperature profile, pressure profile, active surface area, calculation time, calculation tolerances, expected maximum 0th moment of particle size distribution
SWEEP to MATLAB	particle mass profile, particle number profile, diameters of particle ensemble

SWEEP

SWEEP is a population balance solver for particulate systems that are dispersed in a gas-phase [144]. It is based on a Monte-Carlo method and written in Fortran 90. The tool provides the possibility of calculating the complete soot formation and oxidation process and offers the option to import the time resolved gas-phase properties. Further information about the inclusion of SWEEP in the simulation framework can be found in Section 3.3.1.

The simulation tool provides the advantage of getting time-resolved profiles of the particle number, mass and size distribution with a comparatively moderate calculation time effort.

Cantera

Cantera is an object-oriented software tool that is written in C++ and Fortran 90 [74]. It can directly be integrated in MATLAB as a toolbox and offers the possibility of handling arbitrary reaction mechanisms. These mechanisms can be included in Chemkin format and will be converted into the Cantera-specific structure.

In the context of this work, Cantera is mainly utilized to create gas mixtures of different compositions and thermodynamic states (e.g. mixtures of residual gas, air and fuel). The properties of these mixtures, such as density or molecular weights, can then be calculated. Moreover, the production rates of the species are calculated for a given mixture by evaluating the reaction equations of the reaction mechanism. In combination with a reaction mechanism that includes the PAH formation equations, this provides a fast method to solve the species conservation equations of the multi-zone approach.

3.1.3 Programming Information

The complete MATLAB-based simulation framework is programmed object-oriented in a modular approach. This increases the flexibility of the model and allows the possibility of adding or removing specific particle formation processes when it is necessary. This is of special interest for the simulation of complete driving cycles. For example, it is possible to deactivate the spray-wall-interaction model at warm operating conditions to significantly reduce the calculation time for each time step.

The objects are separated into physically-based and general objects. The complete set of objects is shown in Fig. 3.3 and briefly described in the following. The *Engine* object mainly includes the properties that are constant for one operating point and that are included from the engine process simulation. It also includes, in case of model calibration, the measured particle emission values for comparison to the simulation results. The *Cylinder* object is supplied by the crank-angle resolved data of the engine process simulation. Both objects are prepared to get the information either from stationary operating points or during a transient driving cycle at each time step.

The *Injector* object includes the calculation of the remaining injector film at ignition time and initializes the corresponding pyrolysis zone. The pyrolysis zone from wall-films is calculated by the *Spray-Wall interaction* object and includes spray penetration, spray-wall interaction and evaporation processes to calculate the remaining wall film at ignition time.

The *Multinetwork* object calculates the homogenization process and the corresponding zones that result from incomplete mixture formation. Each zone is then included into one *Network* object that

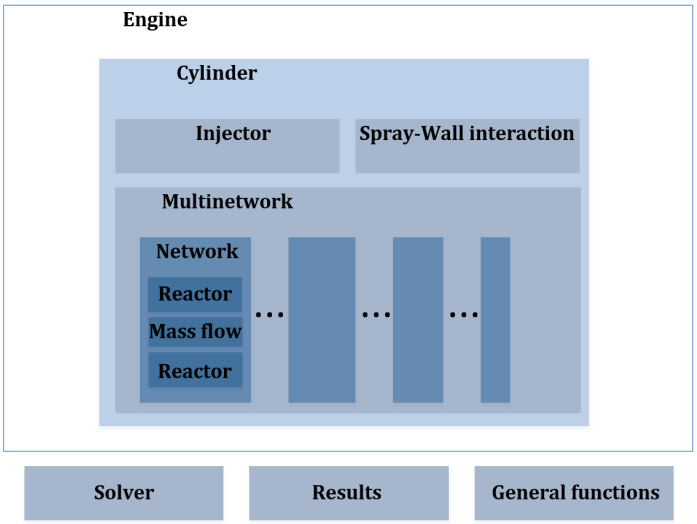

Fig. 3.3.: Object structure of multi-zone approach in MATLAB programming framework.

consists of a burned and unburned *Reactor* object. The reactors are linked by a *Mass flow* object that calculates the species flow from the unburned to the burned zone.

The particle formation processes are calculated separately for each zone. Solving the differential equations is controlled by the *Solver* object that includes numerical information (tolerances, calculation time) and manages the import and export between the MATLAB and SWEEP results.

The *Results* object combines the results for all zones and evaluates the total particle emission value. It also calculates the particle size distribution with the consideration of counting efficiencies of the measurement system. In addition, all relevant results are stored in this object for every operating point / time step for post-processing purposes.

The program is designed to calculate each operating point separately. This enables the simulation process to be split on different CPU cores or workstations to decrease the overall calculation time.

3.2 Solving Gas Phase Kinetics

3.2.1 Calculation of Mixture Induced Reactor Zones

The creation of a zero-dimensional multi-zone model in combination with detailed chemistry is already a common methodology in the context of engine simulation, especially for HCCI engines [1, 13, 19]. The multi-zone approach has also been successfully applied for the calculation of engine knock and NO_x emissions in DISI engines [113, 199]. In most cases, the zero-dimensional multi-zone approach is directly coupled to 3D-CFD simulations. In a recent work of Dorsch [50, 199], the NO_x emission approach was applied to the simulation of a complete driving cycle. In this case, no 3D-CFD information are required and the combustion chamber is divided into one burned and unburned zone that are represented by well-stirred reactors that exchange mass, species and energy.

In the current work, a comparable technique is applied that combines the above described approaches and extends the methodology within the context of particulate emissions. A variable number of zones is created and no direct coupling to 3D-CFD simulations is considered. Note that, in the context of this work, the term *zone* is used to describe a pair of well-stirred reactors that are coupled by a mass flow controller.

The definition of the zones that result from fuel-rich mixtures in the gas phase is based on the mass fraction information of the statistical equivalence ratio (ϕ) distribution in the combustion chamber. This information can either be obtained from 3D-CFD simulations or from the homogenization submodel that is described in Chapter 5. In both cases, the integral distribution function of the equivalence ratio is stored at ignition time for the current operating point. In case of a perfect homogeneous mixture, only one zone is present that is based on the global equivalence ratio. Otherwise, the number of zones is variable and can be defined by a specific equivalence ratio increment EQR_{incr} or mass fraction range. In the current work, the number of zones is defined by a constant equivalence ratio increment because of the expected sensitivity of the particle formation on the equivalence ratio value. An example of the zone definition based on the integral distribution function is shown in Fig. 3.4.

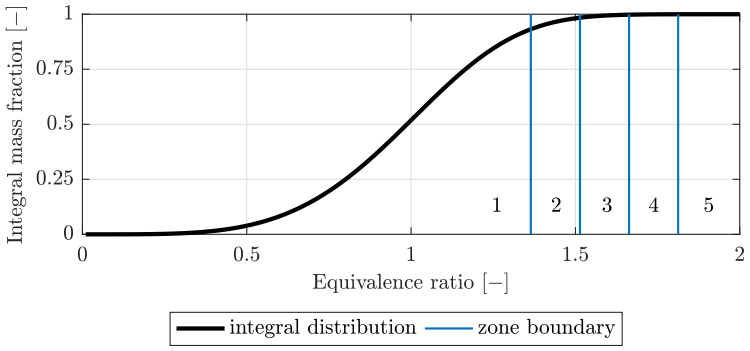

Fig. 3.4.: Definition of zone numbers based on integral EQR distribution function. Number of zones is variable. All values below the soot threshold are lumped into one zone.

As it is shown in the figure, all values that exceed the soot threshold $EQR_{\text{threshold}} = 1.4$ (based on a C/O threshold, as further defined in Section 5.1.1) are lumped into one additional global zone. This is done because no particle emissions are expected there and the required calculation time is significantly decreased if the number of calculated zones is reduced. The number of zones is also decreased by calculating a maximum EQR value from the integral distribution function with $f(EQR_{\text{max}}) = 0.9999$. This reduction of the maximum value does not effect the result but decreases the total zone number.

$$n_{\text{zones}} = (EQR_{\text{max}} - EQR_{\text{threshold}}) / EQR_{\text{incr}} + 1 \tag{3.1}$$

The calculated result is rounded up to the nearest integer number, resulting in a new increment. The corresponding mean EQR value and total mass fraction is calculated afterwards for each zone.

In the context of the simulation framework, every zone consists of a burned and unburned reactor and a mass flow object that connects the reactors. This is resembling the two-zone approach of the combustion process in the engine process simulation. Both reactors are assumed to be perfectly stirred and the reaction kinetics are only considered in the burned reactor as the temperatures of the unburned reactor are not sufficient for particle formation processes. In Fig. 3.5, a schematic visual presentation of the zone and reactor creation is shown. Note that there is no local resolution in the phenomenological model, but the zones are only defined by mass and volume information. During combustion, the volume of the unburned reactor decreases while the burned reactor volume increases. In the following, the initial conditions and thermodynamic properties are explained for the modelled parts.

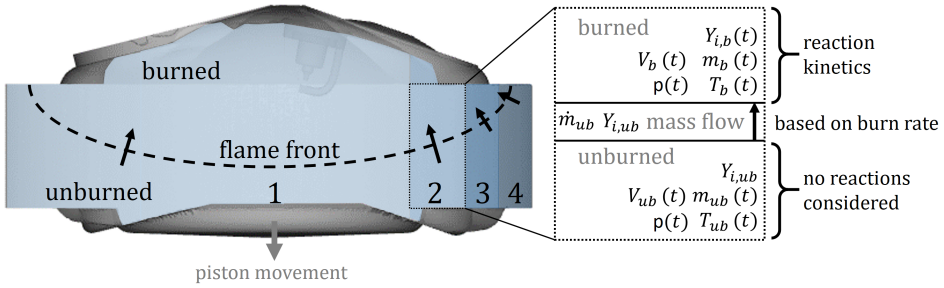

Fig. 3.5.: Schematic presentation of zone creation from inhomogeneous mixture preparation. Parameters of the burned (b) and unburned (ub) reactors and transfer properties of the mass flow controller are given.

Unburned reactor

The unburned reactor is initialized with the pressure and unburned temperature at ignition time and a constant gas composition that is based on the global residual gas mas fraction (Y_{EGR}) and the zone-specific air-fuel ratio λ. In this work, the fuel is approximated by pure iso-octane (C_8H_{18}), leading to a stoichiometric air-fuel ratio of $L_{\mathrm{St}} = 15.1$. The fuel mass m_f can be set to an arbitrary value (here: 1 mg), since a conversion is then carried out in mass fractions.

$$m_{\mathrm{f}} = 1 \tag{3.2}$$

$$m_{\mathrm{air}} = \lambda \cdot L_{\mathrm{St}} \cdot m_{\mathrm{f}} \tag{3.3}$$

$$m_{O_2,\mathrm{fresh}} = 0.233 \cdot m_{\mathrm{air}} \tag{3.4}$$

$$m_{N_2,\mathrm{fresh}} = 0.767 \cdot m_{\mathrm{air}} \tag{3.5}$$

$$m_{\mathrm{EGR}} = \frac{Y_{\mathrm{EGR}} \cdot (\lambda \cdot L_{\mathrm{St}} + 1)}{1 - Y_{\mathrm{EGR}}} \cdot m_{\mathrm{f}} \tag{3.6}$$

$$m_{\mathrm{total}} = m_{\mathrm{air}} + m_{\mathrm{f}} + m_{\mathrm{EGR}} \tag{3.7}$$

The estimation of the residual gas composition is performed with an equilibrium solver of a gas object with the pressure and temperature of the unburned zone at ignition time and the air-fuel ratio of the zone. Only the major species CO, CO2, O2 and H2O are considered while the rest is added to nitrogen as a simplification. The resulting mass fractions are then multiplied with the total residual gas mass m_{EGR} to get the total mass of each species i in a burned state $m_{i,\mathrm{burned}}$. The total mass of the considered species is then calculated by

$$m_{O_2,\mathrm{total}} = m_{O_2,\mathrm{fresh}} + m_{O_2,\mathrm{b}} \tag{3.8}$$

$$m_{N_2,\mathrm{total}} = m_{N_2,\mathrm{fresh}} + m_{N_2,\mathrm{b}} \tag{3.9}$$

$$m_{\mathrm{f,total}} = m_{\mathrm{f}} \tag{3.10}$$

$$m_{[CO,H_2O,CO_2],\mathrm{total}} = m_{[CO,H_2O,CO_2],\mathrm{b}} \tag{3.11}$$

and can be divided by m_{total} to get the information about the species mass fraction $Y_{i,\mathrm{total}}$ in the unburned reactor. The current mass of the unburned reactor in each zone $j = 1 \ldots n$ is based on the zone mass fraction Y_j and the global mass in the combustion chamber, that can be calculated with the ideal gas law at ignition time. At this time state, the complete combustion chamber is in an unburned state.

$$m_{ub,j} = \frac{p_{\mathrm{cyl}} \cdot V_{\mathrm{cyl}} \cdot M_{\mathrm{global}}}{R \cdot T_{ub}} \cdot Y_j \tag{3.12}$$

Burned reactor

At ignition time, the size of the burned zone is theoretically zero because no flame front is present. However, because of numerical stability the burned reactor is initialized with a volume of $V_{b,j} = 10^{-30}$ m^3 and a gas composition that corresponds to the equilibrium solution of the unburned zone. Because of the small reactor size and the mass flow from the unburned reactor, this does not noticeable affect the species conservation equations.

At ignition time, the complete set of mixture-induced zones is defined and each zone consists of a burned and unburned reactor. The number of zones results from the homogeneity information of the combustion chamber. During combustion, a mass flow from the unburned to the burned zone exists, consisting of the unburned mixture composition.

Massflow controller

Using the information of total injected fuel m_{f}, the mass fraction of each zone $Y_1 \dots Y_n$ and the corresponding EQR values, the fraction of total injected fuel mass in each zone $Y_{\mathrm{f},1} \dots Y_{\mathrm{f},n}$ can now be calculated by a system of linear equations.

The boundary conditions are given by mass conservation as $\sum_{j=1}^{n} Y_{\mathrm{f},j} = 1$ (Eq. 3.13) and $\sum_{j=1}^{n} Y_j \left(\lambda_j * L_{St} + 1\right) = 1$ (Eq. 3.14). In addition, the air-fuel ratio of each zone must match the prior determined value (Eq. 3.15). An example for two zones is given as follows:

$$
\begin{aligned}
Y_{\mathrm{f},1} &+ Y_{\mathrm{f},2} &&= 1 && (3.13)\\
Y_{\mathrm{f},1}\left(\lambda_1 * L_{St} + 1\right) &+ Y_{\mathrm{f},2}\left(\lambda_2 * L_{St} + 1\right) &&= 1 && (3.14)\\
Y_{\mathrm{f},1}\left(\lambda_1 * L_{St} + 1\right) &+ 0 &&= Y_1 && (3.15)
\end{aligned}
$$

The system of equations can then be transferred to a matrix for a variable number of zones n. The number of rows and column of the matrix equals the number of zones $n+1$.

$$
\begin{bmatrix}
1 & 1 & \dots & 1 & 1 & 0 \\
\lambda_1 \cdot L_{St} + 1 & \lambda_2 \cdot L_{St} + 1 & \dots & \lambda_{n-1} \cdot L_{St} + 1 & \lambda_n \cdot L_{St} + 1 & -1 \\
\lambda_1 \cdot L_{St} + 1 & 0 & \dots & 0 & 0 & -X_1 \\
0 & \lambda_2 \cdot L_{St} + 1 & \dots & 0 & 0 & -X_2 \\
\vdots & & \ddots & & & \vdots \\
0 & 0 & \dots & \lambda_{n-1} \cdot L_{St} + 1 & 0 & -X_{n-1}
\end{bmatrix}
=
\begin{bmatrix}
1 \\ 0 \\ \vdots \\ 0
\end{bmatrix}
\qquad (3.16)
$$

$$
\lambda_{1\dots n} = \frac{1}{\phi_{1\dots n}} \qquad (3.17)
$$

The linear system of equations is solved by multiplying the inverse matrix with the vector on the right side using a built-in MATLAB function. The corresponding boundary conditions (EQR value, total mass fraction) of the zones must match the preassigned values. With the resulting fuel fraction, the time-resolved mass flow of all zones can be calculated in differential form, starting with the fuel mass flow that is based on the total burned fuel fraction $Y_{\mathrm{f,burned}}(t)$ (cf. engine process simulation). In

addition, the mass flow of fresh air and residual gas (EGR) are calculated and summed up to the total mass flow rate.

$$\frac{dm_{\mathrm{f},j}}{dt} = \frac{Y_{\mathrm{f,b}}(t)}{dt} \cdot m_{\mathrm{f,total}} \cdot Y_{\mathrm{f},j} \tag{3.18}$$

$$\frac{dm_{\mathrm{air},j}}{dt} = \lambda_j \cdot L_{St} \cdot \frac{dm_{\mathrm{f},j}}{dt} \tag{3.19}$$

$$\frac{dm_{\mathrm{EGR},j}}{dt} = \frac{Y_{\mathrm{EGR}} \cdot \left(\frac{dm_{\mathrm{air},j}}{dt} + \frac{dm_{\mathrm{f},j}}{dt}\right)}{1 - Y_{\mathrm{EGR}}} \tag{3.20}$$

$$\frac{dm_{ub,\mathrm{total},j}}{dt} = \frac{dm_{\mathrm{air},j}}{dt} + \frac{dm_{\mathrm{f},j}}{dt} + \frac{dm_{\mathrm{EGR},j}}{dt} \tag{3.21}$$

3.2.2 Conservation Equations

Energy Conservation

At ignition time, the reactors of each zone are defined in terms of thermodynamic state (pressure, temperature, volume) and gas composition. The global energy conservation in the combustion chamber is already solved by the engine process simulation, considering the calorific value of the fuel, wall heat transfer effects and performed piston work. Therefore, the global temperature of the burned area in the combustion chamber is applied and no conservation equations are solved for the different created zones. It is assumed that the reaction kinetics of the particle formation process does not significantly affect the resulting temperature profile in the burned zone. However, the available temperature profile of the engine process simulation is an averaged value based on the global equivalence ratio. The combustion in premixed flames of the fuel-rich zones is expected to be lower than this temperature.

Since no additional information is given by the engine process simulation about the temperature distribution in the burned zone, the auxiliary quantity of the adiabatic flame temperature is taken into consideration. The applied temperature profile is corrected globally for all fuel-rich zones. The adiabatic flame temperature of the burned reactor $T_{b,ad,j}$ is calculated by advancing a perfectly stirred constant volume reactor with the given (unburned) temperature, pressure and gas-phase composition for each zone j at ignition time. The resulting values are divided by the adiabatic flame temperature of the global zone $T_{\mathrm{b,ad,global}}$ (determined by the global engine equivalence ratio value) to obtain the correction factor. This mass-averaged correction factor is then applied to all fuel-rich zones. In addition, the applied temperature is limited to the mean exhaust temperature T_{exh} that is also calculated by the engine process simulation. This is required because the applied burned flame temperature is only valid in the combustion chamber. During exhaust stroke, the gas flows into the outlet channel. The particle-relevant temperature cannot be lower than the exhaust temperature. For each zone, the applied correction factor F_j and the temperature profile $T_{b,j}(t)$ is defined as

$$F_j = \frac{\sum_{j=1}^{n-1} T_{b,ad,j} / T_{b,ad,\mathrm{global}} \cdot Y_j}{\sum_{j=1}^{n-1} Y_j} \tag{3.22}$$

$$T_{b,j}(t) = max(T_{b,\mathrm{global}}(t) \cdot F_j, T_{\mathrm{exh}}). \tag{3.23}$$

An example for the temperature correction and the applied temperature profile is shown in Fig. 3.6. The graphic shows the global temperature profile and the corrected profile for a number of four fuel-

rich zones (left side). The zone-specific results of the adiabatic flame temperature compared to the global value and the applied correction factor are also shown (right side).

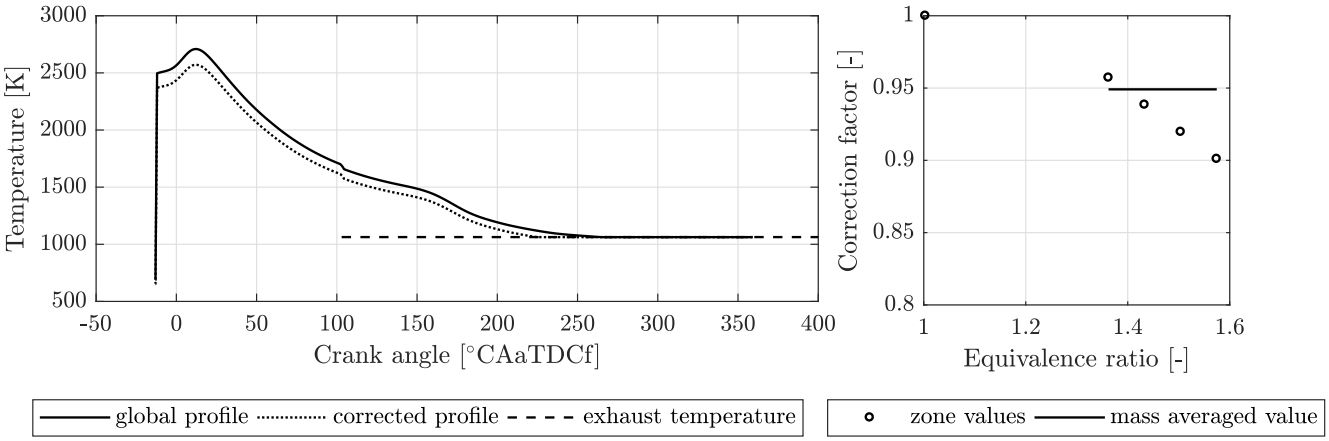

Fig. 3.6.: Temperature correction for fuel-rich zones. Operating point: injection time variation at 2000 rpm/10 bar IMEP.

This temperature correction method does not take into account local effects such as wall influences or a distribution of the fuel-rich zones in the combustion chamber. The temperature correction value also depends on the applied soot threshold that affects the zone definition process. Therefore, it has to be analysed to which extend the temperature influence the calculated mixture-induced particle results.

Species Conservation

The species conservation equations are only solved for the burned reactor of each zone, because the particle formation process is limited to high temperatures. The species conservation equation for each species i considers the species mass flow rate that is transferred from the unburned reactor $\dot{m}_{ub} \cdot Y_{i,ub}$ and the production term that results from chemical reactions $\dot{m}_{i,\mathrm{chem}}$. No species transfer between the different zones is considered for simplification. The changes in species mass fraction $dY_{i,b}/dt$ then are calculated by

$$\frac{d\left(m_b \cdot Y_{i,b}\right)}{dt} = Y_{i,b} \cdot \frac{dm_b}{dt} + m_b \cdot \frac{dY_{i,b}}{dt} = \dot{m}_{i,\mathrm{chem}} + \dot{m}_{ub} \cdot Y_{i,ub} \tag{3.24}$$

$$\frac{dY_{i,b}}{dt} = \frac{\dot{m}_{i,\mathrm{chem}}}{m_b} + \frac{\dot{m}_{ub}}{m_b}\left(Y_{i,ub} - Y_i\right) \tag{3.25}$$

$$\dot{m}_{i,\mathrm{chem}} = \dot{\omega}_i \cdot \frac{M_i}{\rho_b} \cdot m_b \tag{3.26}$$

$$\frac{dY_{i,b}}{dt} = \dot{\omega}_i \cdot \frac{M_i}{\rho_b} + \frac{\dot{m}_{ub}}{m_b}\left(Y_{i,ub} - Y_{i,b}\right). \tag{3.27}$$

The chemical reaction rates $\dot{\omega}_i$ and the burned mixture density ρ_b are obtained by a Cantera gas-object with the current composition and thermodynamic state. The reaction mechanism that has been used was developed by Blanquart et al. [24]. It supports iso-octane as fuel and includes the PAH formation processes up to pyrene (see also Section 2.1.2).

Due to the simplified modelling approach, the species mass from the unburned reactor is perfectly mixed in the burned reactor instantaneously. This leads to a local error in the species concentrations

of the burned reactor by overestimating the mixing state. However, at the start of combustion the size of the burned zone is small compared to the mass flow rate into the zone. The resulting error is thus assumed to be negligible. As the zone size increases and the burn rate decreases, the error also increases. After the combustion is finished, no mass is transferred to the burned reactor and the calculated time (up to top dead centre load exchange) is significantly longer than the burn duration, giving the mixture enough time for the mixing process and reducing the error.

Another simplification is done by feeding a fresh mixture to the burned zone instead of considering the reactions in the flame front. This is justified by the time-scales of the precursor and particle formation process, that are assumed to be much slower than the flame thickness, leading to a particle formation behind the flame in the burned zone.

Mass Conservation

The conservation of mass for the burned reactor is defined by the mass transfer from the unburned reactor (see also Eq. 3.21):

$$\frac{dm_b}{dt} = \dot{m}_{ub,\text{total}}(t) \tag{3.28}$$

No mass transfer between the different burned reactors is considered in the current approach.

Besides the mass conservation of the burned reactor, the considered total mass in the combustion chamber is assumed to be constant after end of injection. This is of special interest when the exhaust valve opens and the residual gas leaves the combustion chamber. From this time step, the considered system boundary is not fixed at the combustion chamber (that would lead to a loss of mass) but propagates into the exhaust system. By solving the differential equations, the thermodynamic state and the mass of each zone is known and the corresponding volume can be calculated by the ideal gas law. This can be used as a control parameter for the numerical calculations and must match the cylinder volume up to exhaust valve open. An example for the calculated volume profile is given in Fig. 3.7. It is clearly visible that the volume profile matches the cylinder volume and only differs by the calculation of the mixture density. The behaviour changes after exhaust open because the mass can freely propagate into the exhaust system and the simulation process changes from an Eulerian formulation to a Lagrangian formulation, following the mixture into the exhaust system. This is required because the measurement system is applied in the exhaust system and the particle formation processes can continue. In addition, the results of the particle formation simulation are always volume-based and therefore the volume increase at exhaust open influences the total number of particles for one work cycle.

Solving the Differential Equations

The initial boundary condition $y_{j,0}$ of the burned reactor is given as a vector by the thermodynamic state, the species composition and the initial mass for zone j

$$y_{j,0} = \begin{bmatrix} m_\text{j} \\ Y_1 \\ \vdots \\ Y_\text{nspecies} \end{bmatrix}. \tag{3.29}$$

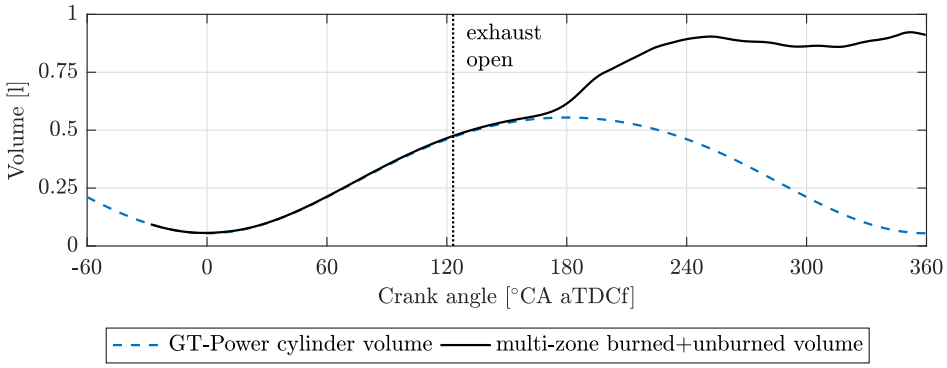

Fig. 3.7.: Comparison between simulated volume profile with the multi-zone approach and total combustion chamber volume. Visualization of the transfer from Eulerian formulation to Lagrangian formulation of the gas.

The set of differential equations is solved by the MATLAB-included solver *ode15s* that is designed for systems of stiff differential equations. The state of the burned zone is calculated for each time step, starting at ignition time up to top dead centre load exchange. This calculation duration is chosen because the complete mixture then is in the exhaust system with a approximately constant volume and pressure values close to ambient pressure. Therefore, it is assumed that the particle formation processes are inhibited by the low temperatures, pressures and particle concentration. However, effects that occur in the exhaust system (e.g. thermophoresis) can not be covered by the model.

It also has to be emphasised that the calculation start and end is equal for all considered zones because no local information is included in the quasi-dimensional model. This leads to the assumption that the flame front passes all zones at the same time. As it was already mentioned, the calculation duration is much longer than the flame propagation in the combustion chamber and therefore the sensitivity on the calculation start is reduced.

After calculating the set of differential equations, the complete species and mass profile of all zones is known. The species information is given in terms of mass fraction. For further usage of the results, it is converted into mole fraction. The conversion of mass fraction Y_i of all n_{species} species i into mole fraction X_i is calculated by

$$X_i = \frac{Y_i}{M_i} \cdot \frac{1}{\sum_{i=1}^{i=n_{\text{species}}} \frac{Y_i}{M_i}}. \tag{3.30}$$

3.2.3 Gas-Phase Coupling

In the above described approach, the species conservation is only affected by gas-phase reactions and the mass flow from the unburned reactor. In addition, the species are also included in the particle formation and growth process and thus are transferred from the gas phase to the solid phase. To take these effects into account, a coupling between the gas phase and the solid phase is required during the calculation of the species conservation. In the current work, this is done by a method that was already described by Balthasar et al. [16]. A method of moments with interpolated closure (MOMIC) is included in the gas-phase calculation to consider the effects of soot on the gas-phase species. The resulting species profiles are then transferred to the Monte-Carlo solver to model the particle ensemble and to obtain additional information about the particle size distribution.

Revzan et al. [151] provide a method of moments in a FORTRAN environment that enables the calculation of the first six moments of the particle distribution. This routine was recoded to fit into the

MATLAB framework and used for further calculations. The method of moments can directly be included within the species conservation equation by adding a term for the soot influence $\dot{Y}_{i,\mathrm{soot}}$ on every species:

$$\frac{dY_{i,b}}{dt} = \dot{\omega}_i \cdot \frac{M_i}{\rho_b} + \frac{\dot{m}_{ub}}{m_b}\left(Y_{i,ub} - Y_{i,b}\right) + \frac{dY_{i,\mathrm{soot}}}{dt} \tag{3.31}$$

The species production or consumption terms are calculated as molar concentration $\dot{c}_{i,\mathrm{soot}}$ and thus have to be transformed to species mass fractions by

$$\frac{dY_{i,\mathrm{soot}}}{dt} = \frac{dc_{i,\mathrm{soot}}}{dt} \cdot \frac{M_i}{\rho_b}. \tag{3.32}$$

Furthermore, the number of differential equations is increased by the number of moments that are calculated with the method of moments. This significantly increases the stiffness of the system of differential equations because of the different scales of the solution. Transforming the moments m_k into the logarithmic space m_k^* improves the stiffness. To perform the transformation, it is required to divide the resulting rates of the moments by the moment values, as it is derived in the following:

$$m_k^* = \ln\left(m_k\right) \tag{3.33}$$

$$\frac{\partial m_k^*}{\partial m_k} = \frac{\partial \ln\left(m_k\right)}{\partial m_k} = \frac{1}{m_k} \tag{3.34}$$

$$\tag{3.35}$$

combined with

$$\frac{\partial m_k}{\partial t} = \frac{\partial m_k}{\partial m_k^*} \cdot \frac{\partial m_k^*}{\partial t} \tag{3.36}$$

$$\frac{\partial m_k^*}{\partial t} = \frac{\frac{\partial m_k}{\partial t}}{m_k} \tag{3.37}$$

The division by the current value of the moments leads to a division by zero in case that there is no particle formation. The addition of a small number of "seed particles" to the initial value solves this problem without affecting the final result. The initial value for the moments in the log-space was thus set to $ln(m_{k,t=0}) = 11$ after varying the value in an appropriate range.

The implementation of the method of moments increases the total calculation time and it has to be ensured that the results are comparable to the Monte-Carlo simulation method. If this is the case, the resulting sink terms for the gas-phase species are also comparable. The method is ensured to give numerical stable results for the investigated perfectly stirred reactor (PSR). This is an advantage compared to other methods, like the operator splitting method (introduced by Celnik et al. [33]), that showed numerical instabilities for PSR simulations.

Another possible application of this method in context of driving cycle simulations is the deactivation of the Monte-Carlo tool SWEEP (see below in Section 3.3.1) if only the moments of the particle distribution are of interest. This is generally sufficient to calculate only the particle number and mass information and significantly decreases the total calculation time ($>$ 50 % reduction).

3.3 Particle Processes

3.3.1 Particle Formation and Growth

Calculating the particle formation and growth processes is done individually for each zone with the corresponding gas-phase results as an input. Therefore, pressure and temperature profiles are transferred to the Monte-Carlo simulation tool SWEEP [144]. In addition, profiles of the species that contribute to the particle processes are transferred (C_2H_2, H_2, H, O_2, OH, H_2O, CO, $C_{16}H_{10}$). A conversion of the species profiles from molar fraction X_i into molar concentration c_i is performed by

$$c_i = \frac{X_i \cdot p}{R \cdot T_b} \tag{3.38}$$

The Monte-Carlo tool SWEEP requires an estimated value of the maximum 0-th moment (M_0) that is expected for each zone as an input parameter. It is crucial to set this close to the actual value in order to avoid numerical instabilities or a complete removing of the stochastic particle set. According to the recommendation of the SWEEP authors [144], this is done by an iterative process that includes multiple executions of the tool. This unfortunately increases the calculation time and is thus only performed in zones where a significant amount of particles is expected. A specifically for the present application developed operating scheme of the iterative calculation with focus on reducing the total required calculation time is presented in Fig. 3.8. In case of an crucial overestimation of the 0-th moment $maxM_0$ (leading to a particle result of $maxM_{0,\mathrm{SWEEP}} = 0$), the next iteration is performed by reducing the value to $maxM_0 \cdot 0.01$. If the deviation between estimated and calculated 0-th moment is above 30 %, the next estimation is done by setting $maxM_0 = maxM_{0,\mathrm{SWEEP}} \cdot 1.05$. A sufficient quality of the estimated 0-th moment is typically received after two calculation steps with this method.

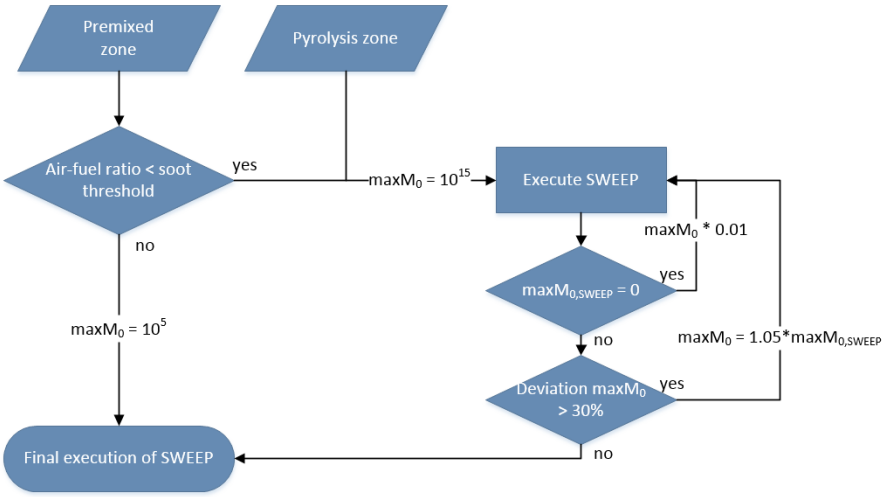

Fig. 3.8.: Strategy of 0-th moment estimation for SWEEP input. Focus on calculation time reduction.

In the following, the applied formation, coagulation and surface reaction processes are briefly explained. For further information, the reader is referred to the work of Celnik [33] and Patterson et al. [145]. Within the calculation process, all particles are assumed to be perfectly spherical and no aggregation processes are considered. The nucleation of primary soot particles is modelled by pyrene coagulation only (see Section 2.1.3 for further explanation). The inception rate R_{incept}, that is defined

per unit volume, is highly dependent on the pyrene ($c_{C_{16}H_{10}}$, also referred to as A_4 in the literature due to the four fused benzene rings) concentration c_{A_4} and is calculated by

$$R_{\text{incept}} = 0.5 \cdot k_{tr} N_A^2 c_{A_4}^2 \tag{3.39}$$

$$k_{tr} = \frac{k_{fm} k_{sf}}{k_{fm} + k_{sf}} \tag{3.40}$$

$$k_{fm} = 2.2\sqrt{\frac{\pi k_B T}{2}} \left(\frac{2}{m_{A_4}}\right)^{0.5} \cdot 4 d_{A_4}^2 \tag{3.41}$$

$$k_{sf} = \frac{2 k_B T}{3\mu} \left(\frac{2 + 2.514 Kn_{A4}}{d_{A_4}}\right) \cdot 2 d_{A_4} \tag{3.42}$$

$$Kn_{A4} = 4.74 \cdot 10^{-8} \cdot \frac{T}{p \cdot d_{A_4}} \tag{3.43}$$

$$d_{A4} = \left(\frac{m_{A_4}}{\rho_{A_4}} \cdot \frac{6}{\pi}\right)^{1/3} \tag{3.44}$$

with the pyrene mass m_{A_4}, density ρ_{A_4} and diameter d_{A_4} and the Avogadro's constant N_A. The transition coagulation kernel k_{tr} is defined as the harmonic mean of the slip-flow kernel k_{sf} and the free molecular kernel k_{fm} [145]. The Knudsen number of a sphere Kn_{A_4}, the Boltzmann constant k_B and the viscosity of the gas-phase μ are used to calculate the coagulation kernel.

The coagulation process is modelled using the Smoluchowski equation and the coagulation kernel $\beta(x, y)$ of two particles x and y to get the number density $n(x)$ of the particle.

$$\frac{d}{dt} n(x) = \sum_{y=1}^{x-1} \beta(x-y, y) n(x-y) n(y) - \sum_{y=1}^{\infty} \beta(x, y) n(x) n(y) \tag{3.45}$$

The surface growth and oxidation reactions are described in terms of Arrhenius equations and consider the addition of C_2H_2 and the oxidation by O_2 and OH. The Arrhenius-specific pre-exponential factor A, temperature exponent n and activation energy E are taken from Appel et al. [9].

$$R_{surf} = A T^n \exp\left(-\frac{E}{RT}\right) \prod_{j=1}^{J} \theta_j^{p_j} \prod_{i=1}^{I} c_i^{\nu_i} \tag{3.46}$$

$$C_2H_2 \text{ addition: } 8.0 \cdot 10^7 \cdot T^{1.56} \exp(-3.8/RT) \quad \theta = As, p = 1 \tag{3.47}$$

$$OH \text{ oxidation: } 1.0 \cdot 10^{10} \cdot T^{0.734} \exp(-1.43/RT) \quad \theta = d, p = 2 \tag{3.48}$$

$$O_2 \text{ oxidation: } 2.2 \cdot 10^{12} \cdot T^0 \exp(-7.5/RT) \quad \theta = As, p = 1 \tag{3.49}$$

The property of the particle θ_j (e.g. diameter d or active surface area As) is raised to the power p_j that is given by the surface reaction mechanism. J is the number of soot particle properties used in the rate expression, ν_i is the forward stoichiometric coefficient of species i and I is the number of reactant species.

Finally, the addition of pyrene to the particle is described in terms of condensation processes. The condensation rate per particle R_{cond} yields

$$R_{\text{cond}} = 2.2\eta c_{A_4} \sqrt{\frac{\pi k_B T}{2m_{A_4}}} \left(d_{A_4}^2 + 2d_{A_4} d_P + d_P^2 \right) \tag{3.50}$$

with the collision diameter of pyrene d_{A_4} and the particle d_P and the collision efficiency η.

Although the calculation process includes statistical deviations because specific particles are picked from the ensemble for coagulation and condensation processes, multiple tests at different operating conditions revealed that a single execution of the Monte-Carlo tool is sufficient to get a robust result for the particle number, mass and size information at the end of calculation. This decreases the calculation time effort.

The complete particle number and mass profiles and the full particle ensemble at calculation end are stored for each zone $j = 1 \ldots n$. The zone-specific results can then be combined to the total particle number density $N_{d,\text{total}}$ (and the particle mass density m_d, respectively) inside the combustion chamber by

$$N_{d,\text{total}} = \frac{\sum_{j=1}^{n} \left(N_{d,j} \cdot V_j \right)}{\sum_{j=1}^{n} V_j} \tag{3.51}$$

with the total zone volume V_j. It is assumed that this composition is constant for all cylinders of the engine. Considering a measurement position downstream of the exhaust system, a conversion to time-based values (number $\dot{N}$ and mass $\dot{m}_d$) is performed by multiplying the volume-based values by the total exhaust volume flow $\dot{V}_{\text{exh}}$ to

$$\dot{N} = \dot{V}_{\text{exh}} \cdot N_{d,\text{total}}. \tag{3.52}$$

3.3.2 Particle Size Distribution

A complete set of stochastic particles is calculated by the Monte-Carlo simulation and can be stored at specific time-step values. Additionally, a sample volume V_{sample} is stored to represent the real number density value for the given number of stochastic particles $n_{p,\text{stoch}}$, that can be calculated by

$$N_d = \frac{n_{p,\text{stoch}}}{n_{\text{SWEEP}} \cdot V_{\text{sample}}} \tag{3.53}$$

with the prior defined number of SWEEP executions n_{SWEEP}. Applying this equation to a set of stochastic particles in a specific diameter range i leads to the partial number density $N_{d,i}$. The resulting number density is normalized by the applied lower and upper diameter $d_{P,l_i(d_{P,u_i})}$ to compare the results to a corresponding measurement system by

$$\frac{dN_{d,i}}{dlog\ d_{P_i}} = \frac{N_{d,i}}{log(d_{P,u_i}) - log(d_{P,l_i})}. \tag{3.54}$$

This definition is subsequently referred to as $dndlogdp/cc$. Comparing the simulated overall particle number density to measurement values requires the consideration of the particle counting efficiency,

that is currently determined by law to be at 50 % for a diameter of $d_P = 23$ nm. If the counting efficiency is known as a function of the diameter, each particle $i = 1 \dots n_p$ can be weighted according to its specific diameter value $w_P(d_P)$ to approximate the counting efficiency. This slightly changes Eq. 3.53 to

$$N_d = \frac{\sum_{i=1}^{n_P} w_P(d_{P,i})}{n_{\text{SWEEP}} \cdot V_{\text{sample}}}. \tag{3.55}$$

The approximated development of the counting efficiency as a function of particle diameter is shown exemplarily in Fig. 3.9 for a condensation particle counter system (CPC) [176].

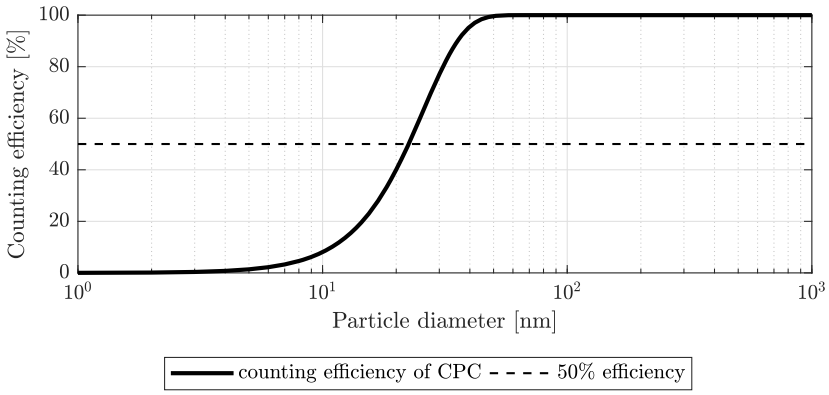

Fig. 3.9.: Counting efficiency as a function of diameter for a condensation particle counter measurement system [176].

3.4 Validation Strategy

3.4.1 Encapsulation of Model Components

In an applicable state, the complete simulation framework is claimed to simulate transient driving cycles without the requirement of additional measurement data (except for model parametrization). It is not possible to evaluate the quality of the different sub-models and to separate which part of the total emissions arises from a certain source by solely comparing the final results with measured particle emissions.

At the current state of technology, information about time resolved quantitative in-cylinder species profiles of soot precursors and the resulting particle emissions (number, mass, size) can not be achieved directly. Measuring the particle emissions in the exhaust system only represents averaged values over time. However, it enables a simultaneous identification of particle number, mass and size distribution. Moreover, the measured values in the exhaust system are regulated by law and therefore form an important target for the simulation framework. Therefore, all model results are compared to these measured values throughout the validation process.

Although it is not possible to validate the gas-phase species and the particle profiles of a single working cycle, the model is validated stepwise to evaluate individual influencing factors and sources of particle emissions. This includes a detailed planning of the measuring program and a continuous analysis of the model results. A visualization of the validation process is shown in Fig. 3.10 and further explained in the following.

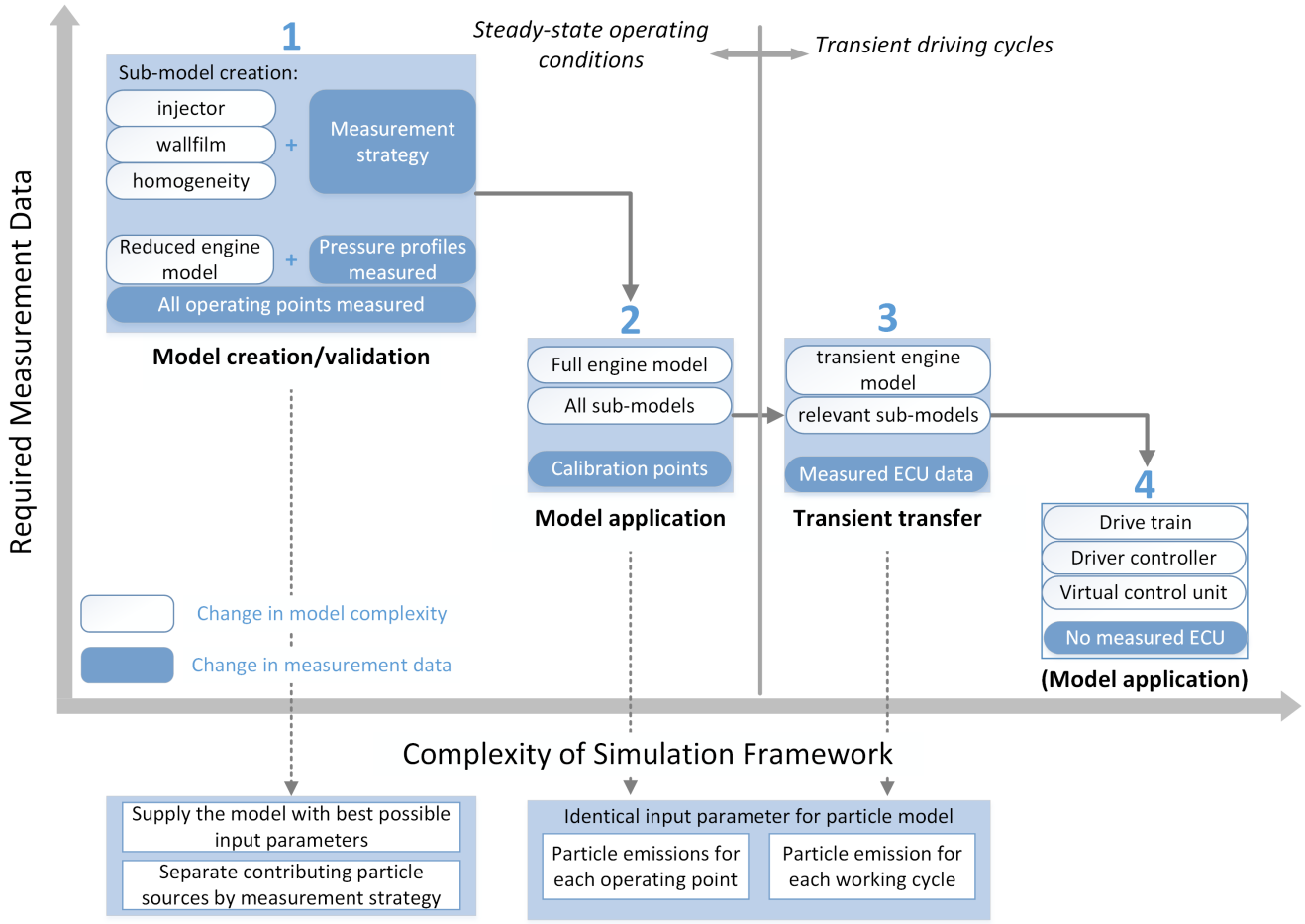

Fig. 3.10.: Model validation strategy.

The evaluation of the single model parts is performed by gradually increasing the complexity of the simulation framework while supplying the model by measurement data of an engine test bench. This reduces the error propagation and ensures that the model is provided with the best possible input data. With an increasing simulation complexity, the number of required measurement data is reduced and the sensitivity on the results is investigated. In addition to comparison to measured data, sensitivity analyses are performed to check the reaction of the model to disturbances of the input variables. The validation strategy includes four major steps:

1. The main part of this work includes the model creation and the calibration and validation of the specific sub-models. In this state, a reduced engine model and additional 3D-CFD simulations are applied (see also Section 3.1.2) to estimate the thermodynamic input properties of the particle model at various stationary operating points with the best possible quality. The measurement program is carried out on an engine test bench that is further described in Section 3.4.2. A custom-built measurement strategy is developed to separate the engines main particles sources and to validate the sub-models separately by minimizing the interdependencies of the different formation processes at steady-state engine conditions (described in Section 3.4.3). Additionally, the interactions of the sub-models are analysed for a number of parameter variations.

2. The parametrized particle emission model remains unchanged. The model complexity is increased by applying a full engine model that includes a phenomenological combustion and turbulence model. This enables the simulation of the engine process with only a few additional data of the engine control unit (ECU) and that reduces the measurement effort to a few calibration points. It is analysed in which extent the changed engine model affects the simulation results in terms of particle emissions (sensitivity of the thermodynamic input parameters, see also Section 7.3.1). By this step, the simulation framework is fully applicable to evaluate particle emissions in a steady-state context.

3. The transfer of the particle model to a driving cycle is performed by a quasi-stationary approach. The transient effects are captured by an engine model that is combined with measured data of a real ECU. The driving cycles are measured on the same engine test bench (see also Section 7.3). A selection of different speed and load profiles shows the applicability of the model for transient operating conditions. In the context of this work, this step represents the final model.

4. Further adjustments only affect the quality of the input parameters of the particle simulation model for the chosen driving profile. From here on, the simulation framework can be coupled with a virtual ECU, a driver controller and a fully modelled drive train [51]. This enables the applicability of the parametrized model in the development process without additional measurement effort.

With the above presented validation strategy and the measurement program described in the following, a step-by-step validation of the complex simulation framework is ensured by comparison to measured particle emissions. Intermediate steps can be evaluated concerning quality and sensitivity.

3.4.2 Measurement System

The complete measurement process regarding particulate emissions is performed on an engine test bench with a turbocharged 4-cylinder DISI engine with variable valve train (engine B). The engine-specific details are shown in Tab. 3.3 and will be further described in the following paragraph. The 3D-CFD simulations for the homogenization sub-module are based on measurements of an engine A

Tab. 3.3.: Specifications of engines

	engine A	engine B	engine C
nr. of cylinders	4		6
stroke / bore [mm]	94.6/82		89.6/84
displacement [cm^3] / compression ratio	1998/10.2 : 1		2979/10.2 : 1
combustion mode	homogeneous		
injection mode	spray-guided		
max. power [kW] / max. torque [Nm]	170/350	185/400	225/400

that slightly differs from engine B in maximum power and torque. However, the in-cylinder specifications and measured operating conditions are identical and the differences do not affect the 3D-CFD results for the investigated operating conditions. The engine test bench measurements of engine C were carried out and provided by the Karlsruhe Institute of Technology (KIT) [46–48]. Engine C is used for validating the spray-wall interaction model against 3D-CFD simulations and to evaluate the re-parametrization possibility of the homogenization sub-module for another engine type. Therefore, the data that is provided by the KIT is used to set the boundary conditions of the 3D-CFD model.

Engine B is equipped with a set of three different measurement systems to get information about particle number, mass and size distribution in the exhaust system downstream of the three-way catalyst. The distance between the measurement position and the engine out emissions (turbocharger exit) is approximately 100 cm. This distance was chosen to enable the longest possible inlet path of the exhaust stream. Otherwise, the particles may be deflected due to inertia because of the bent exhaust pipe. The inlet path is about 50 cm and the measurement positions are distributed over the circumference and over a length of about 20 cm to reduce the interactions of the sampling process. Another sampling point was set upstream of the three-way catalyst to investigate the influence on the resulting particle size distribution. Using both sampling positions is not possible simultaneously and requires a reconstruction and an engine restart. Since this also might change the raw emission values, the measurement position upstream of the three-way catalyst is not further investigated in this work. A schematic presentation of the sampling positions is shown in Fig. 3.11. Engine A has the same measurement system except of the particle size distribution. In the following, the particle measurement system is briefly described. For further information, the reader is referred to the corresponding manufacturers and publications.

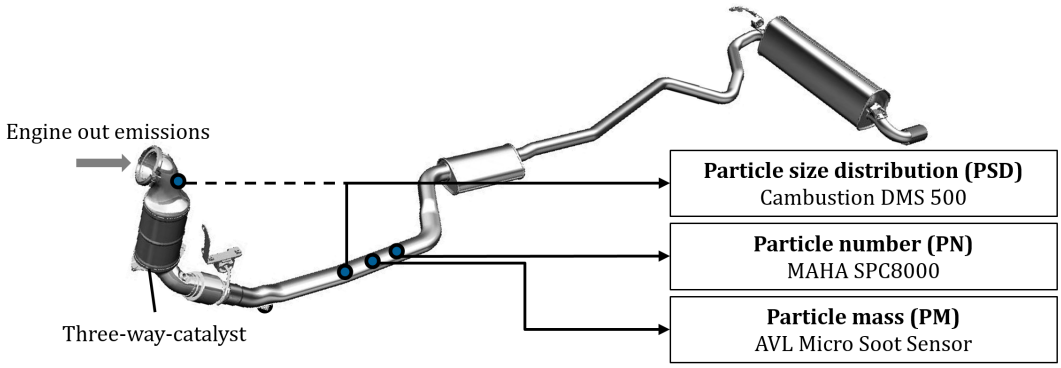

Fig. 3.11.: Position of particle emission measurement system. Schematic presentation only.

Particle Number (PN)

The measurement of the particle number concentrations is performed by a *MAHA SPC 8000* [114]. It consists of a dilution device and a condensation particle counter (CPC). It enables a continuous measurement of solid particles in the exhaust of combustion engines. The system is designed to fulfil the legal requirements for particle exhaust emissions of wheeled vehicles [182].

According to Kulkarni et al. [106], the CPC involves three processes. Ultra-fine particles can not be detected by optical techniques because of their small diameter (about 0.1 μm is required). Therefore, the particles are saturated by n-Butanol vapour. Afterwards, the particles are cooled down and the size increases by condensation of the n-Butanol. The resulting particle size then can be detected by laser diagnostics.

The measuring range is limited to $1-10000\ \#/\mathrm{cm}^3$. This range can be met by appropriate dilution.

Particle Mass (PM)

Particle mass emissions are detected time-resolved by an *AVL Micro Soot Sensor* [11]. The measuring range is limited to $0.001-50\ \mathrm{mg/m}^3$, which is sufficient for the expected engine emissions. The analyser is based on the photo-acoustic effect that is applied to the black soot particles. The particles are heated periodically by a light beam and then dissipate their heat. This results in pressure fluctuations that can be detected by a microphone. The microphone signal is linearly depending on the concentration of the soot particles in the measuring volume. More detailed information are given by Schindler et al. [193].

Particle Size Distribution (PSD)

The particle size distribution is measured by a *Cambustion DMS500* system [32]. According to Reavell et al. [149], the sampled particles are charged by a corona charger. They are then classified by their electrical mobility. The number of classified diameters depends on the number of electrometer detectors that are positioned along the sample flow. The DMS500 uses the signals from 22 electrometer detectors. The measuring range is about $5\ \mathrm{nm}-2.5\ \mu\mathrm{m}$. Theoretically, the size distribution information can be used to calculate the number and mass information. However, the resulting number information does not meet the legal measuring requirements and is thus not used for validation of the simulation results. The calculated particle mass is also not used because of the high sensitivity of the mass m on the error of the measured particle diameter d ($m \sim d^3$). Note also that the measuring principle is not limited to soot particles but also detects liquid volatiles. The condensation of liquid volatiles is prevented by a dilution of the exhaust gas with air (by factor 10) and the use of a sampling tube that is heated to approximately 200°C.

3.4.3 Test Procedure

For measurements at stationary operating conditions, each operating point is held constant until the measured particle emissions reach a stationary state. The pressure profiles of each cycle then are measured and averaged over 256 working cycles. All other measured quantities, such as engine actuator settings, thermodynamic values and particle concentrations, are averaged over about 60 s.

One main part of the test procedure is measuring the standard engine operating map to a great extent. At warm conditions, it is expected that the particle emissions are mainly caused by the remaining injector film because spray-targeting and injection timing of this engine are already adjusted to reduce the particle emissions. At cold conditions, additional wall film effects can occur. An overview of the measured operating conditions of the warm and cold engine map is shown in Fig. 3.12.

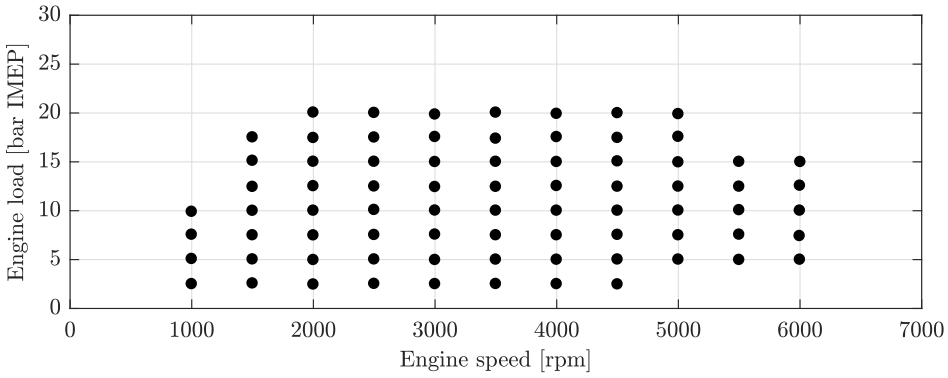

Fig. 3.12.: Measurement strategy stationary operating map (warm and cold).

Besides the standard engine map, a parameter variation has been planned to cover all considered particle emission sources and to separate the effects. For each variation of one or two parameters, such as injection time or rail pressure, all other actuator settings are kept constant to minimize the interdependencies that are caused by the ECU adaption. An overview of the changed actuator settings and thermal conditions is shown in Tab. 3.4.

Tab. 3.4.: Measurement strategy for stationary operating conditions. Changes in engine parameters are marked with ⊗. Expected influence on engine particle sources are marked with ⊘.

	1	2	3	4	5	6	7	8	9	10
Injection time	⊗					⊗	⊗	⊗		
Ignition time		⊗								
Coolant temperature			⊗			⊗			⊗	
Air-fuel ratio				⊗						⊗
Rail pressure					⊗		⊗		⊗	
engine speed								⊗		⊗
expected major effect on:										
Mixture homogeneity	⊘			⊘	⊘		⊘	⊘	⊘	⊘
Wall film			⊘			⊘			⊘	
Injector film	⊘			⊘	⊘	⊘	⊘	⊘	⊘	⊘

Based on this scope, experiments at a number of operating points are used to parametrize and validate the different sub-models. With the fully developed model, parameter variations are compared to measured data to evaluate combinations of particle sources.

For transient operating mode, the engine is set to follow a recorded list of speed and load traces that correlates to a specific driving cycle. This method differs from the real chassis dynamometer tests where the engine is working inside a vehicle and a driver regulates the accelerator. However, this method also decreases the interdependencies that are not directly correlated with the in-cylinder particle emissions but result in different measurement procedures. The measurement process is recorded over time and the results are stored at the end of each driving cycle.

In the scope of this work, two different driving cycles are chosen that differ in dynamic and total maximum engine load.

- The Worldwide Harmonized Light Duty Test Procedure (WLTP) cycle [45] was chosen because it offers a high dynamic range at moderate engine speed and loads.
- A special highway cycle that is based on the “ADAC EcoTest” [2] was chosen to combine constant driving conditions with fuel cut-off phases and tip-in processes that require a high engine torque.

4 Modelling Injector Film and Pyrolysis

4.1 Literature Overview and Concept

The injector tip has been identified as a source of particulate emissions in DISI engines by optical measurements of the spray and combustion process [20, 39, 125]. Moreover, at warm operating conditions and homogeneous mixture preparation, the injector-induced emissions are stated to be the leading contributors to the total emissions in a stationary operating mode throughout the engine operating map [20, 125].

At the injector tip, a liquid film remains at the end of injection and is not fully evaporated until the start of combustion, leading to the creation of soot particles due to the lack of oxygen in this region [39, 125]. The film creation process is mainly influenced by the injector geometry and manufacturing process, deposits from previous engine operation at the injector tip and the amount and pressure of the injected fuel [20, 88, 90, 125]. In matters of the injector geometry, the dimension of the injector pre-stage and the surface roughness affect the remaining film [88, 125]. The creation of injector deposits depends on the injector tip temperature, its position compared to the spark plug, the heat transfer from the injector tip, fuel properties and possible coatings [20, 85]. These deposits are much more distinctive than in a PFI engine because the injector is directly exposed to the combustion process [186]. This leads to the accumulation of soot, lubricating oil and various fuel components such as olefin and aromatic ingredients over time [198]. A detailed literature review concerning the injector deposits was created by Wang et al. [186]. Between end of injection and start of combustion, the remaining liquid film partially evaporates. The evaporation process is influenced by the injector temperature, the surrounding air velocity, the system pressure and fuel properties [90].

To the authors knowledge, no physically based model is available in the literature due to the complexity of the film creating and evaporation process at the injector tip. However, modelling these processes is essential because of the great contribution to the particulate emissions throughout the engine operating map. Therefore, an empirically based model is created using information from optical measurements and detailed 3D-CFD simulations of the injector tip area [17, 125]. The model considers the film creation depending on the injection duration for a given injector condition. A separation between injector tip and pre-stage film is performed because of the different evaporation rates for a given injector geometry. The film evaporation process is modelled using information from 3D-CFD evaporation rates for injector tip and pre-stage with an engine speed dependence. A complete model description of the film creation and evaporation process can be found in Section 4.2. With the information about the remaining film at start of combustion, a perfectly stirred reactor is created to calculate the corresponding soot precursers during fuel pyrolysis. A complete description of the pyrolysis process is presented in Section 4.3.

The model is valid only for a given injector deposition state and injector geometry. Therefore, a calibration of injector specific parameters is required. In addition, calibration parameters for the gas phase and the particle creation process are required because of the lack of information about the fuel concentration in the gas phase and the active surface of the soot particles. No measurements were found in the literature that give quantitative information about the film mass after injection or during combustion. Therefore, the validation of the complete model can only be performed using particulate number and mass measurements. Assuming a complete homogenized mixture at warm

operating conditions, it is justified by optical observation, that the injector is the only source of particulate emissions for the investigated engine [125]. The model calibration strategy and validation is described in Section 4.4.

4.2 Modelling Film Formation and Evaporation

4.2.1 Film Formation

The film formation is modelled based on investigations from optical engine measurements [125]. The following assumptions and simplifications are made and explained afterwards:

- During injection, a part of the injected fuel remains at the injector.
- The remaining film is proportional to the injection duration.
- The film mass is split between injector tip and pre-stage.
- The film formation characteristic is assumed to be constant for a drifted injector. Thereby, drifted means that there is a constant amount of deposits on the injector and the particle emissions do not change significantly at constant operating conditions (as it is the case for a newly installed injector).

The film formation behaviour during injection was observed by Miklautschitsch et al. [125] using a far-field microscope in an static injection chamber, as it is shown in Fig. 4.1. The chamber pressure, temperature and injection pressure were derived from the engine process. It can clearly be seen that

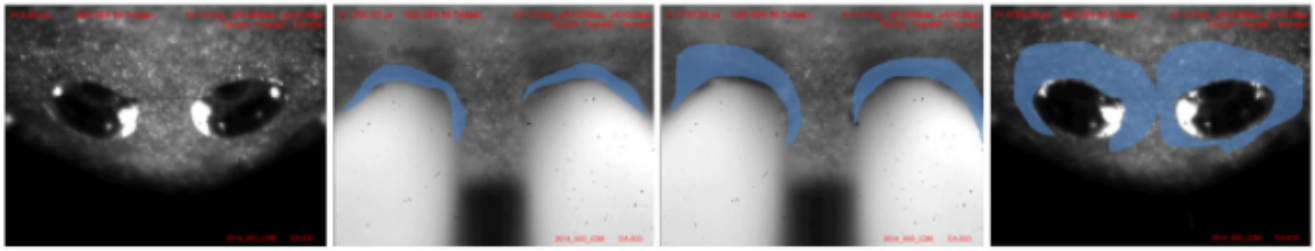

Fig. 4.1.: Film formation on injector tip during injection. Wetted area is marked in blue. Observed with far-field microscope in static injection chamber [125].

the wetted area increases during injection and has a maximum after end of injection. The film mass at end of injection is thus calculated by the empirical correlation

$$m_{\text{film,EOI}} = C_{\text{inj,1}} \cdot t_{\text{inj}}^{C_{\text{inj,2}}} \tag{4.1}$$

with the injection time t_{inj} and two injector-specific parameters $C_{\text{inj,1}}$ and $C_{\text{inj,2}}$. These parameters describe the film creation behaviour for a given injector geometry and have to be calibrated (see also Section 4.4). For a given total injected mass m_{inj}, the injection duration can be calculated with a reference injection mass flow information $\dot{m}_{\text{ref}}$ from the injector manufacturer and the engine speed n:

$$t_{\text{inj}} = \frac{\left(\frac{360 \cdot m_{\text{inj}} \cdot n}{1000}\right)}{\dot{m}_{\text{ref}} \cdot \sqrt{\frac{p_{\text{rail}} - p_{\text{cyl}}}{p_{\text{rail,ref}} - p_{\text{cyl,ref}}}}} \tag{4.2}$$

Additionally, the current rail pressure p_{rail} and cylinder pressure p_{cyl} are included and divided by the manufacturers reference values.

Besides the film at the injector tip, a remaining film is expected within the pre-stage. This is concluded by optical analysis of an injector with deposits (see Fig. 4.2). The deposits are not only found on the injector tip, but also inside the holes, indicating that these are caused by a remaining film [17]. Therefore, the calculated film mass is split between the injector tip and pre-stage. This is necessary because the pre-stage is not in direct contact with the surrounding air stream, causing a significantly reduced evaporation rate [17]. The resulting films are calculated with another injector-specific constant C_{tip}

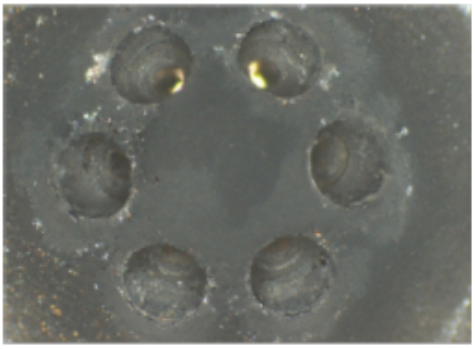

Fig. 4.2.: Picture of injector deposits at injector tip and pre-stage [17].

that describes the film fraction at the injector tip.

$$m_{\text{film,tip,EOI}} = m_{\text{film,EOI}} \cdot C_{\text{tip}} \tag{4.3}$$

$$m_{\text{film,prestage,EOI}} = m_{\text{film,EOI}} \cdot \left(1 - C_{\text{tip}}\right) \tag{4.4}$$

The applied model constants are only valid for a given injector geometry and injector fouling state. A representative fouling state was achieved prior to the engine measurement program by a specific injector fouling procedure [125]. This procedure creates a representative injector state and ensures that the particulate emissions do not significantly vary by altering injector deposits. An exemplary injector fouling procedure is shown in Fig. 4.3 for different injector geometries. For a new injector, the measured particle number emissions change significantly over time, whereas the drifted injector shows comparable emissions over a large number of driving cycles. The figure also shows the different behaviour between two injector types and thus justifies the need of an injector-specific calibration.

Although the validity of the created model is expected to be severely restricted considering injector geometry and fouling state, the focus of the current work is set on engine actuator variations rather than changes in geometry or long term alteration. The film formation model is thus mainly created to cover changes in engine load and rail pressure variations for a constant injector state. Additional investigations and especially film mass measurements are required to specify the film formation process on a physical base.

4.2.2 Film Evaporation

When the film formation process is finished at end of injection, the film evaporation takes place. The injector film evaporation depends on the injector temperature, the surrounding air velocity, the fuel properties and the system pressure [90]. A detailed research on the injector drying process and the essential parameters was done by Karwa et al. [90]. The consideration of all physical relevant variables is beyond the scope of a phenomenological model, especially because the injector tip temperatures

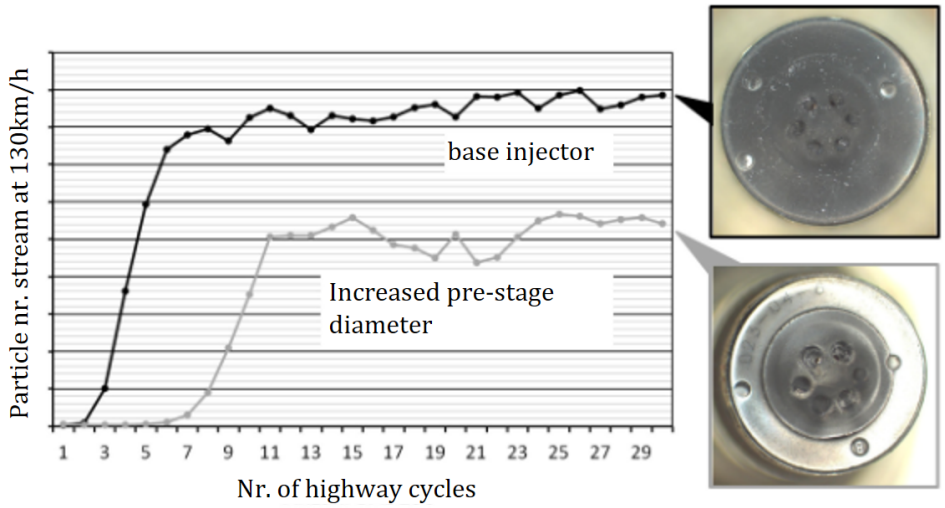

Fig. 4.3.: Exemplary particle number measurements during injector drift procedure for different injector geometries [125] (edited). Measured during highway cycle [2] at 130 km/h.

and the local air velocity can hardly be estimated without corresponding 3D-CFD simulations at each working cycle. For this reason, a simplified model approach is created with only some representative detailed 3D-CFD simulations of the evaporation process that were recently performed by Banholzer [17]. In the reference work, the information of the velocity profile in the combustion chamber was coupled with a detailed injector geometry. An initially created film has then been evaporated for different engine operating conditions (gas phase temperature and velocity), injector geometry and temperatures as well as different fuel compositions. It was summarized that the air velocity and the injector temperature had the most significant influence on the evaporation behaviour [17]. In addition, the evaporation rate of the pre-stage film was clearly below the injector tip evaporation rate because of the reduced air velocity and high fuel saturation in the pre-stage area. An exemplary simulation result for the evaporation process between end of injection and start of combustion at an engine speed of $n = 1500$ rpm is shown in Fig. 4.4. The graphics show the wetted area on the injector tip at different crank angle values and the corresponding wall film thickness.

Considering the identification of the most significant conditions for injector film evaporation, the following parameter variations are available from the given 3D-CFD simulations [17] for further model development:

- variation of the injector film position (pre-stage and tip) at $n = 1500$ rpm
- variation of the engine speed ($n = 1500$ rpm and $n = 5500$ rpm) for injector tip film

The corresponding film mass development over time is shown in Fig. 4.5. The high gradient at start of evaporation indicates that the differences in fuel concentration lead to a high evaporation rate. Over time, the volume around the injector enriches with fuel and thus the evaporation rate is reduced. For modelling purposes, the evaporation behaviour is described as a simplified function from now on. This is necessary because the complex physical interactions of the 3D-CFD simulation can not be covered by a reduced model. The following mathematical approach calculates the remaining film

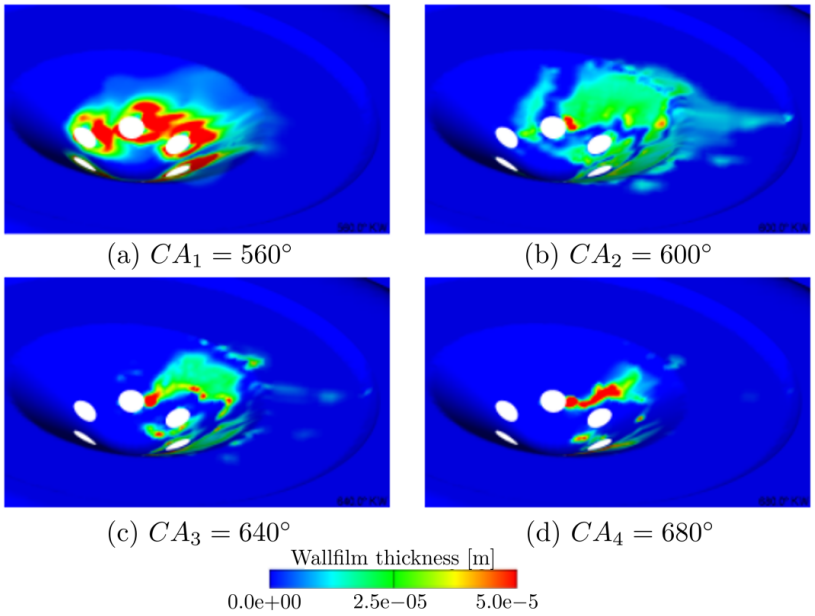

Fig. 4.4.: Exemplary 3D-CFD simulation result of the injector tip evaporation process between end of injection and start of combustion [17] (edited).

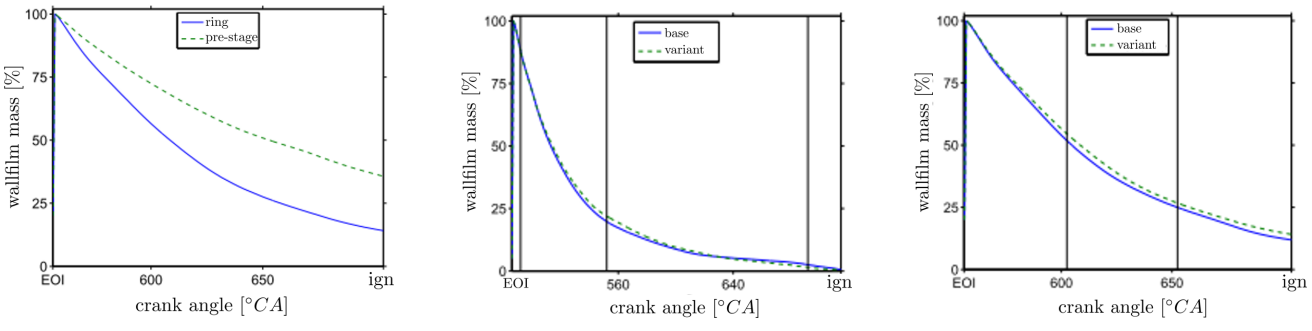

(a) **(b)** **(c)**

Fig. 4.5.: Injector film evaporation for different film positions (a) and engine speeds - 1500 rpm (b) and 5500 rpm (c). Results of 3D-CFD simulations [17] (edited).

mass fraction Y_{film} with an exponential function based on the available evaporation time. This also enables the calculation of the remaining wall film at start of combustion $m_{\text{film,SOC}}$.

$$Y_{\text{film}} = \exp\left(-c_{\text{evap}} \cdot (t - t_{\text{EOI}})\right) \tag{4.5}$$

$$\text{with } c_{\text{evap,1500,tip}} = 198 \text{ , } c_{\text{evap,5500,tip}} = 484 \text{ and } c_{\text{evap,pre}} = 0.5 \cdot c_{\text{evap,tip}}$$

$$m_{\text{film,SOC}} = m_{\text{film,EOI}} \cdot Y_{\text{film,SOC}} \tag{4.6}$$

All given parameter variations show a comparable evaporation behaviour, aside from the identified evaporation constants c_{evap} $[s^{-1}]$ that are estimated by regression at 1500 rpm and 5500 rpm. The evaporation constant of the pre-stage wall film is approximately half of the injector tip film value.

The resulting film evaporation process is shown in Fig. 4.6 with the applied model equations. The evaporation rate is increased at higher engine speeds due to the increased air velocity and injector temperature, but the available evaporation time until start of combustion is considerably reduced. With the given model equations, the film mass at start of combustion can be calculated by a combi-

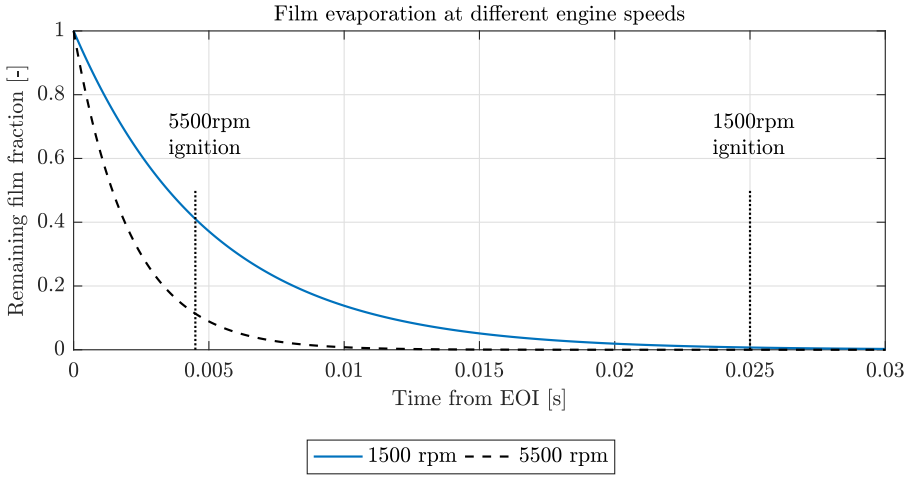

Fig. 4.6.: Injector film evaporation model. Evaporated mass fraction over time for different film positions and operating speeds.

nation of the initial film at end of injection (see Section 4.2.1) and the remaining film mass fraction over time. This film mass value is further used in the film pyrolysis part of the injector film model.

4.3 Modelling Pyrolysis Reactions

Optical measurements of the particle formation process in the combustion chamber, that are sparsely available in the literature (e.g. [20, 125, 174]), show a similar behaviour for both the injector-film-induced particles and the emissions from piston or liner wall films. It is typically described as a bright yellow luminous flame [125]. Therefore, it is expected that comparable physical processes occur in the area of the wall film regardless of the film position.

In most literature studies, the process is described as a diffusion flame (or, in case of the piston wall film, as “pool fire”) caused by a under-stoichiometric combustion of the fuel-air mixture above the film [20, 125, 174]. However, in a recent theory, Ketterer et al. [98] assert that the so-called “pool fire” takes place in the burned region with nearly no remaining oxygen in the mixture because of the global stoichiometric combustion in gasoline engines. Without the availability of oxygen, no real flame can be formed. The visible “pool fire” is more likely caused by the radiation of the solid soot particles and it grows by diffusion and evaporation of the remaining wall film in the burned zone [98].

This also correlates with the observed duration of the visible radiation, that can persist through the expansion and exhaust stroke [174]. To proof this theory, an EQR variation was performed by Ketterer et al. [98], starting at lean engine conditions and adding gaseous propane to increase the EQR value. No significant jump in the particle emissions was observed by increasing the amount of available oxygen in the burned region. It was thus expected that the particles are not formed using the residual oxygen in the burned gas by a diffusion flame [98].

With the results, a conceptual model for the formation of particle emissions from wall films was created [98]. Based on this approach, some simplifications are performed for the application in the current work, mainly because no local information is considered and the diffusion processes above the wall film are not included. The original model concept and the additional simplifications are shown in Tab. 4.1. The main simplification is that the fuel-rich combustion is not considered within the current approach. Instead, the complete remaining fuel mass at start of combustion is assumed to react by pyrolysis in the burned zone behind the flame front. In addition, no diffusion process is modelled in the burned region. The evaporation of the remaining film mass in the burned zone is assumed to be instantaneous because of the high temperatures in this region ($> 2000\,K$).

Tab. 4.1.: Conceptual pyrolysis model of Ketterer et al. [98] and simplification for application in the current work

Summarized conceptual model Ketterer et al. [98]	Simplifications for model application in the current work
1. Evaporation of the liquid film with EQR varying from rich to global value above film, no soot formation because of low gas temperature in unburned region	Evaporated film mass completely mixed with gas-phase at global value until start of combustion
2. Combustion within flammability limit above film at flame arrival, formation of some soot particles in rich flame region, rich mixture outside of flammability limit remains in burned region, pyrolysis initiation at high burned temperature	Instantaneous evaporation of film mass in burned zone, formation of rich fuel/residual gas mixture zone, soot formation by pyrolysis reactions
3. Soot formation in burned zone by heat conduction from burned gas, visible radiation (“pool fire”) from soot particles that grows by diffusion and expansion	Mass conservation within zone by total film mass, volume growth of rich zone by expansion only, no diffusion processes considered

Within the multi-zone framework, an additional pyrolysis zone is created that consists of evaporated fuel from the film at SOC and burned gas from the global EQR combustion. The initial fuel mass fraction $Y_{\text{fuel,pyrolysis}}$ in the zone is determined by parametrization (see also Section 4.4) to compensate the neglected EQR gradient above the film. The mass of the pyrolysis zone is constant and defined by the film mass at start of combustion (SOC) $m_{\text{film,SOC}}$:

$$m_{\text{pyrolysis}} = \frac{m_{\text{film,SOC}}}{Y_{\text{fuel,pyrolysis}}} \tag{4.7}$$

The time-dependent zone volume $V_{\text{pyrolysis}}(t)$ can be calculated by ideal-gas law using the gas pressure $p_{\text{gas}}(t)$, temperature $T_{\text{gas}}(t)$ and molar Mass $M_{\text{gas}}(t)$ information.

$$V_{\text{pyrolysis}}(t) = \frac{m_{\text{pyrolysis}}}{M_{\text{gas}}(t)} \cdot R \cdot \frac{T_{\text{gas}}(t)}{p_{\text{gas}}(t)} \tag{4.8}$$

With this volume information, the total amount of particulate emissions can be calculated for the pyrolysis zone. The reaction kinetics of the pyrolysis zone are calculated as a homogeneous reactor with a constant mass, a given temperature and a pressure profile from the engine process simulation. For this reason, only the species conservation equation is solved to get the gas species concentrations. The temperature profile can not be taken directly from the engine process simulation because the pyrolysis processes take place near the injector tip and the surrounding walls. As a consequence, the calculated global burned gas temperature is too high and must be corrected. This is done by a global temperature correction factor that is also result of the parametrization (see Section 4.4). The reaction kinetic start is at start of combustion, which is also taken from the engine process simulation and it is defined as the sum of ignition timing and ignition delay. The end of calculation is at the end of the exhaust stroke (at TDC).

4.4 Model Parametrization

4.4.1 Parametrization Strategy

A calibration of the injector model is necessary because the injector state and the gas phase concentration can not be identified for a given engine state. The injector film sub-model includes the following set of calibration parameters:

- Two film formation constants that describes the accumulated film mass over time during injection $C_{\text{film},1}$,$C_{\text{film},2}$.
- A constant that represents the ratio of injector tip and pre-stage film C_{tip}.
- The fuel concentration in the burned zone at pyrolysis start X_{C8H18}.
- A global correction factor F_{temp} and a minimum temperature threshold $T_{\text{threshold}}$, applied on the burned temperature profile of the engine process simulation.
- The active surface of the particulate emissions α.

The first three parameters are injector-specific and change whenever another injector is applied or if the deposits change significantly. The temperature correction and gas-phase concentration parameters are assumed to be applicable for all wall film related particle formation processes (injector, liner and piston).

In order to prevent the temperature in the pyrolysis zone from becoming too low by the global correction factor, a limitation is made by determining a lower threshold temperature. Comparing this threshold temperature $T_{\text{threshold}}$ with the peak burned temperature value cf. the engine process simulation then leads to a threshold factor $F_{\text{threshold}}$. The applied temperature profile $T(\Theta)$ is then calculated by adjusting the engine process simulation result T_b as

$$T(\Theta) = \max\left(F_{\text{temp}}, \frac{T_{\text{threshold}}}{\max(T_b(\Theta))}\right) \cdot T_b(\Theta) \tag{4.9}$$

Finally, the applied value for the active surface area of the particle emissions is used by all simulation model parts and affects the particle growth reaction rates. The parameters are adjusted using the emission target values - particle number and mass - of the engine. Unfortunately, only the complete set of parameters can be validated because none of the parameters can be influenced separately from the others. Therefore, it is not possible to transfer the results to a complete different engine without any re-parametrization. However, the parametrized model should facilitate the calculation of the particle emissions within a wide operating range of the engine because the main physical processes are basically implemented.

The calibration of the parameter set must cover a wide range of engine operating conditions that effects the film creation and evaporation process. Mainly, different engine speeds, loads and injection timings are considered. For the reaction kinetics, a variety of engine pressures and combustion temperatures have to be included to ensure the correct particle formation process. A total set of 11 operating conditions at different engine conditions is applied, as it is shown in Fig. 4.7.

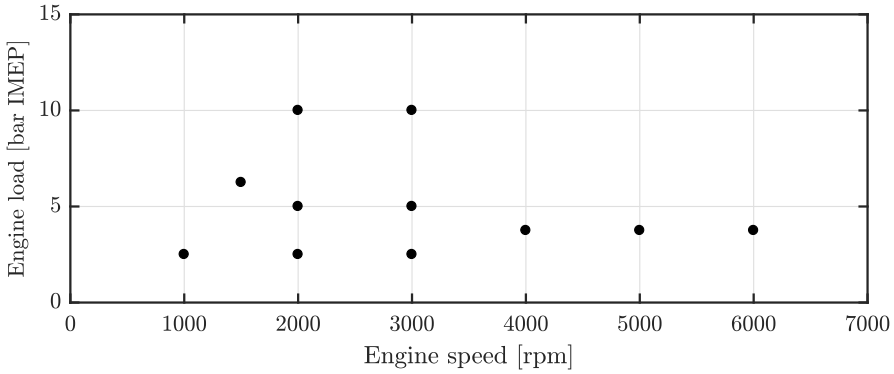

Fig. 4.7.: Operating conditions for calibration of injector film pyrolysis parameter set for the given engine.

The parametrization is performed with the Nelder-Mead simplex algorithm [138] that provides a good reliability to find a global minimum for a small number of parameters. It is essential to define an appropriate error function relative to the reference measurements to achieve a good simulation result both for particulate number and mass emissions. This is especially challenging because of the different order of magnitudes of the results. In general, the deviation between measured and simulated value is summed up over all equally weighted operating points n_{OP}. The particle mass (PM) error Z_{mass} and particle number (PN) Z_{number} error are defined and summed up at each operating point j. Using the absolute deviation between the measured quantity $P\tilde{M}, P\tilde{N}$ and the simulated value PM, PN causes the optimizer to prefer one quantity because of the different scaling of the error values. Therefore, a relative error is defined that considers both the underestimation and the overestimation of the target quantity. The resulting definition of the error function leads to a homogeneous optimization result both for particle mass and number (see also Section 4.4.2).

$$Z_{\mathrm{total}} = \sum_{j=1}^{n_{OP}} \left(Z_{\mathrm{mass},j} + Z_{\mathrm{number},j} \right) \tag{4.10}$$

$$Z_j = \frac{P\tilde{N}_j, P\tilde{M}_j}{PN_j, PM_j} - 1 \quad if\ (P\tilde{N}_j, P\tilde{M}_j > PN_j, PM_j) \tag{4.11}$$

$$Z_j = \frac{PN_j, PM_j}{P\tilde{N}_j, P\tilde{M}_j} - 1 \quad if\ (P\tilde{N}_j, P\tilde{M}_j < PN_j, PM_j) \tag{4.12}$$

4.4.2 Results and Model Quality

The result of the optimization is shown in Tab. 4.2 for all calibration parameters. It has to be emphasised that the results are solely based on the minimization of the defined error function (see Section 4.4.1). Although there is a physical explanation for every parameter, it is not expected that the identified values are physically correct for each parameter. The interaction of the parameter rather leads to the best possible results regarding the total calculated emissions. However, with the obtained results it can be validated whether the effects of the injector-induced particle formation process can be covered throughout the operating map of an internal combustion engine with one global set of parameters.

The parametrization results can be interpreted as follows: The calculated burned temperature profile of the engine process simulation is reduced to approx. 84 % in the pyrolysis and particulate formation process due to wall effects. The temperature correction is limited to a minimum peak temperature value of 2230 K. The molar fuel fraction of the pyrolysis zone is set to $X_{C8H18} \approx 1.5$ %. The active surface area of the particles is set to $\alpha = 0.173$.

Tab. 4.2.: Parametrization results for injector film model.

$C_{\text{film},1}$	$C_{\text{film},2}$	C_{tip}	X_{C8H18}	F_{temp}	$T_{\text{threshold}}$	α
0.262	0.057	0.842	0.015	0.843	2230 K	0.173

The injector specific results now enable the calculation of a representative remaining film mass at ignition time. This simulated film creation and evaporation process at the injector tip and pre-stage is shown exemplarily in Fig. 4.8 for the operating point 2000 rpm/10 bar IMEP. During injection, the

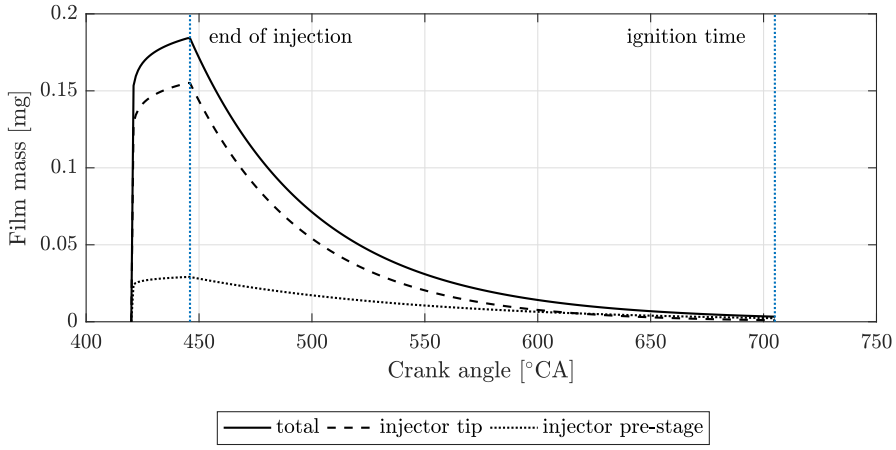

Fig. 4.8.: Simulated development of injector film mass over time with parametrized values at 2000 rpm/10 bar IMEP.

fuel film accumulates with a strongly decreasing gradient (according to Eq. 4.1). About 85 % of the film mass is stored at the injector tip. After injection finished, the film evaporates according to the calibrated film evaporation relation (see Section 4.2.2). Due to the high evaporation rate, the tip film evaporates almost completely, whereas the pre-stage film remains until ignition time. Finally, about 2 % of the maximum film mass remains at ignition time. For different operating conditions, the available film creation and evaporation time changes and significantly affects the final mass value. The total volume of the injector zone is calculated with the film mass information and the fuel concentration. This leads to a direct proportional linear sensitivity of the injector model path on the calculated film mass.

The final particle number and mass results for the optimized operating points are shown in Fig. 4.9 and can be compared to measurements. The simulated particle number stream accurately matches

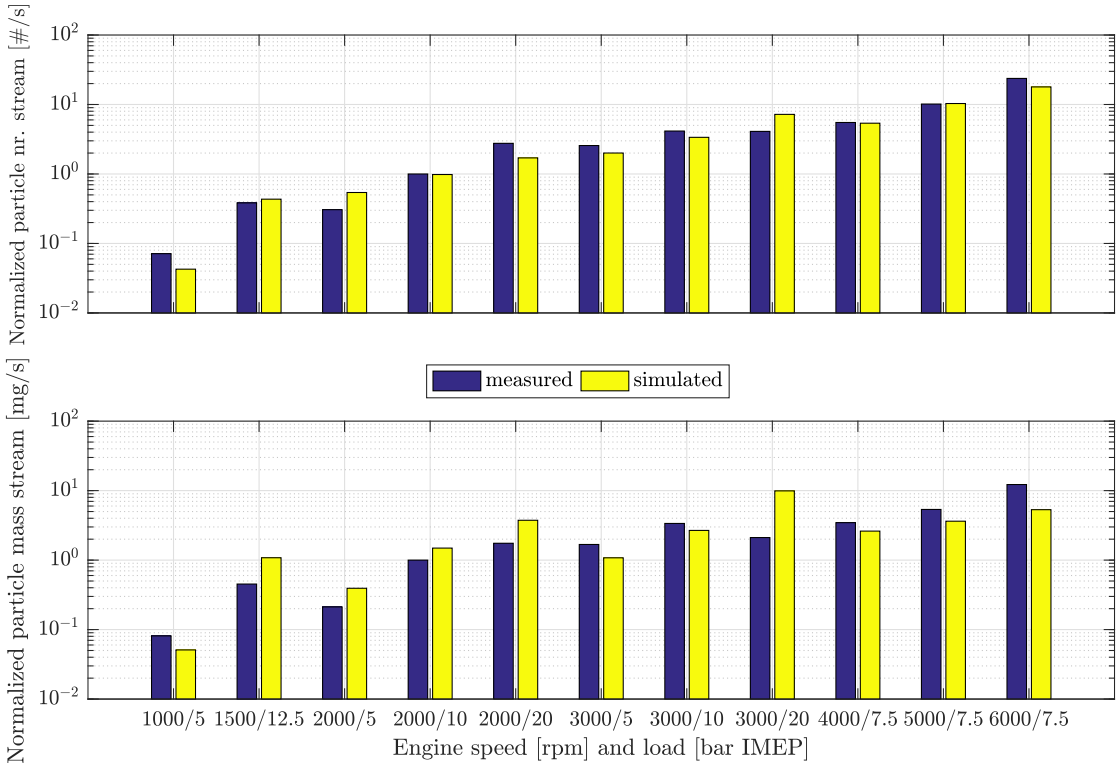

Fig. 4.9.: Particle number and mass results of parametrized injector model compared to measured data. The presented operating points were used for parametrization of the injector model. All values are nomalized by measured data at 2000 rpm/10 bar IMEP operating point.

the measured data both for changes in engine speed and load. The load influence is clearly visible for the different loads at 2000 rpm. At a constant load, the particle number stream increases, as it is noticeable from 3000 rpm to 6000 rpm. For the given set of operating points, the particle number stream includes a range of almost three decades, that is also covered by the simulation. These results for the particle number stream indicate that the particle nucleation and coagulation processes are covered well by the simulation model, because these are the determining process that affect the total number of particles.

The simulated total mass of the particles also shows the correct trend both for speed and load influence, but it shows larger deviations compared to the particle number results. This is especially noticeable at high engine loads, where the simulation significantly over-predicts the measured values. At higher engine speeds and reduced load, the simulation under-predicts the total mass stream. Calculating the particle mass additionally includes the surface growth, condensation and oxidation processes and is more complex than identifying the number value.

The number and mass results can be linked by examining the particle size distribution function. This function was both measured in the experimental procedure and calculated in the simulation framework. In the optimization process, no information about the size distribution were included in the error function. Therefore it must be examined whether the resulting shape of the particle size distribution function is comparable to measurement data. The resulting size distribution function is shown at four representative operating points in Fig. 4.10. All values are based on the corresponding maximum value of the actual operating point to compare the results only qualitatively. This is necessary because the measured total number values vary between the measurement systems. The normalized presentation visualizes the modes and the total shape of the distribution function. At moderate

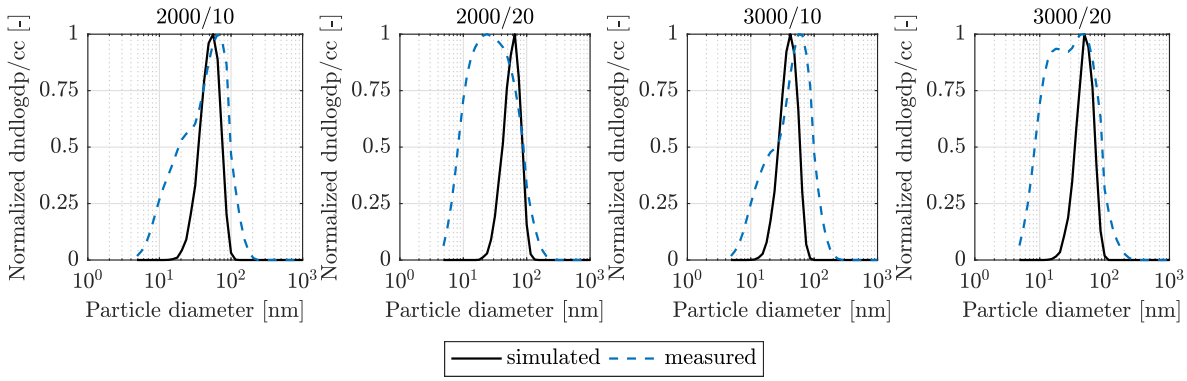

Fig. 4.10.: Particle size distribution of injector model compared to measured data at different engine speed and load. Particle number density based on maximum value of size distribution.

loads, the position of the simulated mode corresponds with the measured accumulation mode. At higher loads, the relative shape of the simulated distribution does not vary, but only the absolute number density increases. The resulting shape of the distribution is a consequence of the simulated formation and growth process. The particle nucleation and mass increase only takes place at the start of simulation. Afterwards, the coagulation processes determine the final size of the particles. No additional small particles are created that could form a nucleation mode in the size distribution. Therefore, the more accentuated nucleation mode at higher loads of the measurements is not covered by the simulation results.

Because of the high influence of the particle diameter on the mass, the calculated total mass significantly increases. At high engine loads, the measured shape of the distribution function changes and the amount of smaller particles increases. This leads to a considerable change of the particle number value, but only slightly affects the particle mass. A possible reason is that another particle formation from the gas phase starts at low engine speed and high engine load. In the simulation, the complete emissions are covered by the injector part of the model for the given operating points. In addition, the size of the simulated particles decreases at higher engine speeds because of the reduced time for particle growth reactions. This effect is also observed in the measurement results, but to a lower degree. Small deviations of the particle diameter then lead to noticeable deviations in the particle mass results.

Summarizing, the particle number results match the measured values for the calibrated operating points. It is thus possible to use a global set of parameters in combination with physical processes to model the injector-induced particle emissions in the operating map of a combustion engine. There are more deviations regarding the particle mass results that can eventually be attributed to the non-consideration of gas-phase inhomogeneities. However, accompanying 3D-CFD simulations did not show significant inhomogeneities in the gas-phase for the considered operating points.

To verify the results for operating conditions that were not parametrized, it is required to simulate a complete engine operating map and compare the results to measurement values. Moreover, the investigation of different injector states is necessary to check the possibility of covering the effects by a re-parametrization of the injector specific parameters.

4.5 Analysis of Simulation Process

For an analysis and evaluation of the simulated particle number and mass formation process, the simulation results are subdivided according to the event chain from the calculation in the injector zone to the comparison of the particle number and mass stream in the exhaust system. This includes

an evaluation of the stability of the simulation method and a sensitivity study of the different input parameters. A classification of the achieved simulation quality of injector induced particle emissions in an engine operating map can then be enabled.

The examination is mainly carried out on the basis of the particle number emissions, because less interdependencies are included compared to the particle mass formation. However, the influence of single parameters on the particle mass formation is also commented.

The results of the simulation process are carried out in three stages (see also Fig. 4.11):

1. The pyrolysis reactions in the injector zone:
   The species conservation equations are solved and the particle concentration of the injector zone is calculated. This stage is mainly influenced by the fuel composition (here: pure iso-octane), the fuel concentration in the injector zone, the thermodynamic properties pressure and temperature and the active surface area of the particles.

2. Calculation of the total particle concentration for one cylinder:
   Initially, the total particle number and mass of the injector zone are calculated including the information from the remaining film mass at ignition time that defines the zone mass and volume. This number is divided by the total volume. During the exhaust stroke with open exhaust valves, the total volume depends on thermodynamic properties and the total in-cylinder mass (load-dependency) and is calculated by the ideal gas law.

3. Conversion of the particle concentration in time-based values:
   Using the exhaust volume stream of all cylinders and assuming an equal contribution of each cylinder to the overall emissions, the prior calculated concentration results are converted into time-based values. These values enable the comparison to the measured quantities and are relevant for engine emission legislation. The last step is both applied to the measured and simulated concentration values and thus affects the results only quantitatively. Additionally, the counting efficiency of the measurement system is taken into consideration for the simulation results by reducing the particle number and mass based on the particle size distribution.

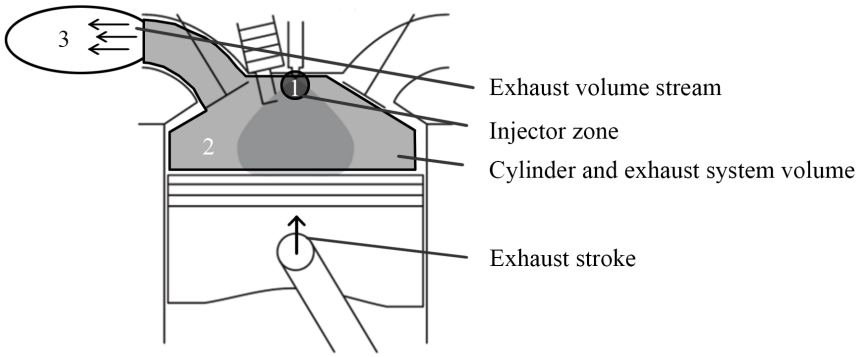

Fig. 4.11.: Simulation process of the injector film pyrolysis calculation.

The analysis of the results is done exemplarily for an engine speed and load variation with the base operating point at 2000 rpm/10 bar IMEP. The results are normalized to this base operating point for better representation (see Tab. 4.3).

On the basis of this presentation, the simulation process can be interpreted and the influence of the model components is evaluated. It is emphasised that only the final results can be compared

with the measurement data. The intermediate results solely clarify the process and it is not ensured that they are physically correct.

In the following, the results and sensitivities of the three simulation process parts are presented.

Tab. 4.3.: Simulation process results for injector-induced emissions at different speed and load conditions. Values based on 2000 rpm/10 bar IMEP operating point for comparison.

	2000rpm 5bar	**2000rpm 10bar**	2000rpm 20bar	3000rpm 10bar	4000rpm 10bar
measured [#/s]	0.31	**1.00**	2.76	4.15	7.54
1. injector zone [#/cm^3]	0.85	**1.00**	1.22	1.40	1.81
2. total volume [#/cm^3]	1.15	**1.00**	0.81	2.46	4.20
3. exhaust values [#/s]	0.56	**1.00**	1.75	3.43	7.24

Injector Zone Pyrolysis

The particle number concentration of the injector zone is determined by the processes of particle nucleation and coagulation.

The nucleation process is mainly driven by the pyrene concentration (squared dependency on nucleation rate), that is calculated by reaction kinetics. The chemical reactions depend on the fuel composition and concentration in the pyrolysis zone. In the simulation, the fuel is considered to be pure iso-octane and the fuel concentration is estimated by parametrization. This poses a simplification of the real engine fuel that consists of numerous different components, including cycloalkanes, aromatics and many more.

To estimate the influence of this simplification on the reaction kinetics and thus on the resulting particle emissions, toluene is added as a fuel component in the simulation framework in various proportions.

A sensitivity study is performed and the results are presented both for the maximum particle number density (nucleation process) and the resulting number density at the end of calculation (top dead centre of exhaust stroke) in Fig. 4.12 (left side) for the base operating point 2000 rpm/10 bar IMEP.

In addition, the fuel concentration is varied around 20 % of the parametrized value (Fig. 4.12, right side).

The maximum value of the particle number concentration, that is driven by nucleation, significantly increases both with addition of toluene in the fuel and the increase of the total fuel concentration. The increase is both continuous and linear to weak exponentially. This simulation result corresponds to the expected behaviour, because the creation of the aromatic ring compounds is mentioned to be the rate limiting step in the reaction kinetics [180]. Increasing the fuel concentration raises the carbon fraction in the gas phase and thus also increases the nucleation rate.

However, it is also clearly visible that this effect does not remain throughout the simulation process. The final particle number concentration is determined by the coagulation rate. This is in agreement with observations by Lahaye [107].

Simulations for different fuel compositions at the base operating point and investigations at all parametrized operating points with 50 % mixtures are shown in Fig. 4.13 and Fig. 4.14.

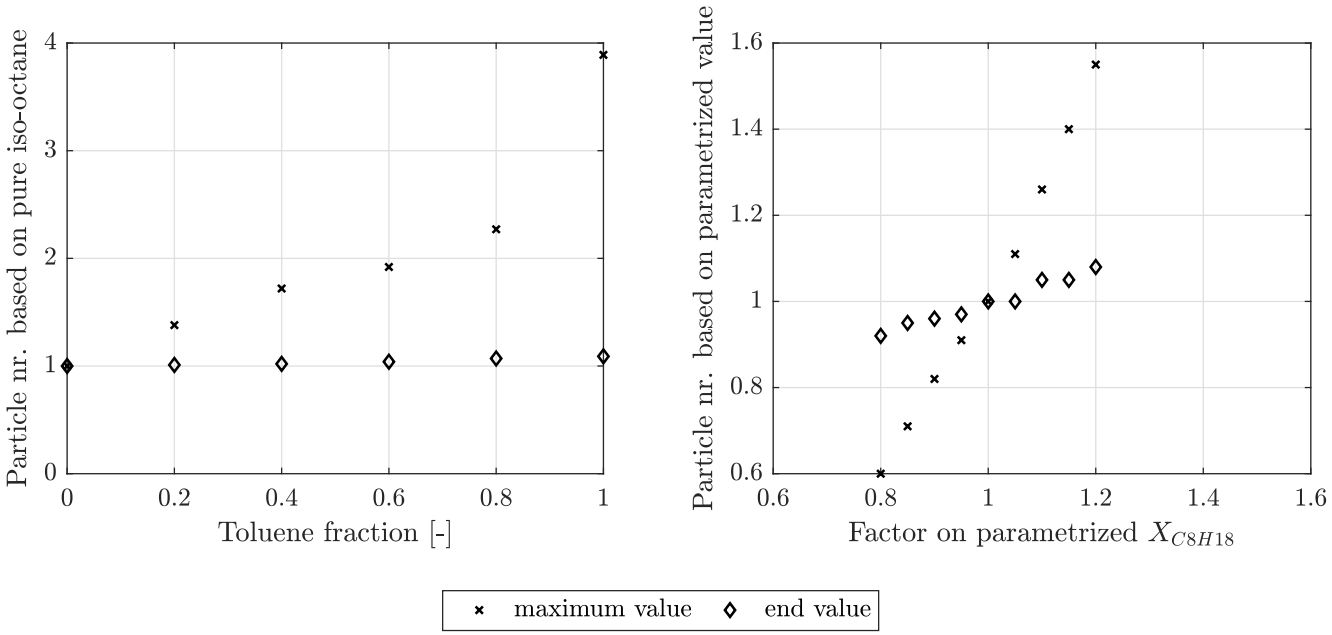

Fig. 4.12.: Sensitivity analysis of fuel composition and fuel concentration in the injector zone on particle number concentration. Different Toluene-iso-octane mixtures (left) and different fuel concentrations (right). Fuel concentrations are evaluated as factors on the parametrized value ($\approx$ 1.5 *mol*%). Maximum value of particle number concentration and value at simulation end (top dead centre exhaust stroke) are presented.

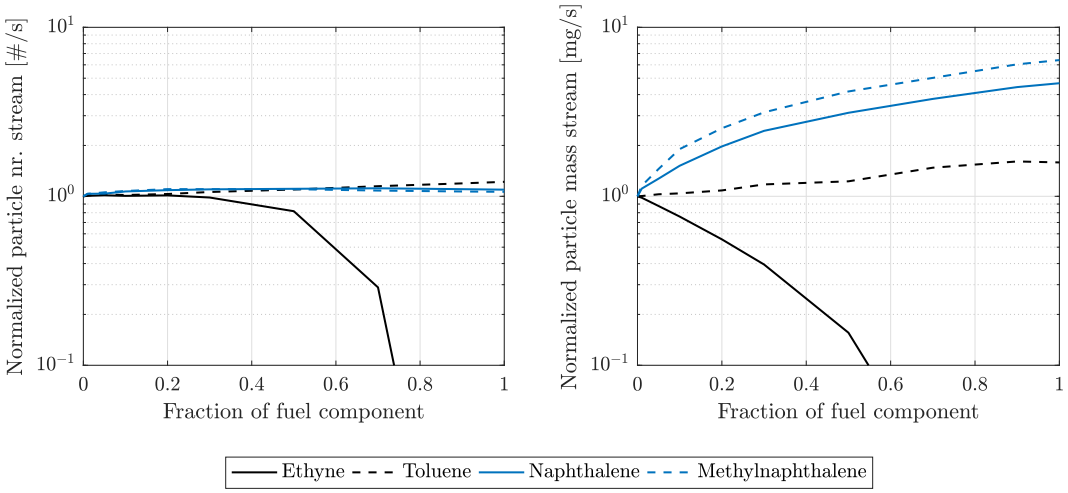

Fig. 4.13.: Sensitivity analysis on particle number and mass stream for different fuel compositions at 2000 rpm/10 bar IMEP. Constant total fuel fraction (parametrized value). Values normalized by pure iso-octane fuel results.

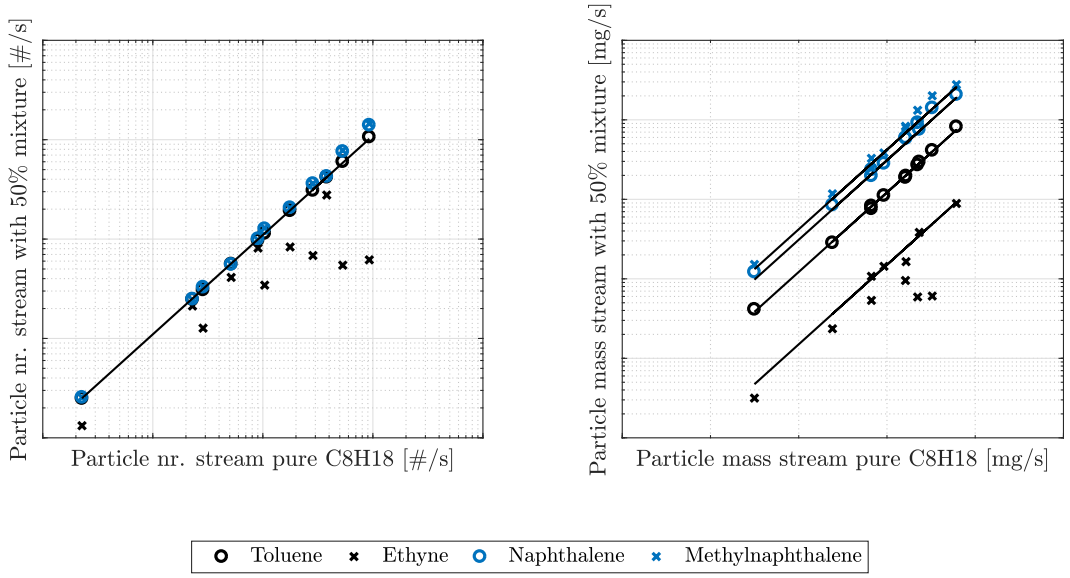

Fig. 4.14.: Sensitivity analysis of different 50 % fuel mixtures on particle number and mass stream for all operating points that were considered during parametrization of the injector zone model. Results based on 2000 rpm/10 bar IMEP operating point. Solid lines represent linear correlation.

In both cases, the total fuel fraction is kept constant at the parametrized value. Because of the different number of carbon atoms in the fuel components, especially for the ethyne component, the resulting particle number stream varies significantly. This can be corrected by changing the total fuel fraction of the injector zone based on the number of carbons in the additional fuel component. This study is shown in Fig. 4.15.

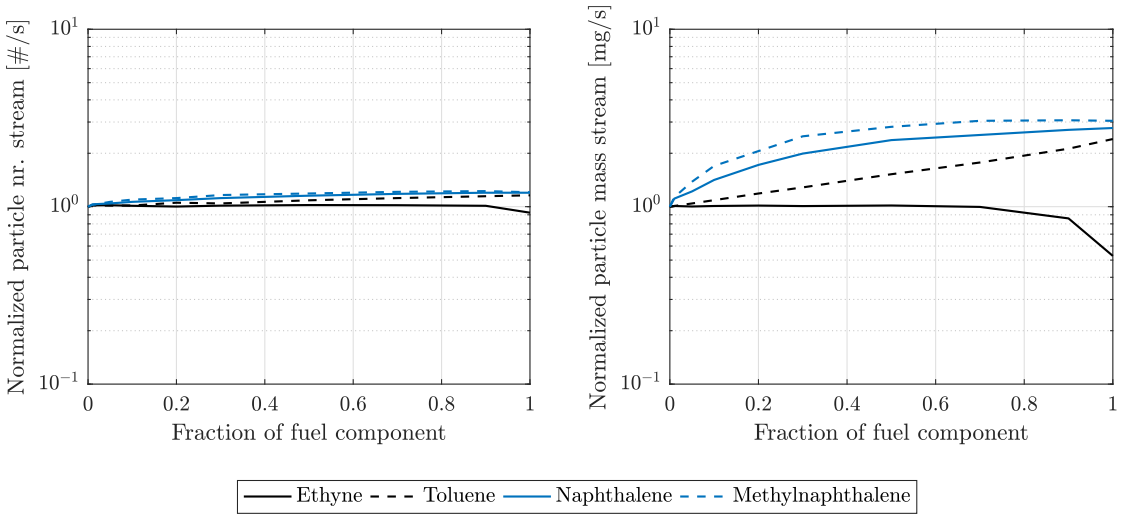

Fig. 4.15.: Sensitivity analysis on particle number and mass stream for different fuel compositions at 2000 rpm/10 bar IMEP. Constant carbon fraction ensured by correction of total fuel fraction.

Now, with an equalized number of carbon atoms, the simulation results show only a small influence on the final particle number stream (about 10 % for the 50 % fuel mixtures).

A more significant, but steady influence on the particle mass stream is visible that is based on the surface growth and condensation processes (see Fig. 4.14 on the right side). This influence can be corrected by parametrizing the active surface area α of the particles, that directly affects the growth reaction rates.

The analysis shows that the particle number results of the injector zone are robust regarding the simulated fuel composition and concentration.

The coagulation process is mainly influenced by the temperature and pressure of the injector zone. Temperature and pressure differences in the operating map are shown in Fig. 4.16 in terms of peak values calculated by the engine process simulation. The temperature information already includes the lower temperature boundary that has been identified during the parametrization process (see Eq. 4.9).

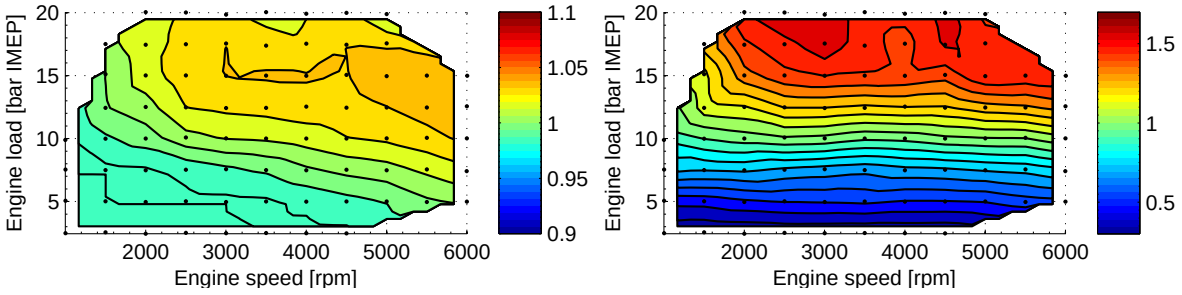

(a) Peak burned temperature values. **(b)** Peak pressure values.

Fig. 4.16.: Peak values in operating map normalized by 2000 rpm/10 bar IMEP value.

The simulated peak temperature of the engine operating map varies only in a range of about 5 % compared to the base operating point. Significant differences can be seen for the peak pressure values compared to the base operating point that are caused by changes in engine load. Of course, this presentation is a simplification of the real temperature and pressure profiles in the simulation. The peak value is used for illustration to be able to compare different operating points easily.

Based on these investigations, a sensitivity study is performed to analyse both temperature and pressure influences on the particle number and mass concentration of the injector zone. This is done by adding a factor on the cylinder pressure profile or on the temperature profile of the burned zone. The results are shown in Fig. 4.17.

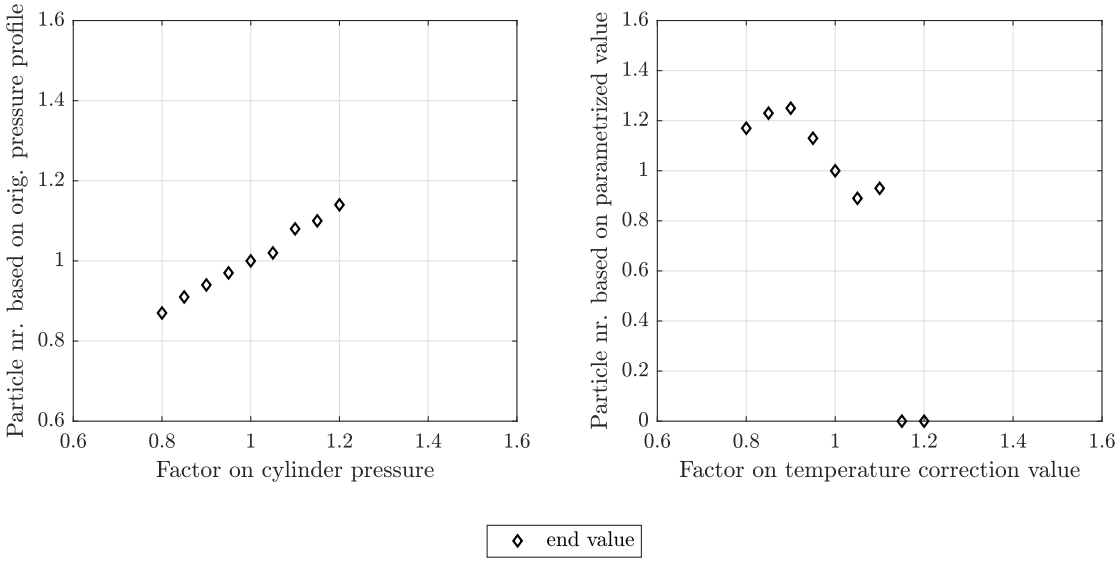

Fig. 4.17.: Sensitivity study of pressure and temperature profile on particle number density in base operating point 2000 rpm/10 bar IMEP.

Changing the temperature correction factor does effect the resulting particle number density of the injector zone. Increasing the temperature too much will completely eliminate the emissions, which can be explained by a lack of pyrene in the gas phase due to the reaction kinetics. It also leads to a reduced particle size and mass result.

Lower temperatures lead to some saturation of the resulting particle emissions. However, combined with the information of the operating map, the small changes in the temperature profile does effect the result in a range of about 10 % only and enables a robust calculation.

Varying the pressure profile also affects the particle formation and growth process. A linear dependency is identified for both the maximum particle number density and the value at the end of calculation (TDC of exhaust stroke). This is due to its effect on the particle coagulation process. In the here presented simulation, increasing the pressure profile increases the particle number density of the injector zone.

With the information of the sensitivity studies, the results of the injector zone for different operating conditions (see Tab. 4.3) can now be explained.

The temperature does only slightly effect the results, whereby higher temperatures lead to reduced particle number results and a reduced particle size. The fuel concentration and composition do not effect the values at simulation end because of the long calculation time.

Significant differences can be observed by the pressure influence on the coagulation process at engine operating points with different loads. A higher engine speed also affect the result because there is less available time for particle growth, leading to a higher particle number density at higher engine speeds and same engine load (see Fig. 4.18).

Summarized, the changes in the number density of the injector zone are mainly driven by changes in engine speed and pressure for the investigated operating points.

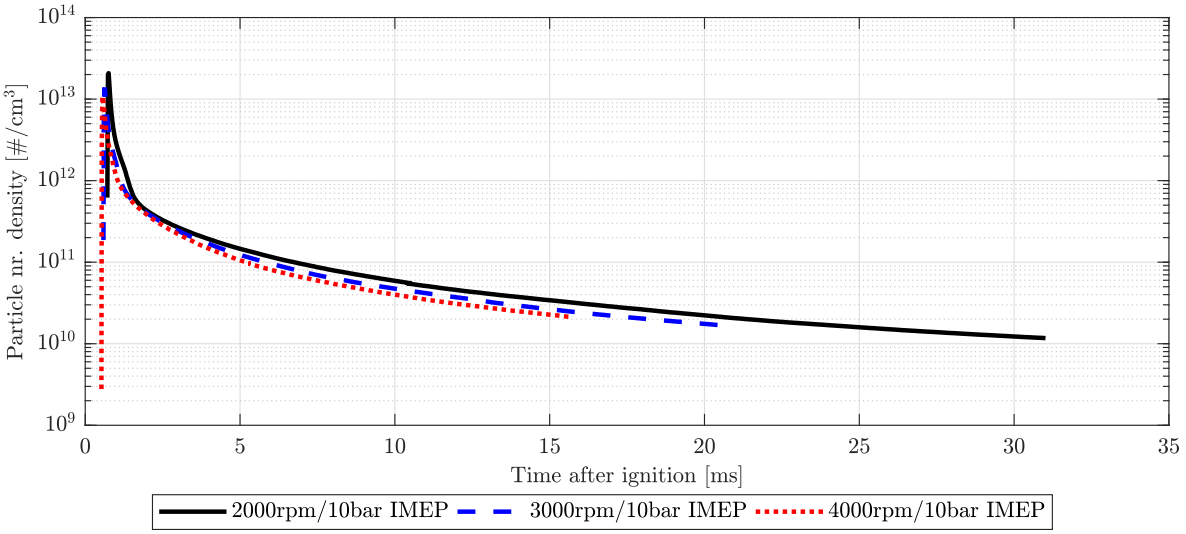

Fig. 4.18.: Influence of engine speed on particle number density of injector zone at simulation end. Different cut-off points caused by reduced available time for coagulation processes.

Number Density of Total Volume

The conversion of the injector zone number density to a total number density is performed with the ideal gas law.

The total number of particles in the injector zone depends on the zone volume, that is affected by the remaining film mass at ignition time and the fuel concentration (see Eq. 4.8). The parametrization of the injector film creation and evaporation process thus affects this part of the simulation results. For the given example set of operating points, the film mass increases at higher loads (increased injection duration) and higher engine speeds (reduced evaporation time).

The total volume is not limited to the cylinder volume, but increases due to the open exhaust valves according to the ideal gas law. Operating points at higher loads (high total in-cylinder mass) exhibit a smaller total particle number concentration in the simulation for the same particle number of the injector zone, caused by the higher overall volume. Therefore, although the particle number concentration of the injector zone and the remaining film mass at ignition time is smaller at the operating point 2000 rpm/5 bar IMEP compared to the base operating point, the simulated overall concentration is higher at simulation end (see Tab. 4.3)).

For increasing engine speed, the overall concentration result is mainly driven by the higher remaining film mass combined with the higher number concentration of the injector zone (see Tab. 4.3).

Conversion to Time-Based Values

The determination of the measured and legislation relevant time-based values is performed with the exhaust volume flow of all engine cylinders. This conversion significantly affects the quantitative result for each operating point. For the analysis in this work, the same exhaust volume flow is applied both for the simulation and the measured particle concentration.

For higher engine load and speed, the increased exhaust volume flow leads to higher total emissions and vice versa. Considering the counting efficiency of the particle measurement system (50 % at 23 nm) also slightly changes the simulations result. Especially at higher engine speeds with decreased particle sizes (higher temperatures and less time for coagulation processes), the number of particles below this threshold increases.

The inclusion of the exhaust volume flow also stabilizes the qualitative simulation result relative to the measured reference (e.g. giving the correct trend for the 2000 rpm/5 bar IMEP operating point compared to the base point, see Tab. 4.3).

The simulated particle size distribution also enables the calculation of the particle mass streams. The processes that influences the particle mass are more complex than the estimation of the particle number (e.g. surface growth and oxidation processes), leading to a decreased quality of the simulation results. These processes are influenced by all parameters of the simulation model but can mainly be parametrized with the active surface of the particles α. This enables the calculation of a comparable size distribution of the injector zone for the complete engine operating map that is in agreement with the accumulation mode of the measured size distribution (see Section 4.4.2).

5 Homogeneity Model

Preface for homogenization sub-model:
Parts of the discussed results have been published previously in the International Journal of Engine Research [68]. This includes the definition of the phenomenological homogeneity model, the evaluation of 3D-CFD simulations and the parametrization strategy and results.

5.1 Mathematical Approaches

5.1.1 Literature Overview

Inhomogeneous mixture preparation is considered to be one of the main sources of particulate emissions in DISI engines in the literature [79, 98, 118, 156]. Knowledge about homogenization quality is thus required to enable the calculation of particulate emissions from the gas-phase. In the literature, measurements were performed with CH_4/O_2 flames and with a DISI engine, identifying the ratio C/O = 0.44...0.46 as soot threshold [40, 79]. This was also confirmed by engine CFD simulations [86]. For iso-octane, a soot threshold of $C/O = 0.45$ corresponds to an equivalence ratio value of $EQR \approx 1.4$. Therefore, it is necessary to identify rich mixture zones within the combustion chamber that exceed this soot threshold.

For the creation of a DISI NO_x emission model, Gong and Rutland (2013) developed a method to shift the global EQR at start of combustion [72]. They defined an inhomogeneity index I_H based on dimensionless considerations.

$$I_H = exp\left(-C_2 \cdot \tau_{\text{mix}} \cdot Re^{-3/2} \cdot We^{2/3}\right) \tag{5.1}$$

They state that the effects of time of injection, in-cylinder bulk flow and spray-gas interaction could be captured by three characteristic numbers. The dimensionless mixing time τ_{mix} considers the injection duration Δt_{inj} and the homogenization time between start of combustion (SOC) and end of injection (EOI).

$$\tau_{\text{mix}} = \frac{t_{\text{SOC}} - t_{\text{EOI}}}{\Delta t_{\text{inj}}} \tag{5.2}$$

The Reynolds number Re includes the mean piston speed $\overline{u}_p$, bore diameter B and a kinematic viscosity ν. It is not further specified how this viscosity can be obtained within the publication [72].

$$Re = \frac{\overline{u}_p \cdot B}{\nu} \tag{5.3}$$

Finally, the Weber number considers the nozzle diameter of the injector d_{noz}, the injection velocity u_{inj}, fuel density ρ_f and surface tension σ.

$$We = \frac{\rho_f \cdot u_{\text{inj}}^2 \cdot d_{\text{noz}}}{\sigma} \tag{5.4}$$

In addition, an adjustable factor C_2 has been added representing the mixing property of the combustion chamber. The resulting index from Eq. 5.1 ranges from zero (complete mixing) to one (inhomogeneous mixture).

5.1.2 Applied Model Equations

The existing approach [72] (see Section 5.1.1) is only sufficient to shift a single global EQR value during combustion to a slightly lean value. No information can be obtained about the EQR distribution within the combustion chamber. In addition, the given definition only enables the mixing state to be calculated during combustion rather then describing the entire homogenization process. In the present work, the main idea of calculating a homogeneity or inhomogeneity index with dimensionless parameters is adopted and modified to suit a more generalized model setup. As a quantification of mixture homogeneity, the EQR distribution function over time can be described at different levels of detail, as shown in Fig. 5.1. Local and time resolved information is available from 3D-CFD simulations. Since no resolution in space is considered by the phenomenological model, a frequency distribution function for each time step can be obtained by omitting the local information. The whole mixing process can be represented by combining these distributions for all time steps considered. The integral distribution function enables the identification of the mass fraction with an EQR exceeding the soot threshold. Therefore, the mixture homogeneity within the combustion chamber can be ex-

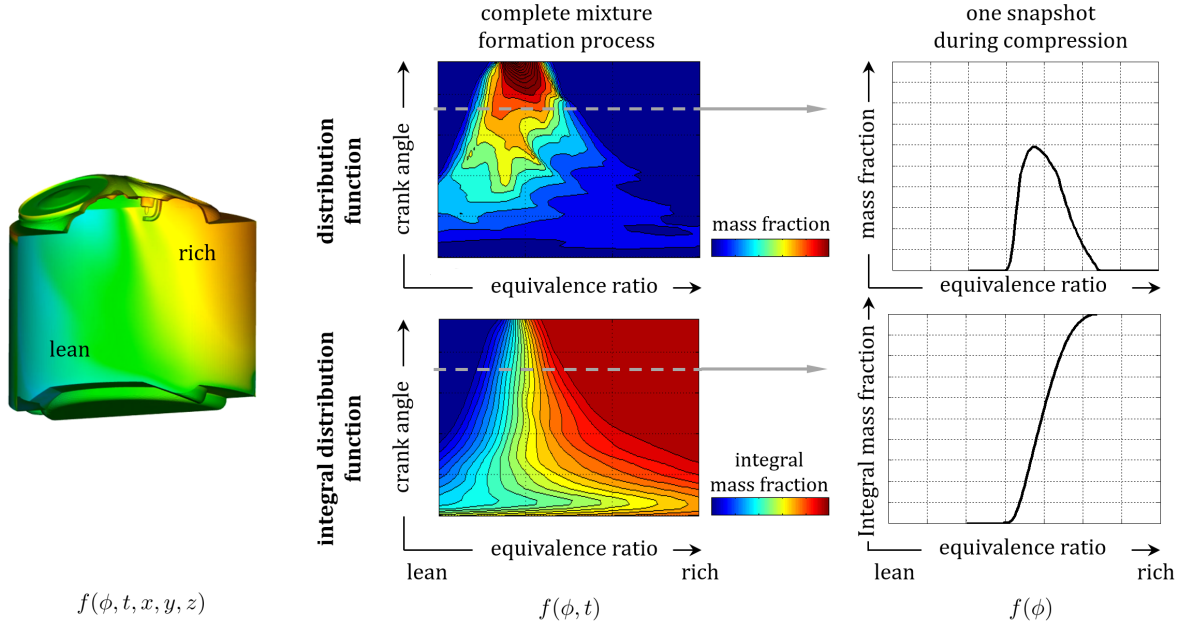

Fig. 5.1.: Distribution of combustion chamber equivalence ratio with local information or as frequency distribution function over time.

pressed by an exponential function at each crank angle value Θ, representing the integral distribution function F of the EQR ϕ.

$$F(\phi,\Theta) = 1 - exp\left(-A \cdot \phi^{E(\Theta)+1}\right) \tag{5.5}$$

The parameter E affects the gradient of the function and thus acts as a homogeneity index. Therefore, it is expressed in the same way as the prevous approach [72].

$$E(\Theta) = exp\left(C \cdot \tau_{\text{mix}}(\Theta)^D \cdot Re^X \cdot We^Y\right) \tag{5.6}$$

The dimensionless mixing time τ_{mix} is slightly redefined in comparison to the reference model. It is now expressed as a function of the current crank angle instead of using a fixed value. This would lead to the effect that $\tau_{\text{mix,EOI}} = 0$ for all injection durations. However, there is already a homogenization during fuel injection. The mixing duration is thus based on the SOI value henceforth.

$$\tau_{mix}(\Theta) = \frac{t(\Theta) - t_{SOI}}{t_{EOI} - t_{SOI}} = \frac{t(\Theta) - t_{SOI}}{\Delta t_{inj}} \tag{5.7}$$

The current formulation is strictly valid only for a single injection pulse but can theoretically be extended to two or more pulses. The Weber number and Reynolds number are taken from the literature (see Eq. 5.3 and Eq. 5.4) with an adjustment of the liquid properties. A correlation of Brock and Bird (1955) is used to estimate the surface tension σ [27, 148].

$$\sigma = p_c^{2/3} \cdot T_c^{1/3} \cdot Q \cdot (1 - T_r)^{11/9} \tag{5.8}$$

$$Q = 0.1196 \cdot \left(1 + \frac{T_{br} \cdot \log \frac{p_c}{1.01325}}{1 - T_{br}}\right) - 0.279 \tag{5.9}$$

$$T_r = \frac{T}{T_c} \qquad T_{br} = \frac{T_b}{T_c} \tag{5.10}$$

For iso-octane, the critial temperature $T_c = 543.9$ K, critical pressure $p_c = 25.7$ bar and boiling temperature $T_b = 372.39$ K are taken from Poling et al. (2001) [148]. The surface tension is calculated with the high pressure rail fuel temperature T.

Within the Reynolds number definition, the engine speed is already taken into account by the mean piston speed, whereas the load influence is considered by a simplified temperature and pressure dependency of the kinematic viscosity ν. The mean viscosity is determined by means of a Cantera [74] gas phase object considering the following properties:

- the species mixture of air and residual gas at start of injection
- the charge pressure
- the reference temperature T_{ref} as a mixture of inlet (downstream of throttle) and outlet (upstream of turbine) temperature, weighted by residual mass fraction Y_{EGR}

$$T_{\text{ref}} = (1 - Y_{\text{EGR}}) \cdot T_{\text{throttle}} + Y_{\text{EGR}} \cdot T_{\text{turbine}}. \tag{5.11}$$

This definition enables the calculation of a mean kinematic viscosity for each operating point and includes an engine load dependency on the Reynolds number.

The exponents D, X, Y and the constant C are determined for each engine type by comparison with 3D-CFD simulations, as it is further described in Section 5.3.

The parameter A can be determined from the fact that a global EQR ϕ_{global} is known, as explained in the following. If the spray injection and evaporation rate and the mass flow through the inlet valve are known, the actual value for ϕ_{global} is used for each time step. Otherwise, use is made of the EQR value resulting from total injected fuel and air mass and the model is only valid once the load exchange and

spray evaporation are completed. With the first derivative of the cumulated frequency distribution, the mass of air $m_{\text{air}}(\phi)$ is obtained for each value of ϕ:

$$f(\phi) = F'(\phi) = A \cdot (E+1) \cdot \phi^E \cdot exp\left(-A \cdot \phi^{E+1}\right) \tag{5.12}$$

$$f(\phi) = m_{\text{air}}(\phi) + m_{\text{fuel}}(\phi) = m_{\text{air}}(\phi) + \frac{\phi \cdot m_{\text{air}}(\phi)}{L_{\text{St}}} \tag{5.13}$$

$$m_{air}(\phi) = \frac{f(\phi)}{\frac{\phi}{L_{St}} + 1} \tag{5.14}$$

With the total mass of air $m_{\text{air,total}}$ and the stoichiometric air ratio L_{St}, the parameter A can be calculated with numerical methods.

$$m_{\text{air,total}} = \int_{\phi=0}^{\infty} \frac{A \cdot (E+1) \cdot \phi^E \cdot exp\left(-A \cdot \phi^{E+1}\right)}{\frac{\phi}{L_{\text{St}}} + 1} dx \tag{5.15}$$

$$\phi_{global} \overset{!}{=} \frac{1 - m_{\text{air,total}}}{m_{\text{air,total}}} \cdot L_{\text{St}} \tag{5.16}$$

An example of the temporal development of the function over the crank angle Θ is shown in Fig. 5.2.

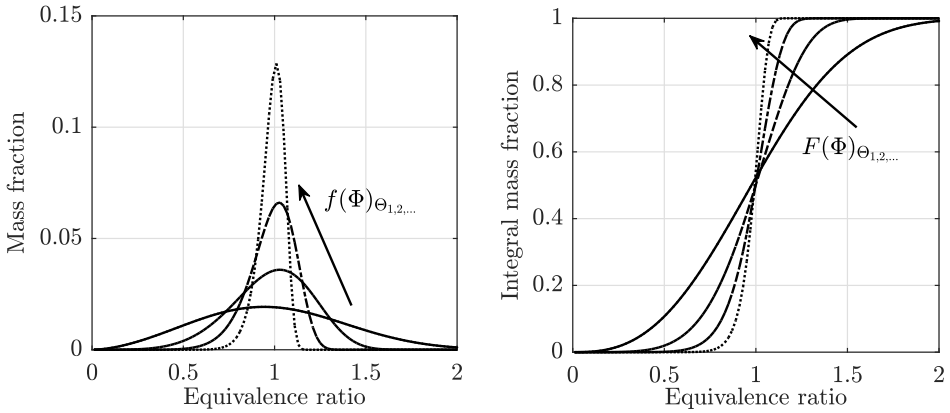

Fig. 5.2.: Development of the mixture homogeneity function with increasing mixing time for different crank angle values Θ.

5.2 Statistical Evaluation of CFD-Simulations

5.2.1 Generation of Appropriate 3D-CFD Model and Operating Conditions

Obtaining information about mixture homogeneity in the combustion chamber by measurement is in most cases not feasible. Optical methods (e.g. the laser-induced fluorescence method (LIF) [44]) are mostly limited to a local area and require an accessible engine. However, combining measurement results with 3D-CFD simulations is a common method to quantify the mixture preparation during load exchange and compression. The boundary conditions for the 3D-CFD simulations are obtained by measurements of a 4-cylinder turbocharged DISI engine with variable valve train and central injector position at homogeneous operating mode (engine A, see Tab. 3.3). The engine is equipped with

sensors measuring the pressure in the combustion chamber and in the intake and exhaust manifold. Using these sensors, a pressure analysis is performed to estimate the wall temperature, the mass flow and the combustion characteristics [122]. Additional information about the 3D-CFD model and the applied boundary conditions are shown in Tab. 5.1.

Tab. 5.1.: 3D-CFD simulation model.

	3D-CFD simulation
Software Code	ANSYS® CFX [8]
Boundary Conditions	
Inlet	mass flow, temperature
Outlet	pressure, temperature
Wall	temperature
Grid	valve lift, piston position
Model Type	
Turbulence	k-ϵ, Kato-Launder production limiter [91]
Spray/Fuel	langrange, no breakup model
Fuel	iso-octane*
Wall Interaction	Elsaesser [59]
*stoichiometric air ratio adjusted to gasoline value	

The quality of the 3D-CFD simulation is evaluated by comparing the in-cylinder pressure profile to measured data. In the presented work, the deviations of the pressure at ignition time lie in the range of ±3 % for all considered operating conditions. The simulation can thus reproduce the load exchange and mixture formation process with sufficient accuracy.

It is crucial to find a set operating points that allows the three different dimensionless parameters, defined in Section 5.1, to be calibrated. This includes variations in available mixing time, charge motion and spray-charge interaction. For this reason, a total set of 9 operating points are selected. The base operating point was set to $n = 2000$ rpm, 10 bar indicated mean effective pressure (IMEP). The available mixing time is reduced by retarding the start crank angle of injection. A variation in rail pressure mainly changes the injection speed, thus affecting the previously defined Weber number. Furthermore, it has an impact on the available mixing time because of the slightly reduced injection duration at higher rail pressures. Changing the Reynolds number without influencing the physical injection duration was achieved by a combined variation of engine speed and load. Increasing the speed while decreasing the load keeps the available mixing time approximately constant. In addition, two points are added with high engine speed and load to simultaneously change the Reynolds number and mixing time. An overview of the points chosen is shown in Fig. 5.3. The simulation results on the one hand side indicate critical operating conditions that can lead to particulate emissions from gas phase inhomogeneities, on the other hand they offer the possibility to calibrate the exponential parameters of the homogenization sub-model. This is achieved by minimizing the deviation of the integral EQR distribution function between the 3D-CFD results and the homogenization model, as further explained in the next chapter.

5.2.2 Evaluation of Simulation Results

The results of the 3D-CFD simulations are shown as contour plots of integral distribution functions in Fig. 5.4. They indicate that reducing the available dimensionless mixing time by delaying the start

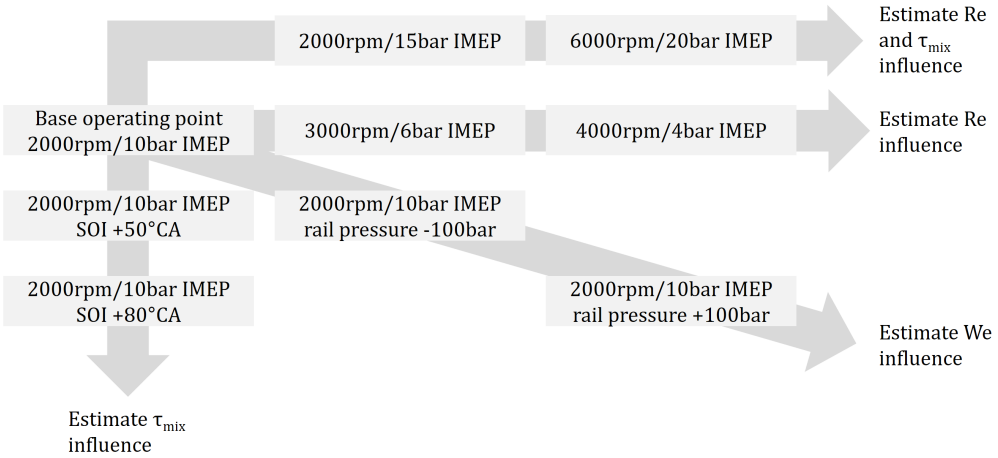

Fig. 5.3.: Set of operating points for identification of influences on mixture homogeneity. Enables calibration of homogeneity model.

of injection significantly decreases the homogeneity at start of combustion (at about 700°CA aTDCf). This is of course expected and just confirms that a sufficient calibration of the model would allow to cover this effect. Furthermore, areas of the combustion chamber exceed the soot threshold for the SOI + 80°CA point. Increasing the engine speed while reducing load, i.e. keeping the mixing time constant, improves the mixing quality as the charge motion increases. This result is in contrast to Gong and Rutland (2013) [72], where an increased Reynolds number was said to decrease the mixture homogeneity. However, they chose this correlation based on investigations on Diesel engines performed by Duffy et al. (1998)[53], where NOx emissions correlated with the engine speed. The currently observed Reynolds number dependency seems plausible for DISI engines. Even if the available mixing time is reduced due to higher injection durations, a positive effect is observed at higher Reynolds numbers. This can be seen particularly clearly at the 2000 rpm/20 bar IMEP and 6000 rpm/15 bar IMEP operating points. Increasing the injection pressure slightly improves the mixture homogeneity. Besides the effect on the Weber number, altering the injection pressure changes the defined dimensionless mixing time, however. To separate these effects, the homogenization process can be plotted as a function of the dimensionless mixing time instead of the actual crank angle (shown in Fig. 5.5). The results indicate that increasing the Weber number (defined in Section 5.1) leads to a reduced mixture homogenization in combination with the definition of the dimensionless mixing time. This is another difference to the literature model [72], where an increased Weber number encourages the homogenization process.

The present results lead to the conclusion that the mixture homogeneity increases significantly at higher dimensionless mixing time and Reynolds number and it decreases slightly at higher Weber numbers. It is important to note that the conclusions made for the dependencies of the dimensionless parameters are only valid in the context of the definitions specifically applied here.

Fig. 5.6 presents an example of an in-depth view of the homogenization process for the base operating point and an injection time variation (SOI +50°CA). The equivalence ratio distribution at the centre plane of the combustion chamber is shown at different dimensionless mixing times. It is obvious that, for both cases, the mixture homogeneity increases over time (subfigures (1)-(3) and (4)-(6)). Considering the homogenization state at $\tau_{mix} = 2$ (subfigures (1) and (4)) or $\tau_{mix} = 6$ (subfigures (2) and (5)) reveals a comparable mixture homogenization. This is also confirmed by the additionally plotted integral distribution function. The mismatch in the distribution function at $\tau_{mix} = 2$ is caused by the fact that there is still an inlet mass flow at the base operating point, whereas the inlet valve is already closed in the case of the delayed injection time. Therefore, the global equivalence ratio in the combustion chamber is slightly rich for the base operating point at this time step. The lower mixture

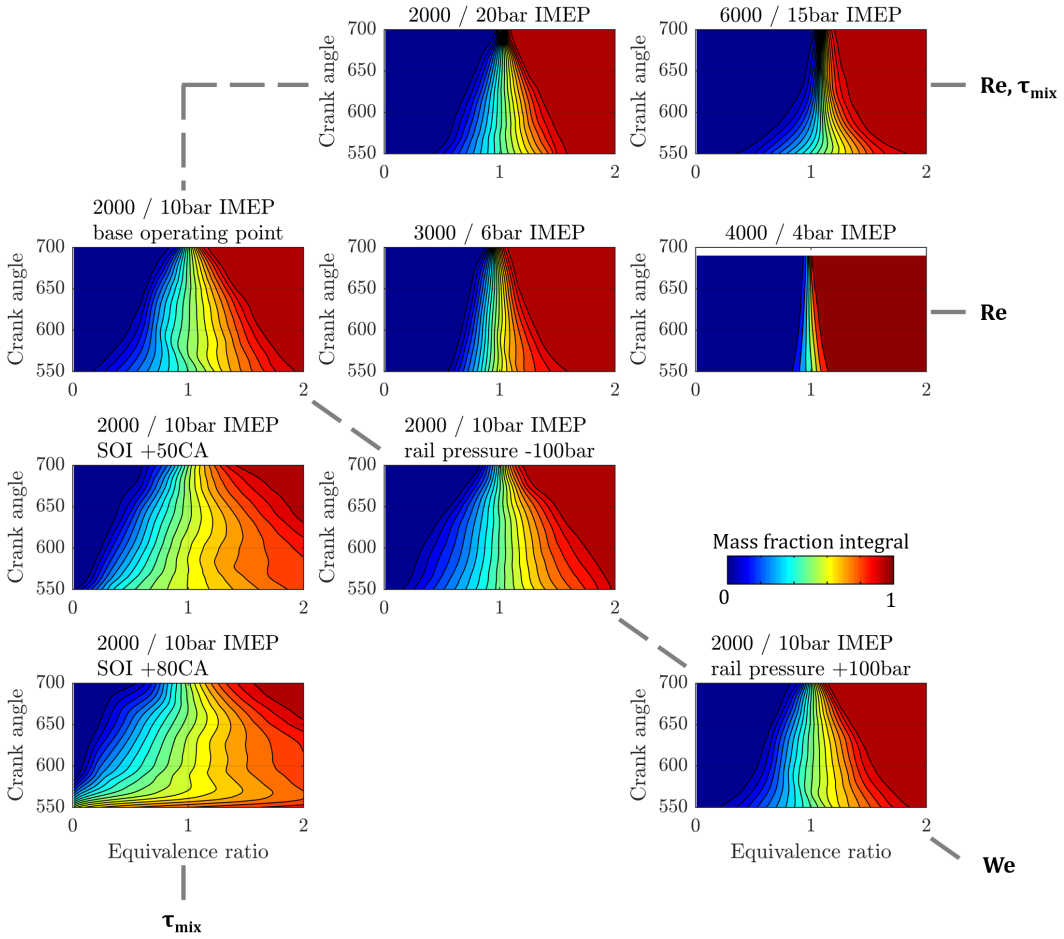

Fig. 5.4.: Evaluation of mixture homogeneity with 3D-CFD simulations at different operating conditions.

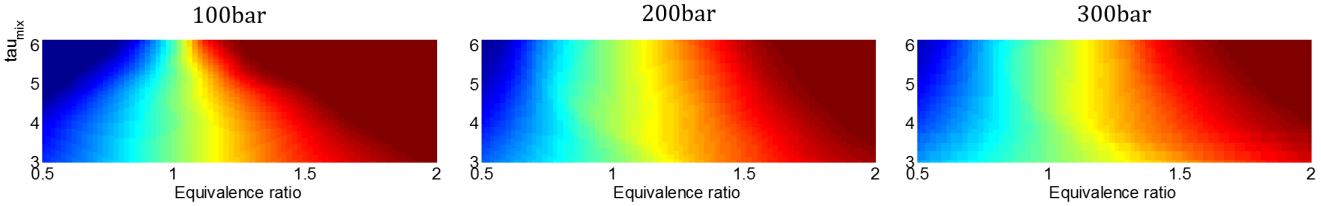

Fig. 5.5.: Effect of rail pressure change on mixture homogenization process by defining the homogenization process as a function of dimensionless mixing time. Results of 3D-CFD simulation.

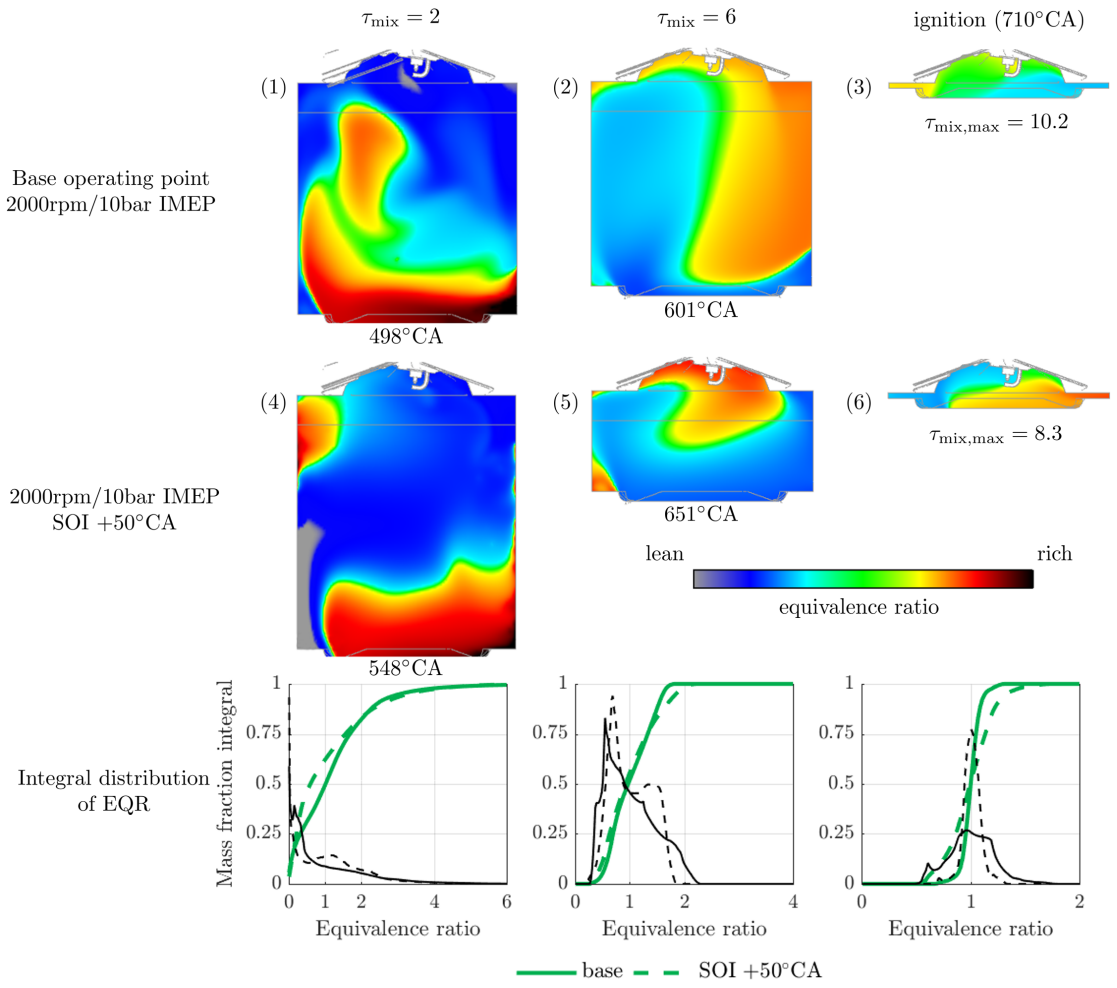

Fig. 5.6.: 3D-CFD results of in-cylinder EQR homogenization process for an injection time variation. Planar cut at centreline of combustion chamber. Inlet valve closing time at 540°CA. Black lines: non-integral distribution (different scaling).

homogeneity at ignition time also correlates with the reduced available mixing time for the delayed injection time (subfigures (3) and (6)). These results confirm that the definition of the dimensionless mixing time can cover the deviations for different injection timings regarding mixture homogeneity. Therefore, it is a suitable parameter to describe the homogenization process with a constant engine speed, load and injector parametrization.

Within the investigated operating conditions, only the latest SOI includes areas in the combustion chamber that exceed the soot threshold criteria for iso-octane. However, the results of the 3D-CFD simulations are only indicators since they only represent an averaged working cycle without cyclical fluctuations or transient effects. To identify operating conditions with mixture-induced particulate emissions, additional investigations are required.

5.3 Model Parametrization

5.3.1 Parametrization Strategy

For calibration purposes, it is possible to compare the results obtained from the 3D-CFD simulation (see Section 5.2.2) with the phenomenological homogenization sub-model for calibration. To do so, one parameter set is calculated to define the homogenization index E in Eq. 5.5.

$$E = exp\left(C \cdot \tau_{mix}^{D} \cdot Re^{X} \cdot We^{Y}\right) \quad \text{(Eq. 5.6)}$$

This calibration of specific exponents is a common method within the context of engine simulations (e.g. for wall heat transfer [194] or combustion modelling [137]), though it is not completely physically based. Considering the 3D-CFD results described in the previous section, the parameters are expected to be $D > 0$, $X > 0$, $Y < 0$, because of the positive effects of the mixing time and Reynolds number and the slightly negative influence of the Weber number on mixture homogeneity. The parameter C is optimized in the form 10^C with $C < 0$ as the overall scaling of the dimensionless numbers has to be very small to match the cumulated frequency distribution function. This was determined by identifying appropriate starting values prior to the optimization.

The calibration was realised with a simplex downhill method proposed by Nelder and Mead (1965) [138]. An objective function is defined to calculate an error value Z. For this purpose, the absolute value of the difference in the integral distribution function is summed up for all EQR values. The error values for all EQR values and all considered time steps are summed up and can be weighted by additional factors $W(\Theta)$ and $W(\phi)$.

$$Z = \sum_{\Theta=\Theta_0}^{\Theta_{ign}} \left[W(\Theta) \cdot \sum_{\phi=0}^{\infty} (W(\phi) \cdot |z(\phi,\Theta)|) \right] \tag{5.17}$$

$$z(\phi,\Theta) = f(\phi,\Theta)_{\text{model}} - f(\phi,\Theta)_{\text{CFD}} \tag{5.18}$$

$$\Theta_0 = \max(\Theta_{\text{EOI}}, \Theta_{\text{IVC}}) \tag{5.19}$$

To achieve an overall agreement of the homogenization process, the weighting factors are both set to unity. The considered time steps start at end of injection (EOI) or inlet valve closing (IVC), depending on what is greater. This enables the function parameter A to be calculated with the global EQR value coming from the lambda sensor. The last time step considered is the ignition time Θ_{ign}, at which the homogenization process is frozen for further calculations.

The simultaneous optimization of multiple parameters can result in several local minima. Therefore, two methods are tested to optimize the set of four parameters: the parallel optimization of all parameters with all operating points and a three-stage optimization of the different parameters. The second method is physically based since each variation of the operating conditions affects one dimensionless parameter. However, the result of the overall optimization method showed lower error values and is preferred henceforth. This is mainly because finding correct initial values is more important for the three-stage optimization than for the one-stage optimization.

5.3.2 Results and Model Quality

The results of the optimization strategy described previously are shown in Tab. 5.2. The calculated homogeneity index E mainly depends on the Reynolds number and is also significantly influenced by the mixing time. The Weber number has only a linear effect and reduces the exponent. This mathematically optimized result is in qualitative agreement with the analysis of the 3D-CFD simulations (see Section 5.2.2). Therefore, the optimization results are physically logical although the optimizer has adjusted all parameters simultaneously.

C_1	D	X	Y
-10.40	2.72	3.30	-1.14

Tab. 5.2.: Optimization results of homogeneity model for engine A, Eq. 5.6.

The complete model results are shown in Fig. 5.7 for the entire mixing process and can be compared to the 3D-CFD results in Fig. 5.4. The influence of injection time variation corresponds well with the 3D-CFD results. Adaptions of engine speed and load are also covered by the model. However, the increased mixture preparation at the end of compression that is slightly visible in the CFD results for different rail pressures is not fully covered by the phenomenological model. This is acceptable owing to the low influence of the Weber number. Overall, the results show satisfying agreements for all considered operating conditions regarding the homogenization process over time.

For the further processing of the data in the particle model, the frequency distribution values at time of ignition are used. A comparison of the phenomenological model to 3D-CFD results is shown in Fig. 5.8 for this time step. The model slightly underestimates the homogeneity for the base operation point and the rail pressure variation. However, these mixing qualities are outside of the soot threshold and the model quality is sufficient. The particulate emission relevant change of injection time is covered by the model. In addition to the results shown above, another set of operating points is compared between the 3D-CFD model and the phenomenological model. These operating conditions are not used for calibration and cover a wide range of engine speeds (2000−6000 rpm) at higher loads (10 − 20 bar IMEP) and are therefore employed for further validation. This leads to a variation in the Reynolds number caused by the different engine speeds and loads. The available mixing time varies because of different injection time values and injection durations. The Weber number is kept constant due to its small influence on the homogenization process for this engine (constant rail pressure). The corresponding results are shown in Fig. 5.9 at ignition time. The overall model quality is also satisfying under these operating conditions. Again, the model underpredicts the homogeneity at 2000 rpm/15 bar IMEP and thus confirms the previous results. It has to be emphasized that only the EQR values above the soot threshold criteria are used for the particle simulation framework. Thus, it remains open if the model quality is sufficient in this area of the frequency distribution function with the optimized parameter set. The final model quality must be assessed against measured particulate emissions.

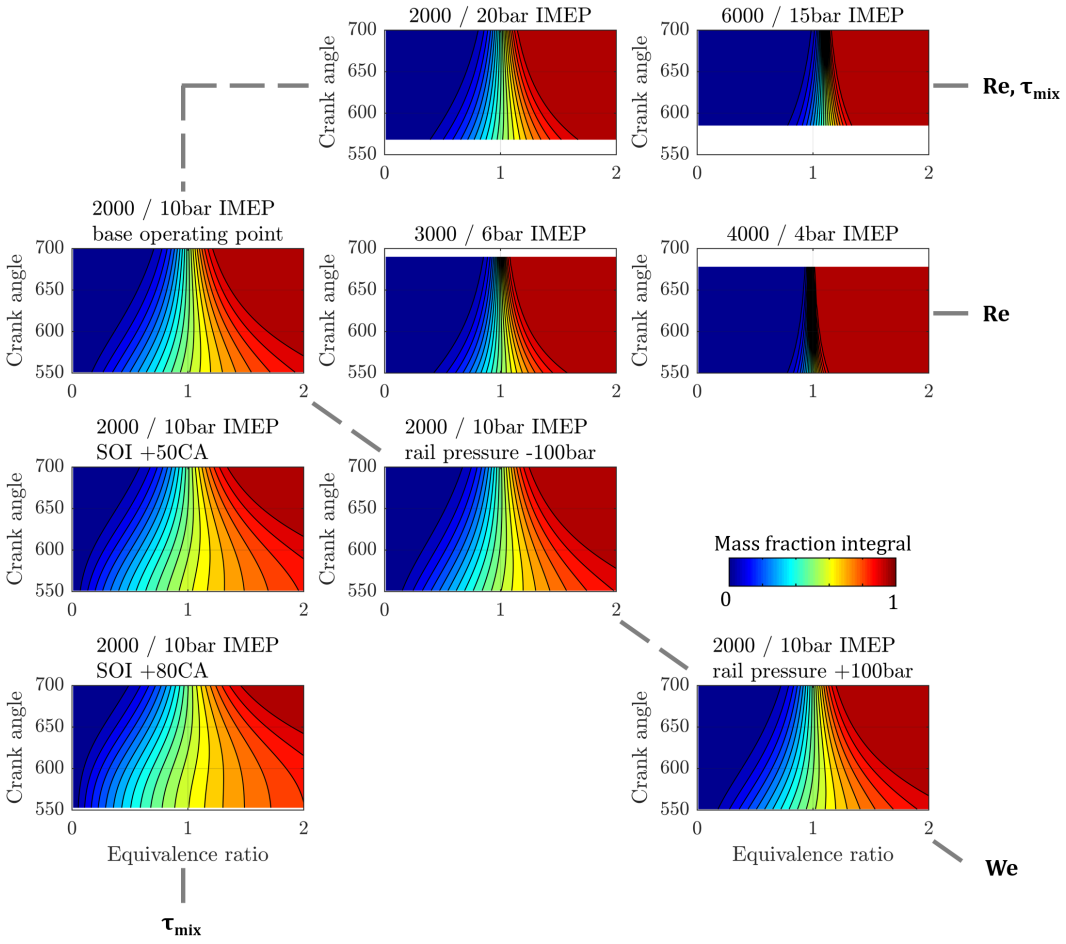

Fig. 5.7.: Results of homogenization model after calibration for all considered operating conditions at all time steps between inlet valve closing / end of injection (whichever is greater) and ignition time.

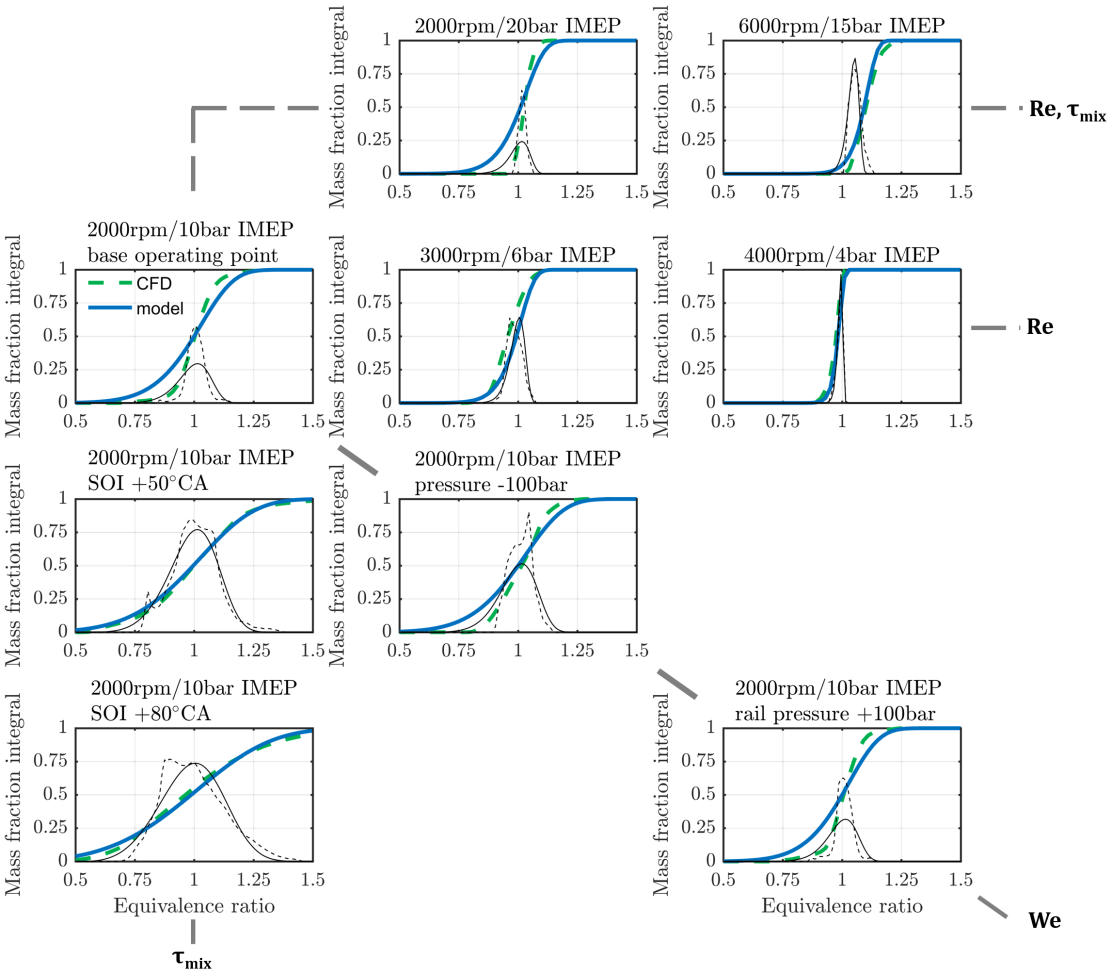

Fig. 5.8.: Comparison between homogeneity model (blue) and 3D-CFD results (green) at ignition timing for all considered operating conditions. Black lines: non-integral distribution (different scaling).

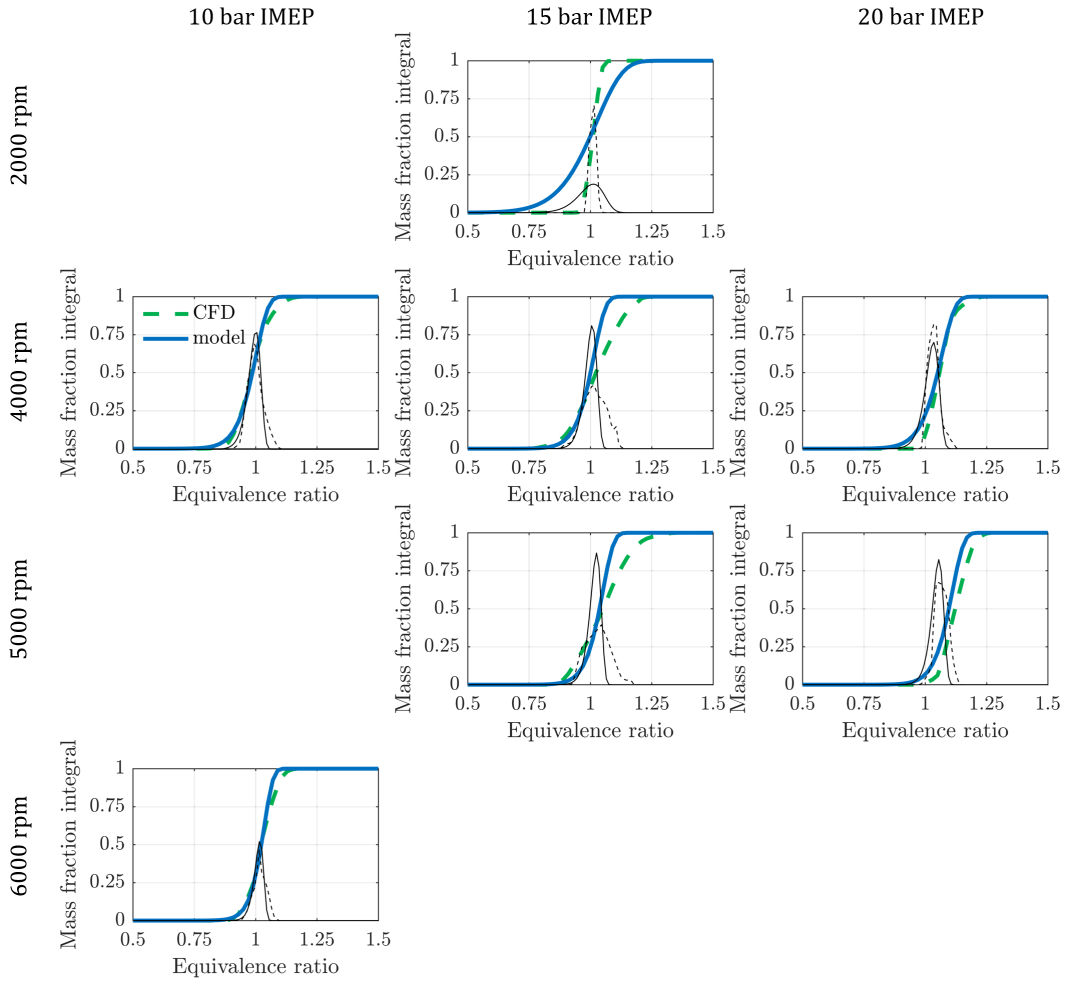

Fig. 5.9.: Additional operating conditions for model validation without further calibration. Comparison between phenomenological model (blue) and 3D-CFD results (green) at ignition time. Black lines: non-integral distribution (different scaling).

5.3.3 Transfer to Different Engine

The applicability of the homogeneity model with a calibrated set of parameters has been shown for a given engine at different operating points and parameter variations. Since the model is based on phenomenological assumptions, it is expected to be possible, in principle, to transfer it to another engine. Hence, a different engine (engine C, see Tab. 3.3) is selected to evaluate the possibility of transferring the model by re-calibrating of the exponents inside the homogeneity index definition. The calibration process is performed at different speed and load conditions and at a variety of rail pressures, similarly to the process applied to engine A. The calibration results are shown in Fig. 5.10. The exponents determined differ only slightly compared to engine 1. This indicates that engines with

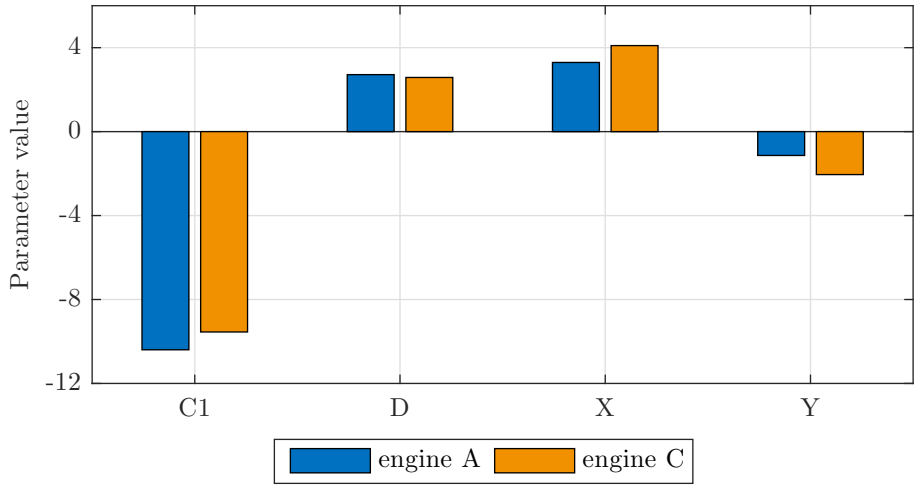

Fig. 5.10.: Comparison of calibration results between engine A and engine C (Eq. 5.6).

comparable combustion methods lead to a comparable set of parameters. Differences are mainly included in the calculated influence of the Reynolds and Weber numbers.

In Fig. 5.11, the resulting homogeneity at the time of ignition is compared to 3D-CFD simulations for engine C with the re-calibrated model. The quality of the phenomenological model is nearly of similar quality to engine A for the given operating conditions. However, since comparable parameter variations are performed for this engine, the homogenization quality at ignition time does not differ much over the engine map. Additional investigations should investigate how the model can be transferred to a number of different combustion concepts and verify the model quality for a variety of parameters.

5.4 Implementation in Overall Model

5.4.1 Parameter Variation Results

According to the 3D-CFD results in Section 5.2.2, the injection time variation is expected to cause particle emissions from inhomogeneous mixture preparation. Therefore, the homogenization model results of this variation are implemented and evaluated in the simulation framework. Additional zones from gas phase inhomogeneities are created as it is described in Section 3.2.1 with the integral distribution function of the equivalence ratio at ignition time. The resulting number of zones and the mean EQR value of each zone are shown in Fig. 5.12 for each operating point. A constant interval of $\Delta\phi = 0.075$ was defined for zone creation (a sensitivity analysis of the number of zones on the final

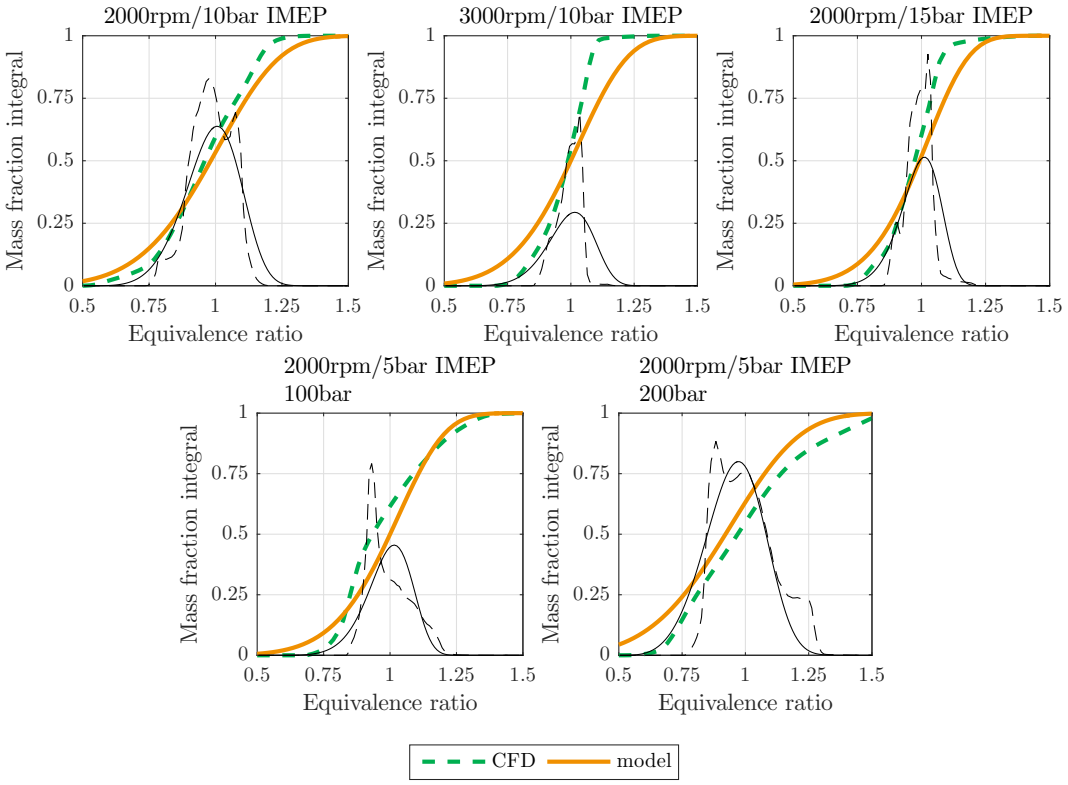

Fig. 5.11.: Homogenization model results compared to 3D-CFD (engine C) at ignition time. Black lines: non-integral distribution (different scaling).

result is shown in Section 5.4.2). The total mass fraction that does not exceed the soot threshold is lumped into one zone with the global air-fuel ratio because no particle emissions are expected and the calculation time can be reduced by reducing the total zone number.

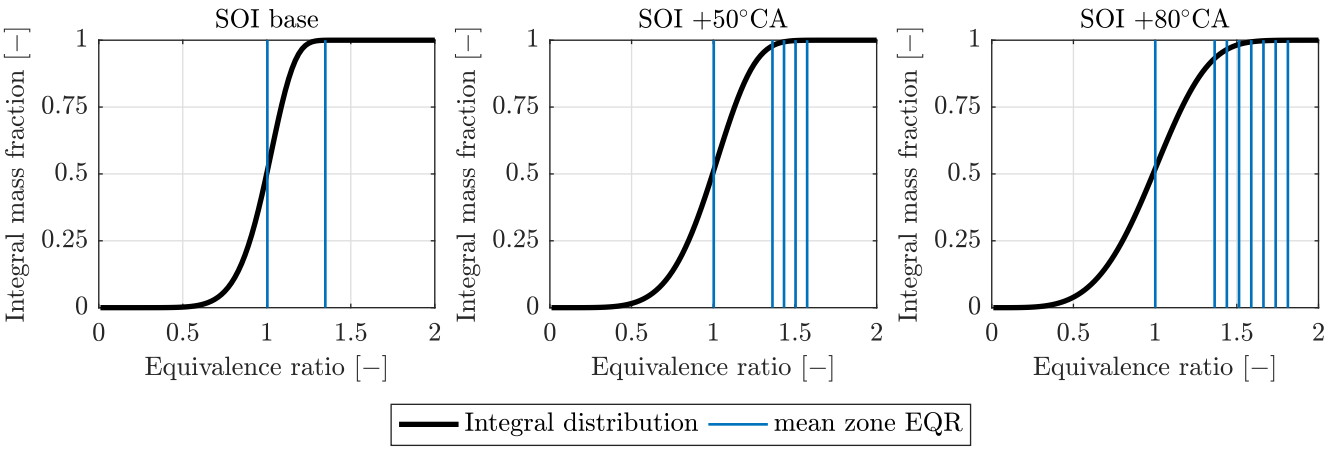

Fig. 5.12.: Simulated integral distribution function at ignition time and definition of mean zone EQR for injection time variation. EQR difference of each zone: $\Delta\phi = 0.075$.

The fuel-rich zone of the base operating point is negligible because of its small total mass fraction. The injection time that is delayed by 50°CA already leads to a total number of four fuel-rich zones that exceed the soot threshold. Further delaying the injection time leads to a total number of seven fuel-rich zones. An overview of the zone creation results is shown in Tab. 5.3, including the total number of zones, the maximum considered value of the EQR and the mass averaged temperature correction factor that is applied to each fuel-rich zone.

Tab. 5.3.: Zone information of injection time variation at 2000 rpm/10 bar IMEP. Simulated ratio of mixture-induced (mix) to injector induced (inj) particle number (PN) and mass (PM) emissions.

	Nr. of zones	max. EQR	Temp. Correction	PN mix/inj	PM mix/inj
Base	2	1.35	0.96	0.0	0.0
SOI +50	5	1.57	0.95	0.2	0.0
SOI +80	8	1.81	0.94	3.5	1.0

To compare the particle emission results with measured data, the remaining injector film at ignition time is adjusted to match the particle number emissions of the base operating point. This is necessary because the parameter variation of the homogenization model was measured with engine A (see Tab. 3.3 for specifications) that has a different injector state compared to engine B. However, this does not affect the mixture-induced particle emission results and is only required because the total emissions are a combination of injector and mixture sources. In this section, focus is set on evaluating the simulated particle emissions from mixture-induced zones. The simulation results for time-based particle number and mass emissions are shown in Fig. 5.13.

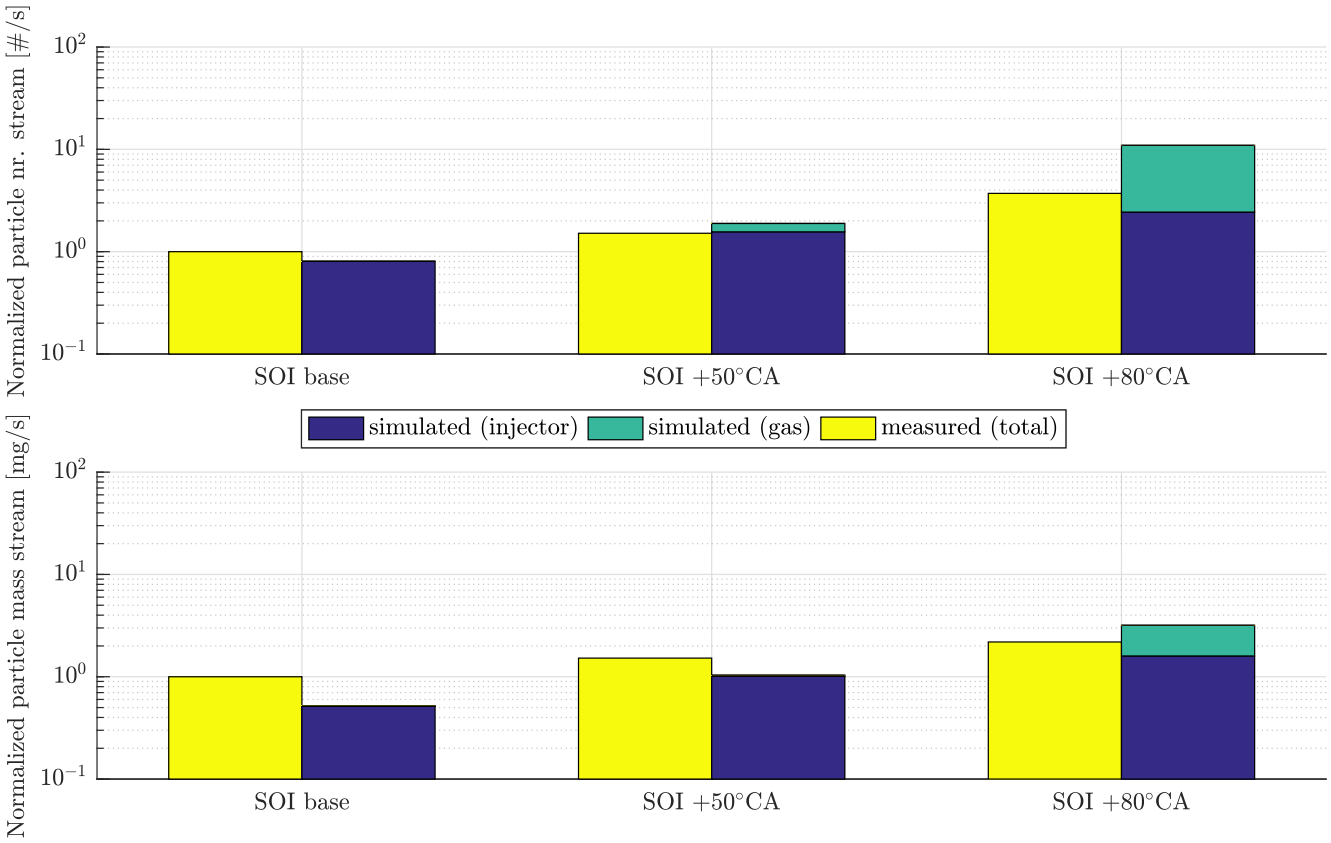

Fig. 5.13.: Simulation results injection time variation compared to measured data. Operating point: 2000 rpm/10 bar IMEP. Values normalized by measured particle emissions with base injection time.

Analysing the simulation results and comparing them to the measured values leads to two main conclusions:

1. Delaying the injection time leads to a reduced injector film evaporation time. This already increases the injector-induced particle emissions and covers the measured emissions at SOI + 50°CA. However, the simulated injector-induced emissions at SOI + 80°CA are not sufficient to describe the increase in the measured particle number emissions. This already indicates that a second source of particle emissions is required here.

2. As it is expected, no mixture-induced emissions are simulated at the base operating point because of the high degree of homogenization at ignition time. At SOI+50°CA, a small contribution to the particle number emissions (about 20 % of the injector-induced emissions) is visible. The particle mass is not affected at this operating point. This indicates that the resulting particle diameters are small compared to the particles from film pyrolysis. A significant contribution to the total emissions is simulated at SOI + 80°CA that leads to an over-prediction of the measured values. However, the impact on particle number results is still higher than on the particle mass. In Tab. 5.3, the ratio of mixture-induced to injector-induced particle number and mass emissions is presented to clarify this behaviour.

Summarizing, the combination of injector- and mixture-induced zones can explain the measured particle number and mass emissions qualitatively. Especially the change in the number/mass ratio of the latest injection time is covered by the simulation with satisfying agreement. However, the total results are over-predicted compared to the measured values at this operating point. It is assumed that this is mainly caused by the uncertainties of the integral distribution function. Therefore, an in-depth analysis of the simulation results, including the particle size distribution and a sensitivity study, is presented in the following.

5.4.2 Analysis of Simulation Process

It is clearly visible in Fig. 5.12 that the zones which are relevant for particle emissions from mixture inhomogeneities are distributed along the boundary region of the distribution function. Thus it needs to be investigated to which extend the resulting particle concentration depends on the air-fuel ratio of each simulated zone. The results are presented in Fig. 5.14.

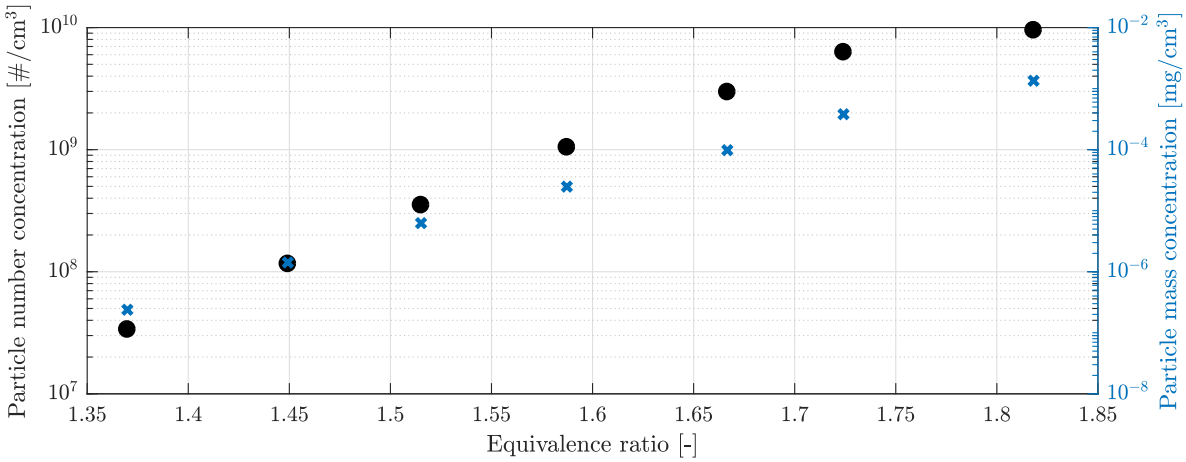

Fig. 5.14.: Influence of air-fuel ratio on simulated mixture induced particle number and mass concentrations at the SOI + 80°CA operating point.

Both the particle number and mass emissions show an exponential dependency on the air-fuel ratio. Although the total mass fraction of the fuel-rich zone decreases, this shows the high sensitivity of the simulated results from mixture inhomogeneity along the boundary region of the EQR integral distribution function. This is one possible explanation for the deviations between measured and simulated emissions at the SOI+80°CA operating point. However, implementing the distribution function of the 3D-CFD results would lead to even greater deviations because of a more distinctive inhomogeneity at ignition time. In this context, it has to be emphasised that the 3D-CFD simulation does not consider cyclic fluctuations. The results indicate that it is not sufficient to parametrize the homogenization model solely by 3D-CFD simulations if the results are intended to be used for particle simulation.

The results of the sensitivity analysis for the mixture composition are in contrast to the previously described sensitivity on the injector pyrolysis zone composition (described in Section 4.5, e.g. Fig. 4.12). The particle number emissions of the injector pyrolysis zone mainly depend on the coagulation processes. In Fig. 5.15, the temporal evolution of the particle number and mass concentration is shown for the different mixture-induced zones. In contrast to the injector pyrolysis results, nearly no reduc-

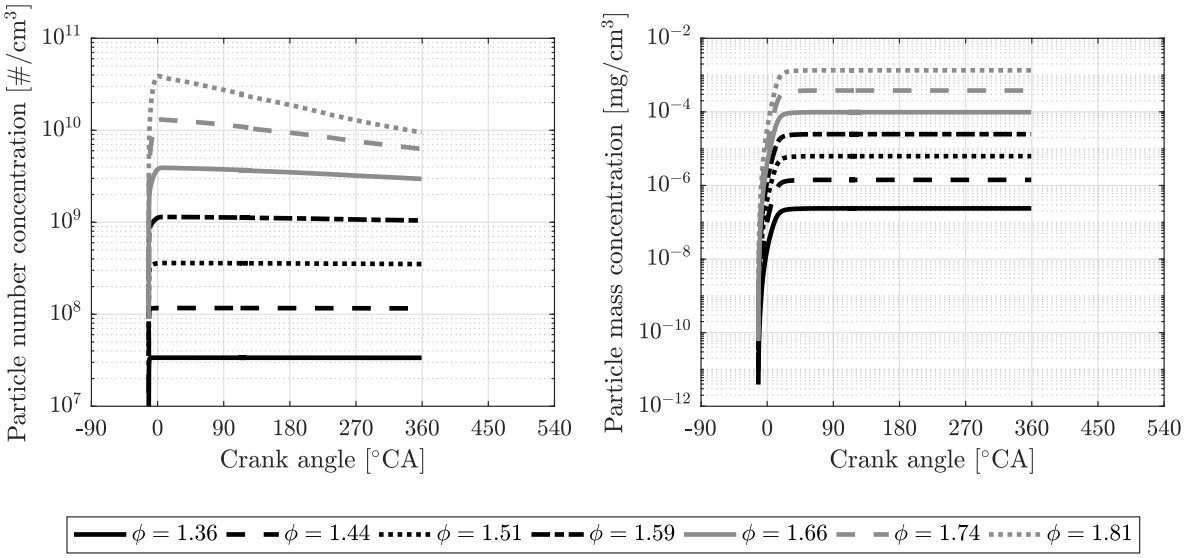

Fig. 5.15.: Simulated equivalence ratio influence on particle number and mass profile of mixture induced emissions at the SOI + 80°CA operating point.

tion of the particle number concentration by coagulation processes is visible for most of the zones. The coagulation processes only affect the zone with the highest EQR value. This can be explained by the low total particle number concentration of the mixture-induced zones compared to the injector pyrolysis zone (see also Fig. 4.18). The final results are therefore mainly caused by the nucleation process that is highly sensitive on the pyrene concentration and the EQR value of the mixture.

Besides the mixture composition, the temperature of the reaction kinetics is expected to highly influence the pyrene concentration and the inception rate because of the included Arrhenius equations. Therefore, a sensitivity analysis is performed by varying the temperature correction factor by ±20 %. The influence on total particle number and mass emissions is shown in Fig. 5.16.

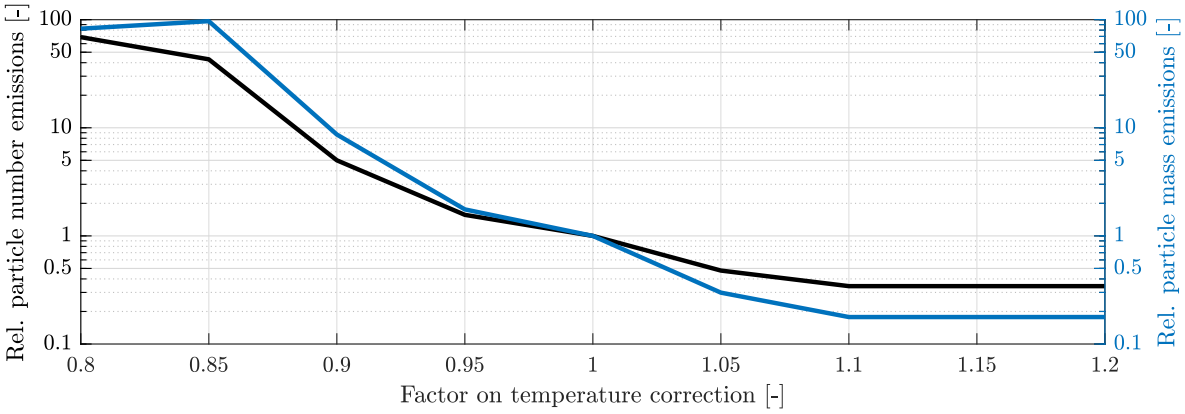

Fig. 5.16.: Sensitivity of particle number and mass emission of mixture-induced zones on temperature correction factor at the SOI + 80°CA operating point.

The particle results have an exponential dependency on the temperature level in the mixture-induced zones for both number and mass emissions. In the considered operating point, the original tempera-

ture correction factor was calculated to be $T_{corr} = 0.94$, leading to an over-prediction of the emissions. Neglecting the temperature correction in the fuel-rich zones would increase the absolute quality of the results in this case (corresponds to factor of 1.06 in the figure).

However, both sensitivity analysis show a significant influence of the mixture composition and temperature profile on the results, because of the high impact of the nucleation rate. Therefore, it is assumed that mixture-induced particle emissions can hardly be predicted with sufficient accuracy because of the lack of information in a zero-dimensional approach. Further parameter variations are required to evaluate the quality of the results.

A variable parameter for the implementation of the homogenization model results is the number of zones that are created from the integral distribution function. It is thus required to verify whether the results converge for a specific number of zones. This is again analysed at the SOI + 80°CA operating point. The original EQR step of $\Delta\phi = 0.075$ leads to a total number of eight mixture-induced zones. In Fig. 5.17, the particle number and mass results are shown for a variable zone number. Obviously, the results converge at at a total zone number greater than five, confirming that the selected EQR step is sufficient.

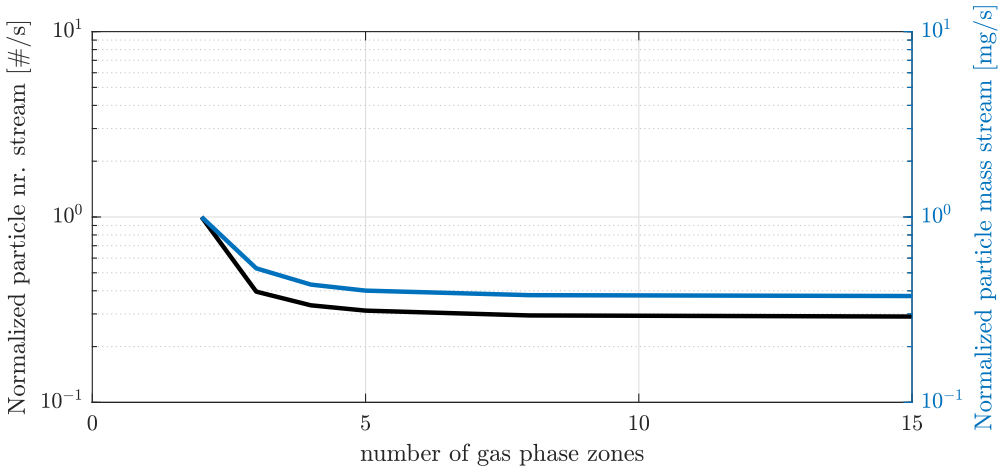

Fig. 5.17.: Influence of zone number on simulated mixture induced particle number and mass emissions at the SOI + 80°CA operating point. Particle results are based on original temperature correction factor $T_{corr} = 0.94$. Results normalized by values considering two simulated zones.

In addition to the total simulated particle number and mass values, the particle size distribution is also analysed for the injection time variation. Note that, for the measurement of engine A, no information about the particle size distribution is available. However, the measured results already show a change in the particle number to mass ratio for the late injection time case. This is confirmed by the simulation results. The total simulated particle size distribution of the injection time variation is shown in Fig. 5.18.

The particle size distribution that is generated by the injector film pyrolysis zone shows a peak value at about 50 nm. This value remains nearly constant for all three operating points. The particle distribution of the mixture-induced zones has a varying behaviour. At the latest injection time case, the absolute concentration of the mixture induced zones exceeds the value of the injector pyrolysis zone. The particle diameter is significantly smaller and shows different peak values from about $10-30$ nm. This can be explained by the focus on nucleation (mixture induced zones) in contrast to coagulation (injector film pyrolysis zone). Besides the nucleation process, the pyrene condensation also affects the particle diameter. This leads to the conclusion that the single peaks are caused by the different zones. Zone-specific results of the size distribution are therefore shown in Fig. 5.19 for the latest injection time case. Due to the discrete number of zones, the resulting size distribution shows a finite

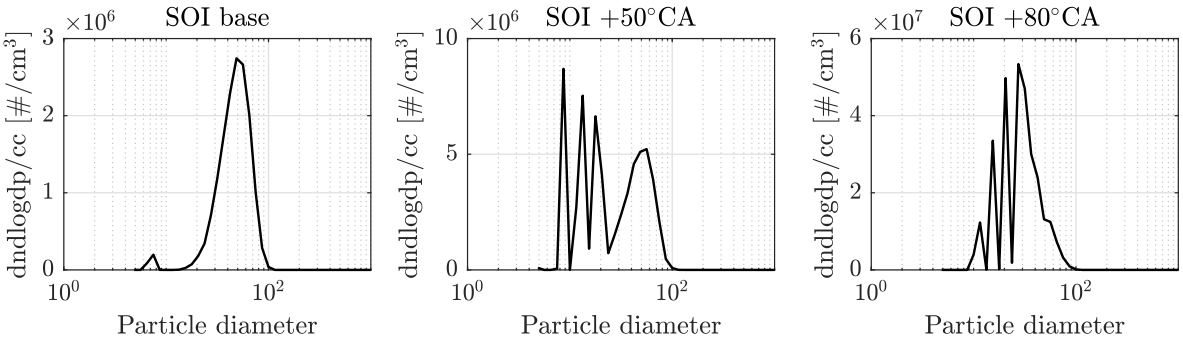

Fig. 5.18.: Simulated results of particle size distribution for injection time variation results. Injector zone and rich mixture zones included.

number of peaks. Combining the results by an envelope shows the possible size distribution for an infinite number of zones.

The shape of the discrete distribution function not only depends on the number of zones, but also on the number of particle diameter supporting points. The supporting points of the simulation are set to the values of the Cambustion DMS500 [32] (total number of 38 nodes between 5 and 1000 nm) for reasons of comparability. In order to substantiate the representation of the envelope, an additional simulation was performed. This simulation includes an increased number of 500 nodes and two different zone numbers of 8 and 15 zones. The results are presented in App. A.1.1, Fig. A.1 and confirm the shape of the mixture induced distribution function. It should be noted that the absolute particle concentration value of each zone depends on the total mass fraction of the zone. Therefore, the scaling of the y-axis depends on the zone number.

It is clearly visible that the mixture-induced zones form a mode at about 20−30 nm. In the context of simulation, this enables the separation of the mixture-induced effects and the film pyrolysis. Further comparison to measured particle size distributions are required to proof if this behaviour is physically plausible.

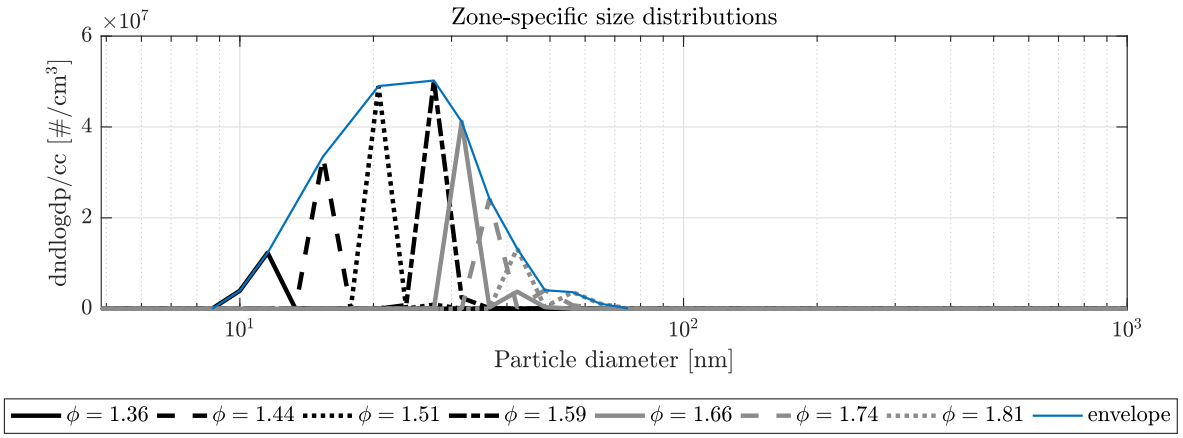

Fig. 5.19.: Simulated particle size distribution for each zone from inhomogeneous mixture preparation (black) and envelope for all considered zones (blue). Operating point 2000 rpm/10 bar IMEP, SOI+80°CA.

6 Modelling Wall Film Formation and Evaporation

Preface for wall film formation and evaporation sub-model:
Parts of the discussed results presented below originate from the master thesis of Hanisch [81], which I supervised during my time as doctoral candidate. This includes the approaches of the spray model, the spray-wall interaction model, the wall film evaporation model and the identification of the corresponding calibration parameters.

6.1 Spray Model

6.1.1 Mathematical Approaches

Droplet size distribution

In DISI engines, the injected fuel is atomised into a fuel spray almost immediately after leaving the nozzle [163], including the breakup of the droplets. Since the in-nozzle flow is not considered within the here presented spray model, no breakup models are included. Instead, the spray is represented by a prior defined droplet size distribution that is based on a so-called representative droplet diameter d_{pq} [10].

One possible representative diameter is the Sauter mean diameter (d_{32} or SMD). The SMD is the diameter of a representative droplet having the same volume to surface area ratio as all droplets in the entire spray. In the present thesis, a complete droplet size distribution is calculated based on the SMD. The SMD can be determined by experimental data or has to be approximated, e.g. by the correlation of Merker et al. [122]:

$$SMD = 6156 \cdot 10^{-6} \nu_{f,l}^{0.385} \rho_{f,l}^{0.737} \rho_a^{0.06} \Delta p_{\text{inj}}^{-0.54} \tag{6.1}$$

with the kinematic viscosity $\nu_{f,l}$ and density $\rho_{f,l}$ of the liquid fuel, the density of the ambient gas ρ_a and the difference between injection pressure and gas pressure within the cylinder Δp_{inj} (in kPa).

A total number of N equally spaced diameter classes d_i is calculated between a minimum ($d_{\min}$) and maximum ($d_{\max}$) diameter for the calculated droplet size distribution [192]:

$$d_i = \begin{cases} d_{\min} & \text{for } i = 1 \\ d_{i-1} + \frac{d_{\max} - d_{\min}}{N_{\text{classes}} - 1} & \text{for } i > 1 \end{cases} \tag{6.2}$$

The probability of each diameter class is determined by a χ^2-distribution $g(d_i)$ with the number-averaged droplet diameter $\overline{d}$ [110]:

$$g(d_i) = \frac{d_i^3}{6\overline{d}^4} \cdot \mathrm{e}^{-d_i/\overline{d}} \tag{6.3}$$

$$\overline{d} = \frac{1}{6} SMD \tag{6.4}$$

Spray Motion and Evaporation

Fuel sprays can be characterized as two-phase flows of liquid and gaseous phases. Intensive quantities (e.g. pressure, density or temperature) can only undergo continuous changes within each phase, whereas discontinuous transitions occur at the phase boundary [192]. In the context of fuel sprays, the liquid phase is present as droplets in the continuous gaseous carrier phase (referred to as dispersed two-phase flow) [169].

Two-phase flows can generally be described by two approaches:

1. The *Eulerian-Eulerian method* is applied for very dense sprays. Both phases are considered to be continuous and a set of continuum mechanical equations (mass, momentum, energy) is solved for each system including exchange terms to describe the interactions of the phases [62].
2. The *Eulerian-Lagrangian method* is used for dilute sprays with lower mass loading and small droplets. A finite number of particles (i.e. droplets) is used to represent the disperse phase. The position is tracked and the motion is calculated in a Lagrangian manner. This leads to the necessity of solving the conservation equations for each particle [62].

In the here presented approach, the second definition is applied using a single-component model for the liquid phase with a uniform temperature and composition of each droplet. The gas-phase is assumed quasi-steady and quiescent. Suitable corrections are employed for convection effects on heat and mass transfer in non-quiescent atmospheres. According to Stengele [172], the quasi-steady approach is justified because the convective time scale, determining fuel transport away from the droplet, is much smaller than evaporation time.

The thermodynamic and transport properties of the gas phase are obtained using an ideal gas object in Cantera [74] (see also Section 3.1.2).

Examining droplet evaporation and drag is a challenging task both for simulations and experiments. Analytical solutions are only available for very simplified cases because of the complex processes that are involved. Experimental studies usually only cover single droplets or are not capable of fully observing the underlying processes (see Ashgriz et al. [10] for an overview). Thus, direct numerical simulations (e.g. Burger et al. [29], Bukhvostova et al. [28]) are seen as a common way of understanding droplet evaporation and drag in multiphase flows [10]. The single-component evaporation model that is used in the present work is further reduced by applying these assumptions:

- The ambient gas is insoluble in the liquid phase.
- The droplets are assumed to be spheric.
- Liquid and gas phase have the same pressure.

- Droplet evaporation is not influenced by other droplets in the surroundings.
- There are no chemical reactions at all.
- There is no heat transfer between droplet and ambience through thermal radiation.
- Mass flow due to temperature gradients (Soret effect) and heat flow due to concentration gradients (Dufour effect) are negligible.

Due to strong differences in material properties, the gas and liquid phase are analysed separately. At the droplet surface, a thermodynamic equilibrium is assumed, separating the two phases [104]. The heat and mass transfer of the droplet can be described by several levels of detail:

- In the D^2*-model*, the droplet heating and evaporation are calculated isolated from each other. The droplet is assumed homogeneous with uniform temperature and composition. The evaporation process is calculated after the droplet's temperature reaches the boiling point. This requires that the heating process is short compared to entire evaporation process and that the saturated state is reached. In internal combustion engines, these conditions are not given and heating and evaporation process are coupled [104].
- In the *Uniform Temperature Model*, the coupled calculation and evaporation is considered. The droplets are still not discretised in terms of temperature and an infinitely fast conductive transport inside the droplet is assumed [192]. This model can be applied if external forces induce convective flow inside the droplet or if the droplets are very small. This is suitable for the description of a fuel spray and therefore the model is used within this work.
- The more complex *Conduction Limit Model* regards the temperature distribution inside the droplet. It has a higher accuracy than the Uniform Temperature Model by taking into account the heat transfer inside the droplet, but the computational costs significantly increase because a partial differential equation has to be solved for every droplet.

The liquid droplet can be described by its mass m_d, position x_d, velocity u_d and temperature T_d. For the presented approach, position and velocity are scalar values and the droplet position can be expressed as its penetration depth S_d. The state and interaction with the gas-phase of each droplet can be evaluated by a system of four ordinary differential equations (ODE):

Penetration depth:

$$\frac{\mathrm{d}S_d}{\mathrm{d}t} = u_d \tag{6.5}$$

Conservation of momentum:

$$\frac{\mathrm{d}u_d}{\mathrm{d}t} = \frac{-F_D}{m_d} \tag{6.6}$$

Conservation of energy:

$$m_d c_{p,l} \frac{\mathrm{d}T_d}{\mathrm{d}t} = \dot{Q}_d - \Delta H_v \dot{m}_{\mathrm{vap}} \tag{6.7}$$

Conservation of mass:

$$\frac{\mathrm{d}m_d}{\mathrm{d}t} = -\dot{m}_{\mathrm{vap}} \tag{6.8}$$

with the drag force F_D, the specific heat capacity of the liquid $c_{p,l}$, the heat flow rate between droplet and ambience $\dot{Q}_d$, the latent heat of vaporization ΔH_v and the evaporating mass flow rate $\dot{m}_{\mathrm{vap}}$. The

calculation of the fuel and ambient properties and the unknown quantities on the right hand side of the equation system is briefly explained in App. A.2.1. Detailed explanations can be found in the work of Hanisch [81].

6.1.2 Structure

In most engineering applications, the problem of dispersed two-phase flow phenomena is solved using a statistical approach that was developed by Dukowicz [54] (*Discrete Droplet Method* (DDM)). The approach solves the above described conservation equations for a so-called *parcel* - a statistical number of droplets in which each one represents the behaviour of a group of identical droplets. The parcels are tracked in a Lagrangian manner and interact with the gas phase.

The present approach further simplifies this method and does not solve a statistical number of particles. Instead, a number N_{classes} of droplets with diameters in the range of $d_{\min} \leq d_d \leq d_{\max}$ that represents the droplet size distribution is solved. This is necessary to reduce the calculation duration without neglecting the influence of large droplets that are rarely present in the spray because of their low probability, but have a great influence on wall wetting. Otherwise, the statistical sample would have to comprise a very large number (several thousands) of droplets.

The diameter range is limited by $d_{\min} = 1$ µm and $d_{\max} = 50$ µm, which is in conformity with measurement results of Keller et al. [96], who investigate a comparable injector and reported results for iso-octane. The number of diameter classes N_{classes} is chosen based on a simple parameter variation. At a number of $N_{\text{classes}} \approx 30$, the shape of the distribution function converges and increasing the number of classes does not improve the accuracy. This significantly reduces the calculation time to about 5 min for solving the differential equations once for all droplets. The calculation starts at SOI and runs until the droplet is fully evaporated or until spark ignition. The result is a CA-resolved array containing the values of droplet penetration depth, velocity, temperature and mass for all diameter classes.

The effect that droplets with later injection time than SOI are exposed to other ambient conditions is taken into account by the use of moving average boundary conditions for in-cylinder pressure and temperature. The length of the moving average equals the injection duration t_{inj} and the number of data points N_t depends on the original data set. For example, the averaged temperature profile $\bar{T}(t_i)$ at a certain time t_i is calculated by the original temperature profile $T(t)$ as follows:

$$\bar{T}(t_i) = \frac{\sum_{t=t_i}^{t_i+t_{\text{inj}}} T(t)}{N_t} \tag{6.9}$$

$$\text{with: } N_t = \frac{t_{\text{EOI}} - t_{\text{SOI}}}{\Delta t} = \frac{t_{\text{inj}}}{\Delta t} \tag{6.10}$$

The averaged data is the unweighted mean of the following N_t data points. Thus, the succeeding development of the boundary conditions is taken into account, which is plausible because the solution of the calculated sample (injected at SOI) is transferred to the successive droplets. Since the averaging process is only applied until time of ignition, the averaged data set tends towards the original data set when the crank angle approaches ignition time.

Solving the ODE system for the global sample is only the first step of the spray model to calculate the behaviour of each droplet diameter over time. It does not include any local information or any upscaling procedure to the complete spray. This is done in two subsequent steps:

1. The sample solution is upscaled and transferred to all possible injection states and weighted according to the total droplet number by applying the information of the droplet size distribution.
2. Finally, the droplet position within the combustion chamber is calculated by including nozzle geometry information. Applying geometric information of the combustion chamber then allows the calculation of the wall impingement.

An overview of all three processes that are included in the spray model is presented in Fig. 6.1. The final solution of the spray model is the total impinged mass for each time step, divided into piston and liner impingement. The upscaling process and calculation of the droplet position are further described in the following.

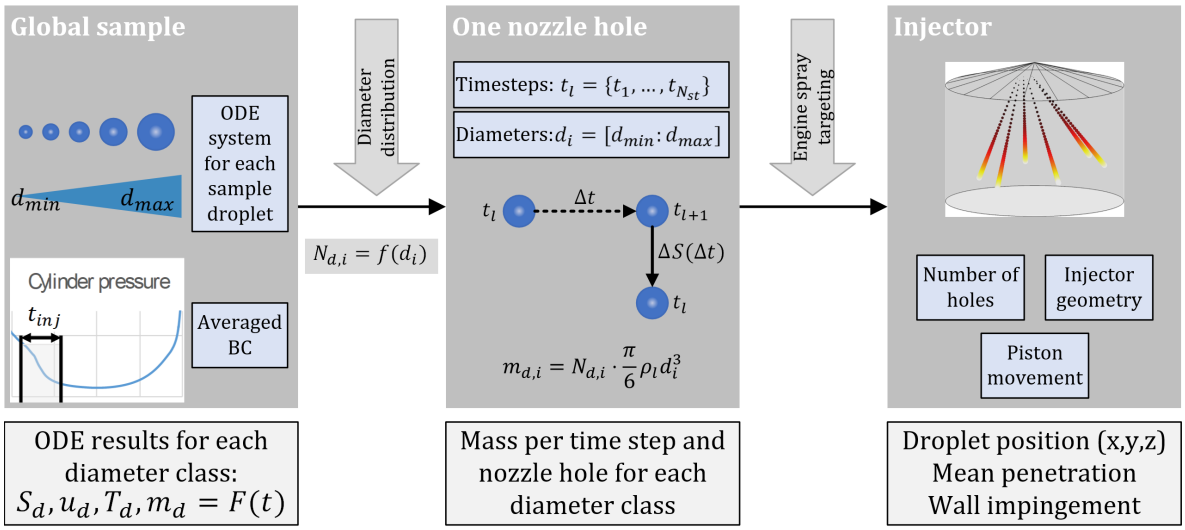

Fig. 6.1.: Overview of the spray sub-module [81].

Upscaling to Total Injected Mass

The injection process with the total injected fuel mass $m_{\mathrm{f,inj}}$ is subdivided into N_{st} shorter injection steps Δt_{st} with a duration of 1 °CA. The total fuel mass that leaves the injector at each injection step is Δm_{st}. Dividing this mass by the number of nozzle holes N_{holes} leads to the total mass per nozzle hole and time step.

Afterwards, the solution is weighted according to the droplet number. The total number of droplets that are injected at each time step ($N_{d,\mathrm{st}}$) is derived from the ratio of total injected fuel mass during the time step and the average single droplet mass $\overline{m}_d$ that is calculated by the volume-averaged diameter d_{30} of the droplet size distribution:

$$N_{d,\mathrm{st}} = \frac{m_{\mathrm{f,inj}}}{\overline{m}_d \cdot N_{\mathrm{st}}} = \frac{\Delta m_{\mathrm{st}}}{\overline{m}_d} \tag{6.11}$$

$$\text{with:} \quad \overline{m}_d = \frac{\pi}{6} \rho_l \cdot d_{30}^3 \tag{6.12}$$

The number of droplets per diameter class, injection step and nozzle hole ($N_{d,i}$) can then be calculated by applying the frequency of the respective diameter $g(d_i)$, as introduced in Eq. 6.3:

$$N_{d,i} = g(d_i) \cdot \frac{N_{d,\mathrm{st}}}{N_{\mathrm{holes}}} \tag{6.13}$$

The droplet number value can then be converted into the mass per injection step, nozzle hole and droplet diameter ($m_{d,i}$):

$$m_{d,i} = N_{d,i} \cdot \frac{\pi}{6} \rho_l d_i^3 \tag{6.14}$$

The sum over all diameter classes, nozzle holes and injection step then conclusively equals the total injected fuel mass:

$$N_{\mathrm{st}} \cdot N_{\mathrm{holes}} \cdot \sum_{i=1}^{N_{\mathrm{classes}}} m_{d,i} = m_{f,\mathrm{inj}} \tag{6.15}$$

Droplet Position and Wall Impingement

The calculated penetration depth $S(t)$ does not provide any information about the spatial position of the droplet within the combustion chamber. This position $\vec{x}(t)$ is calculated afterwards using the spatial coordinates of the related nozzle hole $\vec{x}_{\mathrm{I}}$ and the unit vector of the injection direction $\vec{d}_{\mathrm{I}}$, where $\vec{x}$, $\vec{x}_{\mathrm{I}}$ and $\vec{d}_{\mathrm{I}}$ have three components denoting the Cartesian coordinates. The current droplet position is then evaluated by the following equation:

$$\vec{x}_d(t) = \vec{x}_{\mathrm{I}} + S_d(t) \cdot \vec{d}_{\mathrm{I}} \tag{6.16}$$

Solving the equation enables the identification of the droplet position in Cartesian coordinates (x_d, y_d, z_d) and the distance to piston and liner surface (d_{pis} and d_{lin}) can be determined by:

$$\text{Distance to piston:} \qquad d_{\mathrm{pis}}(t) = s(t) - z_d(t) \tag{6.17}$$

$$\text{Distance to liner:} \qquad d_{\mathrm{lin}}(t) = \frac{B}{2} - R_D(t) \tag{6.18}$$

with the current piston position s, the bore diameter B and the radial distance of the droplet relative to the cylinder axis R_D. The piston position $s(t)$ is based on the kinematics of the crankshaft drive. The radial distance is calculated by $R_D = \sqrt{x_d^2 + y_d^2}$. The model only considers the impingement on piston and liner, because they form the major part of the cylinder walls. The impinged mass per time step and surface is then provided to the spray-wall-interaction module that is described in the next section.

The most significant simplifications of this approach are that there is no interaction between the charge motion and the droplet velocity vector and that there is no formation of an increasing spray cone during spray propagation. Therefore, it has to be evaluated in which way these simplifications affect the results of total impinged mass.

6.2 Spray-Wall Interaction

Numerous studies are available in the literature that investigate the fuel spray impingement and spray-wall interaction in IC engines [14, 130, 133, 147, 160, 171]. In a literature review of Moreira et al. [131], they state that investigations that are based on single droplet impacts are not suitable for IC engines, but correlations gained from investigations of full spray impingement are more advisable to be used. Although these models are not universally applicable [131], they often lead to satisfactory results if the boundary conditions are not too wide.

The observed phenomena during wall impingement are usually subdivided into the categories *stick*, *spread*, *splash* and *rebound* [143, 171]. These categories may be further subdivided [129, 131, 155]. For most of the modelling approaches, the definition of a threshold criterion for splashing is defined that is normally based on dimensionless numbers like Reynolds $Re = \rho u_0 d_0/\mu$, Ohnesorge $Oh = \mu/\sqrt{\rho\sigma_{lv}d_0}$ and Weber $We = (Oh \cdot Re)^2 = \rho u_0^2 d_0/\sigma_{lv}$ number. They include the droplet diameter d_0 and velocity u_0, the surface tension between liquid and vapour phase σ_{lv} and the dynamic viscosity μ. If splashing occurs, the prediction of the fraction of splashed and deposited liquid mass is further described.

The models can also be classified into spray impingement onto dry surfaces or onto wetted surfaces. Generally, there is no restriction on which model is used to consider the spray-wall interaction, especially because the different approaches have a similar structure. Examples for models that consider dry surfaces are the *Mundo-Tropea-Sommerfeld model* [133], the *Bai-Gosman model* [14, 15] for dry surfaces or the *Kuhnke model* [105]. Examples for models that consider impingement onto wetted surfaces are the *Kalantari-Tropea model* [89] and the *Bai-Gosman model* [14, 15] for wetted walls.

In the present thesis, the spray-wall interaction model of Bai et al. [14, 15] for dry walls is applied and further described in the following. It has been validated in DISI engine injection experiments and was successfully applied within CFD simulations. The approach for dry walls is selected because at start of injection or rather impingement, the cylinder walls are normally not covered by any fuel film.

Bai-Gosman Model

The presented model of Bai and Gosman [14, 15] for dry surfaces distinguishes three interaction regimes on the basis of the normal impact Weber number $We_{n,0} = \rho u_{n,0}^2 d_0/\sigma_{lv}$ with the following limits:

$$\begin{aligned} \text{Stick:} \quad & We_{n,0} \leq 2 \\ \text{Spread:} \quad & 2 < We_{n,0} \leq We_c \\ \text{Splash:} \quad & We_{n,0} > We_c \end{aligned} \tag{6.19}$$

with the critical Weber number for splashing

$$We_c = 2360 \cdot Oh^{0.36}. \tag{6.20}$$

All impinging droplets deposit at the wall within the stick and spread regime. In the splash regime, only a part of the mass is reflected. Bai et al. [15] tried to represent the stochastic behaviour by introducing a random procedure that determines the mass ratio of outgoing to incoming mass in the splashing regime:

$$\frac{m_1}{m_0} = 0.2 + 0.6 \cdot \text{rand}(0,1) \tag{6.21}$$

The deposited mass can directly be calculated by the difference of incoming to outgoing mass: $m_{\text{dep}} = m_0 - m_1$. The sum of all droplets' deposited mass per time step yields the total deposited wall film mass per time step which is further included into the wall film evaporation module.

The mean diameter of the reflected droplets d_1 is evaluated according to the model of Han et al. [14, 15, 80] by:

$$\frac{d_1}{d_0} = \left[\frac{\frac{m_1}{m_0}}{30\left(\frac{We}{We_c} - 1\right)} \right]^{1/3} \tag{6.22}$$

By analysing this equation, it becomes evident that the outgoing droplets are very small. The mean diameter of the reflected droplets decreases with increasing Weber number. Therefore, these droplets are assumed to evaporate quickly after splashing. As a consequence, there is no reinitialization of the spray module after splashing occurs and the reflected mass is directly added to the gas phase.

The model of Bai and Gosman depends largely on the momentum and material properties of the impinging droplet, accounted for by the Weber number. Although the model of Kuhnke [105] additionally takes into account the wall temperature, it is not applied because there is a sharp distinction between deposition and reflection based on a fixed critical dimensionless wall temperature. Because of the uncertainties in estimating the wall temperatures, this may lead to erroneous conclusions. The model of Kalantari and Tropea [89] has the disadvantage that it is only applicable for normal impact Weber numbers of $10 < We_{n,0} < 160$ which is hardly reached for very small droplets.

6.3 Wall Film Evaporation

The liquid film that is formed due to wall impingement is influenced both by the surrounding gas phase and the adjacent wall in terms of heat and mass transfer [185, 196]. The processes that are involved in wall film evaporation are presented schematically in Fig. 6.2. In a combustion chamber,

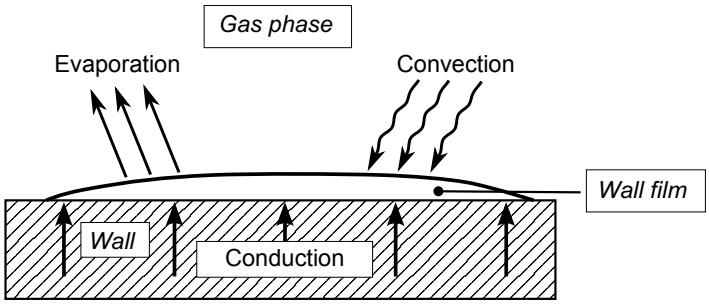

Fig. 6.2.: Schematic chart of the wall film evaporation process. In accordance with Yan et al. [196] (modified).

there is no well-defined liquid film on the walls but the film thickness, area and volume continuously changes throughout the working cycle. Therefore, mean quantities are used and appropriate assumptions are made to reduce the complexity:

- Gas and liquid phase are treated separately with a coupling at the film surface, where saturated conditions are applied.
- Physical and thermodynamic properties are assumed to always be in equilibrium state.
- The wall film has a constant temperature.
- The film surface is supposed to be smooth.
- The liquid film mass m_{wf} that is formed by impinging droplets forms a cylinder with the height h_{wf} and diameter d_{wf}.

Determining the average film thickness is of primary importance, as it has a great influence on the film vaporization rate. Assuming the shape of a cylinder and following the approach of Nagaoka et al. [134], the film thickness h_{wf} and the corresponding film area A_{wf} are defined as follows:

$$h_{\mathrm{wf}} = 2\frac{\sigma_{lv}}{\rho_l u_{n,0}^2} \tag{6.23}$$

$$A_{\mathrm{wf}} = \frac{m_{\mathrm{wf}}}{\rho_l h_{\mathrm{wf}}} \tag{6.24}$$

with the surface tension between liquid and vapour phase σ_{lv}, the normal impact velocity of the droplet $u_{n,0}$ and the liquid density ρ_l.Within each time step, the current wall film mass m_{wf} is evaluated as the sum of the newly deposited mass that is calculated by the spray-wall interaction module and the existing film mass. Following this, the current film area A_{wf} is calculated using Eq. 6.24.

In the present work, a mean value of the film thickness $\overline{h}_{\mathrm{wf}}$ is calculated and used throughout the complete evaporation process to calculate the evaporation rate. Therein, the material properties are evaluated at the mean incoming droplet temperature $\overline{T}_{d,0}$ and mean normal impact velocity $\overline{u}_{n,0}$:

$$\overline{h}_{\mathrm{wf}} = 2\frac{\sigma_{lv}(\overline{T}_{d,0})}{\rho_l(\overline{T}_{d,0})\overline{u}_{n,0}^2} \tag{6.25}$$

According to the work of Habchi [77], who presented an extended wall film boiling model for IC engines, four different boiling regimes can be identified based on the wall temperature T_w (separately considered for piston and liner), the saturation temperature T_{sat} and the Nukiyama and Leidenfrost temperatures T_L and T_N, respectively (see Fig. 6.3). On the basis of the current in-cylinder pressure, the saturation temperature T_{sat} of the fuel is determined and subtracted from the wall temperature T_w in order to calculate the wall superheat ΔT_w and to chose the relevant evaporation regime. In the current work, the saturation temperature is determined for iso-octane by the *Extended Antoine Equation*, as further explained in App. A.2.2, Eq. A.32:

$$\Delta T_w = T_w - T_{\mathrm{sat}} \tag{6.26}$$

Within the first regime (I: liquid film evaporation with $T_w < T_{\mathrm{sat}}$), the vaporization rate mainly de-

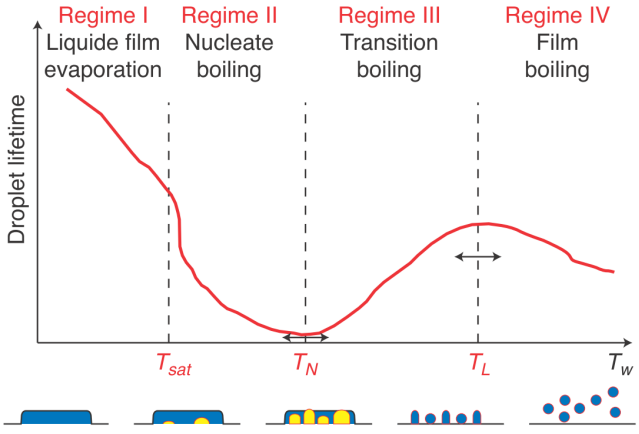

Fig. 6.3.: Droplet lifetime curve and associated boiling regimes. From: Habchi [77].

pends on the gas-side heat transfer driven by forced convection processes. Based on Fick's law of

diffusion and the consideration of a smooth and wall parallel film, the gas-side wall film evaporation rate $\dot{m}_{\mathrm{wf},g}$ can be obtained by [183, 185]:

$$\dot{m}_{\mathrm{wf},g} = A_{\mathrm{wf}} \frac{Sh_L \rho_g D \left(Y_{f,s} - Y_\infty\right)}{L_{\mathrm{ch}} \left(1 - Y_{f,s}\right)} \tag{6.27}$$

with the Sherwood number Sh_L, the density of the surrounding gas ρ_g, the fuel/air binary diffusion coefficient D, the fuel mass fraction at the film surface $Y_{f,s}$ and the surrounding Y_∞, a characteristic length L_{ch} and the film area A_{wf} (calculated with Eq. 6.24). The calculation of the specific terms of Eq. 6.27 is briefly summarized in App. A.2.2, see also [81].

Nucleate boiling starts in the second regime (II: nucleate boiling with $T_{\mathrm{sat}} < T_w < T_N$). The formation of small vapour cavities enable an excellent heat transfer and accelerate the vaporization of the liquid wall film and thus the droplet lifetime decreases until the Nukiyama temperature is reached [77].

In the third regime (III: transition boiling with $T_N < T_w < T_L$), the vapour cavities form a larger vapour columns that prevent the contact between wall and liquid. The overall vaporization rate shrinks and the droplet lifetime increases [77].

After exceeding the Leidenfrost temperature (IV: film boiling with $T_w > T_L$), the complete wall is covered by a thin vapour cushion and the droplet lifetime is on a relatively high level, as the heat transfer is much slower than through the liquid. Increasing wall temperature leads to a decreased droplet lifetime, as the driving force for evaporation increases [77].

Habchi [77] identified two main parameters that influence the vaporization within the boiling regimes II-IV. The first one is the ratio of dry area A_{dry} to the total wetted area in the absence of boiling A_{wet} and is termed the dry fraction $\alpha_{\mathrm{dry}} = A_{\mathrm{dry}}/A_{\mathrm{wet}}$ [77]. The second parameter is the so-called length density of the liquid film's contact lines C_{lld}. The parameter is proportional to the sum of the perimeters of the dry zones [77]. According to Habchi [77], the value of the two parameters is depending on the wall temperature.

The dry fraction rises from 0 to nearly 1 when the wall temperature increases from T_{sat} to T_L. The length density of the contact lines increases within the nucleate boiling regime and reaches its maximum at the Nukiyama point. In the transition boiling regime, the value declines, as more and more vapour cavities coalesce to form a continuous vapour cushion. It then decreases towards a minimum value which mainly depends on the surface roughness [77]. The calculation process for both parameters is briefly presented in App. A.2.2. For further information, the reader is referred to the work of Habchi [77].

As the boiling regimes are characterized based on Nukiyama and Leidenfrost temperatures, their evaluation is done based on a correlation of Habchi [77] that takes into account the ambient gas pressure. Based on experimental studies of Fardad and Ladommatos [61], Habchi proposed the following correlation to calculate Nukiyama and Leidenfrost temperatures:

$$T_{\mathrm{N/L}} = T_{\mathrm{sat}} + \Delta T \tag{6.28}$$

$$\Delta T = \begin{cases} T_{\mathrm{N/L,1bar}} - T_b & \text{for } p \leq 1 \text{ bar} \\ \frac{(T_{\mathrm{N/L,1bar}} - T_b) - A}{T_c - T_b}(T_c - T_{\mathrm{sat}}) + A & \text{for } p > 1 \text{ bar} \end{cases} \tag{6.29}$$

with the normal boiling temperature T_b, the saturation temperature T_{sat} and the critical temperature T_c. $T_{\mathrm{N/L,1bar}}$ is the experimental value of Nukiyama or Leidenfrost temperature at 1 bar and

$A = \max(1, (T_{\mathrm{N/L,1bar}} - T_c))$. Values for $T_{\mathrm{N/L,1bar}}$ can be found in Fardad and Ladommatos [61] or Stanglmaier et al. [170].

With the help of the main model parameters α_{dry} and C_{lld}, the correlation for Nukiyama and Leidenfrost temperatures as well as further derived parameters (based on experimental results and theoretical determination), Habchi defines the wall-side vaporization rate $\dot{m}_{\mathrm{wf},w}$ by the following equation [77]:

$$\dot{m}_{\mathrm{wf},w} = A_{\mathrm{wf}} \frac{\beta_1 \left(1 - \alpha_{\mathrm{dry}}\right) \dot{q}_{wl} + \beta_2 \alpha_{\mathrm{dry}} \dot{q}_{wvl}}{\Delta H_{v,\mathrm{sat}}} \tag{6.30}$$

$$\dot{q}_{wl} = \lambda_{l,\mathrm{sat}} \frac{T_w - T_{\mathrm{sat}}}{h_{\mathrm{wf}}} \tag{6.31}$$

$$\dot{q}_{wvl} = \lambda_v \frac{T_w - T_l}{h_v} \tag{6.32}$$

with the heat of vaporization at saturated state $\Delta H_{v,sat}$, the heat flux from wall to liquid in direct contact $\dot{q}_{wl}$ and the heat flux from wall to liquid through the vapour layer $\dot{q}_{wvl}$. $\lambda_{l,\mathrm{sat}}$ and λ_v are the thermal conductivities of the liquid fuel at saturation temperature and the vapour, respectively. β_1 is a function of the length density of liquid contact lines C_{lld} and represents the fraction of the wetted area where the vaporization is most intensive. On the other hand, β_2 accounts for the fraction of dry area, where vaporization is dampened, because liquid and wall are separated by a vapour layer. For the complete derivation, the reader is referred to the original paper by Habchi [77].

The calculation is performed until the complete evaporation of the wall film or until spark timing. If there is wall film mass remaining at spark timing, it is passed to the main part of the particle emission model.

6.4 Identification of Calibration Parameters

6.4.1 Spray Penetration and Impingement

So far, the presented SWI model does not contain any calibration parameters, except for those taken from the literature. It is therefore possible to examine how the included simplifications affect the spray behaviour and to identify critical simplifications. By identifying suitable calibration parameters, the result quality may then be improved.

For this purpose, the spray model is compared with experimental data and 3D-CFD simulations with regard to droplet size distribution and spray penetration behaviour.

Three studies by Knorsch et al. [102, 103] and Keller et al. [96] are considered for the validation of the simulation model. Within these investigations, spray propagation and evaporation behaviour of DISI biofuel blends (including pure iso-octane) within an optically accessible spray chamber were analysed with a similar multi-hole injector as it is applied in the engines considered in this work. Among others, the experiments included the measurement of liquid and vapour penetration as well as droplet diameter distribution and Sauter mean diameter by means of shadowgraphy, Schlieren imaging and Phase-Doppler Anemometry (PDA). The applied boundary conditions of the experimental data are shown in App. A.2.3 (Tab. A.1)

The basis for a set of 3D-CFD simulations are measurements on an engine test bench at different operating conditions with a six-cylinder turbocharged DISI engine (see Tab. 3.3 for engine-specific information). The comparison of 3D-CFD and the 0D-model is based on a speed/load variation, an injection time variation and the variation of coolant and oil temperature. For detailed information about the measured operating conditions and the applied 3D-CFD model, the reader is referred to App. A.2.3 (Fig. A.3, Tab. A.2, Tab. A.3 and Tab. A.4).

SMD and Particle Size Distribution

The SMD significantly affects the initial droplet size distribution and thus the spray penetration and evaporation behaviour. It is provided by measurements or through correlations (such as Eq. 6.1 in Section 6.1.1). Knorsch et al. [103] measured the droplet sizes via PDA in a plane perpendicular to the injector axis. Fig. 6.4 shows the comparison of calculated and measured SMD for three operating conditions with different ambient gas temperature (OP1/OP2=473K, OP3=673K) and ambient pressure (OP1=5.6bar, OP2/OP3=8.0bar) values of the spray chamber.

In general, the calculated SMD is too small compared to the measured one. OP 3 with higher ambient temperatures shows good agreement between the measured and calculated value. While the ambient pressure has only a minor impact on SMD, rising ambient temperatures lead to decreasing SMD. The applied correlation is not able to capture this gas temperature effect, as it is mainly based on rail pressure and fuel properties. Unfortunately, the study of Knorsch et al. [103] uses the same rail pressure and fuel temperature throughout all operating points. Hence, the influence of these parameters cannot be derived from the measurements.

In Fig. 6.5, the particle size distribution that is calculated from the SMD using a χ^2-distribution (see Eq. 6.3) is compared to measured data. Since the correlated SMD is smaller than the measured one, the location of the maximum is shifted towards smaller diameters. This distribution cannot be used for the subsequent comparison of spray penetration, as it would not resemble the measured spray behaviour. The agreement between the calculated and measured droplet size distribution is very good if the measured SMD is taken as a base. This implies that the applied χ^2-distribution is valid for the derivation of droplet diameter distribution. Therefore, the droplet size distribution calculated from the measured SMD is used for the initialization of the spray module at the nozzle exit without further adjusting the distribution.

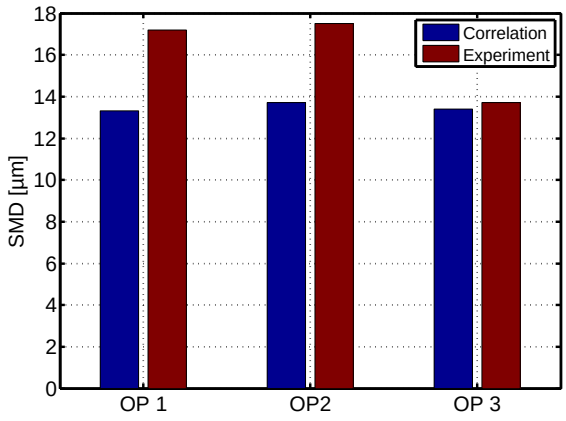

Fig. 6.4.: Comparison of SMD correlation and experiment [103]. [81]

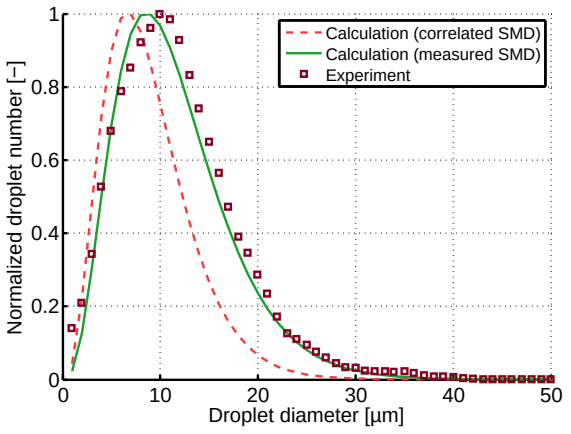

Fig. 6.5.: Comparison of measured [96] and calculated droplet size distribution for p_{gas} =5.6 bar, T_{gas} =473 K (OP 1). [81]

The mean spray penetration in the 0D simulation is calculated by a threshold criterion based on the number of the furthermost droplets. Typically, the 99 % penetration S_{99} is equal to the mass averaged penetration depth of the 1 % furthermost droplets. In the same way, the 90 % and 50 % penetration depth are defined. This is in agreement with the definition of the 3D-CFD values, but it differs from the experimental definition. In the reference measurements within the spray chamber, the spray penetration has been evaluated by shadowgraphy that uses the deflection of back light and evaluating darker regions caused by the droplets. A threshold criterion is necessary to define the penetration depth depending on the brightness of the resulting area. In the given experiment, the threshold was set to 45 of 256 grayscale values [96, 103]. It is thus not possible to clearly identify the amount of droplets that is covered by this definition.

In Fig. 6.6 and Fig. 6.7, the liquid spray penetration depth over time is compared between 0D simulation and experiment for OP1 and OP3 (OP2 can be found in App. A.2.3 Fig. A.4). The following

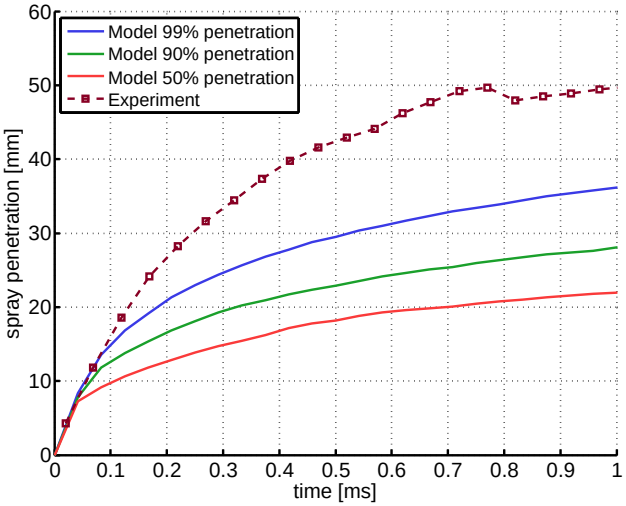

Fig. 6.6.: Spray penetration at OP 1: $T_g = 473$ K, $p_g = 5.6$ bar without calibration. [81]

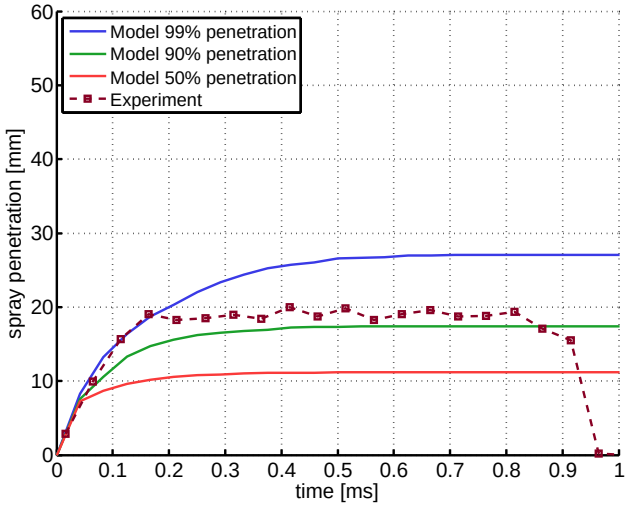

Fig. 6.7.: Spray penetration at OP 3: $T_g = 673$ K, $p_g = 8.0$ bar without calibration. [81]

phenomena can be identified by comparing the results: The simulated spray penetration curves are far too low in the first two operating points with moderate ambient temperature. The trends are similar and the initial gradient corresponds well, but the curves drop off too early. The relative change between OP1 and OP2, that is caused by the increased ambient pressure, can be captured well by the 0D model (the spray penetration is decreased by about 20 %). The measured curves reach an approximately constant penetration depth after about 0.75 ms, indicating the complete vaporization of the spray. The calculated penetration does not reach a constant value in OP1 and OP2. At higher ambient temperatures (OP3), the penetration depth and the time to reach a constant penetration depth are lower, which in this case is captured by the model.

When comparing the results to 3D-CFD simulations of the combustion chamber of an engines, the specific injector nozzle holes are considered. The spray targeting in top and side view is shown in App. A.2.3 (Fig. A.5) for the applied 6-hole injector. Due to symmetry, only 3 spray cones are visible in the side view. Therefore, only nozzle holes 1 to 3 are shown in the subsequent graphs for the 3D-CFD simulation results. In Fig. 6.8 and Fig. 6.9, the 50 % penetration depth and 99 % penetration depth are exemplarily compared to 3D-CFD simulations at CFD OP2 (2000 rpm/220 Nm), respectively. Further operating conditions can be found in App. A.2.3 (Fig. A.6). The capture time is limited to 1 ms, as longer time intervals lead to wall impingements and can hardly be compared any more (piston

impingement is indicated in Fig. 6.9). The 3D-CFD results clearly confirm that the spray penetration

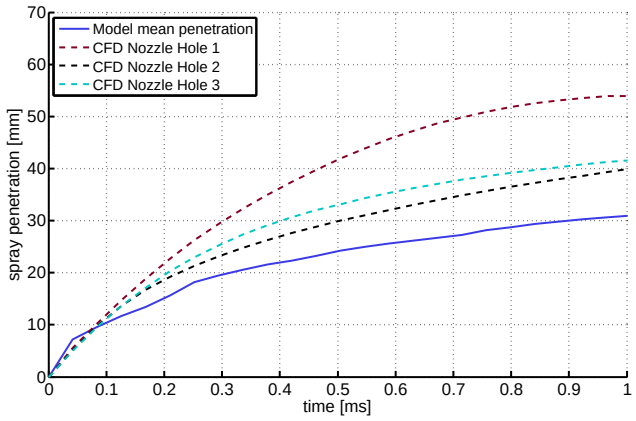

Fig. 6.8.: 50 % Spray penetration at CFD OP 2: 2000 rpm, 220 Nm without calibration. [81]

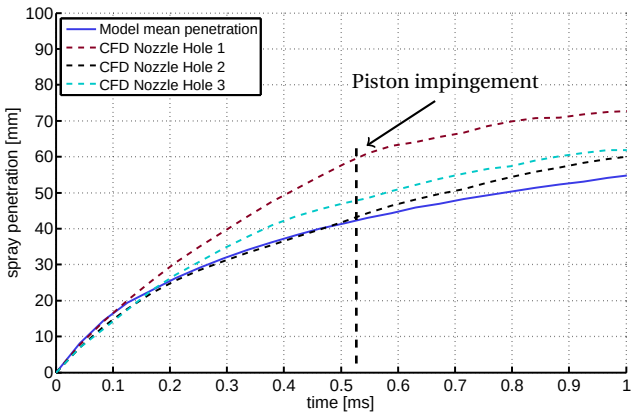

Fig. 6.9.: 99 % Spray penetration at CFD OP 2: 2000 rpm, 220 Nm without calibration. [81]

depth of each spray cone depends on the injection direction due to the influence of charge motion. Therefore, the spray cone from nozzle hole 1 has the largest penetration compared to nozzle holes 2 and 3. This effect is further increased at higher engine loads due to higher charge air velocities and injected fuel mass, leading to higher total penetration depths but also higher deviations between the nozzle holes.

Similar to results of the comparison to experimental data, the spray penetration depth of the 0D simulation is too small compared to the 3D-CFD simulations. This is especially visible for the 50 % penetration. This indicates that smaller droplets (situated in the back of the spray cone) do not penetrate far enough. This might be due to high droplet evaporation rates or because the calculated drag force is too high.

Spray Module Calibration

From the observed deviations, two conclusions can be drawn:

- The drag coefficient from Eq. A.21 is only valid for single droplets. Krüger [104] and Wolf [192] have shown that the drag coefficient decreases heavily for sprays. Droplets in the back of the spray are subjected to a much lower drag force compared to the droplets in the front. Naturally, the largest droplets are in the front, while smaller droplets follow behind.
- The fuel mass fraction increases within the spray, which is in contrary to the first approximation that the ambient fuel mass fraction $Y_{f,\infty}$ is zero. As a result, the evaporating mass flow decreases and spray penetration is larger.

Both effects strongly depend on the behaviour of the droplets within the spray cone and are thus taken into account in a comparable way. In the following correlation, it is assumed that the drag coefficient c_D^{mod} quickly decreases shortly behind the spray front, as the largest droplets absorb most of the drag force. This is represented by drag coefficient factor f_D that is described as a function of droplet diameter d_d. With increasingly smaller droplets, the coefficient decreases slower tending towards a finite value $f_{D,\min}$. The drag coefficient factor is represented by an exponential function:

$$f_D(d_d) = f_{D,\min} + a_1 \cdot e^{a_2 d_d} \tag{6.33}$$

$$c_D^{\mathrm{mod}} = f_D \cdot c_D \tag{6.34}$$

The model coefficients a_1, a_2 and $f_{D,\min}$ are determined by a non-linear regression based on three key support points:

$$P_1\left(d_{\min}, f_{D,\min}\right) \quad P_2\left(\frac{d_{\min}+d_{\max}}{2}, f_{D,\min}+0.05\cdot\left(1-f_{D,\min}\right)\right) \quad P_3\left(d_{\max}, 1\right)$$

It was concluded by analysis of the spray penetration behaviour that consistent results are yielded with $f_{D,\min}=0.5$. The model coefficients were calculated as $a_1=1.0950\cdot10^{-3}$ and $a_2=0.12248$. The resulting regression function is presented in Fig. 6.10 as a function of droplet diameter for droplets between $d_{\min}=1\ \mu$m and $d_{\max}=50\ \mu$m.

In addition to the drag coefficient, the change ambient fuel mass fraction is considered in a similar way, because small and medium-sized droplets are affected most, as these are shielded from the ambience in the bulk of the spray. Therefore, a factor $f_V\left(d_d\right)$ is defined that affects the ambient fuel fraction $Y_{f,\infty}^{mod}$:

$$f_V\left(d_d\right)=f_{V,\min}+b_1\cdot e^{b_2 d_d} \tag{6.35}$$

$$Y_{f,\infty}^{\mathrm{mod}}=\left(1-f_V\right)\cdot Y_{f,\infty} \tag{6.36}$$

In the presented model, the same parameter set is applied to the values: $a_1=b_1$,$a_2=b_2$ and $f_{V,\min}=f_{D,\min}$. While f_D mainly influences the penetration depth, the main effect of f_V is visible for

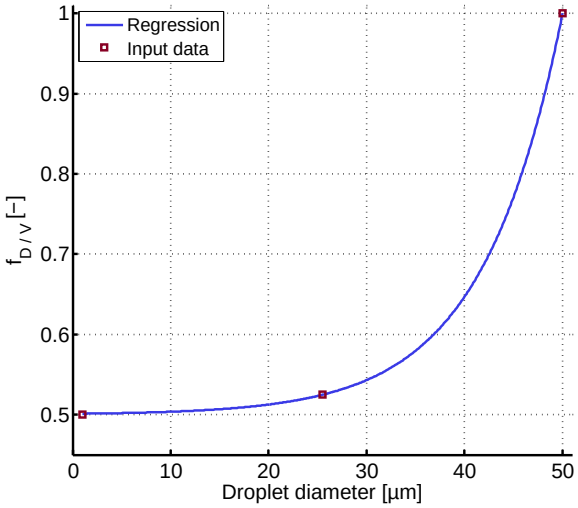

Fig. 6.10.: Results of calibration for drag coefficient factor f_D and fuel fraction factor f_V as a function of droplet diameter for droplets between 1 μm and 50 μm. [81]

the total impinged mass on the cylinder walls which is further discussed later in this section.

After calibration, the model is again compared to measured data, as it is shown in Fig. 6.11 and Fig. 6.12 for OP1 and OP3, respectively (OP2 is shown in App. A.2.3 in Fig. A.6). Because of the reduced drag force, the penetration depths for OP1 and OP2 increased significantly showing an excellent agreement with the measured values. Although the stagnation of the curves is not reached within the presented time interval, the influence of the gas pressure on the penetration is well represented. The OP3 already resembled the measured data before optimization and the quality is still acceptable after calibration. It should be noted that there is no clear evidence if 90 % or 99 % penetration is covered by the applied measurement method. All in all, the agreement between experiment and simulation is summarized to be good enough for use in the particle model framework.

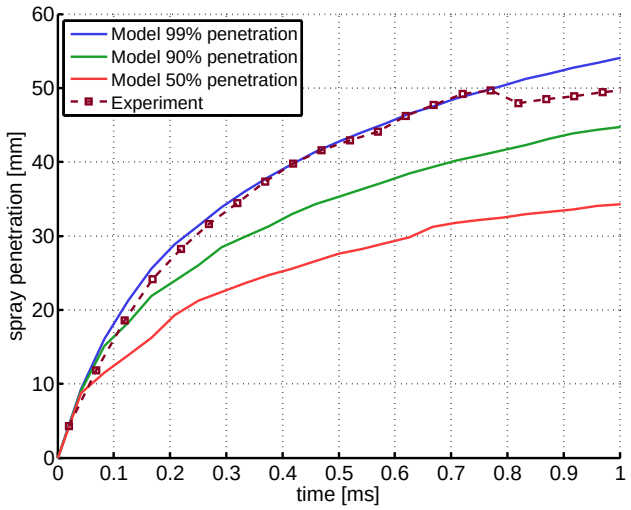

Fig. 6.11.: Spray penetration at OP 1: $T_g = 473$ K, $p_g =$ 5.6 bar after calibration. [81]

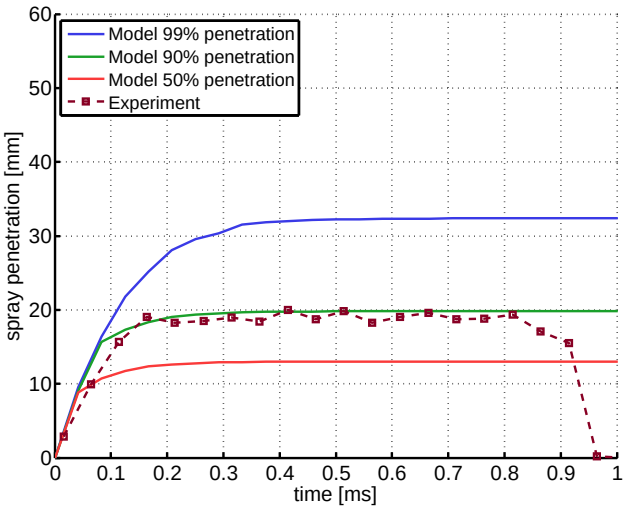

Fig. 6.12.: Spray penetration at OP 3: $T_g = 673$ K, $p_g =$ 8.0 bar after calibration. [81]

The comparison to 3D-CFD results after calibration is shown in Fig. 6.13 and Fig. 6.14 at CFD OP2 (CFD OP1 and CFD OP3 are shown in App. A.2.3 in Fig. A.8). There is a significant higher agreement owing to the calibration of the spray module for all considered operating conditions in comparison to the uncalibrated simulation results. However, the spray model is still not capable to cover the effects of the charge motion on the single spray cones. In the subsequent step, the influence on the total impinged mass is investigated to further evaluate the quality of the model.

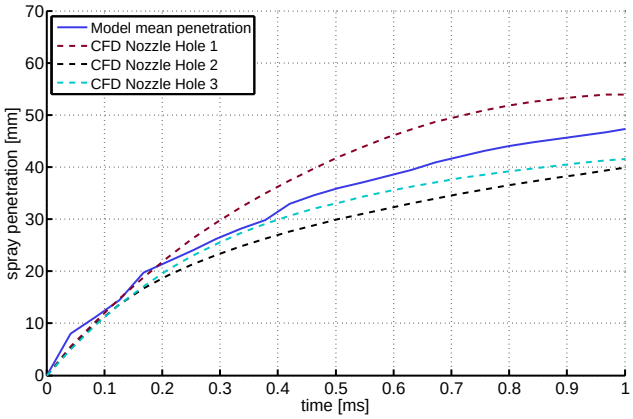

Fig. 6.13.: 50 % Spray penetration at CFD OP 2: 2000 rpm, 220 Nm after calibration. [81]

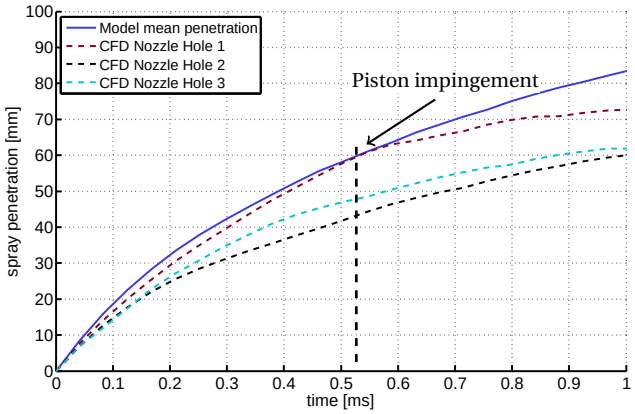

Fig. 6.14.: 99 % Spray penetration at CFD OP 2: 2000 rpm, 220 Nm after calibration. [81]

Spray-Wall Interaction

The determination of the total penetration depth shows the basic quality in the calculation of the spray propagation, but does not allow quantitative statements about the fuel mass which comes into contact with the walls. Therefore, the impinged and deposited mass is compared between 0D model and 3D-CFD simulations for the already presented operating points (see Tab. A.2 and Tab. A.3). The results are based on the calibrated spray module and the additional simplifications of the spray-wall interaction module. It has to be noted that no further calibration is performed for the spray-wall interaction behaviour.

The results of the comparison at five engine operating points is shown in Fig. 6.15. Within the engine operating map, the load increase from CFD OP1 to CFD OP3 is captured quiet well by the 0D model regarding the increase of overall impingement and the fraction of deposited mass to total impinged mass. Since the injection time value changes at these operating conditions, it can be stated that the agreement becomes worse when the injection time is shifted towards earlier values (CFD OP1). This is mainly due to the high ambient temperatures at early intake stroke, leading to a fast evaporation of the droplets in the 0D model. The best agreement is achieved for CFD OP3 to CFD OP5. Considering the relation of splashed to deposited fuel mass, it can be said that the 0D model results consistently exceed the CFD values. However, both CFD and 0D simulations depend on empirical spray-wall interactions models with unavoidable, inherent inaccuracies. Therefore, the comparison is only valid qualitatively.

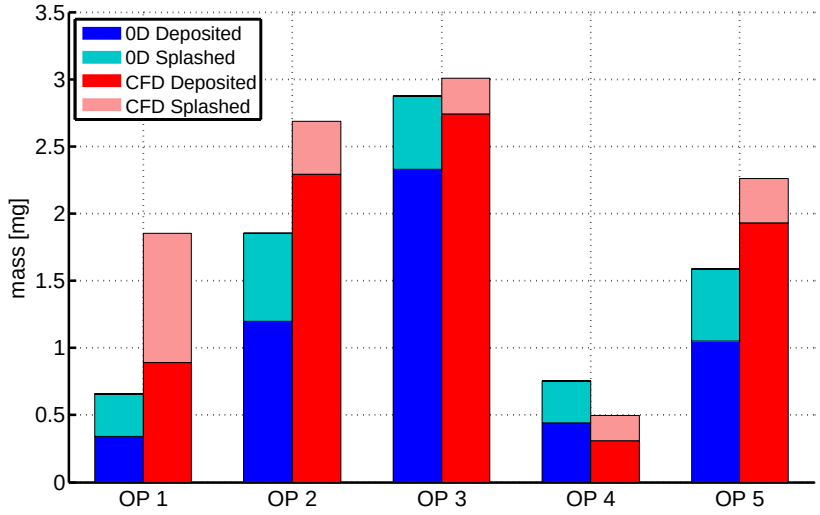

Fig. 6.15.: Comparison of spray-wall interaction between 0D model and 3D CFD after calibration for engine map variation. [81]

Besides the base operating points, the results are also compared for the injection time variation (503°CA at CFD OP6 to 383°CA at CFD OP7) and the coolant temperature variation (decrease of liner and piston temperature of about 40 K from CFD OP8 to CFD OP9), which is shown in Fig. 6.16 and Fig. 6.17.

Similar to CFD OP1, the operating points CFD OP7 to CFD OP9 have an early injection time. Hence, the amount of impinged fuel mass is under predicted by the 0D model. Besides this, the splash to deposited ratio is in high accordance with the 3D-CFD results. The difference in the absolute value of deposited mass logically influences the following wall evaporation module. Despite this, the 0D model takes account for the influence of the boundary conditions. Shifting the injection time to an early value significantly increases the piston impingement and thus the overall mass that is deposited on the wall in the 0D model. Furthermore, the model captures the effect of different coolant temperatures. This is mainly due to the lower injected fuel temperature, leading to an increased evaporation time at CFD OP9. The presented results involve a strong concatenation of the individual modules regarding the calculated wall film mass. The overall possibility of the model to react on changes of the boundary conditions was confirmed in this section. However, compared to 3D-CFD simulations, there are still distinct deviations in the absolute quantity of the wall film mass. In the next section, the quality of the wall film evaporation module is evaluated to assess the overall quality and usability of the model.

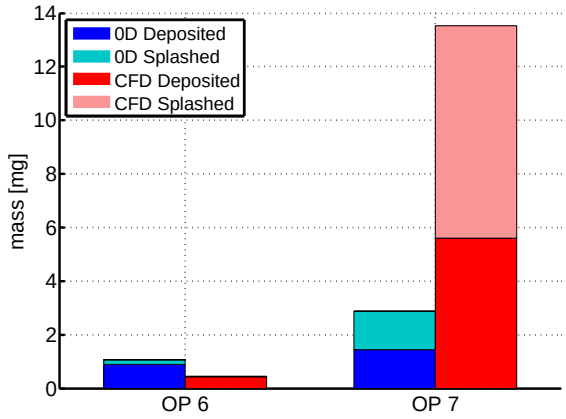

Fig. 6.16.: Comparison of spray-wall interaction between 0D model and 3D CFD after calibration for SOI variation. [81]

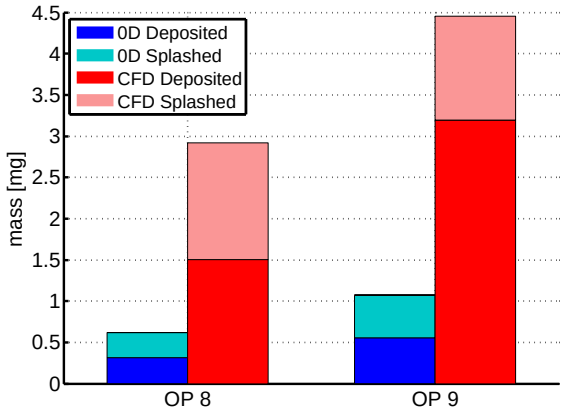

Fig. 6.17.: Comparison of spray-wall interaction between 0D model and 3D CFD after calibration for coolant temperature variation. [81]

6.4.2 Evaporation Rate

To evaluate the quality of the evaporation module and its potential for calibration, it is necessary to ensure the same prerequisites in terms of deposited wall film mass. In Section 6.4.1, it was shown that there are discrepancies between 0D model and 3D-CFD simulations even after a calibration of the spray module. Therefore, the wall film module is evaluated using the information of the 3D-CFD simulation as input value for the deposited mass in the 0D model. The initial results are compared between 0D model and 3D-CFD simulation in Fig. 6.18 for four different operating conditions. The displayed evaporated mass is normalized to the maximum value of deposited mass of the 3D-CFD simulations. CFD OP1 and CFD OP2 are taken from the standard engine map, CFD OP6 and CFD OP7 represent a variation of injection time. The 0D model shows slower evaporation rates compared to the 3D-CFD in the first three operating points, but it over-predicts the evaporation in CFD OP7. One main difference in this operating point is the early injection time. Furthermore, a dependency of injection time is visible for all presented operating conditions. The earlier the injection time, the faster the evaporation of the 0D model is, relative to the 3D-CFD simulation. This leads to a hypothesis that is described in the following:

In Section 6.3, it was explained that the wall film evaporation module presumes a mean wall film thickness $\overline{h}_{\mathrm{wf}}$ throughout the complete evaporation process. The correlation to calculate this film thickness considers droplet velocity, surface tension and density. However, the 0D spray model does not account for radial expansion of the spray and thus the width of the spray cone is missing when hitting the wall. However, due to spray cone expansion, the wetted area increases when the duration between injection and impingement is higher, leading to a decreased mean film thickness. The opposite effect occurs at early wetting after injection. Based on these considerations, a correlation is introduced that is based on the time between spray injection and impingement Δt_{imp} and that influences the wall film thickness $\overline{h}_{\mathrm{wf}}$:

$$f_h = \begin{cases} c_1 \cdot \left(\Delta t_{\mathrm{imp}}\right)^{c_2} & \text{for } \Delta t_{\mathrm{imp}} \leq \Delta t_{\mathrm{lim}} \\ f_{h,\mathrm{min}} & \text{for } \Delta t_{\mathrm{imp}} > \Delta t_{\mathrm{lim}} \end{cases} \tag{6.37}$$

$$\overline{h}_{\mathrm{wf,mod}} = f_h \cdot \overline{h}_{\mathrm{wf}} \tag{6.38}$$

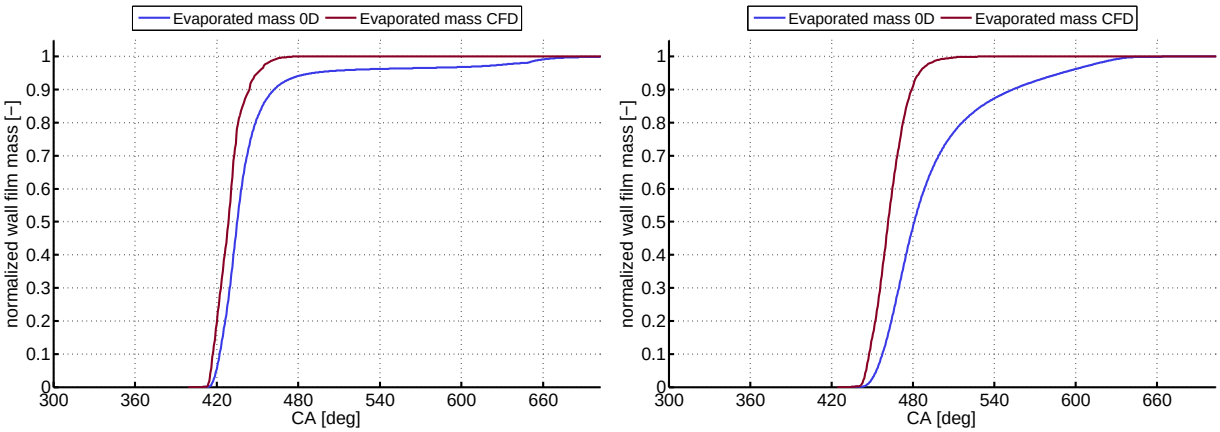

(a) OP 1: 2000 rpm, 120 Nm, SOI = 408 °CA

(b) OP 2: 2000 rpm, 220 Nm, SOI = 433 °CA

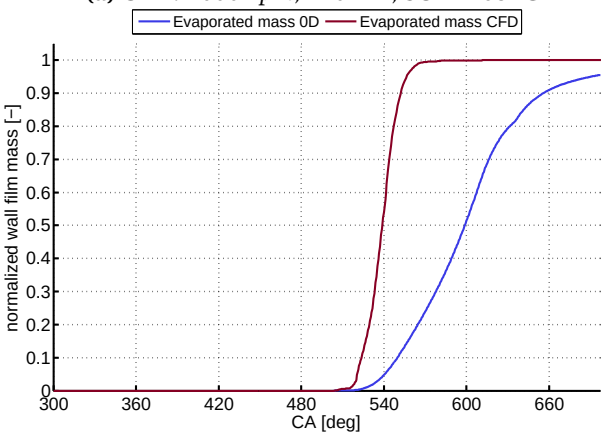

(c) OP 6: 2000 rpm, 130 Nm, SOI = 500 °CA

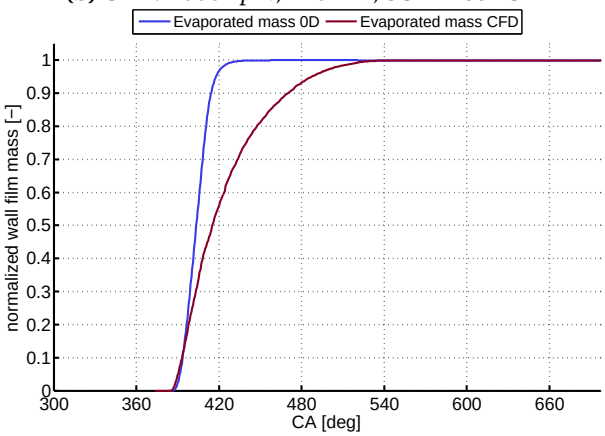

(d) OP 7: 2000 rpm, 130 Nm, SOI = 380 °CA

Fig. 6.18.: Wall film evaporation of 0D model and 3D-CFD simulations before calibration. CFD deposited mass over crank angle was taken as input value. Evapoarated mass is normalized to the maximum value of the deposited mass in the CFD simulations. [81]

In the here described model, the correlation is based on a power function and includes a limiting value $f_{h,\min}$ in case that the injection duration exceeds a value $\Delta t_{\lim}$ as a first approach. The parameter are estimated separately for piston and liner walls, as the impingement angle significantly differs.

The first calibration was performed without a special optimization method, but by analysing the results of a total number of seven operating points. The parameter results of the primary calibration are presented in App. A.2.3 (Tab. A.5). The evaporation behaviour of the 0D model after calibration is presented in Fig. 6.19 and compared to the 3D-CFD results. A significant improvement is now noticeable for all considered operating points. Although there are still deviations visible at CFD OP2 and CFD OP7, the agreement is regarded as sufficient after the effect of time to impingement has been considered.

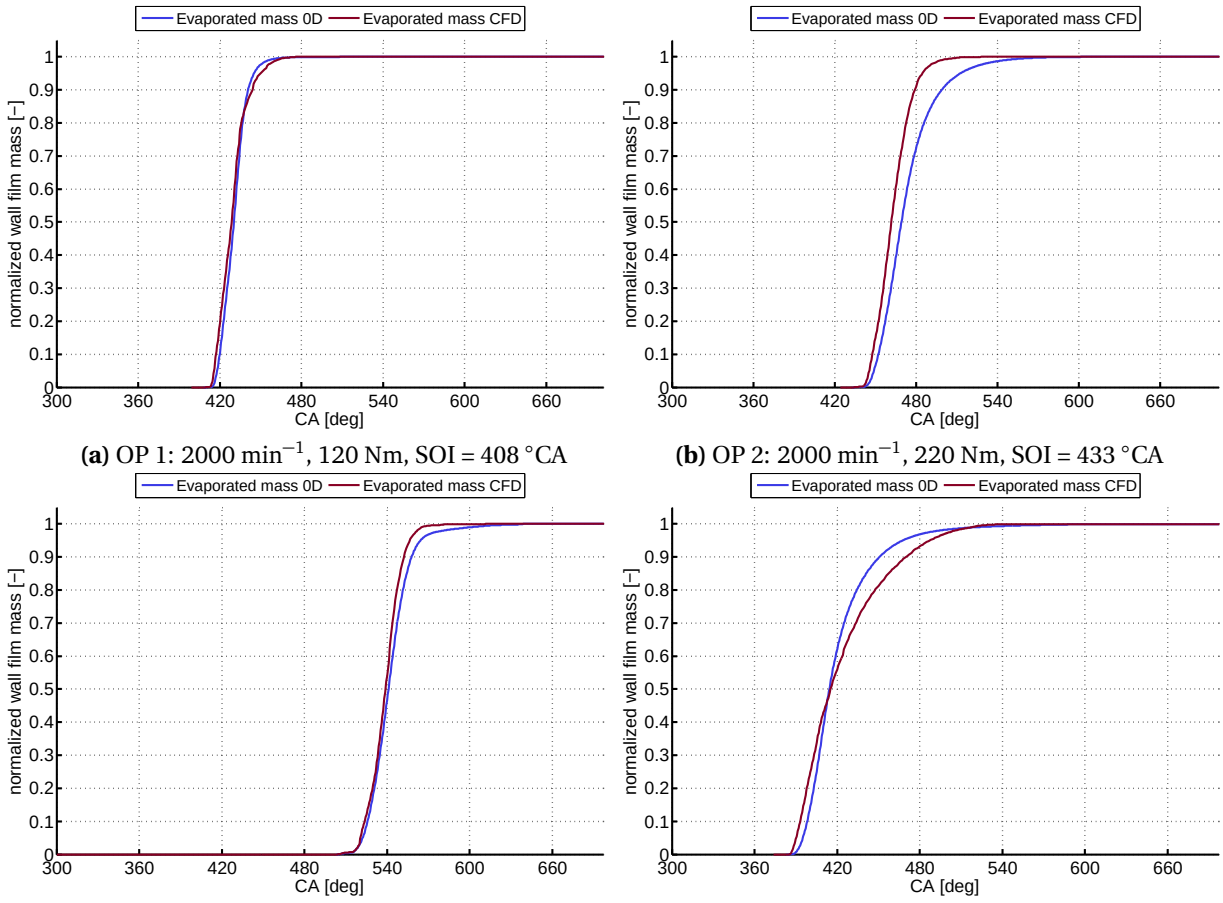

(a) OP 1: 2000 min^{-1}, 120 Nm, SOI = 408 °CA

(b) OP 2: 2000 min^{-1}, 220 Nm, SOI = 433 °CA

(c) OP 6: 2000 min^{-1}, 130 Nm, SOI = 500 °CA

(d) OP 7: 2000 min^{-1}, 130 Nm, SOI = 380 °CA

Fig. 6.19.: Wall film evaporation of 0D model and 3D-CFD simulations after calibration. CFD deposited mass over crank angle was taken as input value. Evapoarated mass is normalized to the maximum value of the deposited mass in the CFD simulations. [81]

6.4.3 Conclusion on the Applicability

In this section, it was confirmed that the model is basically capable to describe the spray penetration, spray-wall interaction and wall film evaporation for different engine operating conditions qualitatively. Due to the physically based formulations in the model, changes of the engine operating conditions affect the results in a plausible way. However, due to the simplifications in the different modules, significant deviations were detected when comparing the results to experiments or detailed 3D-CFD simulations in terms of spray penetration and wall film evaporation.

Based on these observations, three suitable calibration parameters were defined. Two of the parameters take into account that the droplets within the spray behave differently from single droplets in terms of applied drag force and surrounding fuel fraction. The third parameter takes into account that the wetted surface depends on the time between injection and impingement because of the increasing spray cone diameter, leading to a different wall film thickness.

A first calibration strategy was presented and showed significantly improved agreements for the considered engine operating conditions. It has to be noted that no dedicated optimization process was established to identify the parameter values yet. Therefore, the here presented results do not represent an optimum in the mathematical sense, but show only the fundamental possibility to improve the result quality by calibration. Remaining deviations can be explained by the use of different fuels in the simulation. In the 3D-CFD simulation, a gasoline fuel has been used to be consistent with engine test bench measurements. The 0D model uses iso-octane as substitute fuel, leading to differences in physiochemical properties, such as vapour pressure and latent heat of vaporization.

In the context of the particle simulation, the target quantity for validation is the remaining wall film mass at ignition time, which greatly depends on all described modules. The calibration of the identified parameters by 3D-CFD simulations is not recommended because of the following limitations of the here applied 3D-CFD model:

Although the spray penetration and evaporation can be simulated with a high level of detail by the 3D-CFD method, the spray-wall interaction is typically based on empirical correlations and the results (deposited wall film mass over time) can not be verified explicitly by the available experimental results within the present thesis. This leads to a high degree of uncertainty in the quality of the 3D-CFD simulation results. In addition, the calculated evaporation rate strongly depends on the wall temperature boundary conditions. Since these values are rarely measured, they are a result of 1D engine process simulations that included measured coolant and oil temperatures. In a 3D-CFD sensitivity study presented in Fig. 6.20, the impact on the calculated remaining wall film mass is shown [81]. In the base scenario, the wall film mass evaporates at approx. 600°CA, whereas increasing the wall

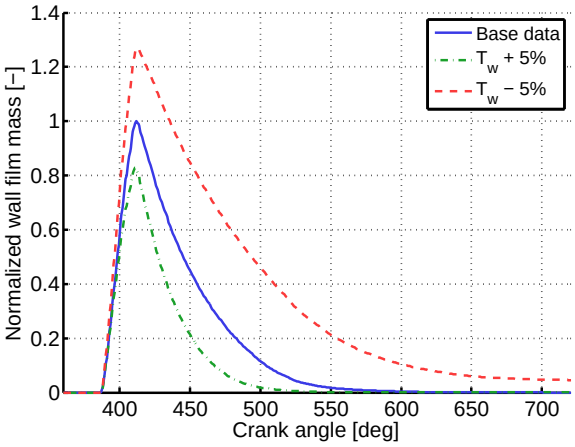

Fig. 6.20.: Influence of wall temperature on current wall film mass calculated by 3D-CFD simulation at CFD OP7: 2000 rpm, 130 Nm. [81]

temperature by 5 % leads to a reduction of the peak film mass by 20 % and to a reduction of the total evaporation time of about 60°CA. If the wall temperature is reduced, the differences are even more substantial. The maximum value increases by 25 % and the wall film mass remains until ignition time. For the investigated operating point, a significant increase of particulate emissions was measured relative to OP6 with base injection time, indicating that the early injection time very likely also leads to a remaining wall film. Therefore, absolute statements concerning wall film mass should be made with care, as the here applied wall temperatures in the 3D-CFD simulation can be erroneous.

Increasing the quality of the 3D-CFD simulation would be a possible solution, but with a very high effort, which is difficult to implement within the framework of the engine development. Instead, it is more effective to calibrate the spray and evaporation model directly by using the desired target values, namely particle number and mass emissions. It should be noted that the intermediate results of the model (impinged and deposited mass, evaporation rate) can not be verified by measurement technology and are thus not necessarily physically correct. However, based on the previous investigations, it is assumed that the trend basically can be represented by the model.

In addition, the model is not capable to consider the influence of charge motion on the spray behaviour, which is especially important at high engine load conditions. Therefore, the quality of the results in terms of particle emissions needs to be evaluated at these conditions. In the following section, the implementation of the sub-model in the particle simulation framework is presented and the model calibration strategy is described. Afterwards, the quality of the particle emission result is presented at different engine operating conditions.

6.5 Implementation in Overall Model

6.5.1 Parametrization Strategy

The final parametrization of the wall film formation and evaporation model is performed by comparing the resulting particle number and mass emissions to measured values at selected operating conditions. This method is chosen mainly because the boundary conditions of the available 3D-CFD simulations are not sufficient to match the exact engine conditions (especially the wall temperatures that are calculated by the engine process simulation and the spray characteristics). The parametrization process is performed analogously to the injector film module that is described in Section 4.4.1. This also includes the applied error function that compares the relative deviation between measured and simulated particle number and mass stream values (see Eq. 4.10).

In contrast to the parametrization of the injector model, the wall-film-induced emissions are usually not the only source of the total emissions for the given engine. Therefore, the already parametrized values of the injector module are included. Some of the applied parameters are used by both modules. This includes the active particle surface, the temperature correction factor and the fuel fraction of the pyrolysis zone. These values are taken from the injector module without further calibration. The following parameters remain for parametrization:

- One drag coefficient factor f_D (see Eq. 6.33).
- One fuel fraction factor f_V (see Eq. 6.35).
- Two parameters $c_{1_{\text{piston/liner}}}$ and $c_{2_{\text{piston/liner}}}$ to calculate a factor f_h that is applied to the film thickness of piston and liner wall films as a function of time to impingement $f_h(\Delta t_{imp}) = c_1 \cdot \Delta t_{imp}^{c_2}$ (see Eq. 6.37).

The optimization process again is carried out by the Nelder-Mead simplex algorithm [138] because of the low number of parameters.

Special attention is paid to the selection of the operating points that are used for parametrization. A combination of warm and cold engine conditions is chosen to ensure that the simulated wall-film-induced emissions only occur at cold conditions. In addition, the relative change of emissions between warm and cold operating conditions can be evaluated for each operating point. This is of

special interest because it allows to estimate the proportion of the emissions that arise from wall films at cold conditions (assuming that the injector film remains approximately constant).

A total number of six operating points at different engine speeds and high engine loads is chosen throughout the engine map because the wall-film-induced emissions are expected to be dominant at these conditions. This is due to the high injection duration, leading to an increase of wall-impingement and a reduced time for film evaporation. However, the temperature of the engine coolant could not be kept constant due to the restrictions in cooling performance. Therefore, the coolant temperature increases at higher engine speeds and is in a range of $40°C - 50°C$ (named as "cold" in this context, compared to "warm" conditions at coolant temperatures of $\approx 90°C$). Due to the injection time, which is approximately in the middle of the intake stroke, all of the selected operating points force a significant impingement on the liner. Therefore, another operating point was added with an early injection time at cold engine conditions (2000 rpm/5 bar IMEP) that enforces an impingement on the piston surface. The measurement results of the selected operating points are shown in Fig. 6.21 along with the simulation results of the injector film module.

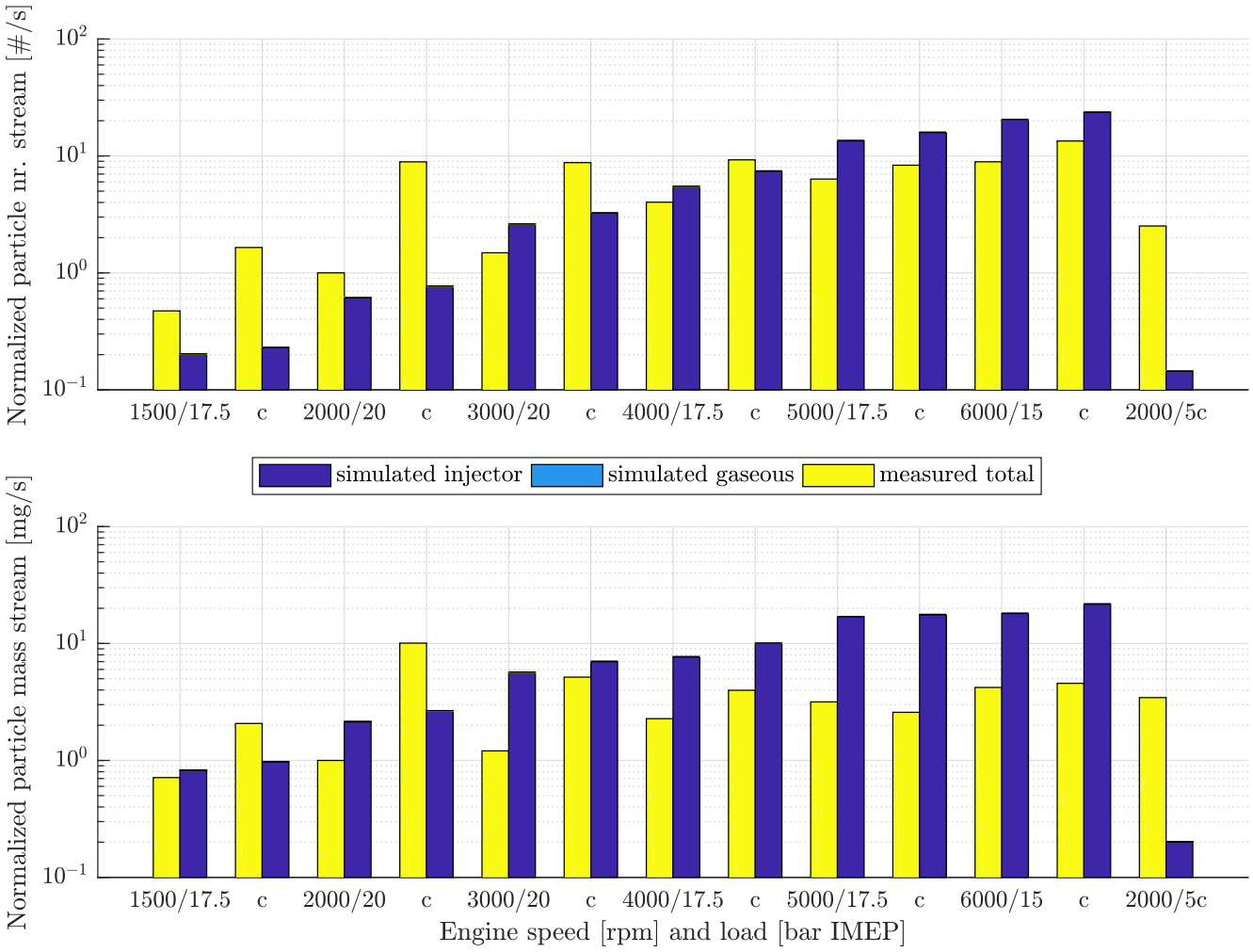

Fig. 6.21.: Operating points for parametrization of SWI module. Simulation results without SWI module. Comparison of warm and cold (c) engine conditions. All values based on measured results at 2000 rpm/20 bar IMEP.

At warm engine conditions, the quality of the simulation is based on the parametrization of the injector module that is presented in Section 4.4.2. The measured results show a significant increase in particle emissions at cold engine conditions for engine speed values up to 4000 rpm. This increase can not be covered by the simulation because of the missing wall film module and increases the error function value for these operating conditions. At higher engine speeds, the effect is reduced because

of the increased engine coolant temperature. A significant wall film effect is also visible at the cold 2000 rpm/5 bar IMEP operating point that is also not covered by the simulation.

The combination of the operating conditions enable the parametrization of the wall film module to cover the effects at low engine speeds and cold engine conditions. In addition, they limit the effect of the module at higher temperatures because the emissions are already covered by the injector module. However, since the error function is based on the total emission value and includes the quality of the injector module, the results has to be checked for plausibility after parametrization. In the next section, the final parameter set is presented and the results of the wall film module are explained in more detail.

6.5.2 Results and Model Quality

The final results of the parametrization process are shown in Tab. 6.1. The values reveal that the impinged fuel mass is already sufficient with the unchanged drag and fuel coefficients. Therefore, both values are kept at their base values of one, i.e. $f_{\mathrm{D,min}} = f_{\mathrm{V,min}} = 1$, $a_1 = b_1 = 0$.

The resulting fuel mass would lead to an over prediction of the particle emissions in the given simulation framework because of the low evaporation rate that arises from the originally calculated wall film thickness. Therefore, both the liner and piston film thickness is decreased ($f_h << 1$) by the calibration parameter to increase the evaporation process.

Tab. 6.1.: Parametrization results of SWI module

f_D	f_V	$f_{h_{liner}}$	$f_{h_{piston}}$
1	1	$6.69e-12 \cdot \Delta t_{imp}^{-2.84}$	$6.99e-12 \cdot \Delta t_{imp}^{-1.29}$

The comparison of particle number and mass emissions to measured values with the parametrized model is presented in Fig. 6.22 for the already presented operating points at warm and cold conditions. Generally, the SWI module does not create any wall-film-induced emissions at warm engine conditions, which is the expected behaviour. At cold engine conditions, the module provides a proportion of about 80 % at 2000 rpm and 3000 rpm based on the total number emissions. The proportion is reduced to about 60 % at 4000 rpm and further reduced to 25 % at 6000 rpm. These proportions correlate to the measured increase of the emissions with acceptable agreement. This is of special interest at engine speed values of $5000-6000$ rpm where the injector module already over estimates the measured emissions at warm and cold conditions. The wall film module still provides a contribution to the total emissions which goes along with the increase in measured number emissions. The particle mass results are consistently over predicted by the injector film module, which is further described in Section 7.1.2 in the context of the complete engine map simulation.

However, no contribution is made by the wall film module at 1500 rpm/17.5 bar IMEP and 2000 rpm/5 bar IMEP. A more detailed analysis of the SWI module is carried out in order to find the cause for this behaviour. Hence, the impinged fuel fraction and the created film mass is presented in Fig. 6.23 for each of the operating points.

The liquid film mass is divided into liner and piston film. The spray shows a similar behaviour for the operating conditions with an injection time in the middle of the intake stroke. About 5 % of the total injected fuel impinges on the liner walls and most of the mass remains as liquid wall film. Approximately the same wall film mass is attached for the 1500 rpm/17.5 bar IMEP and 2000 rpm/20 bar IMEP operating conditions. However, the available evaporation time at 1500 rpm is higher than at 2000 rpm and therefore the complete wall film evaporates until ignition time. This can

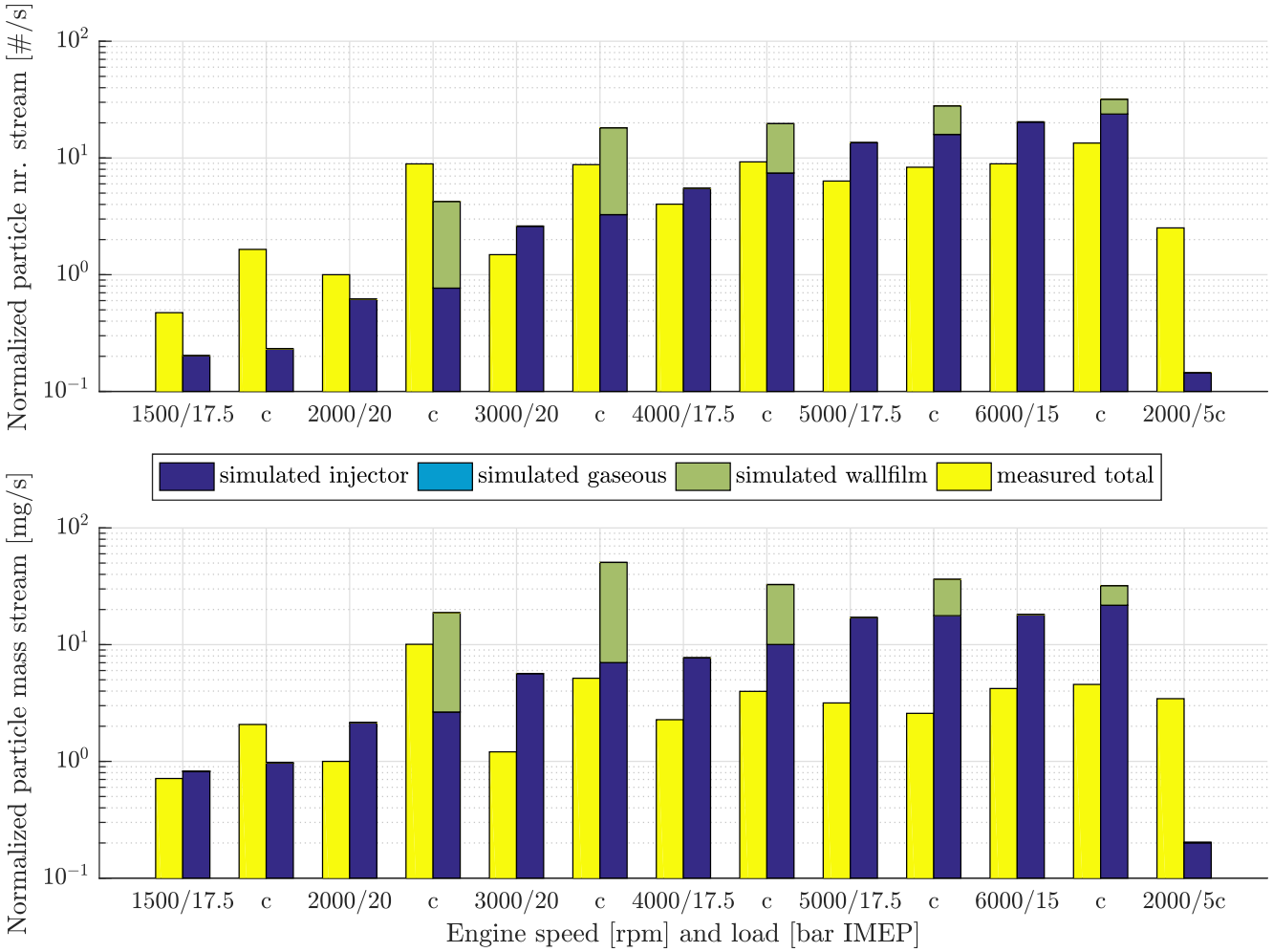

Fig. 6.22.: Results of SWI module parametrization in engine operating map at warm and cold (c) conditions. All values based on measured results at 2000 rpm/20 bar IMEP.

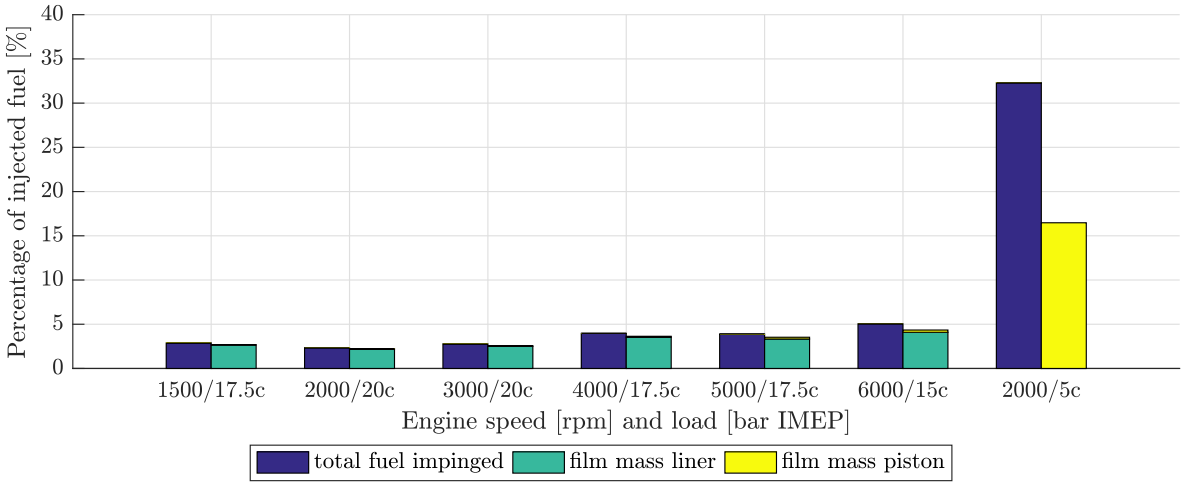

Fig. 6.23.: Calculated total impinged fuel and created film mass (liner and piston) for parametrized operating points at cold engine conditions (c). Presented as fraction of total injected fuel mass of the corresponding operating point.

not be prevented by the parametrization of the film thickness parameter since the impingement time is similar for both operating points.

The early injection point at 2000 rpm/5 bar IMEP shows a completely different behaviour. A much larger proportion of the injected fuel hits the piston and roughly half of it remains on the wall. This can be explained by the high droplet speed after injection that is considered by calculating the splashed fuel fraction. The results confirm that the spray module and the spray-wall interaction generate physically plausible results for the investigated impingement regimes. The cause of the complete disappearance of the piston wall film at ignition time must therefore originate from the calculation of the film evaporation.

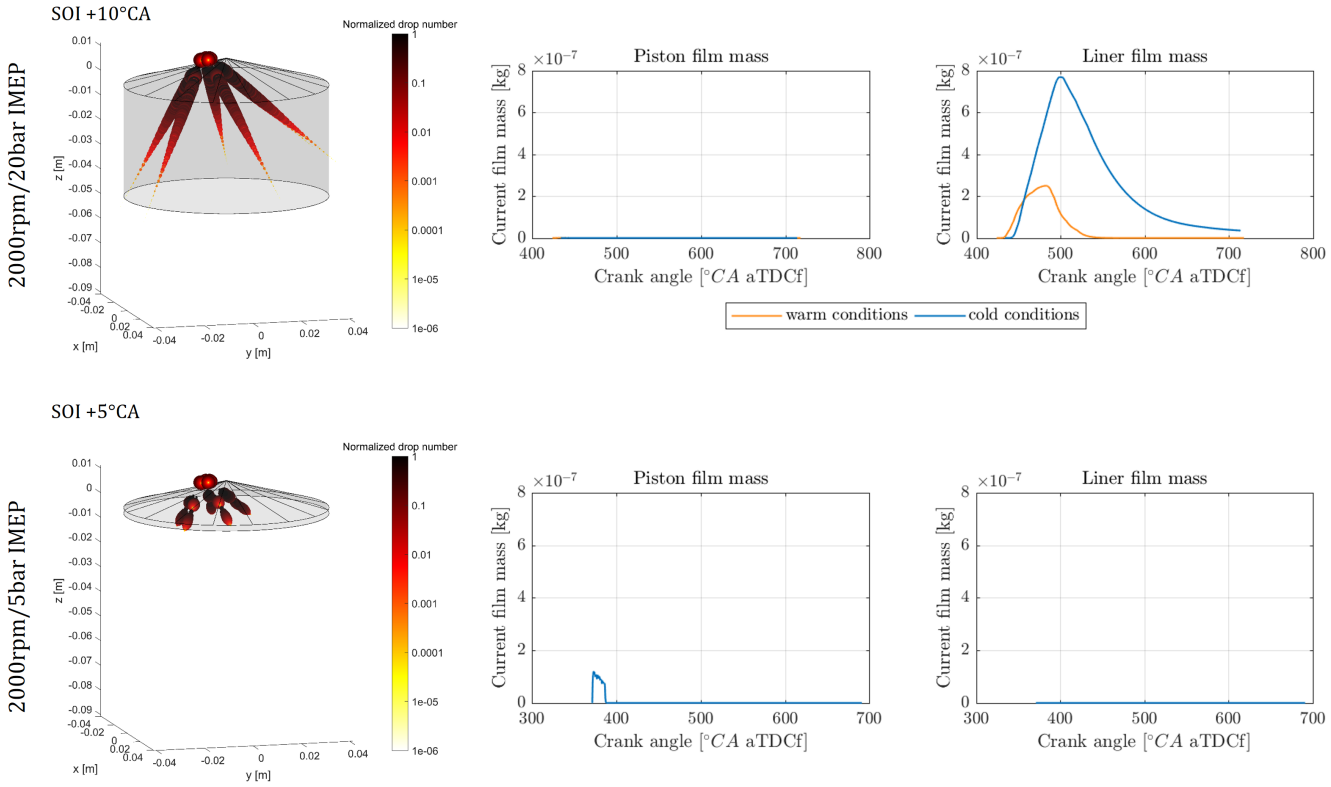

Fig. 6.24.: Analysis of wall impingement (left side) and remaining film mass (right side) at 2000 rpm/20 bar IMEP (warm and cold) and 2000 rpm/5 bar IMEP with early injection time (cold).

The remaining wall film is presented in Fig. 6.24 as a function of crank angle for piston and liner film mass for two representative operating points. In addition, a schematic presentation of the spray penetration is shown at the time step of the first impingement.

At 2000 rpm/20 bar IMEP the spray impinges on the liner walls both at warm and cold engine conditions. Only a negligible amount of fuel hits the piston. The differences between warm and cold conditions are solely caused by the liner wall temperature. The higher temperatures lead to a rapid evaporation, whereas a part of the wall film remains until ignition time at reduced temperatures. The same effect is responsible for the behaviour at 2000 rpm/5 bar IMEP. In this case, the fuel only hits the piston, which has a higher temperature than the liner (+40 K). Therefore, the remaining wall film fully evaporates very quickly.

A sensitivity analysis of the evaporation process is presented in the next section to determine the influence of deviations in the wall temperatures on the simulation results.

Summarizing, the SWI module can basically cover the effects on particle emissions at cold engine

conditions that occur due to liner impingement. The evaporation rate is overestimated at low engine speeds. The model takes into account that the remaining wall film quantity is reduced at higher coolant temperatures.

However, with the given parametrization strategy, it is not possible to cover the effects that occur when the piston is hit by the spray due to the higher wall temperatures. In addition, the effects of injector-induced and wall-film-induced emission can hardly be separated at the measured values. The parametrized results only represent a first assessment of the model quality and show the ability of the model to react to wall film formation processes. Further investigations are required with numerous changes of engine and spray parameters to verify the model quality. Furthermore, the results have to be evaluated throughout the engine map.

6.5.3 Analysis of Simulation Process

In the previous section, the evaporation rates of liner and piston film were found out to differ significantly because of the temperature offset. Therefore, further investigations of the model sensitivity on the applied wall temperature are performed in the following by a sensitivity analysis at the operating point 2000 rpm/20 bar IMEP at cold engine conditions. Applying the original wall temperature values lead to the formation of liner wall-film-induced emissions that dominate the overall particle emissions.

The input value of the wall temperature is varied between 80 % and 120 % of the original value. The results are presented in Fig. 6.25 (left side) based on the original particle number and mass stream values. It is clearly visible that reducing the wall temperature affects the emissions only slightly. This is comprehensible since the wall temperature mainly affects the calculation of the material properties, whereas it is not directly an input value of the evaporation rate calculation described in Section 6.3.

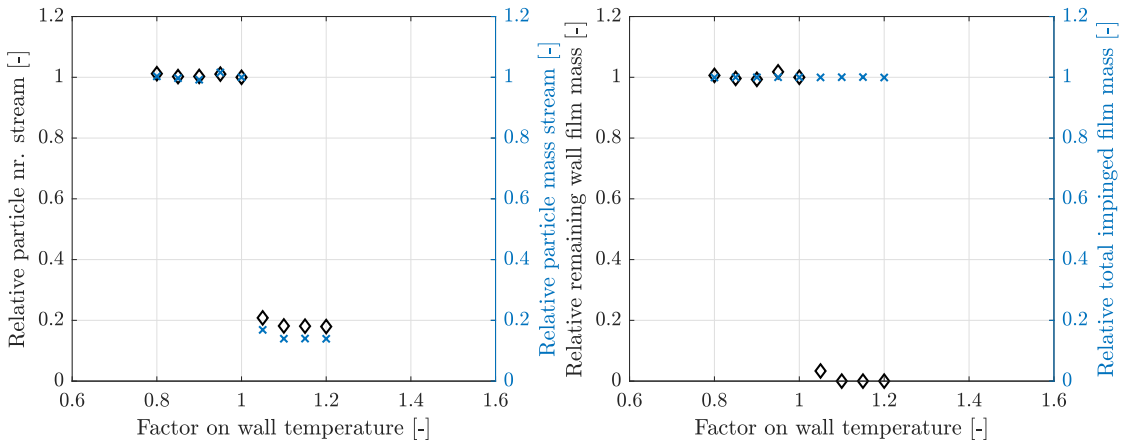

Fig. 6.25.: Sensitivity analysis of wall film model on wall temperature. Base operating point 2000 rpm/20 bar IMEP (cold). Values based on original wall temperature results.

A completely different behaviour can be determined when the wall temperature is increased. The emission values drop by 80 %, indicating that the wall film fully evaporates at these conditions. This is also confirmed by comparing the total impinged film mass and the remaining film mass at ignition time with the base values in Fig. 6.25 (right side). The total impinged film mass is not affected by the wall temperature, whereas the remaining film mass drops to zero at higher wall temperatures.

This behaviour is caused by the calculation of the evaporation regime in the wall film evaporation model. In general, the model considers a gas-side and wall-side evaporation rate (see Section 6.3, Eq. 6.27 for gas-side wall film evaporation and Eq. 6.30 for wall-side evaporation rate). A selection of

the dominant evaporation rate is made by calculating the difference between the saturation temperature of the fuel T_{sat} (see Eq. A.32) and the current wall temperature T_{wall} (wall superheat temperature, see Eq. 6.26).

For wall superheat values below a defined value of $T_{\text{wall}} - T_{\text{sat}} < 5\ K$, the calculated dry surface fraction α_{dry} and the fraction of the wetted area that contributes to vaporization β_1 is zero and thus the calculated wall-side evaporation rate in Eq. 6.30 vanishes.

If the wall temperature exceeds the saturation temperature by more than 5 K, the wall-side evaporation rate is considered to be dominant (start of nucleate boiling regime, see Fig. 6.3). Now, the value of the wall-side evaporation rate is significantly higher.

The fuel saturation curve T_{sat} depends on the fuel type and the ambient pressure. For the investigated base operating point (sensitivity analysis factor 1.0 on liner temperature), the saturation curve of iso-octane is presented in Fig. 6.26 as a function of the current crank angle together with the wall temperatures of piston and liner, the time of injection start, start of impingement and end of impingement.

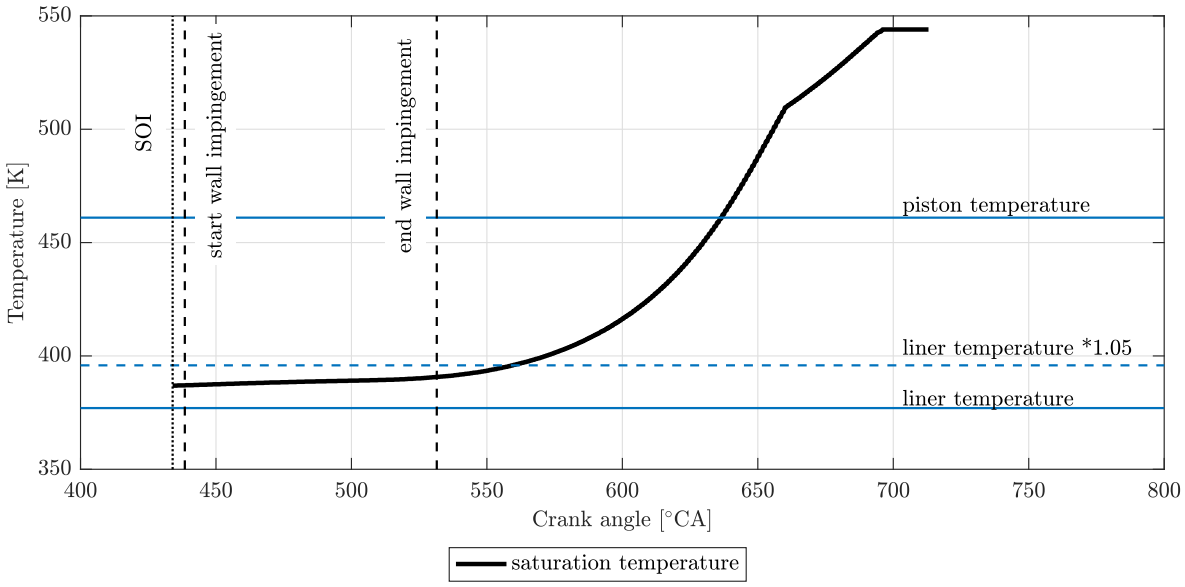

Fig. 6.26.: Saturation T_{sat} and wall temperatures T_{wall} at 2000 rpm/20 bar IMEP (cold). Change from gas-side to wall-side heat transfer at $T_{wall} - T_{sat} > 5\ K$. Sensitivity analysis factor of $T_{\text{liner}} \cdot 1.05$ on liner temperature is illustrated by dashed line.

The saturation curve includes a large temperature range due to the pressure change during compression. Therefore, the injection and impingement time influences the calculation of the excess temperature of the wall. For the investigated case, the calculated piston temperature always leads to a wall-side dominant evaporation because of its overheating during the impingement process ($T_{wall} - T_{sat} > 5\ K$). This behaviour also applies in the same form to the operating points at which the piston is wetted because of the comparable engine, wall and thus saturation temperatures (e.g. 2000 rpm/5 bar IMEP).

The base value of the liner temperature is always below the calculated saturation temperature and thus leads to gas-side dominant evaporation ($T_{wall} - T_{sat} < 5\ K$). By increasing the input value of the liner temperature in the context of the sensitivity analysis, the saturation temperature is exceeded and the evaporation regime changes. Generally, the calculated wall-side evaporation rate then is about 15 times higher than the gas-side evaporation rate. This leads to the complete evaporation of the wall

film for the investigated sensitivity analysis. This effect also explains that the complete piston wall film evaporation at 2000 rpm/5 bar IMEP.

Although this change of the behaviour is physically based because of the start of nucleate boiling, the saturation temperature at which the wall-side evaporation process starts leads to a high sensitivity on the applied wall temperature. However, for the current work, no additional information are available that include measured wall temperatures for the investigated operating conditions. Therefore, it is not possible to estimate whether the calculated evaporation rate or the wall temperature value is over-estimated for the operating conditions with a distinctive piston impingement. Furthermore, detailed investigations are required to correctly estimate the evaporation behaviour in the transition area between gas-side and wall-side dominant heat transfer.

Nevertheless, most of the injection time values do not lead to a significant piston impingement (see also Section 6.5.2) for the investigated engine. In these cases, the gas-side dominant evaporation regime is active and the model quality is sufficient to calculate the resulting particle emissions.

7 Proof of Concept

7.1 Validation at Engine Operating Map

7.1.1 Fluctuation of Measured Data

To evaluate the simulation results during engine operation, it is crucial to get additional information about the fluctuation of the measured values. This is of special interest for particle emissions because of the complex measuring systems and the dependency on the specific engine conditions. The quality of the simulation results can then be verified within the confidence range of the measured values.

The general test procedure is already explained in Section 3.4.3. Two additional measurement strategies were added to get statistical information about the particle emission fluctuations:

1. A specific base operating point (2000 rpm, 10 bar IMEP) was measured over several days and before and after each test series. This leads to a total number of 14 measuring points.
2. The complete engine operating map (warm, total number of 76 operating points) was measured four times on several days. This leads to a total number of 4 series of measurement for each point in the operating map.

The combination of these two methods still contains few statistical information. It allows to analyse the behaviour of one single engine operating point with numerous measurement data and a set of operating points that includes most of the engines operating map on several days.

For both particle number and mass emissions, the coefficient of variation c_v can then be calculated. This is done by determining the mean value $\bar{x}$, the variance $Var(x)$ and the standard deviation σ_x with the total number n of measured operating points x_i.

$$\bar{x} = \frac{1}{n}\sum_{i=1}^{n} x_i \tag{7.1}$$

$$Var(x) = \frac{1}{n}\sum_{i=1}^{n} (x_i - \bar{x})^2 \tag{7.2}$$

$$\sigma_x = \sqrt{Var(x)} \tag{7.3}$$

$$c_v(x) = \frac{\sigma_x}{\bar{x}} \tag{7.4}$$

The calculation was performed separately for each strategy, the results are shown in Tab. 7.1. Considering a 1σ interval, the coefficient of variation is in a range of $0.25 - 0.31$ for particle number stream emissions and $0.32 - 0.41$ for particle mass stream emissions, respectively. In Fig. 7.1, the measurement history of strategy 1 is presented with the corresponding 1σ interval boundaries. It is clearly visible that there is a significant fluctuation between the values that is assumed to result from changing engine conditions (e.g. by different injector or wall deposits). Due to the definition of the

Tab. 7.1.: Calculated coefficients of variation for engine operating map.

	base operating point	operating map
number of operating points	1	76
number of repetitions	14	4
coefficient of variation PN	0.25	0.31
coefficient of variation PM	0.32	0.41

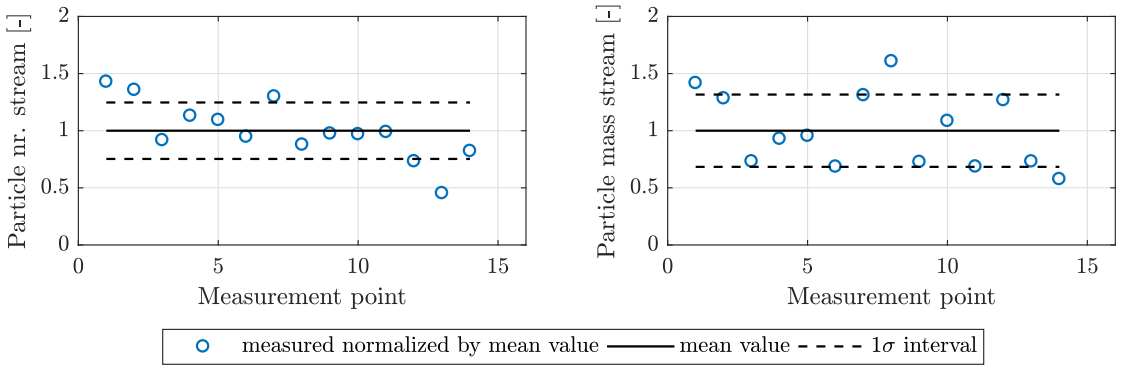

Fig. 7.1.: Coefficient of Variation at 2000 rpm/10 bar IMEP measurement. Measured values are normalized by total mean value for particle number and mass stream. Total number of measurement points is 14.

confidence interval, only about two thirds of all measured values are included by these boundaries. Therefore, a 2σ interval is used for further comparison (this includes about 95 % of the values).

The results for strategy 2 is presented in Fig. 7.2 with the corresponding 2σ interval boundaries. The

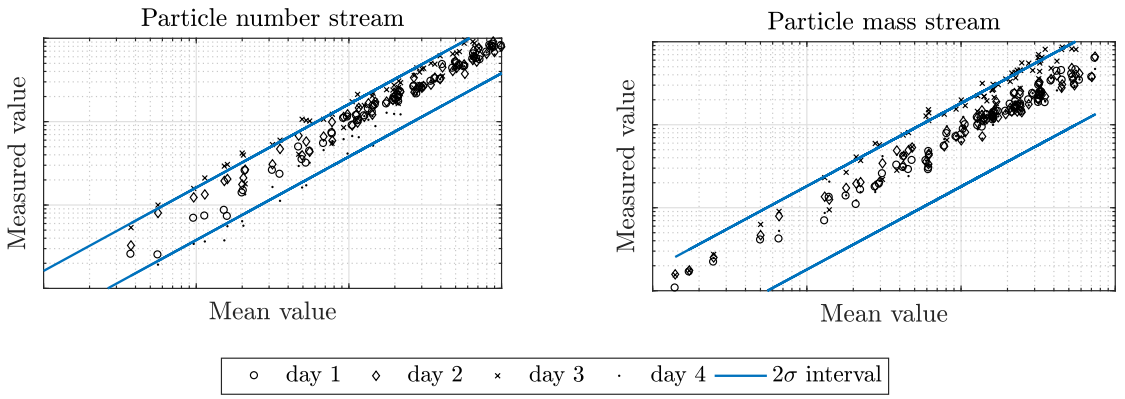

Fig. 7.2.: Fluctuation of measurement values for warm eingine map. Total number of points in engine map is 76. Engine map is measured on 4 days.

resulting measurement values are presented as a function of the corresponding mean value at the specific operating point. The analysis shows that the fluctuations of particle number values increases with decreasing absolute emissions. This can be explained by the measurement uncertainty of the measuring systems. Considering the particle mass emissions, measuring series 4 shows clearly higher emissions than the other series. It is assumed that this is caused by a temporal change of injector deposits. Based on these results, the 2σ interval of the operating map (0.62 for particle number stream, 0.82 for particle mass stream) is chosen and applied to the measured values as the maximum confidence interval for the simulation results. In terms of warm operating conditions, the mean value of the measurement is utilized for comparison because of the total number of 4 repetitions. The cold engine map was only measured once, hence the simulation is compared to the resulting values with the applied confidence boundaries.

7.1.2 Warm Engine Conditions

In Fig. 7.3 and Fig. 7.4 the particle number and mass results of the simulation model are presented and compared to measured data for different engine speeds and loads. The results are calculated including all model components and they are presented in terms of time based values. The measured data is plotted in terms of mean values of four measurement series and includes the confidence boundaries that are described in Section 7.1.1. The operating points that were used for calibrating the injector film module are marked with black dots and have already been described in Section 4.4.2. However, the simulation is now extended to a large part of the engine map and the mixture homogeneity module is included. Because of the warm engine conditions, the spray-wall interaction module does not contribute to the particle results here.

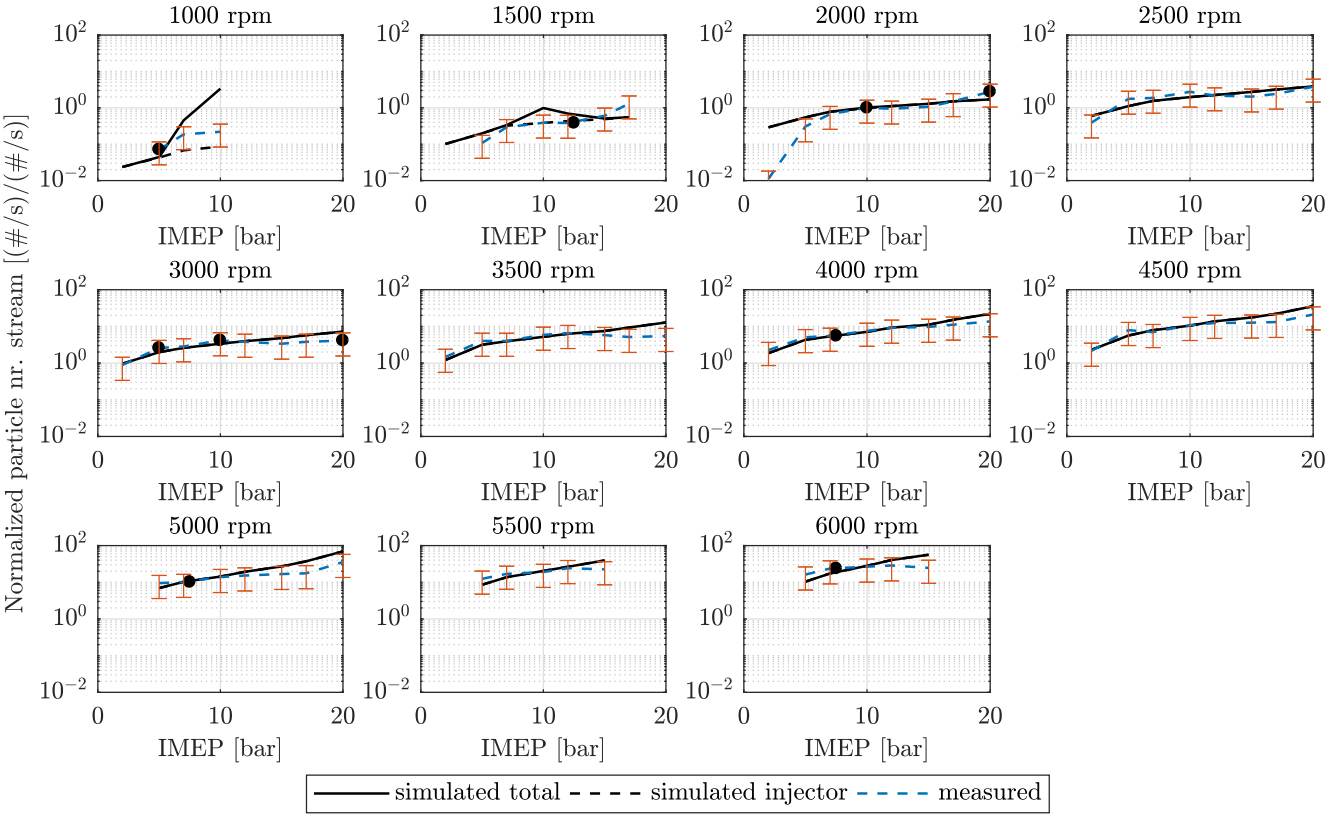

Fig. 7.3.: Comparison between measured and simulated particle number emissions for warm engine conditions in operating map. Operating points that were used for parametrization marked by black dots. Error bars represent 2 σ interval. All values normalized by measured results of 2000 rpm/10 bar IMEP.

Generally, the measured particle emissions show increasing values with both speed and load. This is plausible because of an increase in fuel injection and decrease in available mixing and evaporation time of the injector film. The measuring range of particle number emissions covers two orders of magnitude and three orders of magnitude for particle mass emissions, respectively.

This trend is also visible for the simulation results. At moderate speed and load conditions there is an excellent agreement for particle number emissions, including the values outside of the calibrated operating points. In most areas of the operating map, the simulated particle emissions are exclusively caused by the injector, which is in agreement to investigations of Miklautschitsch et al. [125]. The particle mass emissions are also in accordance to the measured data for moderate speed and load conditions but with noticeably higher deviations to the measured data. This can be explained by the particle formation theory. Particle number emissions are mainly influenced by nucleation and coag-

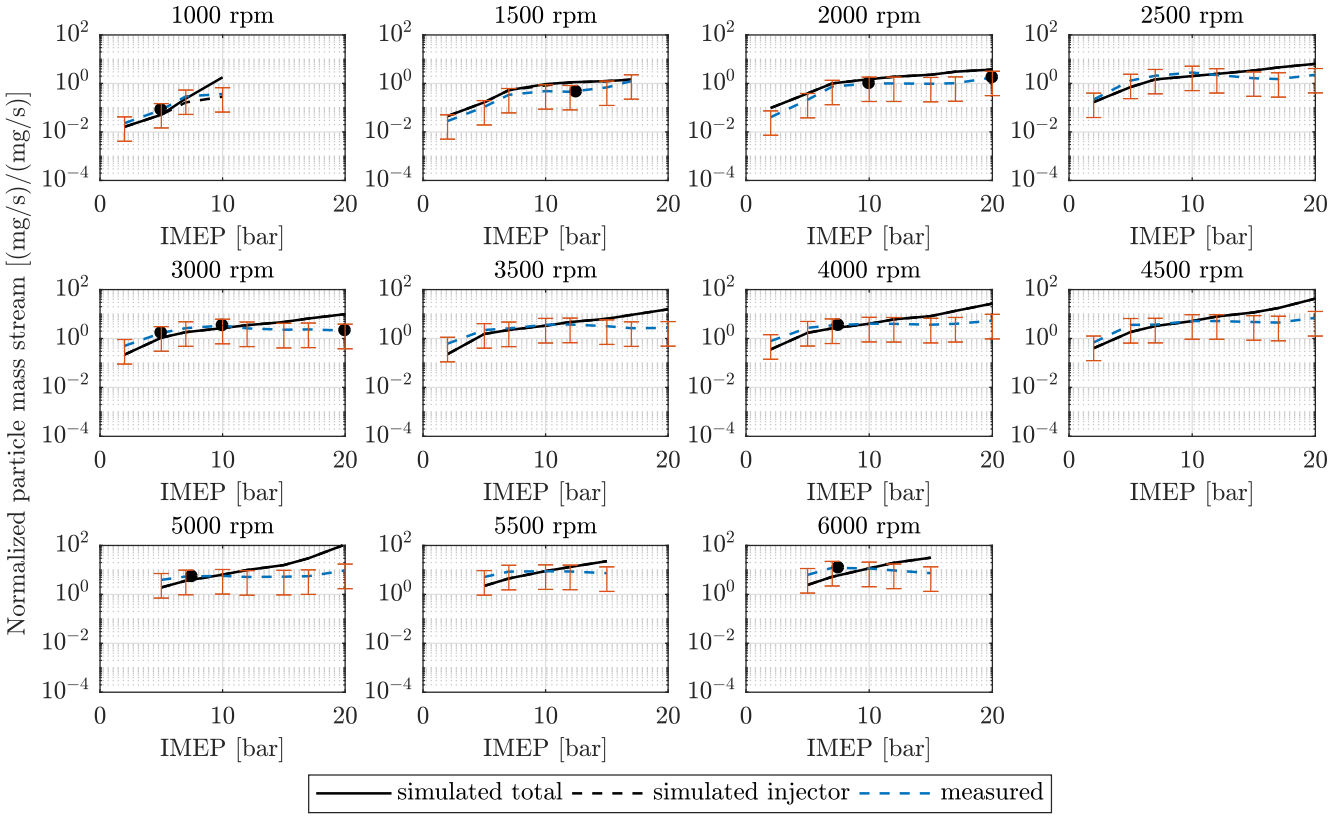

Fig. 7.4.: Comparison between measured and simulated particle mass emissions for warm engine conditions in operating map. Operating points that were used for parametrization marked by black dots. Error bars represent 2 σ interval. All values normalized by measured results of 2000 rpm/10 bar IMEP.

ulation processes, whereas particle mass is mainly affected by surface growth processes that include a number of additional gas-phase species and a high temperature sensitivity. However, the particle mass is within the confidence boundaries for large parts of the operating map as well.

At high engine speed and loads, the particle number and mass emissions are over-predicted by the simulation model. It is hypothesized that this is due to an over-prediction of the injector film mass at ignition time. The film creation module already includes a decreasing amount of fuel that is added over time, but there is possibly a maximum film mass that can be hold by the injector, which is currently not considered. In addition, the evaporation function for the injector film mass at representative engine speeds is taken from 3D-CFD simulations without additional information about the temperature of the injector tip and the gas-phase. At high engine speed and load conditions, it is expected that the injector film evaporates much faster than at lower temperatures. In the current modelling approach, no gas-phase inhomogeneities are calculated at this part of the operating map.

At low engine speeds (up to $\approx$ 1500 rpm), major deviations occur because of the simulation of mixture-induced particle emissions. This is caused by the Reynolds dependency of the homogenization model. At low engine speeds with reduced mixing time, the homogeneity model underestimates the mixing process. It has to be noted that the calibration of this sub-model was done for engine speeds of 2000 rpm and above, leading to an extrapolation for lower values. This deviation mainly affects the particle number results because of the reduced particle diameter.

A comparison of the injector-induced emissions to the measured values at low engine speeds (up to $\approx$ 2500 rpm) and high engine loads exhibits a special phenomenon. The particle number emissions are underestimated or agree with the measured data, whereas the mass emissions are overestimated by the simulation. This was already observed during the calibration of the injector model in Section 4.4.2.

Combining the results of the simulated injector- and mixture-induced emissions and comparing them to measured particle size distributions indicates the reason for this behaviour and is further analysed in the context of the complete particle emission model. Hence, the particle size distribution for different engine speeds at the highest measured load is presented in Fig. 7.5. The values are normalized by the corresponding maximum number density for both the simulated and measured data. Therefore, the position of the modes of the size distribution and its shape can be compared.

In general, the diameter of the mixture-induced particles matches the measured nucleation mode (about 10-30 nm), whereas the injector induced particle diameter correlates with the measured accumulation mode (about 60-80 nm). Combining the results for particle mass, number and size distributions leads to the assumption that there is a imbalance of the model parts that are caused by the optimization strategy. In the next section, a calibration strategy is presented that checks the possibility of the model to cover the correct size distribution by an alternative parametrization method.

7.1.3 Alternative Calibration Strategy

As it is already explained in Section 2.2, different literature studies conclude that there is an influence of the particle formation process in DISI engines on the corresponding particle sizes. Generally, mixture-induced soot particles are stated to be smaller then film-induced particles emissions [18, 98, 156]. This leads to the hypothesis that the measured particle size distribution offers an indication of the formation processes. At low engine speed and high loads, the shape of the measured particle size distribution significantly changes, as it is shown in Fig. 7.6 for different engine loads at 2000 rpm.

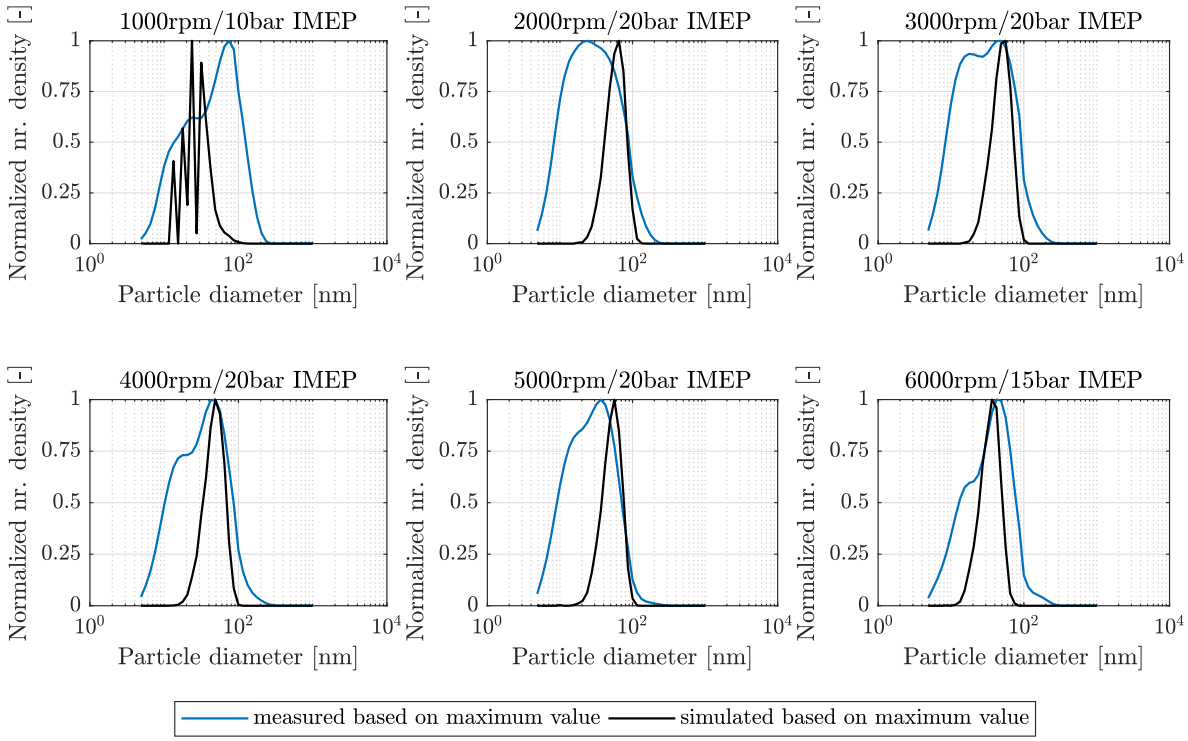

Fig. 7.5.: Comparison between measured and simulated particle size distribution for warm engine conditions in operating map. Results individually normalized by corresponding (measured and simulated) maximum value of distribution.

The number density of small diameter particles increases with a constant nucleation mode diameter, whereas the number of larger particles remains approximately constant and the accumulation mode is slightly shifted towards smaller diameters. This confirms the hypothesis that the injector-induced particle emissions do not further increase at high engine loads, but additional gas-phase inhomogeneities arise. This is in contrast to the results of the 3D-CFD simulations that are described in Section 5.2. At 2000 rpm/20 bar IMEP, no mixture inhomogeneities were identified by statistical evaluation of the 3D-CFD results. However, the 3D-CFD simulations were realised with mean values of several working cycles and do not included cyclic fluctuations. Thus it is possible that only a small amount of working cycles in each cylinder include rich mixture zones. Another possible reason is the evaporation of the liquid injector film that may cause locally rich mixtures in the gas phase, as it is explained by Ketterer et al. [98] for liquid wall films and briefly explained in Section 4.3. Detailed investigations of the mixing process for different engine conditions that include cyclic fluctuations or rich vapour areas near to the injector tip are beyond the scope of this work. It is though possible to investigate the ability of the particle simulation model to cover these mixture-induced effects by re-parametrization.

Therefore, the measured particle size distributions of two representative engine speed and load conditions are divided into mixture-induced and film induced proportions of the total emissions. Different engine speeds were selected to enable the re-parametrization of the homogeneity model with additional Reynolds number information. Calculating the bi-modal size distribution based on the measured total size distribution by regression is not suitable because small changes in the shape of the total PSD leads to large changes in the estimated functions for the bi-modal PSD. Therefore, a fixed particle diameter at 30 nm was chosen approximately to divide the measured PSD. In Fig. 7.7, the corresponding PSD for the investigated operating conditions are shown with the separation of mixture-induced and film-induced particle diameters. It is clearly visible that most of the differences in the size distribution are present below 30 nm. The results of the separation are presented

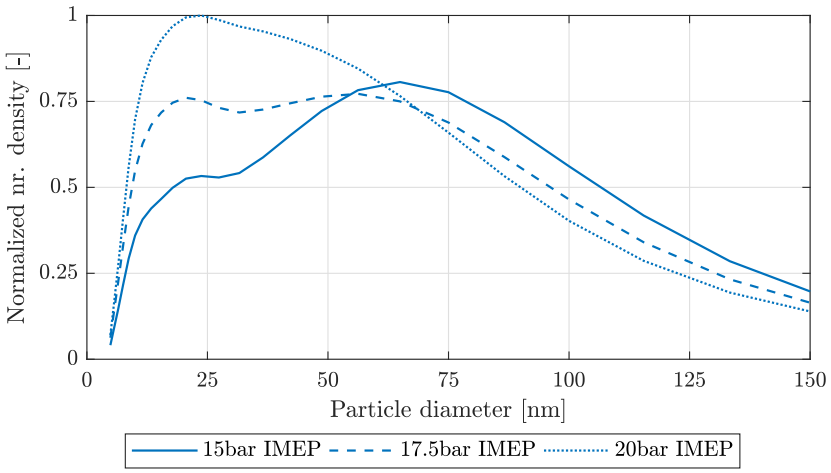

Fig. 7.6.: Measured particle size distribution for different loads at 2000 rpm. Values normalized by maximum number density at 2000 rpm/20bar IMEP

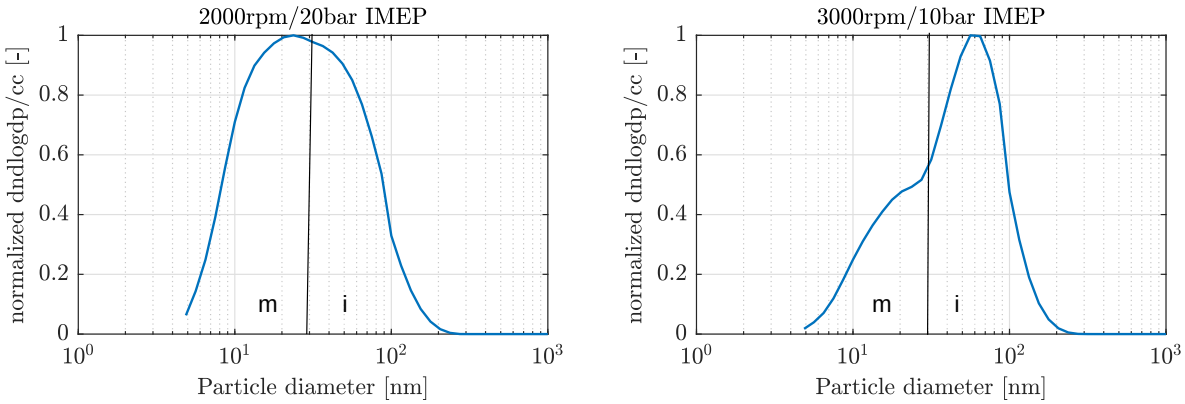

Fig. 7.7.: Measured particle size distribution for different loads at moderate engine speeds. Separation in mixture-induced (m) and injector-induced (i) particle emissions at 30 nm. Values normalized by maximum number density for each operating point.

in Tab. 7.2. At 2000 rpm, about 78% of the total particle number density includes particles above the 30 nm threshold, but 93% of the particle mass (particle mass is calculated by assuming spherical particles with a density of $\rho = 1.8$ g/cm^3). At 3000 rpm, 90% of the particle number and 97% of the particle mass is based on larger particles. With the current model parametrization, the resulting particle emissions are solely caused by the injector film and the corresponding simulation particle size distributions are shown in Fig. 7.8 as dashed lines.

In the re-parametrization process, the error function for number and mass emissions is identical to the injector parametrization method (see also Section 4.4.1). In addition, the proportion of the simulated particles > 30 nm to the total number and mass is calculated and compared with the measured values (see Tab. 7.2). The value is weighted by factor of 10 in order to sufficiently influence the total error value. Hence, the error function does now include particle number, mass and size information. The results of the re-parametrization in terms of particle size distribution is presented in Fig. 7.8 (solid lines). At 2000 rpm/20 bar IMEP, the re-parametrized PSD shows significantly more small particles

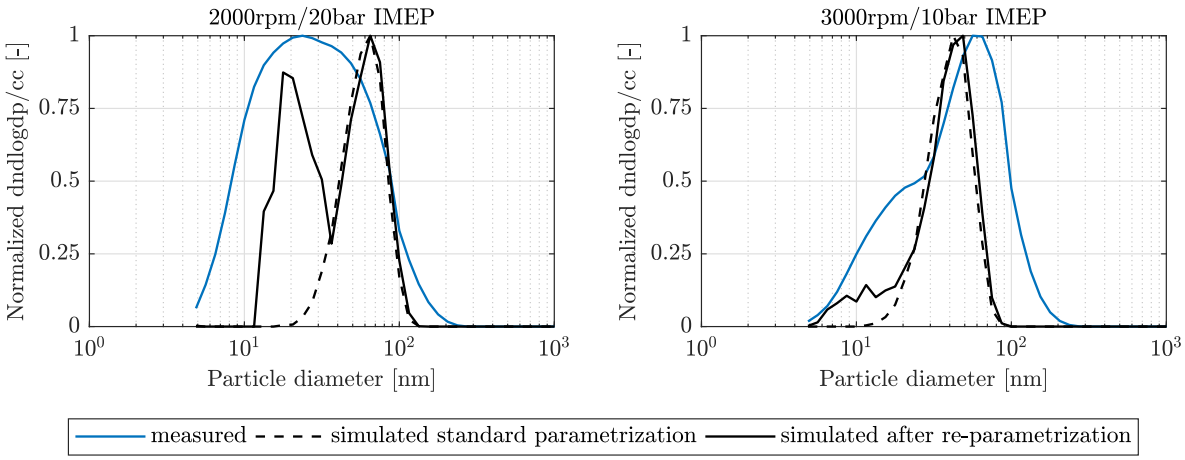

Fig. 7.8.: Comparison between measured and simulated particle size distribution after re-calibration of homogeneity model. Values normalized by maximum number density for each operating point.

that are caused by mixture inhomogeneities. The nucleation mode is at about 20 nm and correlates with the measured value. The accumulation mode that is caused by the injector film module is not affected by the re-calibration. At 3000 rpm/10 bar IMEP, the number of particles below 30 nm is only slightly increased. This is plausible because at this operating point, less mixture inhomogeneities are expected. With the new balancing of the simulation modules, 80% of the particle number density and 92% of the particle mass density are caused by injector film at 2000 rpm/20 bar IMEP. At 3000 rpm/10 bar IMEP, the values result in 88% and 95%, respectively (shown in Tab. 7.2).

Tab. 7.2.: Fraction of injector induced particle emissions at different engine speed and loads. Calculation based on particle size distribution (assumption: >30 nm for injector induced emissions).

	2000/20	3000/10
PN:	78% (80% sim)	90% (88% sim)
PM:	93% (92% sim)	97% (95% sim)

Besides the impact on the particle size distribution, the total particle number and mass results are compared to measured data in Fig. 7.9. The particle number results that were slightly underestimated by the original parameter set-up (see Fig. 7.3) are increased after the re-calibration. This leads to an improvement of the overall quality at 2000 rpm, because the particle mass is not influenced by the additional small particles. At 3000 rpm, no changes are visible, which is mainly because of the included

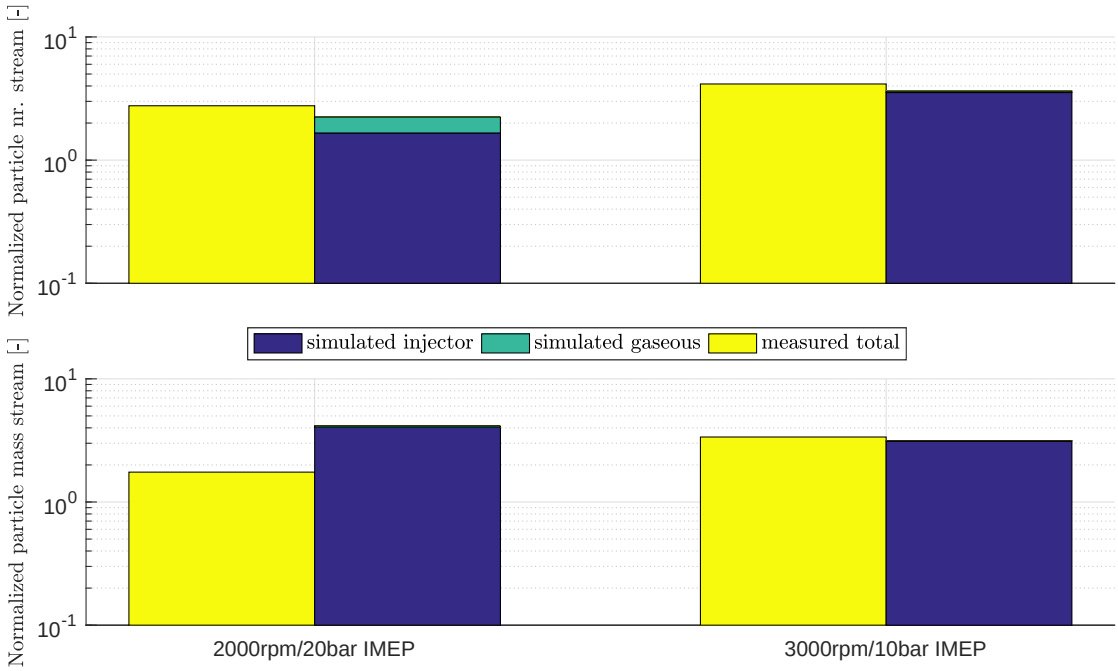

Fig. 7.9.: Comparison between measured and simulated particle number and mass emissions after recalibration of homogeneity model. All values normalized by measured results of 2000 rpm/10 bar IMEP.

counting efficiency that is explained in Section 3.3.2. The counting efficiency is only included for the evaluation of the total particle number and mass results. The consideration of these small particles will be even more important when the counting efficiency of the measurement systems increases for particles below 23 nm.

Summarizing, the simulation model is able to cover both the nucleation and accumulation modes with high concordance if the homogenization module and the injector module are balanced by their contribution to the overall emissions. This is capable by including measured particle size information in the parametrization process instead of solely using 3D-CFD results. The measured particle size distribution indicates that throughout the operating map, mixture-induced particle emissions may occur at high engine loads and low to moderate engine speeds. Further investigations are required to localize the effects that lead to inhomogeneities in the mixture. Possible causes are cyclic fluctuations or rich vapour zones around the injector tip because of film evaporation.

7.1.4 Cold Engine Conditions

The engine temperature was changed by applying coolant water at a reduced temperature to investigate the behaviour at cold conditions. With the available measurement setup, minimum coolant water temperatures of about 40°C were realisable. At higher engine speeds, the temperature increased up to about 50°C because of a limited cooling capacity. In Fig. 7.10 and Fig. 7.11, the results for particle number and mass emissions are presented at different engine speeds and loads. The simulated results are divided into the specific module components that represent mixture-induced, injector-induced and wall-film-induced soot particles. The operating conditions that were used for parametrization of the wall film module are marked by black dots. The parametrization of the injector module and the homogeneity module is not changed.

The simulated mixture-induced particle emissions are comparable to the results at warm engine conditions (see Section 7.1.2 for further explanations). The injector-induced emissions dominate at all

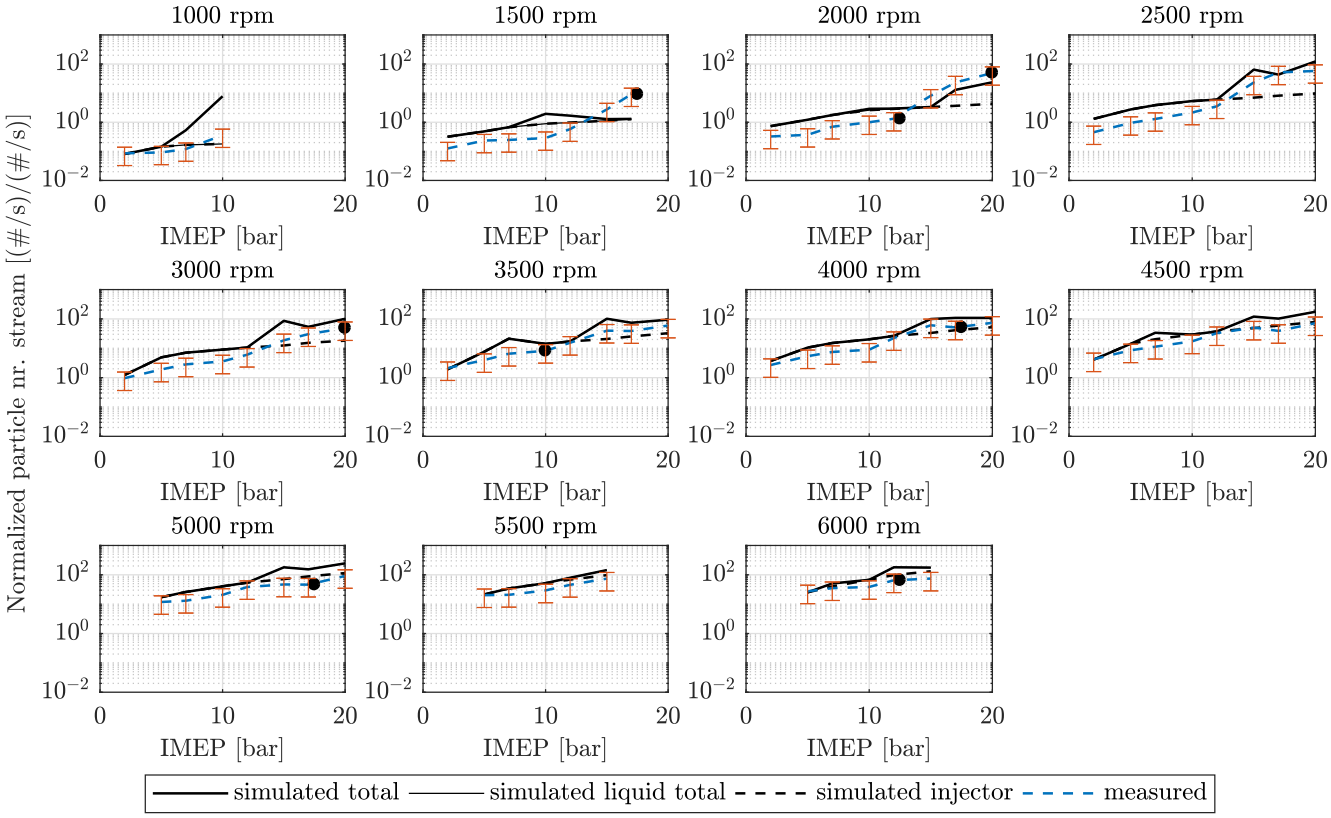

Fig. 7.10.: Comparison between measured and simulated particle number emissions for cold engine conditions in operating map. Operating points that were used for parametrization marked by black dots. All values normalized by measured results of 2000 rpm/10 bar IMEP.

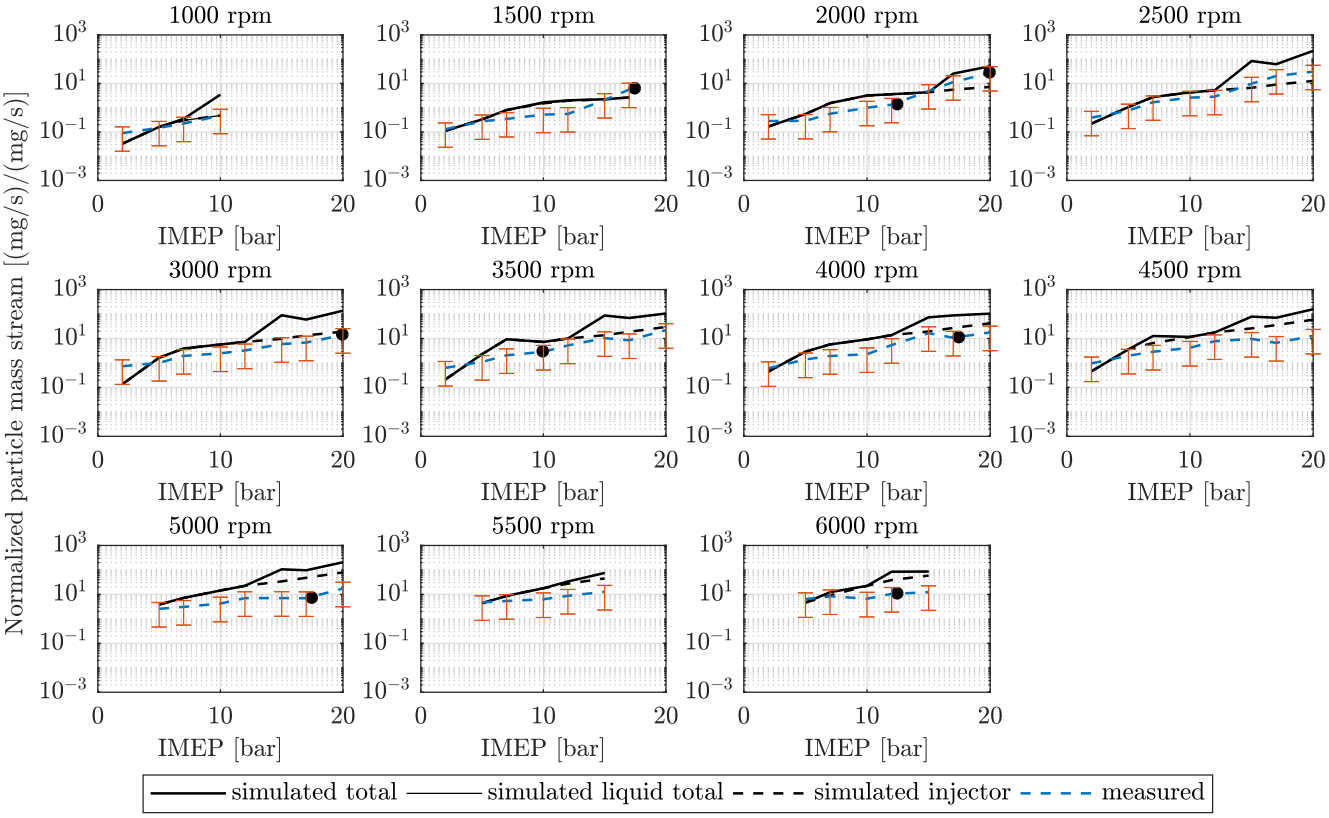

Fig. 7.11.: Comparison between measured and simulated particle mass emissions for cold engine conditions in operating map. Operating points that were used for parametrization marked by black dots. All values normalized by measured results of 2000 rpm/10 bar IMEP.

engine speeds for moderate load conditions up to approximately 10-15 bar IMEP. It is noticeable that the particle number and mass emissions are over-predicted by the simulation in this area of the operating map compared to the measured data. This is further explained by comparing the measured values at warm and cold operating conditions.

In Fig. 7.12, a contour plot is presented that includes the increase of measured particle emissions at cold conditions compared to warm conditions. Light blue to yellow colours indicate that the total emissions increase at cold conditions. The dark blue colour represents areas with decreased emissions. It is noticeable that the emission level at cold conditions is lower than at warm conditions at all speeds and moderate loads. Presuming that the injector film is dominant in this area leads to the conclusion that the injector conditions must have been changed between the two measuring series. This leads to a different film creation or evaporation behaviour that affects the emissions. Obviously, This is not captured by the simulation model because the parametrization of the injector module was not changed. It is thus not possible to compare the absolute values between simulation and measurement data in this area of the operating map.

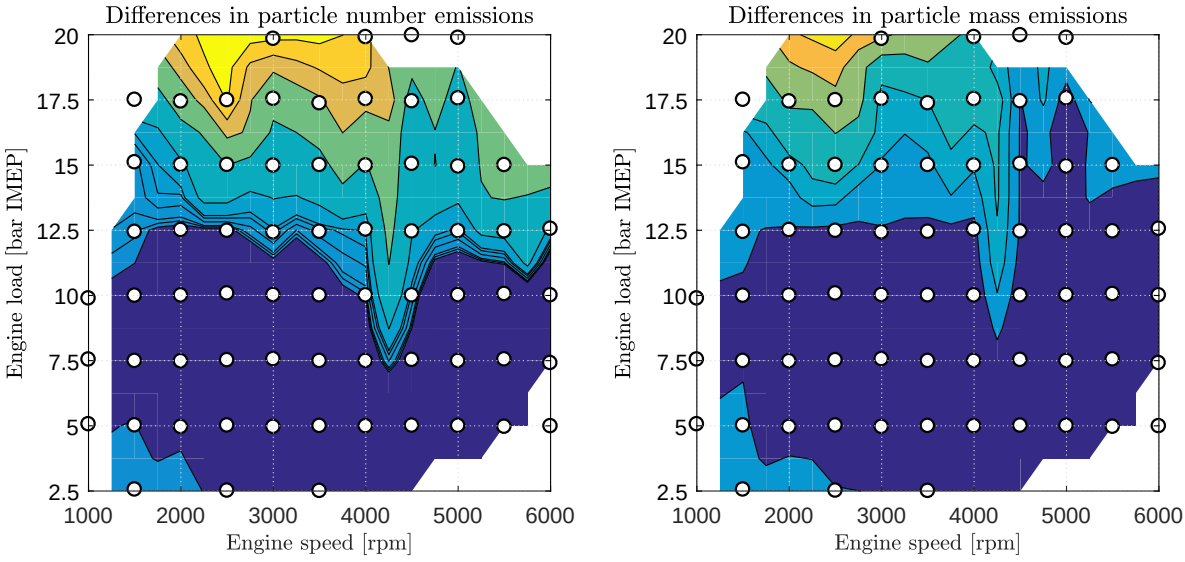

Fig. 7.12.: Absolute differences in measured particle number and mass emissions for warm and cold operating conditions. Contour plot represents total increase in emissions for cold operating map. Light blue to yellow colours indicate increase of total emissions at cold conditions. Dark blue colour represents decrease in total emissions at cold conditions.

However, the main subject of the investigation at cold operating conditions is to evaluate the wall film influence on the particle emissions. This effect is clearly visible at high engine loads by a significant increase in the measured overall emissions. The effect decreases at higher engine speeds, which correlates with the increased engine temperatures in this area. The simulated particle number emissions from the injector film are not sufficient to cover this increase at low engine speeds. Instead, the wall film module is capable to close the gap with a good overall agreement (see Fig. 7.10). An exception is point 1500 rpm/17.5 bar IMEP, at which no wall film is simulated. At small engine speeds and low engine temperatures, the injection time is set to an early value by the default engine parametrization. This leads to an spray impact on the piston. Because of the simulated piston temperature and the parametrization of the SWI module, this wall film evaporates before start of combustion.

At high engine speed and load, the particle results are already over-predicted by the injector model, as it is explained in Section 7.1.2. It is thus difficult to compare the absolute value of the emissions to the measured data because the effects can not be separated by the measuring system. Instead, the proportion of the wall-film-induced particles can be evaluated with respect to the total emissions for the

simulation results. This is presented in Fig. 7.13 for particle number and mass values. Comparing the

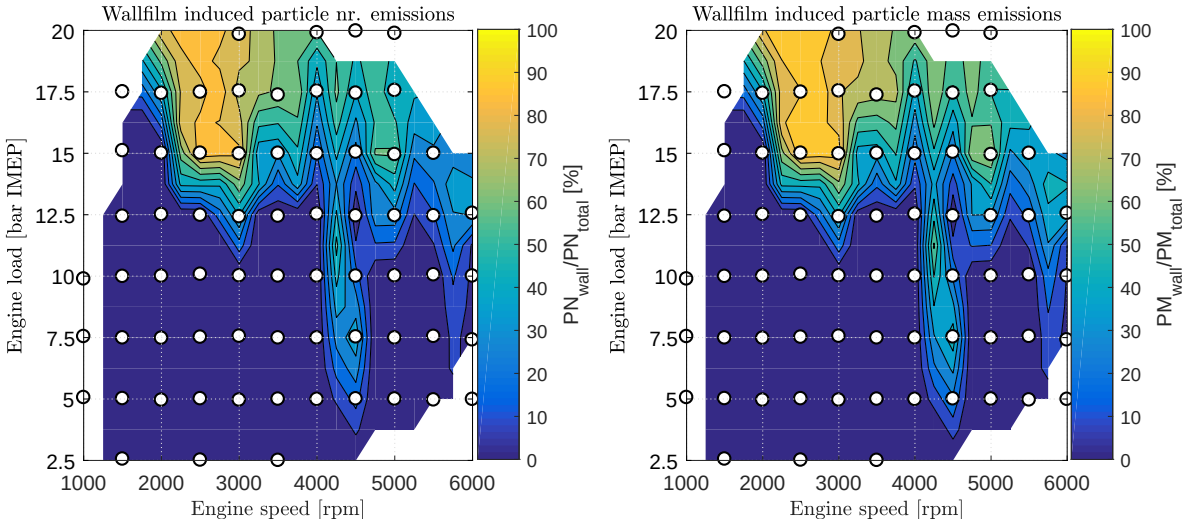

Fig. 7.13.: Simulated fraction of wall-film-induced particle number and mass emissions compared to total values at cold engine conditions.

contour plot with the measured increase of emissions at cold conditions shows clear coincidences across the entire engine map. The simulated areas that are dominated by the wall film emissions correlate well with the measured areas that show a significant increase in the total emissions. The reduced impact of the wall film at higher engine speeds also matches the measured differences. Therefore, the qualitative results of the wall film module within the engine operating map show a good overall agreement.

However, the complexity of the overall model increases because of the combination of the different sub-modules. This leads to higher absolute deviations when comparing the simulation to measured values because the errors of the specific modules are superimposed. This now leads to an overprediction of the particle number and mass results throughout the operating map at cold conditions.

Analogously to the warm engine map, the shapes of the measured and simulated PSD functions are compared. The simulated values again are divided regarding the three applied modules. The results are shown in Fig. 7.14 at four operating points. To enable a comparison to warm conditions, the same operating points were chosen that are presented in Fig. 4.10 for warm engine operation. The distribution function is normalized by the maximum value of measured particle emissions and overall simulated particle emissions, respectively.

The shape of the 10 bar IMEP size distribution is similar at warm and cold conditions. This is expected because the injector wall film dominates this area.

In contrast to the measurement results of the warm engine map, the relative portion of the nucleation mode only increases slightly at the 20 bar IMEP operation. The accumulation mode keeps the dominating contributor to the total emissions. Since these operating conditions are expected to include mixture inhomogeneities, wall film mass and injector film mass, the shape can be explained by the relative proportion of each contributor. Since the physical mechanisms of formation are equal for wall film and injector-induced particle emissions, this again leads to the conclusion that the wall film dominates the overall emissions in this case and the increase of mixture-induced emissions is of less importance at cold conditions.

The simulated shape of the injector and wall-film-induced emissions at the 20 bar IMEP operation is equal because the pyrolysis reactions are modelled in the same way. The position of the accumu-

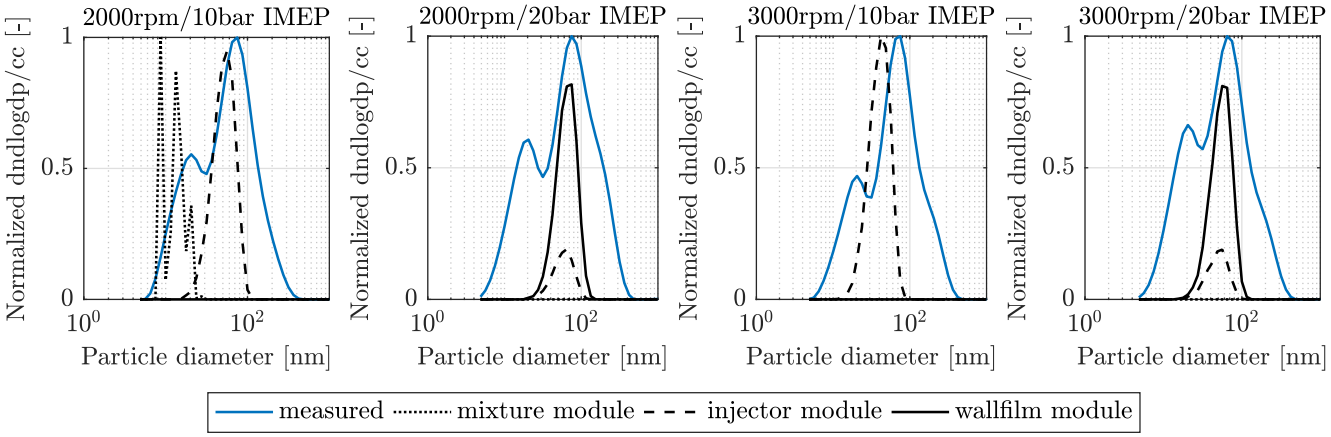

Fig. 7.14.: Measured and simulated PSD at cold engine conditions. Measured and simulated PSD based on corresponding maximum number density value for each case. Due to normalization, the size distributions can only be compared qualitatively between measurement and simulation.

lation mode again is represented correctly. With the present parametrization, the simulation model does not cover the mixture inhomogeneities at high load and low speed. The simulated mixture inhomogeneities that are visible at 2000 rpm/10 bar IMEP result from a slightly delayed injection time at cold conditions by default engine parametrization. This reduces the available mixing time and hence leads to rich mixture zones. The measured and simulated results at 3000 rpm, that are also shown in Fig. 7.14, have a comparable behaviour. Due to the higher calculated homogenization rate at 3000 rpm, no mixture inhomogeneities are calculated at this engine speed.

7.2 Parameter Variations at Stationary Operating Points

7.2.1 Warm Engine

An engine parameter variation is performed to examine the sensitivity of the particle simulation model on actuator settings. The simulated particle number and mass stream results are compared to measured data qualitatively and quantitatively. Additionally, the proportions of the corresponding modules are presented. The base operating point for the variations is set to 2000 rpm/10 bar IMEP at warm engine conditions. This operating point already accurately matches the measured data in the overall engine map. In contrast to the engine operating map measurement series, all engine actuator settings are kept constant except of the investigated values. This reduces the risk of transversal effects that are caused by the ECU. In the following, an injection time variation, ignition time variation, rail pressure variation and engine speed variation is presented. All shown results are normalized by dividing the measured and simulated values by the measured base operating point value for particle number and mass stream, respectively.

Injection Time Variation

At the base operating point (SOI = 300°CA bTDCf), the simulation underestimated the particle number emissions by about 40 % (shown in Fig. 7.15), which is inside the confidence boundaries that were already explained in Section 7.1.1. The particle mass nearly perfectly matches the measured values. The simulated particle emissions are completely formed by the injector module, which is the expected behaviour at this operating point.

Early injection values increase the available evaporation time at the injector tip, leading to reduced particle emissions. This effect is also visible in the measurement series. Although it is expected that the spray hits the piston at early injection time, the resulting wall film completely evaporates until start of combustion. Late injection times lead to an increase of the injector-induced emissions, but also cause mixture inhomogeneities beyond the soot threshold in the simulation. Therefore, the amount of simulated mixture-induced particle emissions start to increase at SOI = 263°CA bTDCf. In contrast, the measured emissions remain nearly constant or are reduced. This is not plausible

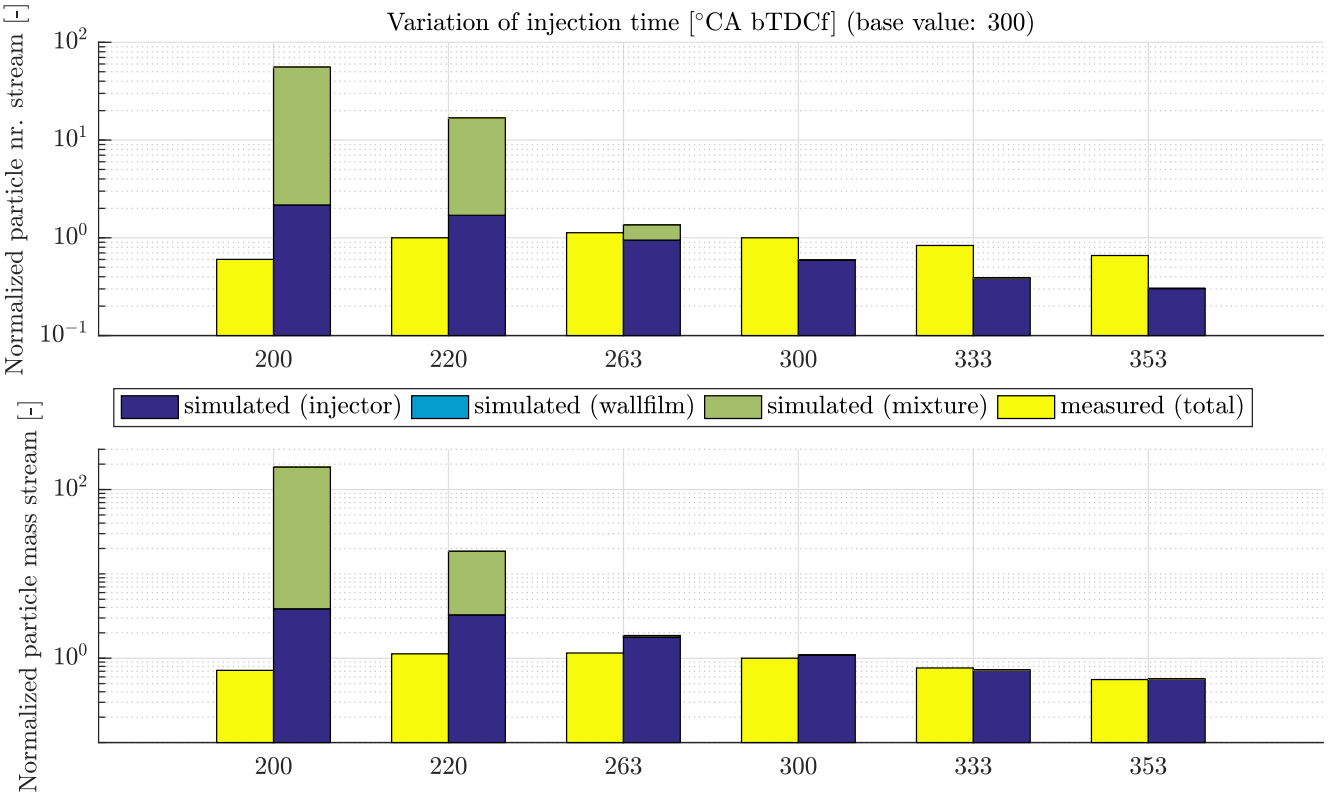

Fig. 7.15.: Injection time variation at 2000 rpm/10 bar IMEP. All values based on measured data at 300 °CA bTDCf.

because of the reduced mixing and evaporation time. In Section 3.4.2, it is explained that the measuring position for particle number and mass is set downstream of the three-way catalyst. At late injection time values, the measured engine out (upstream of three-way catalyst) hydrocarbon emissions significantly increase, which is an indicator of an inhomogeneous combustion process. The resulting hydrocarbon emissions are then oxidized in the three-way catalyst under exothermic conditions. In Tab. 7.3, the corresponding hydrocarbon emissions and catalyst structure temperatures are presented. Due to the hydrocarbon oxidation, the gas temperature in the catalyst also increases. This may cause an oxidation of the particle emissions in the global stoichiometric exhaust stream. Therefore, the measured and simulated particle emissions can not directly be compared for these late injection times.

Tab. 7.3.: Additional engine parameters for injection time variation at 2000 rpm/10bar IMEP.

Injection time [°CA bTDCf]	200	220	263	**300**	333	353
Total hydrocarbon emissions [ppm]	772	701	497	481	474	477
Temperature inside catalyst [°C]	724	702	696	677	683	688

Ignition Time Variation

Changing the ignition time mainly influences the combustion process. A delayed ignition time increases the temperature during expansion and in the exhaust system. In the presented parameter study, the exhaust temperature increases by about 100 K from 15° CA to 5° CA bTDCf. The combustion temperatures that were calculated by the engine process simulation differ up to 200 K. This leads to a reduction of measured particle number emissions by about 30 % (shown in Fig. 7.16). This behaviour is in agreement with the literature (see Section 2.2.3). The simulation model also responds to the thermodynamic changes and the simulated number emissions are reduced by about 20 %. The trend is also visible for particle mass emissions. Note that the increased evaporation time at the injector tip is not sufficient to cover this change in emissions (simulated injector film at ignition time is only reduced by about 7 %). Rather, the change is due to the reduction of soot precursor formation (pyrene) at higher temperatures.

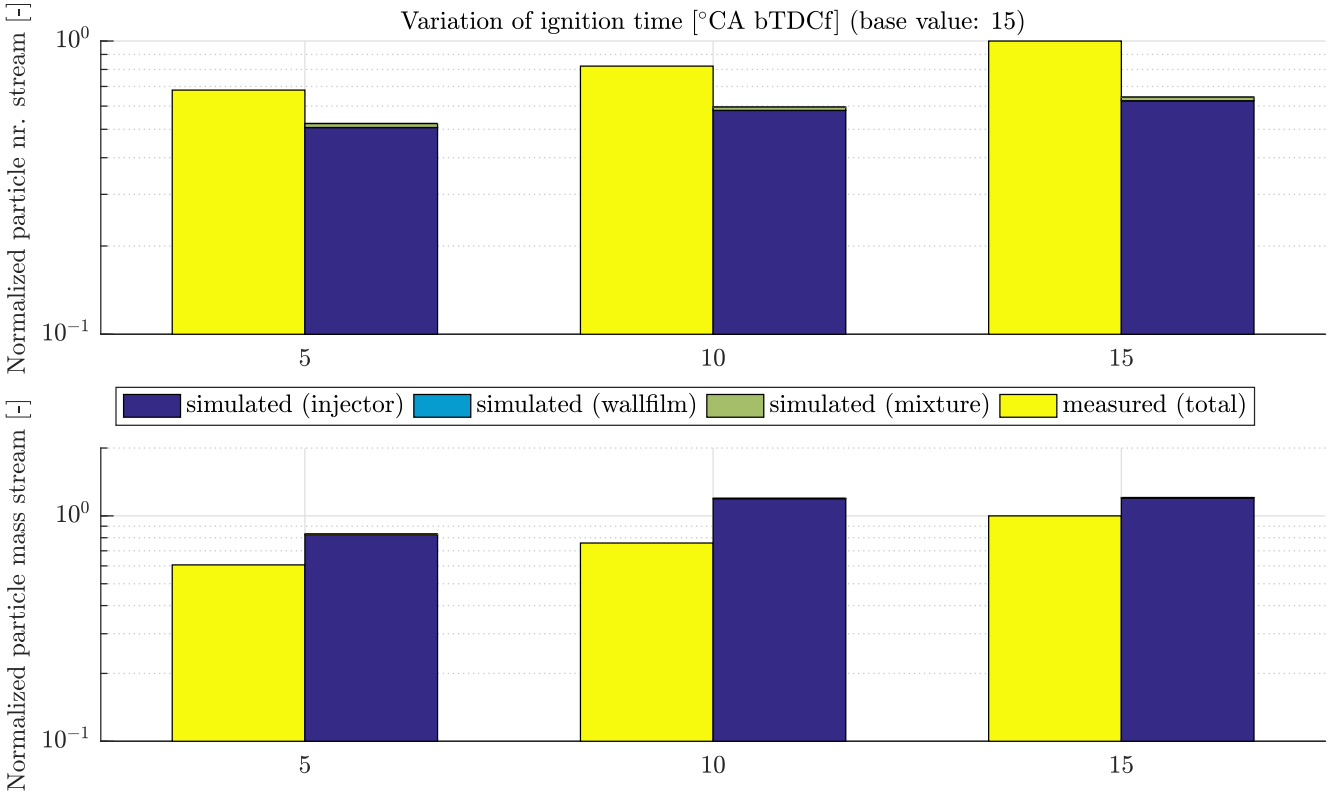

Fig. 7.16.: Ignition time variation at 2000 rpm/10 bar IMEP. All values based on measured data at 15 °CA bTDCf.

Rail Pressure Variation

Changing the rail pressure in a direct injection engine leads to a complex sequence of influences on particle emissions. The injection duration is increased in case of a reduced rail pressure. This leads to an increase of the created injector tip film and reduces the available evaporation time. Additionally, the available mixing time in the gas-phase decreases. Finally, the rail pressure affects the spray characteristics and the droplet diameter. At decreased rail pressure values, the droplet size grows and the required spray evaporation time increases.

The increase of particle number emissions at reduced rail pressures matches well between the simulation and the measured values (shown in Fig. 7.17). The measured values increase up to 235 % of

base emissions, the simulated particle number emissions increase up to 285 %. For the considered rail pressure variation, the simulation results are a combination of injector-induced and mixture-induced emissions. This is caused by the increased injection duration that affects the homogeneity and injector module.

Increasing the injector pressure to 250 bar significantly changes the measured particle number results. This behaviour can not be reproduced by the simulation model mainly because of the simplification in the injector film formation process. In the current modelling approach, the formation process is only depending on injection duration. This is sufficient for most of the given rail pressures, but especially at very high pressures the injector film creation is directly influenced by the spray dynamics (e.g. by removing injector deposits).

Due to the low particle diameter of the mixture-induced particles, the simulated mass only slightly increases at lower rail pressures. In contrast, the measured particle mass increases analogous to the number emissions. This means that the size distribution does not change significantly. A possible explanation of this behaviour is the increase of the droplet diameter. The evaporation time of bigger droplets increases and thus there is a higher risk of wall film creation. This reduces the fuel amount that has to be homogenized in the gas-phase and leads to a different weighting of the particle formation sources. The changes in droplet diameter are not covered by the spray-wall interaction model because of a constant value for the Sauter mean diameter (SMD). To identify the exact area of particle formation, additional optical measurement techniques are required, which is beyond the scope of this work.

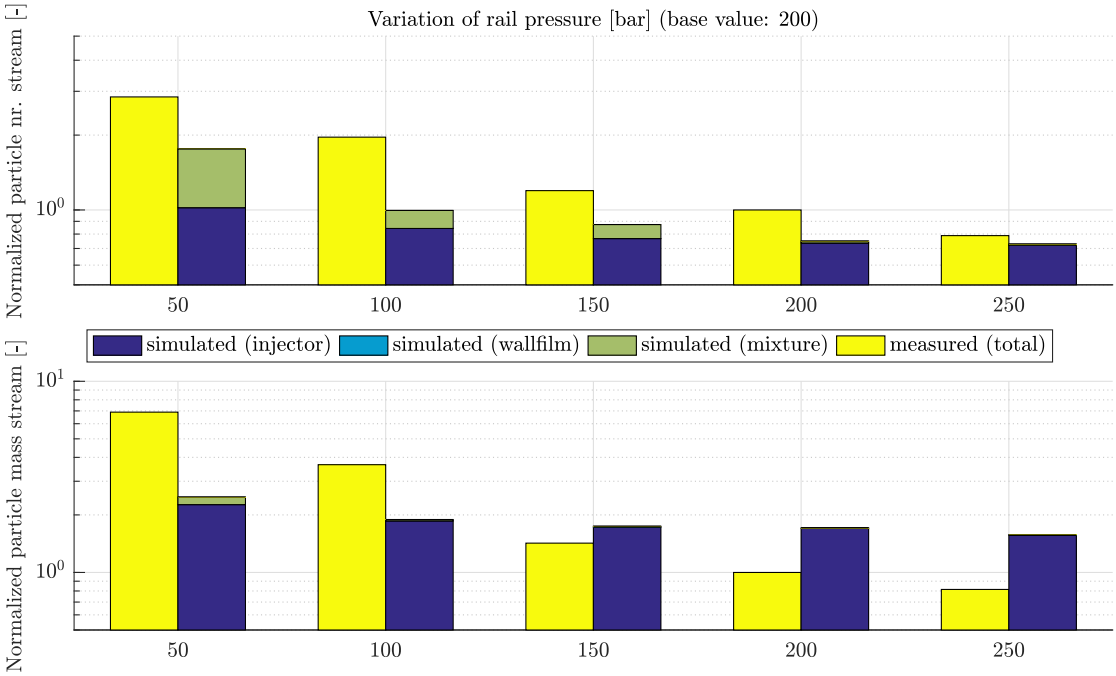

Fig. 7.17.: Rail pressure variation at 2000 rpm/10 bar IMEP. All values based on measured data at 200 bar.

Engine Speed Variation

For this parameter variation, the engine actuator settings are kept constant except the engine speed and the total injected fuel mass. The engine speed is increased and the global equivalence ratio is set to $\phi = 1.1$ for the increased speed values. Therefore, the available mixing time in the gas-phase and the evaporation time for the injector film are reduced. In contrast, the charge motion and turbulence

increases. The results are shown in Fig. 7.18. Due to the high Reynolds number dependency of the homogeneity model, the reduced mixing time and increased total fuel mass is compensated by the speed increase. Thus mixture-induced emissions occur only at 3000 rpm. The majority of the total emission increase is caused by the injector film module.

The particle number results matches the measured values with sufficient agreement. The simulation model generally overestimates the increase at fuel-rich conditions and higher engine speeds. Especially from 4000 rpm to 4500 rpm, the measured values remain constant. This behaviour matches the observations throughout the engine operating map. At higher engine speeds, the injector film evaporation is underestimated by the simulation model because of the temperature-independent evaporation function. The particle mass increase is also overestimated by the simulation results at rich conditions.

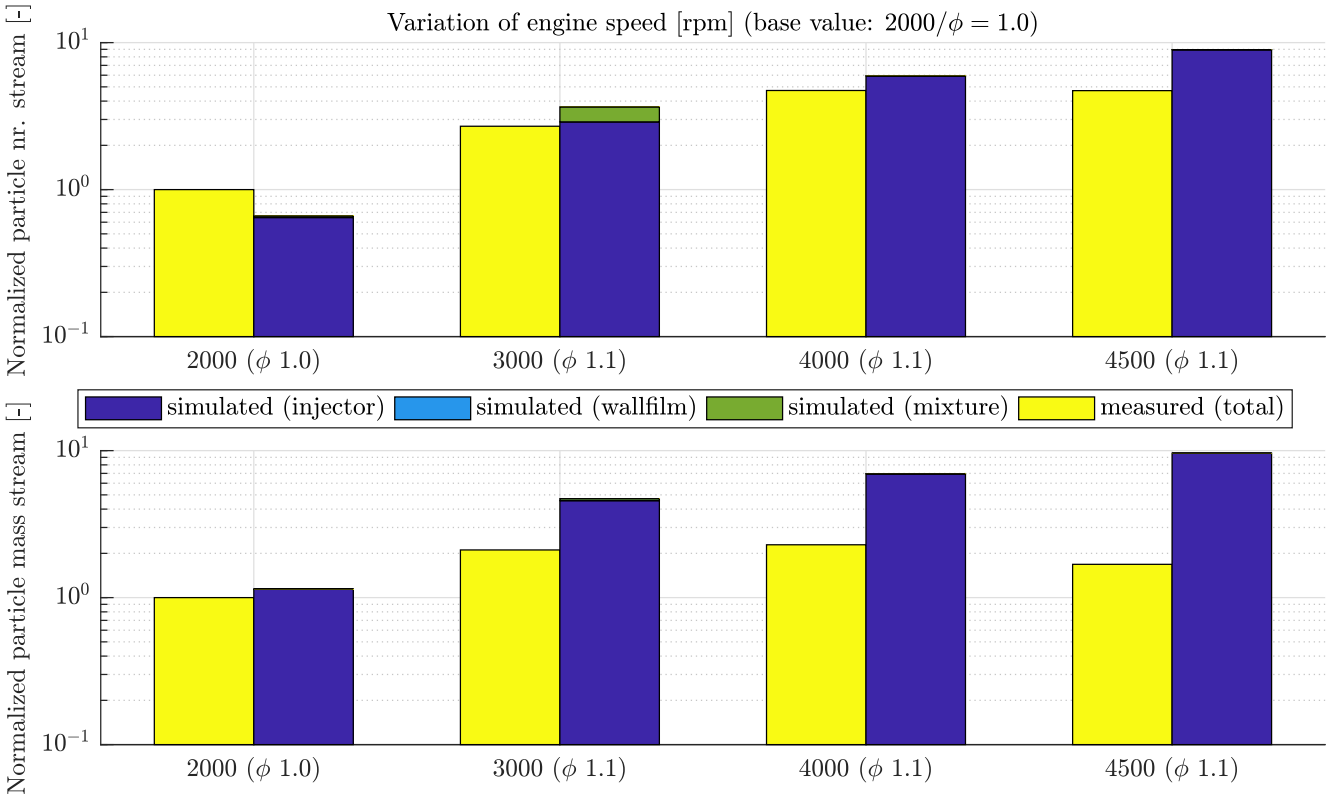

Fig. 7.18.: Engine speed variation with start value at 2000 rpm/10 bar IMEP ($\phi = 1.0$) in combination with EQR variation ($\phi = 1.1$). All values based on measured data at 2000 rpm.

7.2.2 Cold Engine

The parameter variation is performed analogous to the warm engine conditions that are described in Section 7.2.1, but at reduced coolant temperature ($T_{\text{coolant}} = 40\ ^\circ\text{C}$). In the following, an injection time variation and rail pressure variation is presented to investigate the influence of liquid wall film creation at 2000 rpm/10 bar IMEP. The results again are compared to measured particle number and mass stream data.

Injection Time Variation

Changing the injection time value at cold engine conditions leads to the risk of incomplete mixture formation (delayed injection time) or increased piston impingement and resulting wall film formation (early injection time). In Fig. 7.19, the measured and simulated results for particle number and mass emissions are presented for six different injection time values.

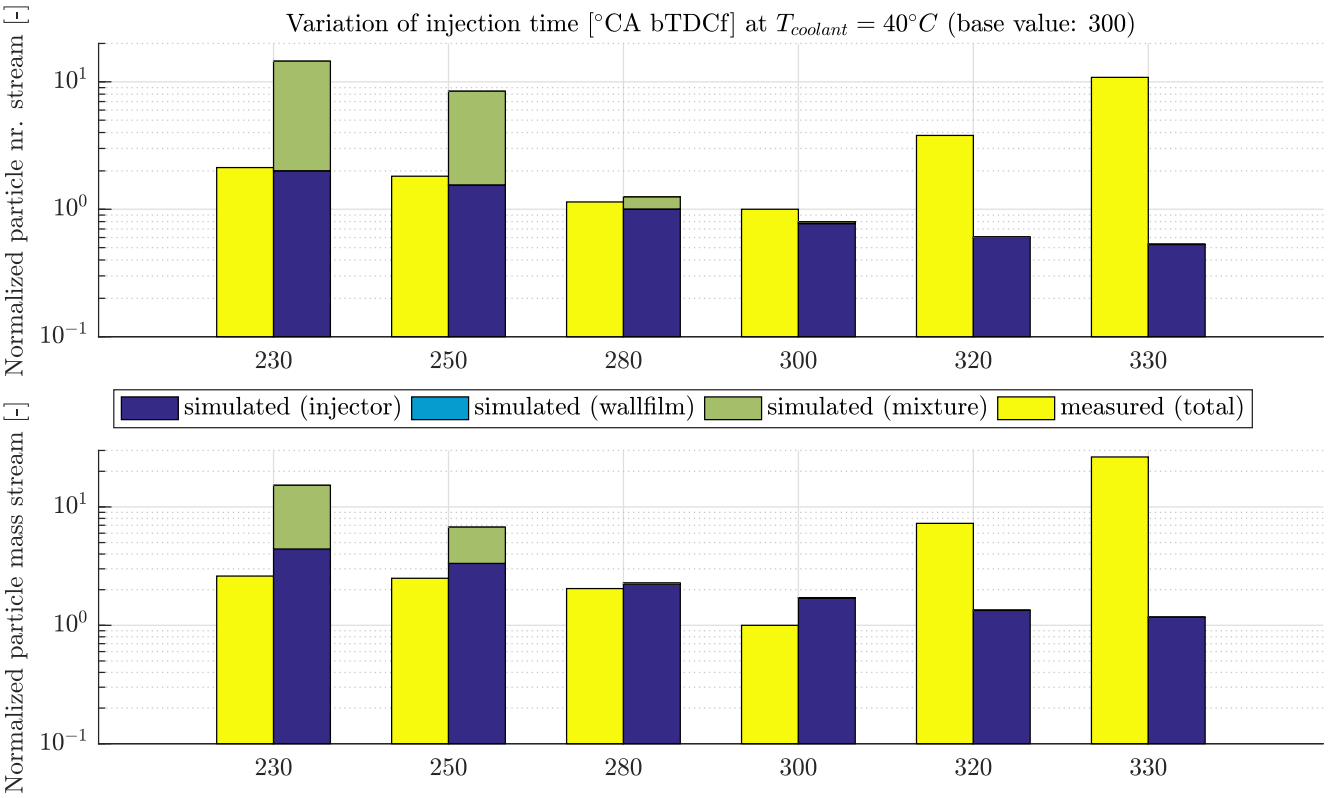

Fig. 7.19.: Injection time variation at 2000 rpm/10 bar IMEP under cold conditions ($T_{\text{coolant}} = 40$ °C). All values based on measured data at 300 °CA bTDCf.

Delaying the injection time clearly leads to an increase in measured particle number and mass emissions. This behaviour differs from the warm engine conditions (see Section 7.2.1). At cold engine conditions, the engine out hydrocarbon emissions likewise increase with delayed injection time because of an incomplete combustion process. In contrast to the warm engine, the three-way catalyst temperature does not reach the values of the warm operating point. This indicates that less particle oxidation reactions can take place in the three-way catalyst. The simulation results resembles the measured values for the injector film module. However, the total emission results are overestimated because of the small particles that are calculated by the mixture homogeneity module. With the given measurement information it can not be determined whether the deviations are due to reactions in the three-way catalyst that affect small particles or because the mixture homogeneity is underestimated by the homogenization sub-module of the simulation.

In contrast to the warm engine conditions (see Fig. 7.15), early injection time values significantly increase the measured particle emissions for this parameter variation. This is a result of the decreased engine temperature in combination with an increased spray impingement on the piston. For the given variation, the simulation does not show this behaviour and the calculated emissions are reduced because of an increased injector film evaporation time instead. However, the simulation model generally does react on the injection time value, as it is shown in Fig. 7.20 (left side). At the base operating value (300°CA bTDCf), a combination of liner and piston wall film is present. Earlier

injection time values lead to a significant increase of the piston wall film mass and an increased total created wall film. Although there is a significant wall film created by the spray, it does not remain until start of combustion because of high evaporation rates (right side). This effect was already observed within the cold engine operating map at low engine speeds and high engine loads (see Section 7.1.4). The reason in these cases is the high sensitivity of the wall film evaporation model on wall temperature and the parametrized film thickness parameter that has already been described in Section 6.5.3.

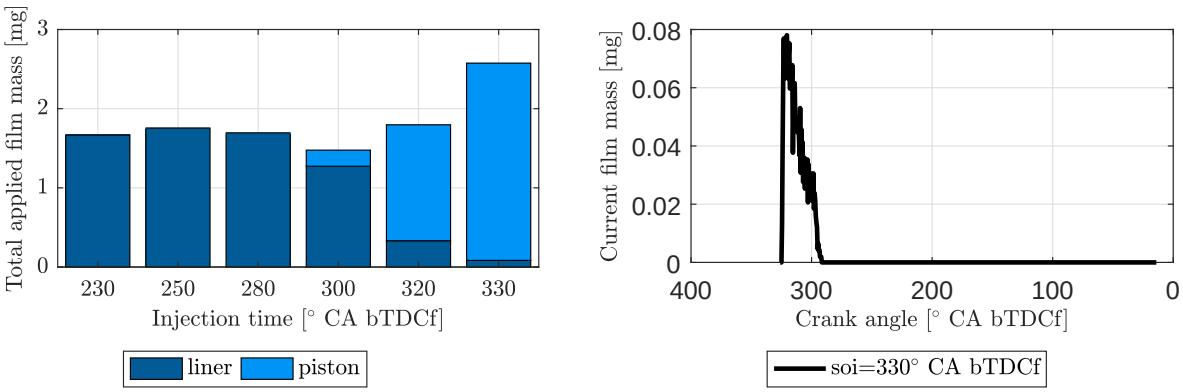

Fig. 7.20.: Simulated film mass for injection time variation under cold conditions ($T_{coolant}$ = 40 °C). Total applied film mass for different injection time values (left). Current film mass (liner and piston) over time for early injection time at 300°CA bTDCf (right).

Rail Pressure Variation

The rail pressure variation at a reduced coolant temperature, presented in Fig. 7.21, shows comparable results to the values at warm conditions (see Section 7.2.1). The particle number and mass emissions decrease at higher injection pressures. In the presented variation, the particle number emissions decrease by about 20 % at 250 bar (12 % in simulation) and increase by about 140 % at 50 bar (220 % in simulation) compared to the base values at 200 bar. The simulation results cover this effect with sufficient agreement with an overestimation of the total number increase. Although there is a reduced engine temperature, no wall-film-induced particle emissions are calculated. The resulting total emissions are a combination of an increased injector film mass and mixture-induced particles. The here presented variation confirms that a combined calculation of different causes of origins is necessary to determine the overall emissions. Solely using the injector module would not be sufficient in this case.

7.3 Transfer To Transient Operation

7.3.1 Engine and ECU Data

In Fig. 7.22, different methods and required input values are presented to simulate the combustion engine in the context of particulate emissions. In the previous chapters, a reduced 1-cylinder engine model was coupled with measured engine test bench data (see also Section 3.4.1). The reduced engine model requires crank-angle-resolved pressure data to calculate the in-cylinder combustion process. In addition, engine actuator settings and thermodynamic properties are measured for each operating point.

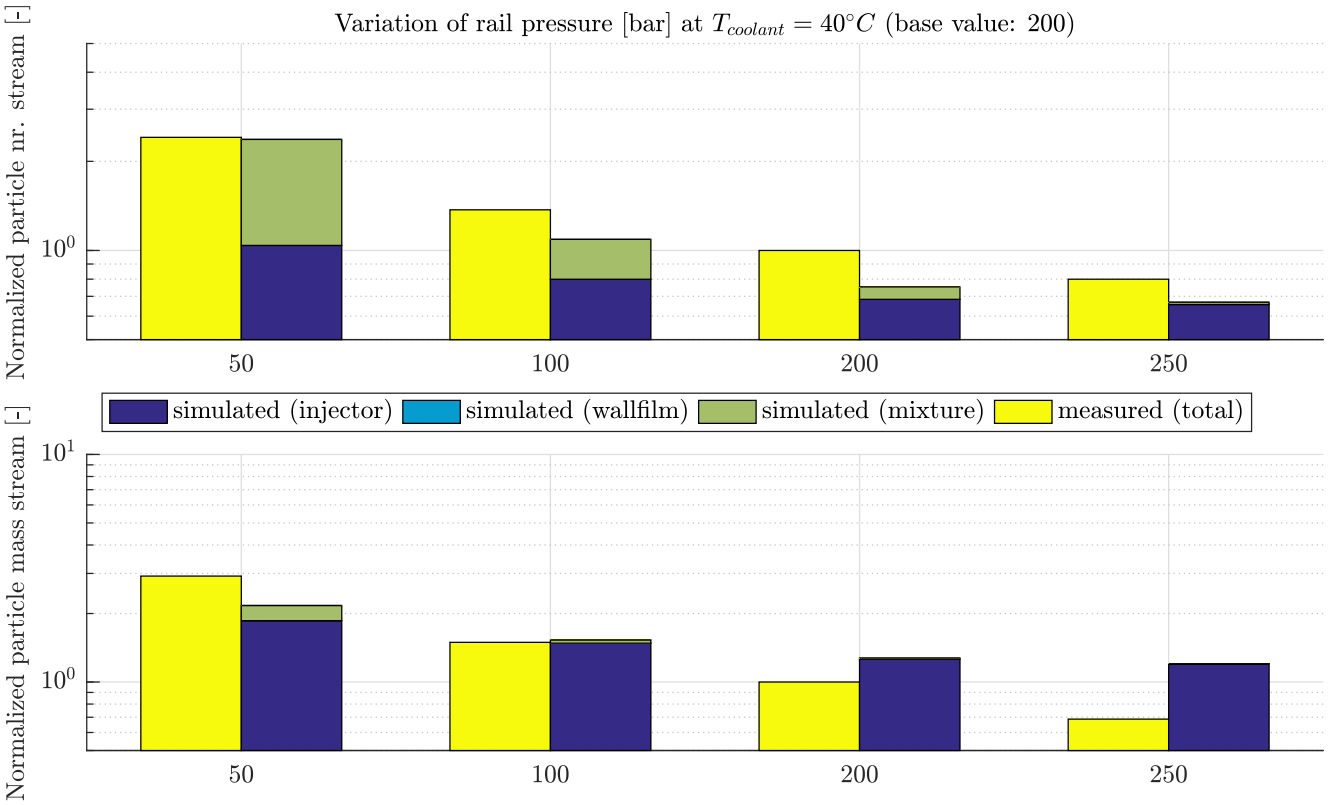

Fig. 7.21.: Rail pressure variation at 2000 rpm/10 bar IMEP under cold conditions ($T_{\text{coolant}} = 40$ °C). All values based on measured data at 200 bar.

The next step towards a transient operation is to expand the engine model. The complete 4-cylinder engine model includes a phenomenological combustion and turbulence model. This enables the predictive calculation of the in-cylinder combustion and pressure data. The simulation results regarding particle emissions need to be evaluated with this model because changes in the combustion process affect the particle model components (see Section 7.3.2 for further explaination). The actuator settings again are taken from measurement data for each operating point, except two values that are calculated by the engine model:

- The total injected fuel mass is calculated by including the measured global EQR value, the stoichiometric air-fuel ratio and the simulated in-cylinder mass.
- The wastegate angle is controlled to match the measured engine brake torque.

Because of these degrees of freedom, the simulated brake torque and the EQR value are used as monitoring variables to evaluate the quality of the engine process simulation in the corresponding driving cycle.

As it is already briefly described in Section 3.4.1, the engine test bench set-up is not changed for investigations at transient operating mode. In contrast to the stationary operation, a time-depending engine torque and speed profile is applied to the engine. The engine actuator and thermodynamic properties are measured time-resolved. The engine model simulates each working cycle in a quasi-stationary manner. The generated results can directly be transferred to the particle model. The simulated particle emission results are then compared to the measured data.

In general, the engine model is not dependent on experimental data to get the required input values. Instead, the engine model can be coupled with a driver controller, a virtual drivetrain and an ECU

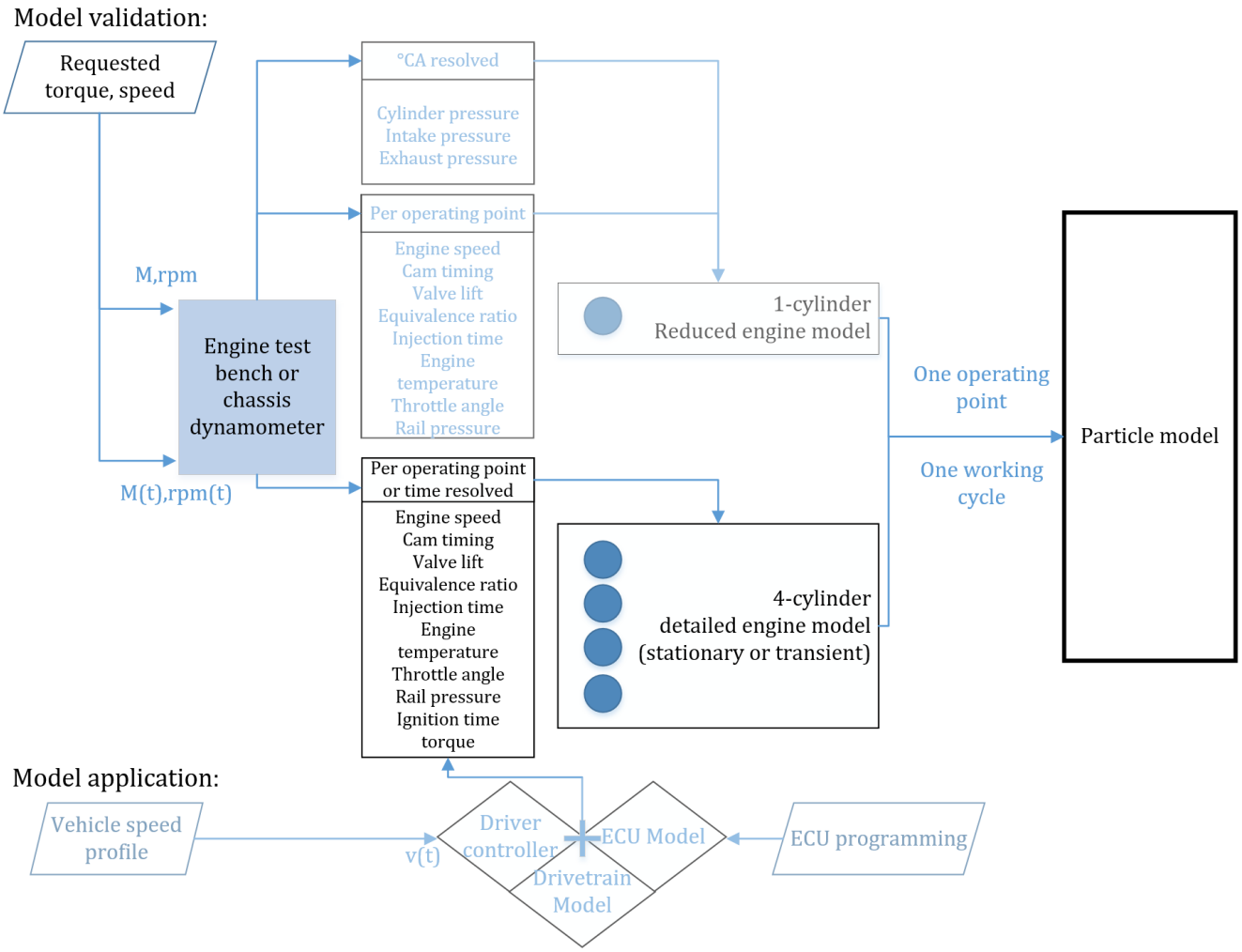

Fig. 7.22.: Overview on required input data of engine model for different operating conditions and model complexities. Transfer to transient operation by extending the engine model and applying time-resolved measurement data to the model.

model. It is then possible to input the requested vehicle speed profile directly without using any measurement system [50, 51].

The driving cycles that are applied to the engine are already explained in Section 3.4.3. In the following, the corresponding measured engine speed and torque values are presented for the highway cycle (Fig. 7.23) and the WLTP cycle (Fig. 7.24).

Due to the generic structure of the highway cycle, a representative area was chosen for simulation ($\approx 160-310$ s). This area includes a constant driving part at moderate engine load, fuel cut-off phases and two major load steps (maximum torque of ≈ 370 Nm). The first load step also includes a engine speed increase (maximum speed of ≈ 4200 rpm).

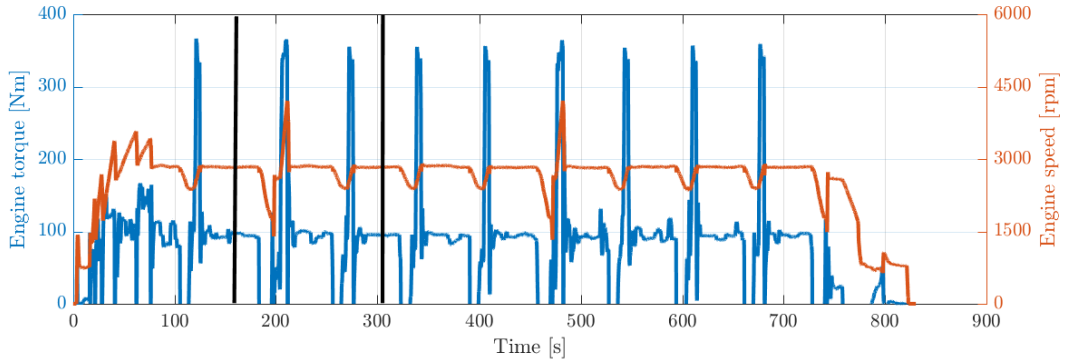

Fig. 7.23.: Measured engine speed and load values for the highway cycle. Engine test bench results. Black lines represent time interval for simulation.

The WLTP cycle does include a number of different load and speed conditions. Two representative areas are chosen for the simulation:

- A time sequence of the highway part ($\approx 1040-1140$ s): This part includes moderate to high engine load values with with moderate to high engine dynamics.
- A time sequence of the urban part ($\approx 130-470$ s): This part includes low to moderate engine speed and load values with moderate to high engine dynamics.

7.3.2 Particle Model

The particle model is designed to be independent of the corresponding engine model environment. Therefore, the required input parameter types are equal for the reduced and detailed engine model and for stationary and transient operation. In the case of time-resolved input data, the particle model calculates each work cycle of the engine in a quasi-stationary way. With additional time step information, the corresponding particle emission results can then be integrated to calculate the overall emissions of a driving cycle.

However, the quality of the input values do change between the different engine models. Especially the combustion process parameters (pressure, burn rate, gas temperature, ignition delay, etc.) change between the reduced engine model and the complete model. This increases the total error chain on the input side of the particle model. Hence, the detailed engine model is first applied to generate the input data for the stationary engine operating map (total number of 76 operating points). As presented in Fig. 7.25, the particle number and mass emissions are compared to the results that are based on the input values of the reduced engine model.

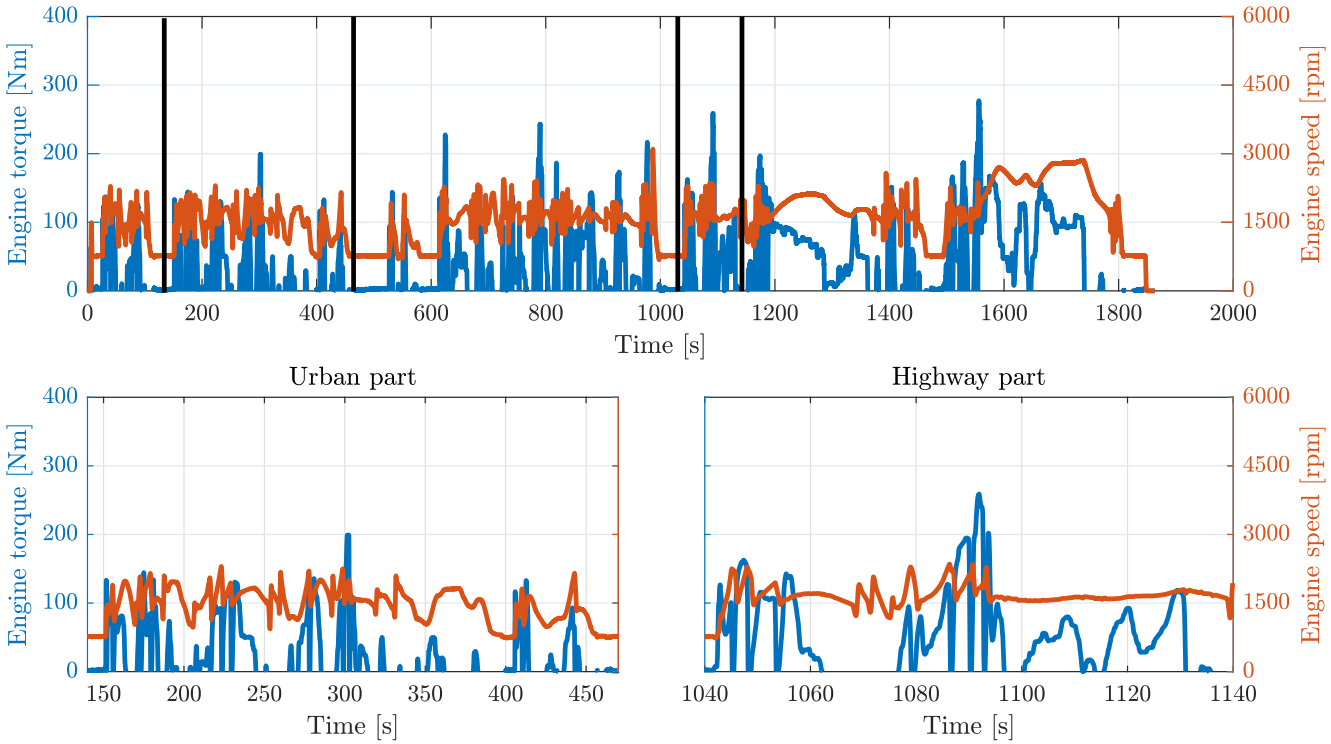

Fig. 7.24.: Measured engine speed and load values for the WLTP cycle. Engine test bench results. Black lines represent time intervals for simulation of urban and highway part.

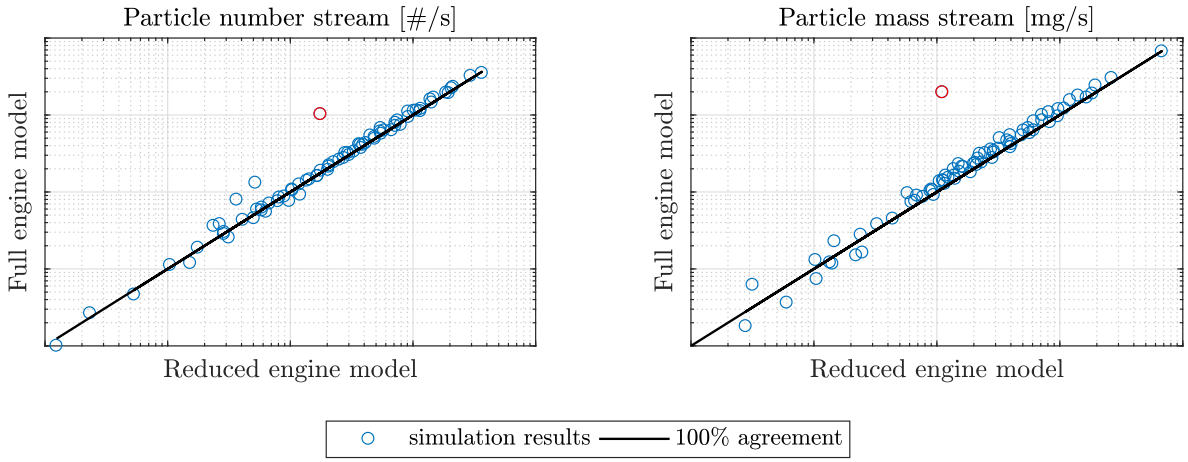

Fig. 7.25.: Comparison between simulation results of reduced engine model and full engine model. Simulated particle number and mass emissions were taken for comparison. Red dot represents 1000 rpm/10 bar IMEP operating point.

The results show that the majority of the particle results agree to a great extend regarding number and mass stream emissions. There are generally only slight fluctuations close to the 100 % agreement value (black line). However, some of the results that are created with the detailed engine model noticeably overestimate the number emissions.

The deviations only occur at low engine speeds up to 1500 rpm and high engine loads and they are solely caused by the mixture-induced zones. The red dot in Fig. 7.25 represents the operating point at 1000 rpm/10 bar IMEP and is further analysed in the following:

- The application of the detailed engine model leads to the calculation of slightly different pressure values upstream of the cylinder because of the more complex gas dynamic calculations. In the considered case, the deviation of the mean pressure value over one work cycle is approximately +6 %.
- The pressure deviations cause an increased air mass in the cylinder. The fuel mass is thus also higher to match the correct global equivalence ratio.
- The increased total air and fuel mass affect the calculation of the parameters E (+1 %) and A (−5 %) of the homogeneity model (see also Section 5.1.2). This leads to a slightly decreased mixture homogeneity at ignition time.

The resulting mixture homogeneity function is shown in Fig. 7.26. The high sensitivity of the particle model on the equivalence ratio value in the mixture-induced zones (that is described in Section 5.4.2) causes the final deviation in the particle emission results.

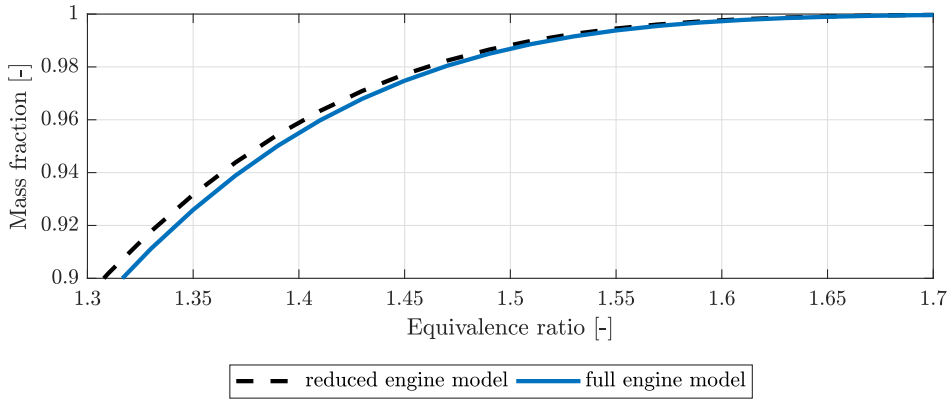

Fig. 7.26.: Calculated mixture homogeneity function at 1000 rpm/10 bar IMEP for different engine models.

The particle simulation framework is designed to calculate the complete information about particle number, mass and size distribution. This is achieved by coupling a Monte-Carlo method (program SWEEP [144]) to the simulation process, enabling the calculation of a complete stochastic particle ensemble (see also Section 3.1). This method will be used primarily in the next section to compare the simulated emission results to measured values.

Although the complete model is parametrized for this method, it is possible to deactivate the Monte-Carlo part to reduce the total calculation time by approximately 40 %. In this case, the included method of moment (MOMIC) is not only used to calculate the species sink terms. Instead, the moments are exported to calculate particle number and mass information. However, the calculation of the formation and growth rates differ between the two methods and thus the deviation of the results has to be compared. In addition, the method of moments does not offer the possibility of including the counting efficiency (50 % at 23 nm) into the results because no size information is given. However, a consideration of the counting efficiency is necessary when comparing the results with the CPC

measuring system. In Fig. 7.27, the results of the method of moments and the Monte-Carlo simulation are presented for all available operating points of the engine map. The total number of particles

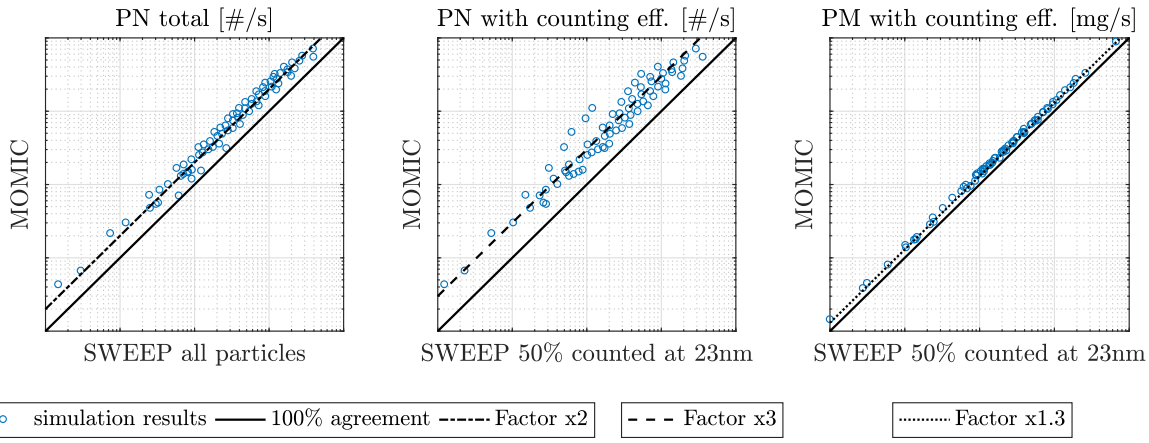

Fig. 7.27.: Comparison of particle results between coupled SWEEP and MOMIC calculation and MOMIC only. Counting efficiency can not be applied directly to MOMIC because of missing PSD values.

that is calculated by the method of moments shows a fairly constant deviation to the Monte-Carlo results with only small fluctuations (left picture). The deviation can be approximated by setting a factor of two on the Monte-Carlo results. This is caused by lower coagulation rates in the method of moments. The fluctuation and deviation is even increased when the counting efficiency is taken into consideration (middle picture). The deviation can be approximated by a factor of three now.

The particle mass results do not heavily change if the counting efficiency is included because the mass is mainly caused by large particles (right picture). The particle mass results match fairly well because the nucleation and surface growth rates are similar for the two methods. The deviation can be approximated by a factor of 1.3.

The results of the comparison show that it is recommended to include the Monte-Carlo method for the transient operating mode, especially because of the consideration of the counting efficiency. In case that calculation time is of special interest, the method of moment values needs to be corrected by a factor of three (particle number) or 1.3 (particle mass), respectively. As a consequence from these observations, the quality of the simulation results is evaluated exemplarily for the highway part of the WLTP cycle in the next section.

7.4 Transient Results

7.4.1 Highway Cycle

The quality of the engine process simulation is evaluated by comparing measured and simulated values for engine brake torque and global EQR (described in Section 7.3.1). In Fig. 7.28, the results are presented for the investigated sequence of the highway cycle. The very high agreement compared to the measured values shows that the cylinder mass and air-fuel-residual gas composition and the simulated combustion process lead to a correct estimation of the cylinder pressure. Therefore, the quality of the engine process is sufficient to include the results into the particle simulation framework.

Time-resolved values for particle mass and number stream emissions are presented in Fig. 7.29. In the simulation, a distinction is made between the use of a coupled Monte-Carlo / method of moments

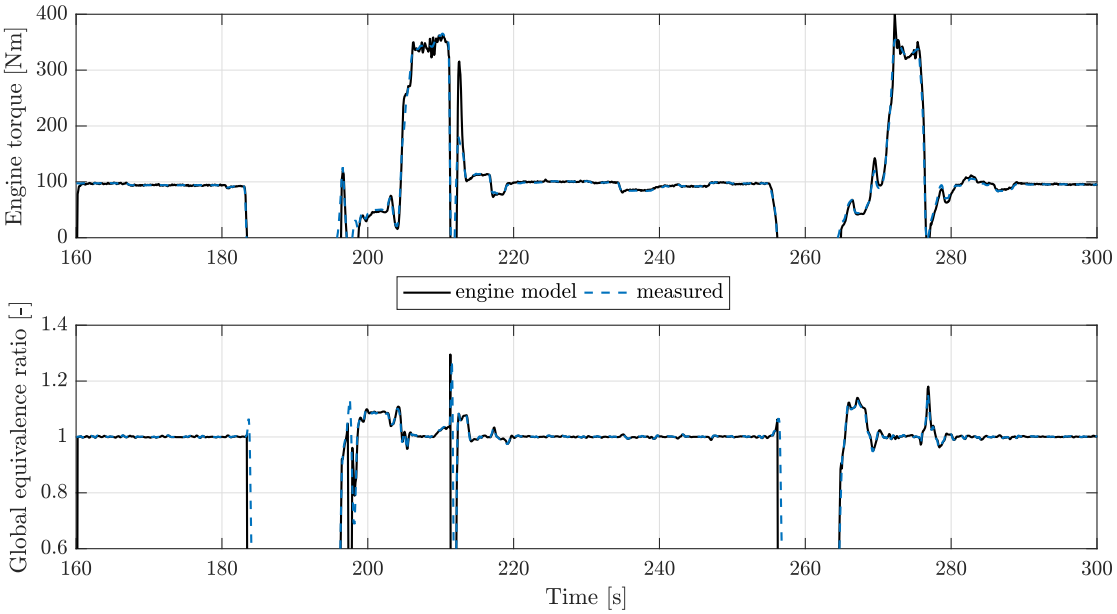

Fig. 7.28.: Highway cycle - comparison between measured values and engine model results for engine brake torque and global equivalence ratio.

simulation (i.e. the complete model) and the exclusive use of the method of moments (corrected by a factor that is described in Section 7.3.2).

Generally, a sufficient agreement is achieved both for the constant driving part of the sequence and the two load steps. The corrected method of moments results underestimate the particle number values of the complete model, whereas the particle mass values are consistent with the Monte-Carlo results.

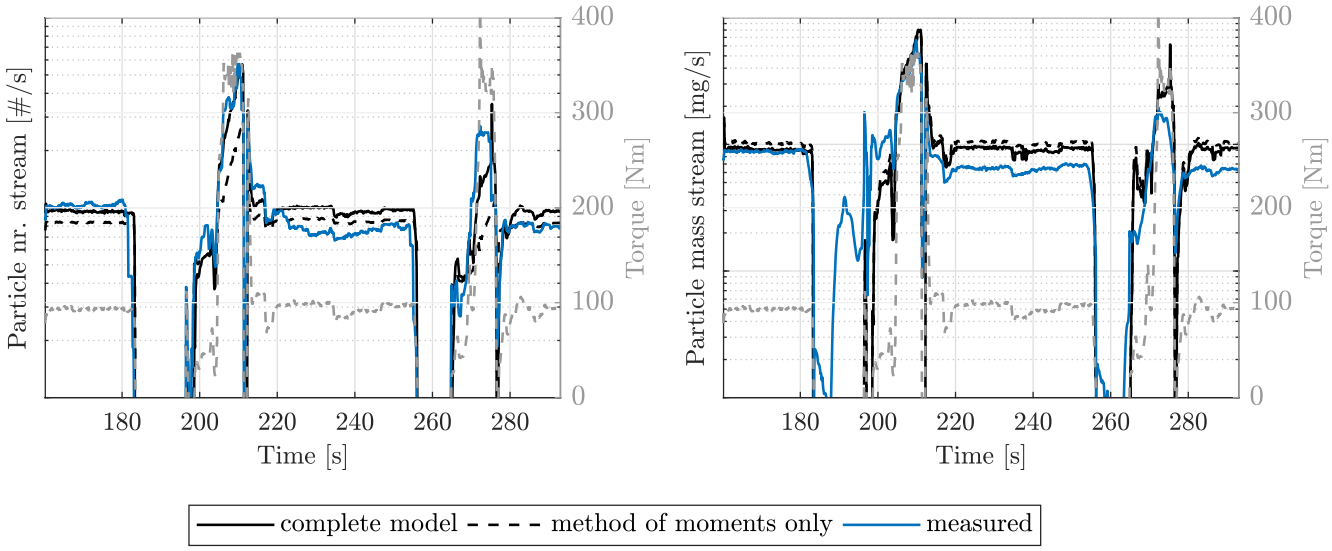

Fig. 7.29.: Comparison of simulated and measured time-resolved particle number and mass stream emissions for highway cycle. Simulation results with (method of moments) and without (complete) calculation time reduction.

The agreement also confirms that this transient cycle can be simulated by a quasi-stationary method with an independent calculation of each work cycle. In addition, it confirms that the engine state did not significantly change between the stationary and transient operating mode. An estimation of the

overall agreement is possible by by the integral emission value over the investigated sequence, as it is shown in Fig. 7.30.

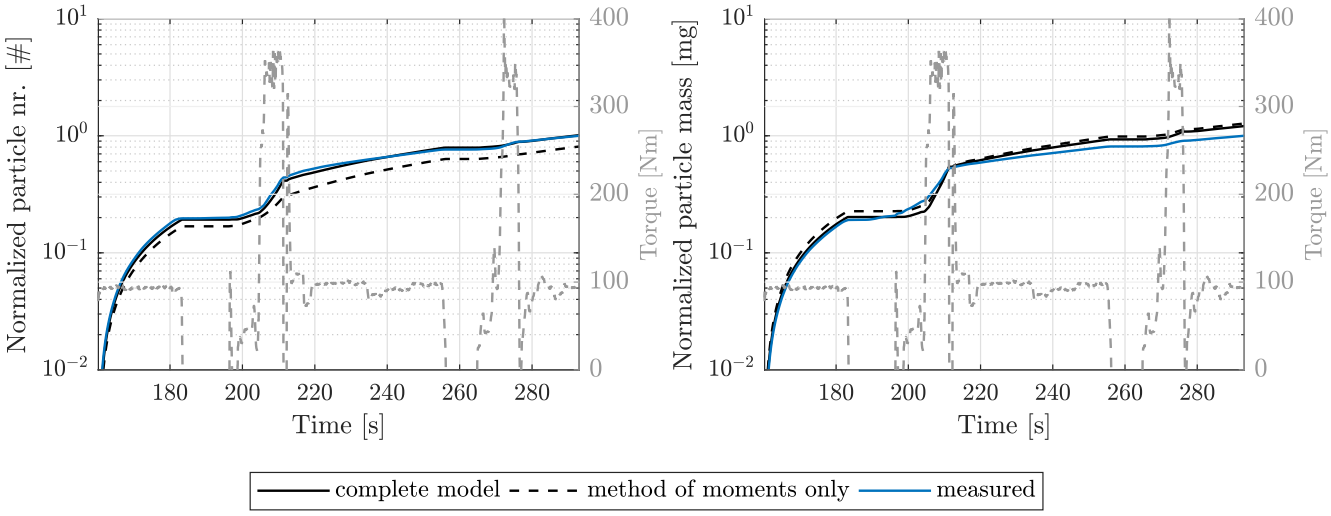

Fig. 7.30.: Comparison of simulated and measured integral particle number and mass emissions for highway cycle. Simulation results with (method of moments) and without (complete) calculation time reduction. All values normalized by maximum measured value.

The overall emissions that are simulated with the complete simulation model almost perfectly matches the measured results in this sequence. The total deviation of the reduced simulation model yields 22 % regarding particle number emissions. This confirms the recommendation to use the full model for the transient calculation.

For the investigated sequence of the highway cycle, none of the calculated emissions comes from liquid wall films because of the high engine temperatures. In addition, only a negligible proportion of the calculated emissions is based on mixture inhomogeneities because of the engine speed (approximately 2000−3000 rpm). Instead, the overall emissions are solely based on the injector tip module of the simulation framework that has been parametrized with satisfying results for the engine operating map.

The stationary operating points that matches the presented engine load and speed range of the highway cycle showed very high accordance to measured data in the stationary operating mode. In addition, the sensitivity of the injector module is mainly limited to the pressure profile (see also Section 5.4.2), which is calculated by the engine process simulation to a great extent. This explains the good overall quality of the presented transient sequence. However, the results are not only based on calibrated values, because the engine torque during the load step is higher than the measured stationary operating points and thus represents an extrapolation. Due to the physically based injector module, the results during the load step also matches the measured values.

7.4.2 WLTP Cycle

Highway Sequence

The engine process simulation results of the WLTP cycle highway sequence are presented in Fig. 7.31. The simulated engine torque nearly perfectly covers the measured data. The engine torque is overestimated for a few seconds after high load requests because of the wastegate controllers response behaviour.

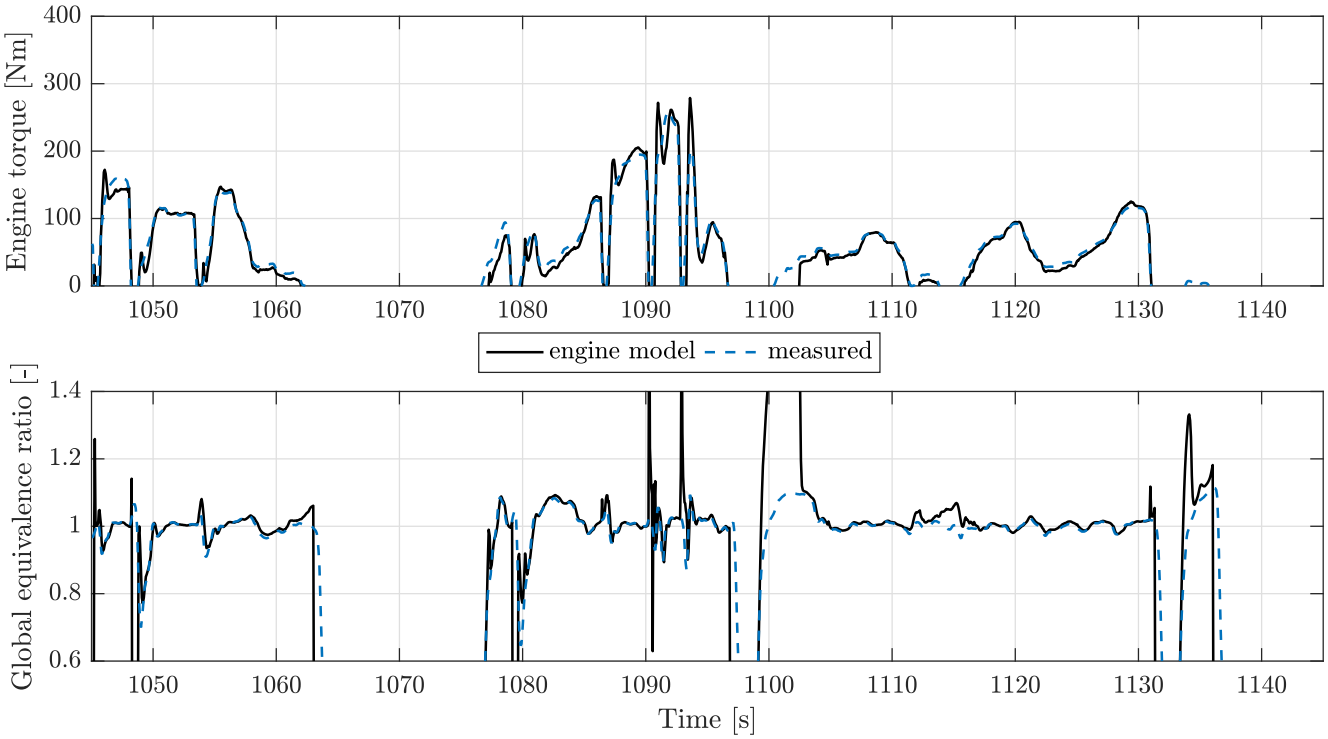

Fig. 7.31.: WLTP cycle highway part - comparison between measured values and engine model results for engine break torque and global equivalence ratio.

The global equivalence ratio also matches the measured results for most parts of the cycle. There are some deviations at low to negative engine torque under fired conditions (fired coasting mode). During these driving conditions, a low trapped air mass and high residual gas mass fractions are present in the cylinder because of the cam timing and low valve lifts. This leads to the simulation of an incomplete combustion process and high unburned hydrocarbons in the exhaust gas. Therefore, the calculation of the injected fuel mass is over predicted and the total equivalence ratio is fuel-rich. However, due to the low exhaust mass flow rates and the low total injected fuel, these operating conditions are not assumed to be relevant for the total particle emissions of this sequence.

The time-resolve particle number and mass stream results are presented in Fig. 7.32. Generally, the simulation model reacts on the dynamic load steps in a correct way. Compared to the results of the highway cycle, the simulation has larger deviations and constantly overestimates the measured values. The main contributor to the emissions again is the injector module. One exception is visible by a particle number peak at 1101 s, where the mixture-induced emissions are dominant. This is caused by the fuel-rich equivalence ratio at these time steps. Due to the high sensitivity of the mixture-induced particle number concentration on the equivalence ratio, the overall value at this time step is very high despite a low exhaust mass flow rate. All other results are not influenced by this effect.

The integral values are presented in Fig. 7.33 to identify the influence on the total emissions of this sequence. These values also illustrate that the number and mass emissions are overestimated by the simulation. However, it is clearly visible that the simulation shows the correct trend. This becomes obvious when applying a constant factor of 1/1.6 on the simulation results. The behaviour indicates that the injector tip formation process is reduced by permanent changes of the engine state. This hypothesis is examined in the following on the basis of the urban sequence of the WLTP cycle.

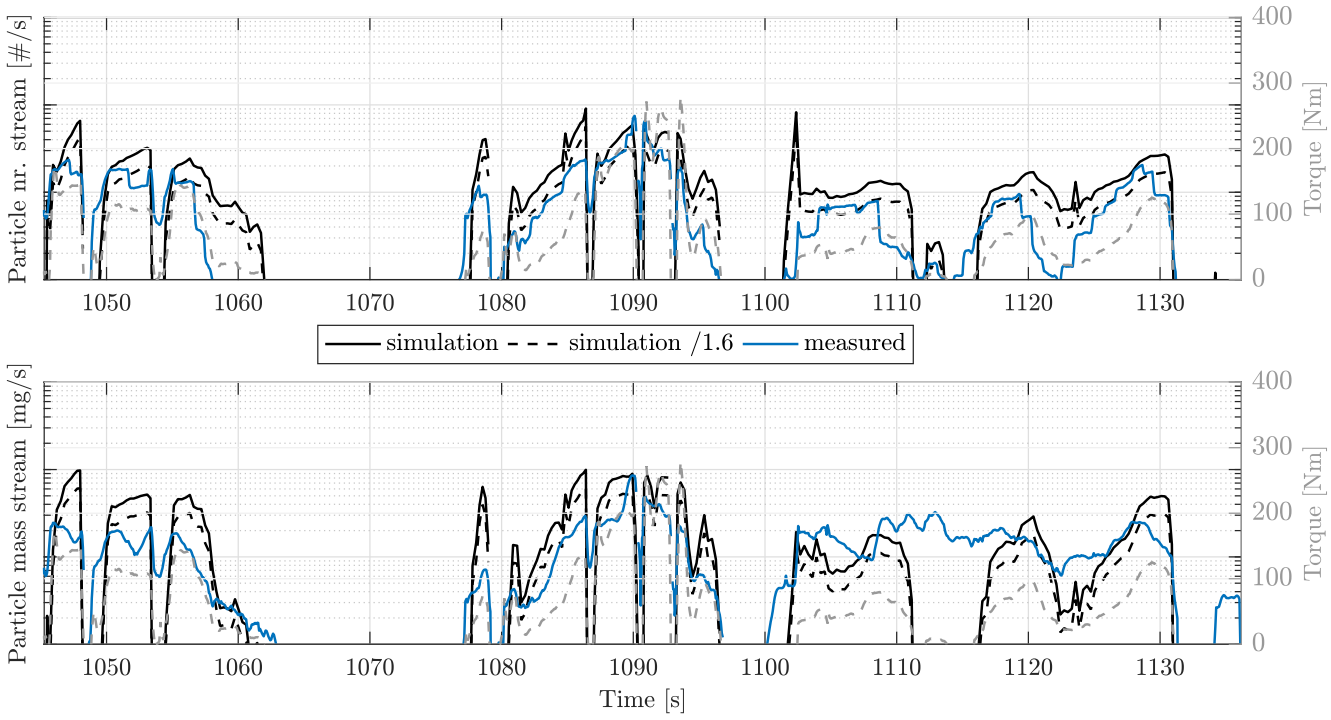

Fig. 7.32.: Comparison of simulated and measured time resolved particle number and mass stream emissions for WLTP cycle (highway part). Simulation result offset visualized by dashed line (factor of 1.6).

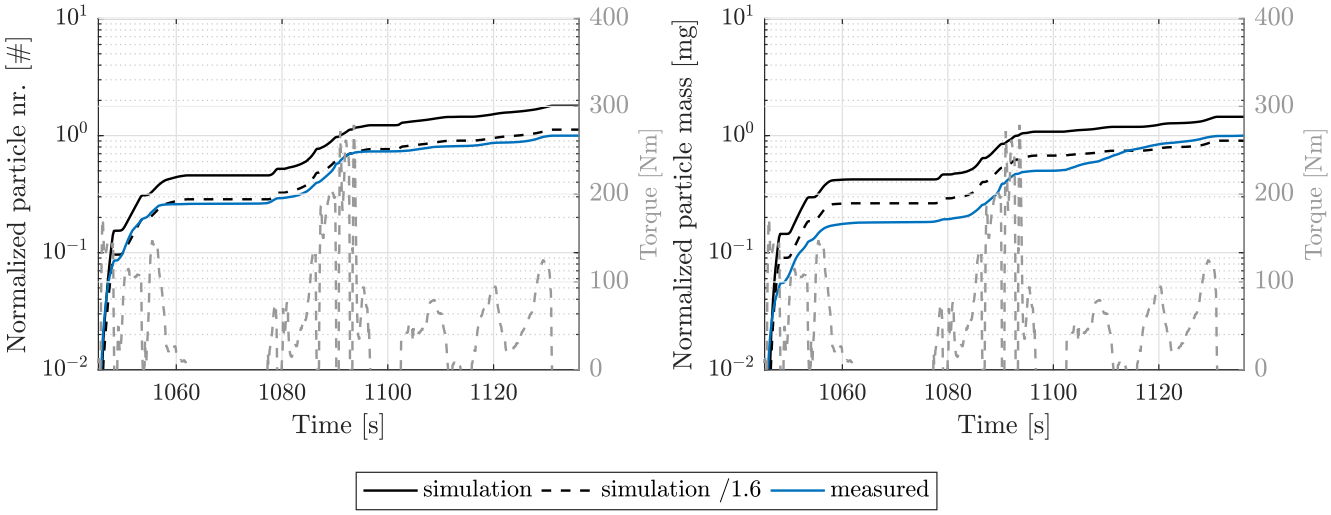

Fig. 7.33.: Comparison of simulated and measured integral particle number and mass stream emissions for WLTP cycle (highway part). Simulation result offset visualized by dashed line (factor of 1/1.6).

The results of the urban sequence are consistent with the previously presented highway sequence results. In Fig. 7.34, the engine torque and equivalence ratio is presented. The engine torque matches

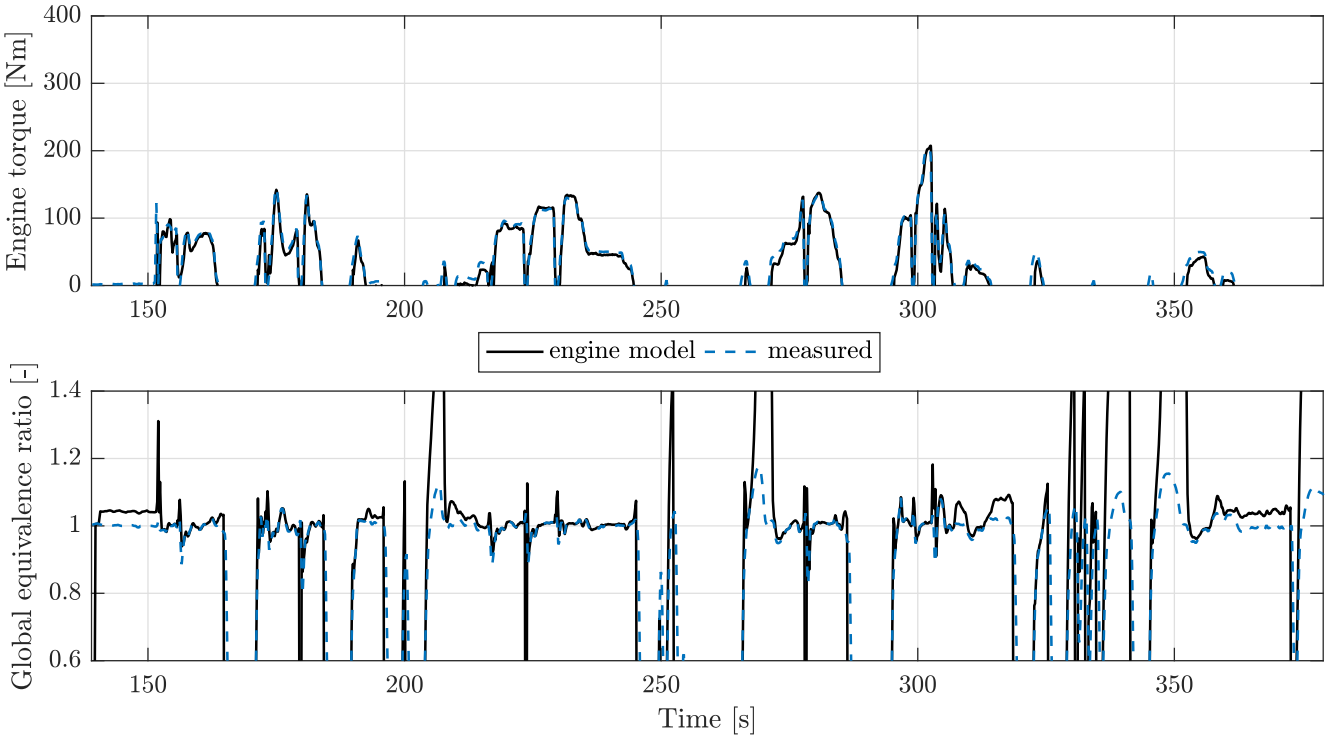

Fig. 7.34.: WLTP cycle urban part - comparison between measured values and engine model results for engine break torque and global equivalence ratio.

the measured values with almost perfect agreement. The simulated global equivalence ratio shows numerous time steps at which a fuel-rich mixture is calculated. This again is caused by high residual gas fractions and low to negative engine torques. The urban sequence includes more of these engine states than the highway sequence. Therefore, the effect on the mixture-induced particle emissions has to be evaluated for this case.

The time-resolved emissions are presented in Fig. 7.35. A qualitatively agreement is visible for the number and mass emissions, but the absolute values are overestimated by the simulation. In the urban sequence, the number of work cycles that are dominated by mixture-induced number emissions is increased because of the global equivalence ratio values. This is mainly visible at 270 s and at the end of the sequence by peaks of the particle number stream emissions.

The integral values are presented in Fig. 7.36 for the urban sequence. The results are consistent with the highway sequence values. This includes the nearly constant offset of factor 1.6 to the measured values. The overall emissions match with sufficient agreement for both particle number and mass stream results. This is in line with the hypothesis that a change in the injector state is responsible for the lower level of emissions. The deviations in time-resolved values that are caused by mixture-induced particles do not visibly influence the integral results. This is in agreement with the assumption that the fired coasting mode of the engine is not relevant for the overall emissions of the sequence. However, an improvement of the simulation is possible if a more detailed calculation of the injected total fuel mass is performed in the engine process simulation to match the measured global equivalence ratio.

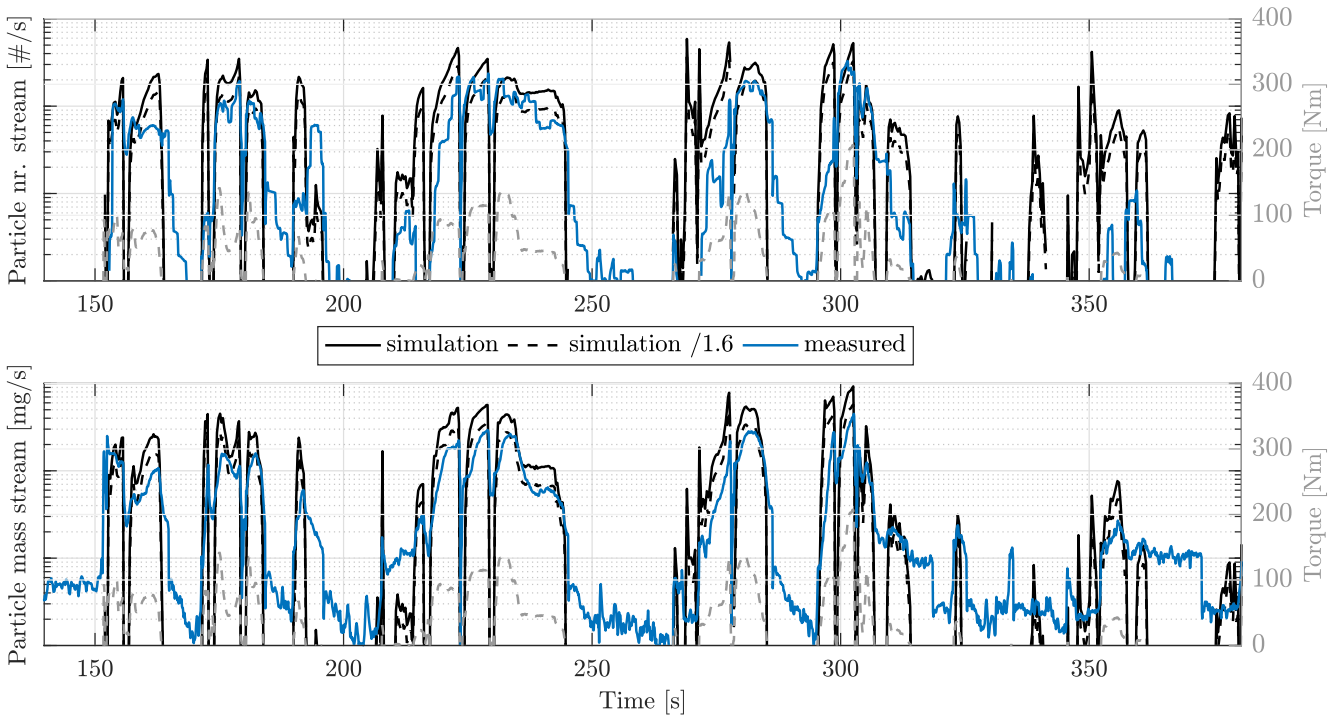

Fig. 7.35.: Comparison of simulated and measured time resolved particle number and mass stream emissions for WLTP cycle (urban part). Simulation result offset visualized by dashed line (factor of 1/1.6). All values normalized by maximum measured value.

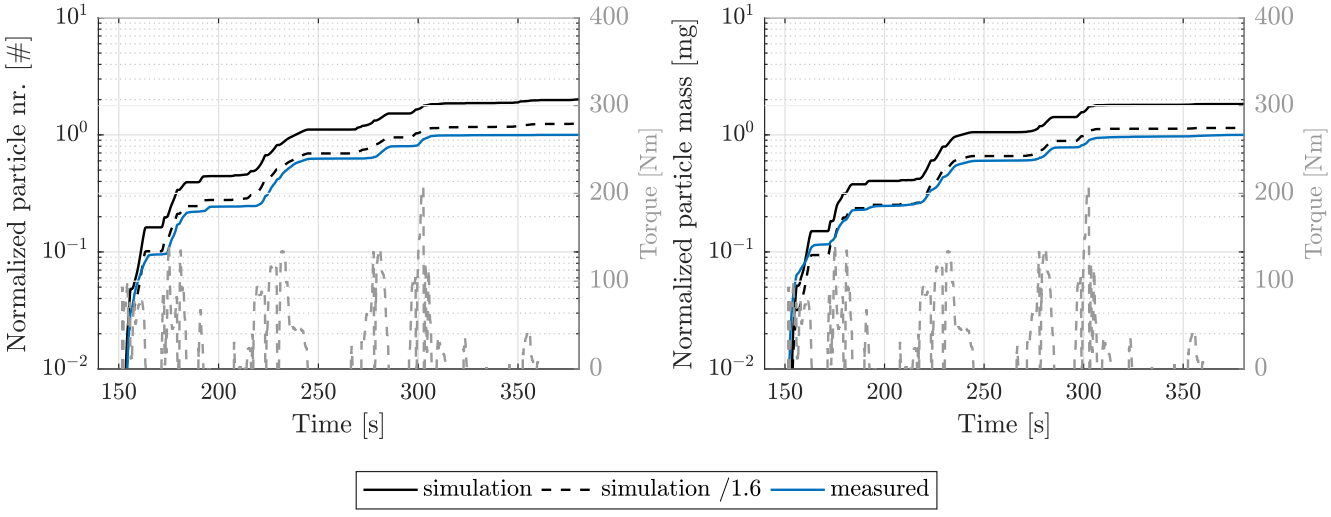

Fig. 7.36.: Comparison of simulated and measured integral particle number and mass stream emissions for WLTP cycle (urban part). Simulation result offset visualized by dashed line (factor of 1/1.6). All values normalized by maximum measured value.

Summarizing, the transfer of the engine operating map to a high dynamic driving cycle at moderate engine speed and load is possible and accurately matches the measured data. Almost all of the simulated emissions are caused by the injector module at warm condition. The results also show that it is not possible with the existing model to predict enduring changes of the injector state (e.g. injector drift), but the effect can be taken into consideration by applying a constant offset on the simulated values.

7.4.3 Sensitivity Study

The particle simulation framework is mainly developed to estimate the influence of engine actuator settings and thermodynamic conditions on the particle number and mass emissions during driving cycles. Therefore, a synthetic sensitivity study is performed to evaluate the reaction of the model when the input values are changed. A sequence of the already presented highway cycle is used for this analysis that includes a load step from 204 – 214 s (see also Section 7.4.1 for further information).

Starting from the original parametrization, the rail pressure, the global equivalence ratio and the wall temperatures are changed individually while all other input parameters are kept constant. Note that no additional engine process simulation is performed (especially for a changed global equivalence ratio) because a synthetic change of the parameter reduces the interdependencies and allows a more simple evaluation of the results. The influence on time-resolved and integral particle number and mass emissions is evaluated. Special attention is paid to the impact of the changes on the different simulation modules. In the base operation mode, all calculated emissions result from the injector tip module.

The base value for the rail pressure of the presented sequence is 200 bar. It is reduced stepwise by 50 bar and 100 bar, respectively. This increases the injection duration and thus decreases the available time for mixture homogenization and injector tip film evaporation while increasing the deposited film mass on the injector. The results of the variation are shown in Fig. 7.37. The integral particle number and mass values are increased equally by 20 % (−50 bar) and 60 % (−100 bar), respectively. All emissions originate from the injector module because of the high wall temperatures and the sufficient homogenization time. This behaviour is in agreement to the prior presented results at stationary operating mode with constant engine speed and load conditions.

The global equivalence ratio is changed by increasing the value of total injected fuel mass by 10 % and 20 %, respectively. This affects the injector film and the mixture homogeneity for the considered transient sequence. The results are presented in Fig. 7.38 for particle number and mass emissions. The simulated integral particle number stream is increased by 22 % and 137 % (particle mass stream by 69 % and 166 %). This non-linear increase is caused by the additional emissions that are caused by mixture inhomogeneity. The time-resolved function over time clearly shows a mixture-induced peak at the start of the load increase phases. This effect vanishes after a few seconds during the first load increase because of the increase in engine speed. The second load increase occurs at a constant low engine speed and thus the mixture-induced emissions remain dominant.

Finally, the wall temperature is reduced by 10 % and 20 % to represent cold engine conditions (e.g. after a long fuel cut-off phase). The results are shown in Fig. 7.39. This variation does not affect the injector tip and homogenization module. It does, however, significantly change the behaviour of the wall film module. The low wall temperatures lead to a reduced evaporation rate and thus cause particle emissions from liner wall film. This is caused by the switch from wall-side evaporation to gas-side evaporation in the wall film module. However, the evaporation rate is further declined when reducing the wall temperature in the gas-side evaporation regime.

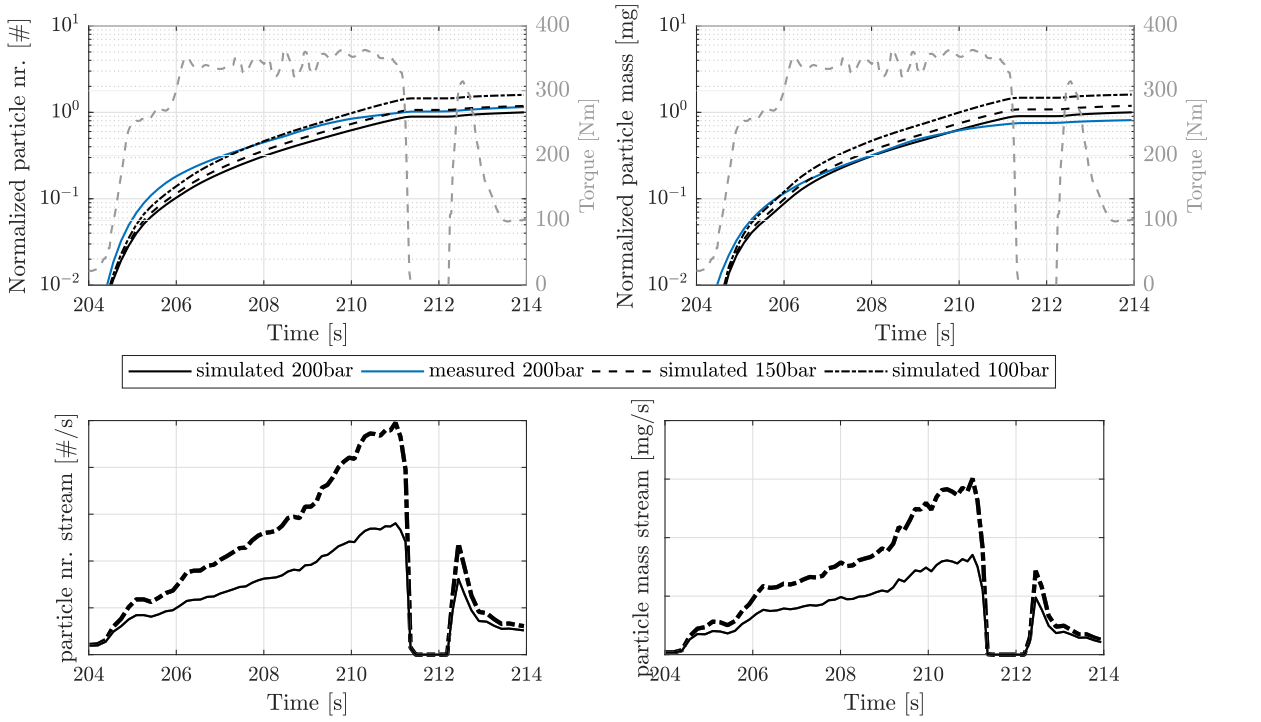

Fig. 7.37.: Sensitivity analysis of transient model on rail pressure. Sequence of highway cycle. Integral values (upper pictures) normalized by maximum value of simulation results at 200 bar. Time-resolve values of combined sub-modules (lower pictures) compared between 100 bar (dashed lines) and 200 bar (solid lines).

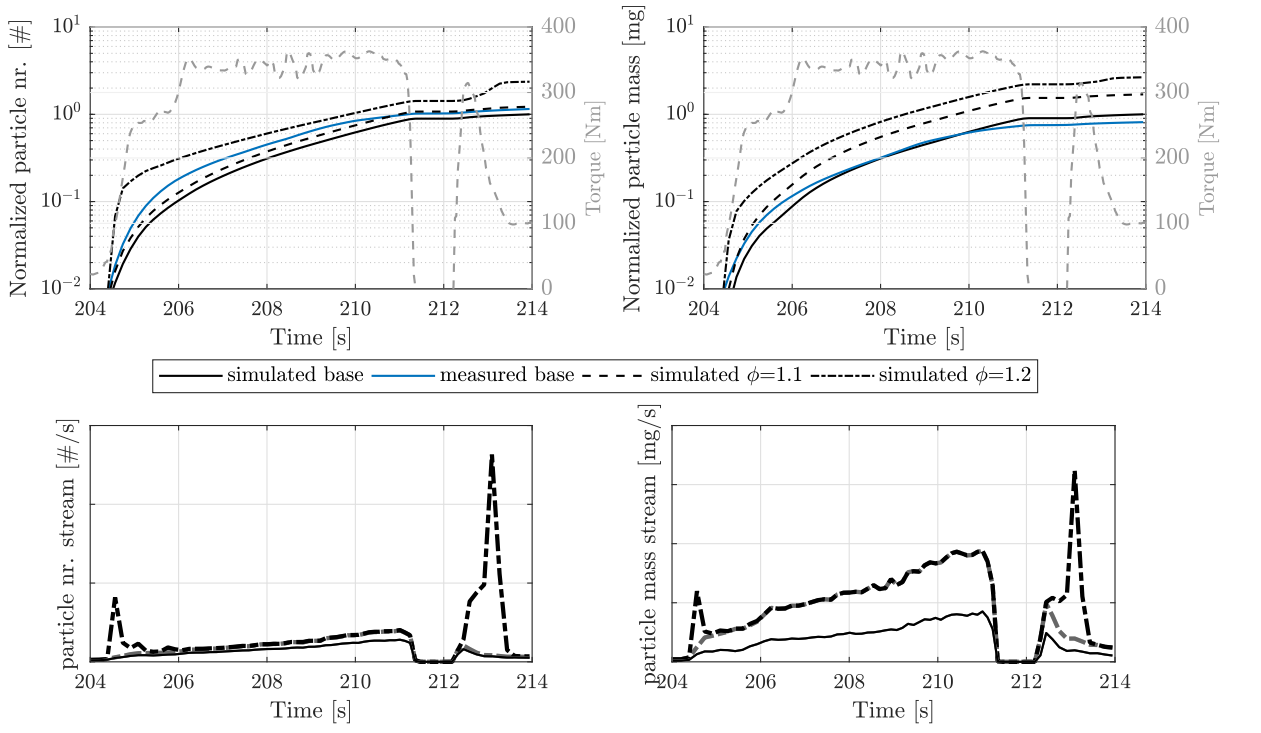

Fig. 7.38.: Sensitivity analysis of transient model on global equivalence ratio ϕ. Sequence of highway cycle. Integral values (upper pictures) normalized by maximum value of simulation results at $\phi = 1.0$. Time-resolved values of combined sub-modules (lower pictures) are compared between $\phi = 1.2$ (dashed lines) and $\phi = 1.0$ (solid lines).

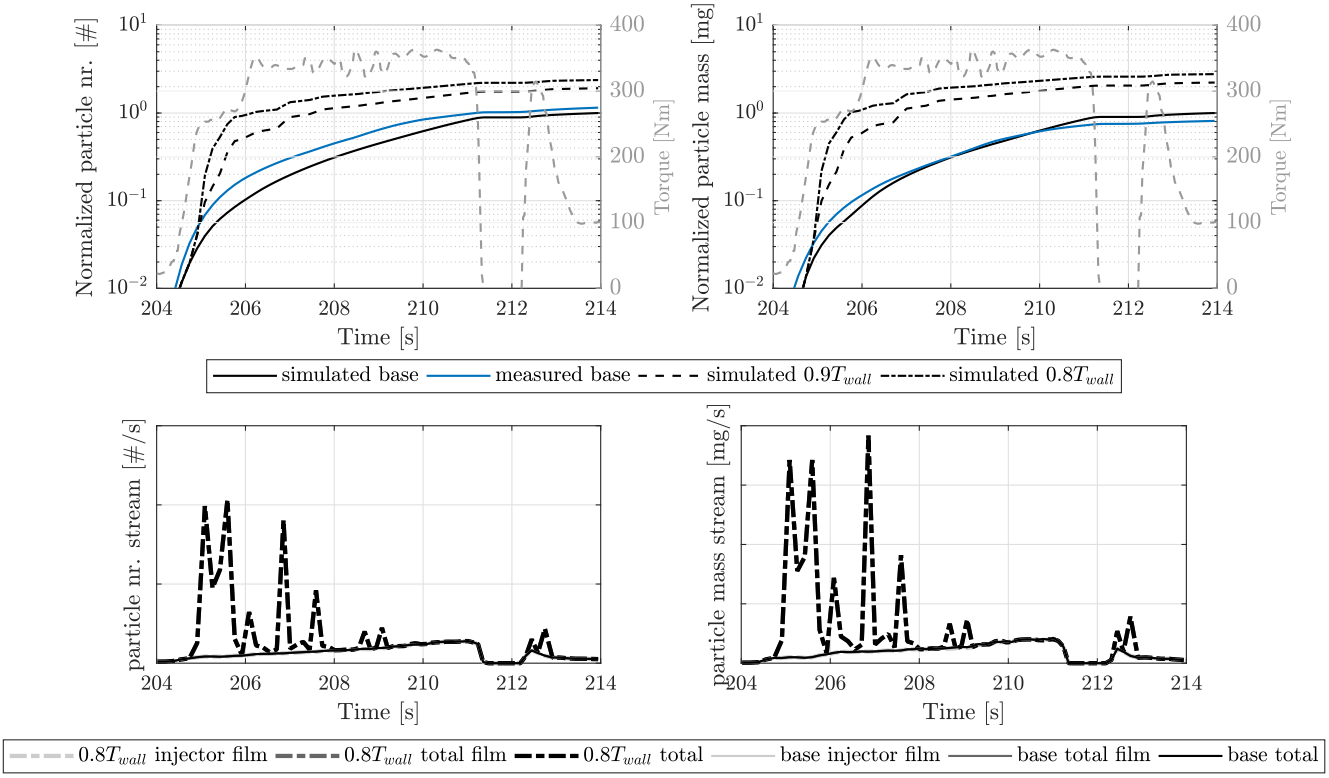

Fig. 7.39.: Sensitivity analysis of transient model on wall temperatures. Sequence of highway cycle. Integral values (upper pictures) normalized by maximum value of simulation results at $T_{\text{wall}} \cdot 1.0$. Time-resolved values of combined sub-modules (lower pictures) are compared between $T_{wall} \cdot 0.8$ (dashed lines) and $T_{\text{wall}} \cdot 1.0$ (solid lines).

The integral particle number emissions are increased by 90 % and 140 %, respectively (particle mass by 125 % and 180 %). Analysing the time-resolved values show that most of the wall-film-induced emissions are caused at the start of the load step after the fuel cut-off phase. Afterwards, the wall temperature increases and the additional emissions decreases.

Summarizing, the simulation model reacts on changes of the engine actuator settings in a physically plausible way at transient operating conditions. Depending on the changed parameter, the weighting of the different modules changes and the main particle source is either caused by the injector tip film, the inhomogeneous mixture preparation or the cylinder wall films. However, the sensitivity study is not sufficient to evaluate the effects quantitatively. Therefore, further measurement results are required that cover different engine parameter variations in a transient operating mode.

8 Summary and Conclusion

In this thesis, a new phenomenological approach is introduced to calculate the raw soot particle emissions of modern turbo-charged, direct-injection gasoline engines. The model is capable of calculating particle number, mass and size distribution values. This is enabled by coupling an engine process simulation with detailed reaction kinetics, a stochastic particle formation model and several newly developed sub-models that take account for different particle formation sources.

An engine-specific model calibration at a couple of selected operating points is required to take account for engine individual conditions (such as injector deposits or bulk flow characteristics). Due to its physically based structure, the model can then take into account changes in thermodynamic boundary conditions and engine actuator settings. The generalized model structure facilitates the simulation of stationary operating conditions as well as transient driving profiles, since the required model input values are similar. The creation of the final simulation framework is accompanied by an engine measurement program. By means of specially defined engine parameter variations, the individual particle formation sources could thus be changed in their share on the total particle emissions. In addition, the general morphology of particles of different origins is investigated by measuring and analysing the particle size distribution.

The starting point of the work is a literature review on the current understanding of particle formation, including gas-phase and solid phase processes. The particle number, mass and size are influenced by various physical and chemical processes during formation, defined as soot precursor formation, inception, coagulation, surface growth and oxidation. Therefore, these fundamental events should be described with a high level of detail, which is achieved by including a detailed reaction mechanism and soot model.

The main sources that have been identified to produce soot particles in modern gasoline engines are injector film deposits, inhomogeneous gaseous mixture preparation and remaining fuel wall film. Due to the complexity of driving cycles, it was decided to consider all main causes, as they contribute to the overall emissions by a different proportion. Existing empirical correlations are not considered sufficient to provide the required quality of boundary and starting conditions for the soot formation process. Detailed 3D-CFD simulations, on the other hand, are in conflict with the computation time requirements of a driving cycle simulation. Phenomenological approaches have been identified to be able to close the gap between empirical correlations and detailed simulations.

The implemented phenomenological approach is based on the coupling of a GT-Power based engine model, a MATLAB based multi-zone gas-phase solver with detailed reaction kinetics and a Fortran based Monte-Carlo solver. The gas-phase boundary conditions of the multi-zone structure are based on the individual formation processes. In zones that arise from inhomogeneous mixture preparation, the particle relevant zones of the air-fuel mixture react under sub-stoichiometric conditions. In zones with remaining liquid fuel film, pyrolysis reactions take place including residual gas and fuel. In each zone, the thermodynamic and chemical boundary conditions are provided for the calculation of the particle formations processes in the Monte-Carlo solver.

The validation strategy is based on the encapsulation of the model components, starting with reduced model complexity and validating all sub-models individually.

The calculation of the remaining injector film mass is based on 3D-CFD investigations and an empirical correlation that takes into consideration the film formation during injection and the film evaporation between end of injection and ignition.

The homogenization sub-model calculates the in-cylinder mixing process over time by considering dimensionless numbers for charge motion, spray-charge interaction and a dimensionless mixing time. This enables the estimation of the statistical equivalence ratio distribution function and the identification of the mass fraction with fuel-rich conditions.

The spray propagation is considered by solving the droplet conservation equations for a prior defined number of droplet sizes. These sizes are then scaled based on the droplet size distribution and the total amount of injected fuel. The formation of liquid wall films is calculated by an additional spray-wall interaction model that is mainly based on the impingement energy of the droplets. The wall film evaporation rate mainly depends on wall-side and gas-side heat transfer, leading to a total remaining wall film mass at ignition time.

Based on the validation strategy, the particle number and mass results are evaluated stepwise, from stationary results at operating conditions that are used for model parametrization up to transient driving profiles. Compared to engine test bench measurements, the overall simulation results are within the prior determined confidence intervals throughout the investigated area of the warm engine operating map. Due to inconstancies in the measurement of the cold engine map, only qualitative results could be compared, showing that the model is also capable to determine wall-film-induced particles in the relevant operating conditions. In terms of particle size distribution, the simulation calculates a characteristic nucleation mode coming from mixture inhomogeneities and an accumulation mode that arises from liquid fuel films. The sum of those modes substantially matches the measured mode values when the particle sources are weighted correctly. However, due to the calibration strategy that is based on particle number and mass emissions only, the bimodal size distribution is not estimated correctly. Therefore, a recommendation is given to parametrize the model with additional information about the size distribution in the context of this thesis.

The model responds to changes in the actuator variables (e.g. injection time, rail pressure, ignition time) in a physically plausible way. The calculation of particle emissions from wall- and injector film reacts most sensitive to engine pressure and speed, whereas the calculation of mixture-induced particles mainly reacts on engine air-fuel ratio and gas temperature. The estimation of the remaining wall film mass shows high sensitivities on the applied wall temperature values. These high sensitivities, combined with a limited quality of the input data lead to increased deviations regarding the injection time variation and variations at cold engine conditions. However, the parameter variations that mainly affects the injector film show good agreement.

Increasing the model complexity by including a full engine model only slightly affects the overall results and thus also provides satisfying results. The transfer to transient driving profiles that have been measured at the engine test bench can also be carried out with the model and matches the measured results to a high extent. This includes driving profiles with reduced dynamics, but high engine load as well as driving profiles with high dynamics and low engine load.

Due to the phenomenological structure, the model has some fundamental limitations. It is not able to calculate the particle emission a priori without any measurements for a new engine type, but a basic number of measurements and 3D-CFD simulations are required to parametrize the model. In addition, it is not possible to a priori take into account transient processes which lead to a permanent change in engine conditions (such as injector deposits, incorrect injection, etc.). However, it is possible to take these changes into account afterwards by making slight adjustments to the parametrization, providing a new basis for further investigations. Furthermore, at its current state

it is not possible to consider non-reproducible single effects (such as misfire, engine knock, cyclic fluctuations), because these are not considered in the engine process simulation. It should also be noted that the results from the engine test bench are assumed to be transferable to complete vehicle dynamometer tests only to a limited extent, as these results can differ from engine test bench results, for which the model has been developed primarily.

Further investigations are proposed in the light of the results of this thesis. An essential part of this should be how the developed model can be applied to other combustion processes and engine concepts. In particular, the question is whether a re-calibration of the model is sufficient or whether further physical effects have to be considered.

Furthermore, the soot particle formation sources should be measured even more differentiated, as individual sources, such as the injector film, could not be eliminated for the investigated engine. Therefore, the measured emissions are almost always an interaction of different sources.

Finally the model should be coupled with a virtual drive train and a driver controller to generate results without the need for measured variables. This is the basic step that allows the model to be used in the engine development process.

A Appendix

A.1 Homogeneity Model

A.1.1 Analysis of Simulation Process

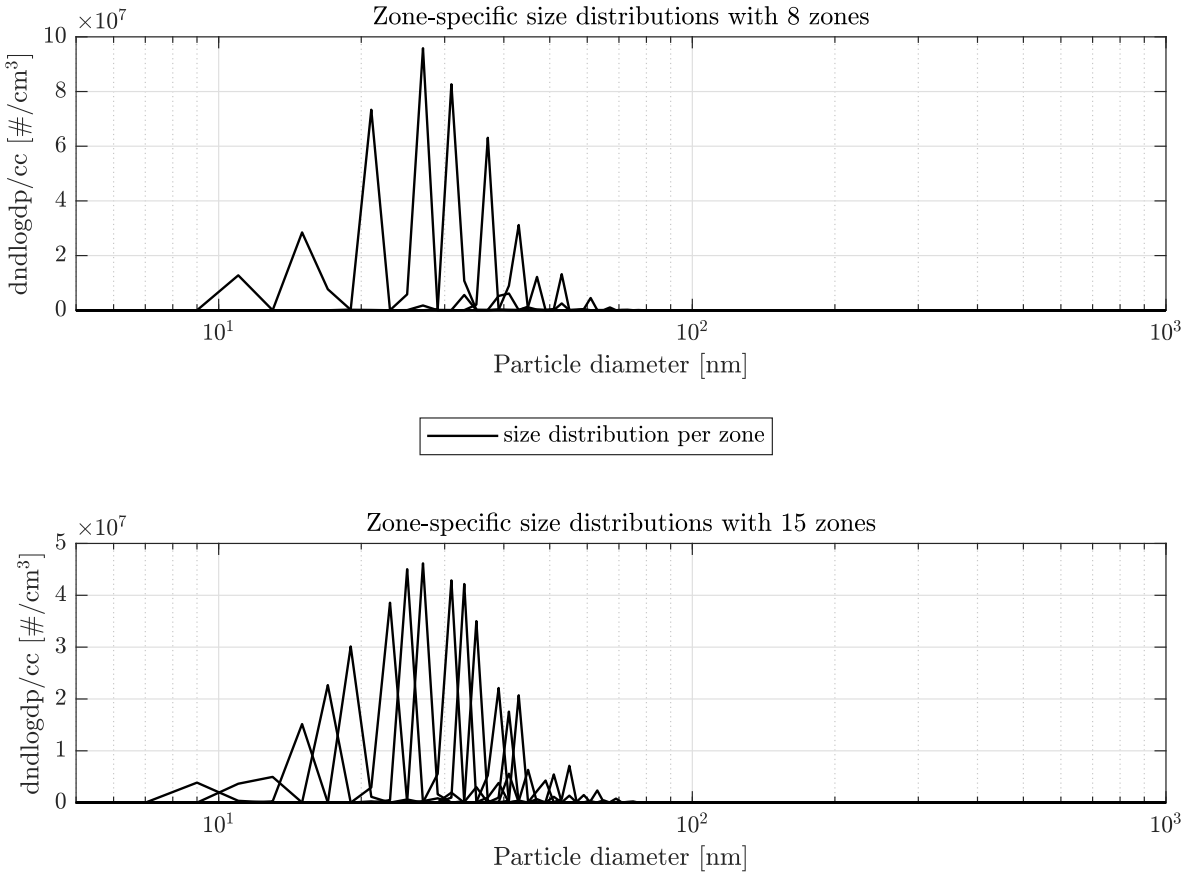

Fig. A.1.: Simulated particle size distribution for each zone from inhomogeneous mixture preparation. Increased number of particle diameter bins (500 nodes) and variation of calculated zone number. Operating point 2000 rpm/10 bar IMEP, SOI+80°CA.

A.2 Modelling Wall Film Formation and Evaporation

A.2.1 Spray Model

Model Properties of Liquid Phase

In the following, the applied equations are listed that calculate the liquid material properties of the fuel spray. A more detailed explanation can be found in the work of Hanisch [81].

A reduced temperature T_r is used in some of the equations, which is defined as the temperature of the liquid phase T divided by the material's critical temperature T_c:

$$T_r = \frac{T}{T_c} \tag{A.1}$$

The equations for density, specific heat capacity, vapour pressure, latent heat of vaporization and surface tension of the liquid phase are defined as (taken from Poling et al. [148]):

$$\rho_l = \frac{M}{V_{m,l}} \tag{A.2}$$

with the liquid phase molar volume $V_{m,l}$ that can be calculated with the experimental value $V_{m,\mathrm{ref}}$ at reference temperature T_{ref} by (Yamada and Gunn [195]):

$$\begin{aligned} V_{m,l} &= V_{m,\mathrm{ref}}(0.29056 - 0.08775\omega)^{\phi} \\ \text{with } \phi &= (1-T_r)^{2/7} - \left(1-T_{\mathrm{ref},r}\right)^{2/7} \end{aligned} \tag{A.3}$$

The molar heat capacity of the liquid phase $c^l_{p,m}$ is based on the ideal gas molar heat capacity $c^0_{p,m}$ and the universal gas constant R :

$$\frac{c^l_{p,m} - c^0_{p,m}}{R} = 1.586 + \frac{0.49}{1-T_r} + \omega\left[4.2775 + \frac{6.3(1-T_r)^{1/3}}{T_r} + \frac{0.4355}{1-T_r}\right] \tag{A.4}$$

The vapour pressure is estimated by the extended Antoine equation [95]:

$$\begin{aligned} \log_{10}\, p_v &= A - \frac{B}{T + C - 273.15} + 0.43429x^n + Ex^8 + Fx^{12} \\ \text{with } x &= \frac{T - t_0 - 273.15}{T_c} \end{aligned} \tag{A.5}$$

With tabulated values for the constants A, B, C, n, E, F and t_0 [148]. The latent heat of vaporization is calculated by (Riedel method [154]):

$$\Delta H_{v,b} = \frac{1}{M} 1.093 R T_b \frac{\ln p_c - 1.013}{0.930 - T_{b,r}} \tag{A.6}$$

The temperature influence is considered by The Watson relation [179]:

$$\Delta H_v = \Delta H_{v,b}\left(\frac{1-T_r}{1-T_{b,r}}\right)^{0.375} \tag{A.7}$$

Surface tension is calculated based on a correlation of Brock and Bird [27] and using a suggestion by Miller [127]:

$$\begin{aligned} \sigma_{lv} &= p_c^{2/3} T_c^{1/3} Q (1-T_r)^{11/9} \\ \text{with } Q &= 0.1196\left[1 + \frac{T_{b,r}\ln(p_c/1.01325)}{1-T_{b,r}}\right] - 0.279 \end{aligned} \tag{A.8}$$

The thermal conductivity of liquid iso-octane is approximated by an exponential function based on experimental results of Liessmann et al. [112], Naziev et al. [136] and Watanabe [190]:

$$\lambda_l = A \cdot \mathrm{e}^{B(T+C)} + D \quad \text{with } A = 0.16,\ B = -0.00106,\ C = -700,\ D = -0.148 \tag{A.9}$$

The dynamic viscosity μ_l is based on experimental results of Dymond et al. [56]:

$$\mu_l = AT^B \quad \text{with } A = 54835,\ B = -3.26 \tag{A.10}$$

The mole fraction $X_{f,s}$ and mass fraction $Y_{f,s}$ of fuel vapour at the droplet surface are obtained by assuming ideal gas behaviour:

$$X_{f,s} = \frac{p_v(T_{sat})}{p_g} \tag{A.11}$$

$$Y_{f,s} = \frac{M_f}{M_f + M_a\left(\frac{1}{X_{f,s}} - 1\right)} \tag{A.12}$$

with the molar mass M. The index f is for fuel, a is for charge air and g is for the gas mixture, respectively.
Since material properties change between droplet surface and ambience, mean material properties are used (denoted by $(.)_{\mathrm{ref}}$). Following Renksizbulut and Yuen [150], properties are taken at the following reference conditions using the so-called $\frac{1}{2}$-rule:

$$T_{\mathrm{ref}} = T_{sat} + \frac{1}{2}(T_\infty - T_{sat}) \tag{A.13}$$

$$Y_{\mathrm{f,ref}} = Y_{f,s} + \frac{1}{2}\left(Y_{f,\infty} - Y_{f,s}\right) \tag{A.14}$$

The evaporating mass flow $\dot{m}_{\mathrm{vap}}$ that is caused by the concentration gradient between droplet surface and ambience is calculated by:

$$\dot{m}_{\mathrm{vap}} = Sh\left(\rho_g D\right)_{\mathrm{ref}} \pi d_d B_m \tag{A.15}$$

with the spalding mass transfer B_m

$$B_m = \frac{Y_{f,s} - Y_{f,\infty}}{1 - Y_{f,s}}. \tag{A.16}$$

The Sherwood number Sh is given by [192]

$$Sh = 2 + \left(0.4Re^{1/2} + 0.06Re^{2/3}\right)Sc^{1/3}. \tag{A.17}$$

The convective heat transfer between droplet surface and ambience reads as:

$$\dot{Q}_d = \alpha A_s (T_\infty - T_s), \quad A_s = \pi d_d^2 \tag{A.18}$$

with the calculation of the convective heat transfer coefficient α by the Nusselt correlation Nu [192]:

$$Nu = \frac{\alpha d_d}{\lambda_{g,\mathrm{ref}}} = 2 + \left(0.4Re^{1/2} + 0.06Re^{2/3}\right)Pr^{1/3} \tag{A.19}$$

The droplet motion is decelerated by a drag force F_D:

$$F_D = \frac{\pi}{8} d_d^2 \, c_D \rho_{g,\mathrm{ref}} \, |u_d| \, u_d \tag{A.20}$$

The drag coefficient for non-vaporizing droplets $c_{D,\mathrm{nv}}$ is obtained by an empirical correlation of Schiller and Naumann (taken from Ashgriz et al. [10]):

$$c_{D,\mathrm{nv}} = \begin{cases} \frac{24}{Re}\left(1 + 0.15Re^{0.687}\right) & \text{for } Re \leq 1000 \\ 0.44 & \text{for } Re > 1000 \end{cases} \tag{A.21}$$

The dimensionless numbers used in the correlations are based on the following definitions (see Aggarwal and Peng [3], Krüger [104]):

$$\text{Reynolds number:} \qquad Re = \frac{\rho_{g,\infty} \, |u_d| \, d_d}{\mu_{g,\mathrm{ref}}} \tag{A.22}$$

$$\text{Schmidt number:} \qquad Sc = \frac{\mu_{g,\mathrm{ref}}}{\left(\rho_g D_{im}\right)_{\mathrm{ref}}} \tag{A.23}$$

$$\text{Prandtl number:} \qquad Pr = \frac{\mu_{g,\mathrm{ref}} \, c_{p,g,\mathrm{ref}}}{\lambda_{g,\mathrm{ref}}} \tag{A.24}$$

A.2.2 Wallfilm Model

Gas-Side Heat and Mass Transfer

In the following, the calculation of the material properties and dimensionless numbers is listed that are required to obtain the gas-side wall film evaporation rate $\dot{m}_{\mathrm{wf},g}$. The equation for the evaporation mass flux $j_{m,g}$ is presented by Wang et al. [185]:

$$j_{m,g} = -\frac{Sh_L \rho_g D \left(Y_{f,\infty} - Y_{f,s}\right)}{L_{\mathrm{ch}} \left(1 - Y_{f,s}\right)} \tag{A.25}$$

The material properties are based on a reference temperature T_{ref}, which is an averaged value of wall film and ambient gas temperature:

$$T_{\mathrm{ref}} = \frac{T_{\mathrm{wf}} + T_{g,\infty}}{2} \tag{A.26}$$

The characteristic length L_{ch} is defined as

$$L_{\mathrm{ch}} = \frac{L_0}{h_0} h_{\mathrm{wf}} \tag{A.27}$$

According to French et al. [63], the ratio of characteristic length to film thickness L_0/h_0 is supposed to be 100.
Using boundary layer theory, Sherwood number Sh_L is calculated according to the following correlation [191]:

$$Sh_L = 0.664 Re_L^{1/2} Sc^{1/3} \tag{A.28}$$

Re_L is obtained from the characteristic length L_{ch} and the gas velocity in the ambience sufficiently far from the film surface $u_{g,\infty}$:

$$Re_L = \frac{L_{\mathrm{ch}} u_{g,\infty}}{\nu_{g,\mathrm{ref}}} c_m = 2 \cdot n \cdot s \tag{A.29}$$

Wall-side heat and mass transfer

The two main model parameters α_{dry} and C_{lld} are calculated using equations presented by Habchi [77]. The dry fraction rises from 0 to nearly 1 when the wall temperature increases from T_{sat} to T_L. The dry fraction at the Leidenfrost point $\alpha_{\mathrm{dry}}^{\mathrm{PL}}$ is assumed to be 0.98 [77].

$$\alpha_{\mathrm{dry}}(T_w) = \alpha_{\mathrm{dry}}^{\mathrm{PL}} T_*^{1/4} \tag{A.30}$$

where T_* is the dimensionless wall temperature defined by:

$$T_* = \frac{T_w - T_{\mathrm{sat}}}{T_L - T_{\mathrm{sat}}} \tag{A.31}$$

The saturation temperature T_{sat} is calculated by evaluating the *Extended Antoine Equation* that is a correlation for the vapour pressure $p_{\mathrm{vap}=f(T_{\mathrm{sat}})}$. In this equation, the values of iso-octane were applied based on Poling et al. [148]. The last three terms are only applied if x is positive. The equation is valid between $T_{\mathrm{sat}} = 275.5$ K and $T_{\mathrm{sat}} = 543.15$ K. Above this value, the saturation temperature is held constant:

$$\log_{10} p_{\mathrm{vap}} = 3.93646 - \frac{1257.85}{T_{\mathrm{sat}} + 220.767 - 273.15} + 0.43429 x^{2.13261} + 134.5 x^8 + 12998 x^{12} \tag{A.32}$$
$$x = \frac{T_{\mathrm{sat}} - 124 - 273.15}{543.90}$$

With the given in-cylinder pressure, the corresponding saturation temperature can then directly be derived.
The length density of contact lines C_{lld} is modelled by a dimensionless function k_{clld}:

$$k_{clld} = \frac{C_{lld}(T_w)}{C_{lld}^{\max}} \tag{A.33}$$

with values of $C_{lld}^{\max} \approx 3000$ m/m^2 (Nishio and Tanaka [139]). Within the nucleate boiling regime, k_{clld} is calculated by:

$$k_{clld} = \frac{\alpha_{\mathrm{dry}}(T_w)}{\alpha_{\mathrm{dry}}^{\mathrm{PN}}}, \quad \text{with } \alpha_{\mathrm{dry}}^{\mathrm{PN}} = \alpha_{\mathrm{dry}}(T_w = T_N). \tag{A.34}$$

Within the transition boiling regime, k_{clld} drops quickly and approaches a minimum value $k_{clld}^{\min}$ at the Leidenfrost point:

$$k_{clld}(T_w) = \left(1 - k_{clld}^{\min}\right) \cdot T_{**}^4 + k_{clld}^{\min} \tag{A.35}$$

where $k_{clld}^{\min}$ is estimated according to surface roughness and T_{**} is the dimensionless wall temperature defined by:

$$T_{**} = \frac{T_L - T_w}{T_L - T_N} \tag{A.36}$$

Fig. A.2 illustrates the behaviour of the two main parameters in the case of iso-octane at atmospheric pressure.

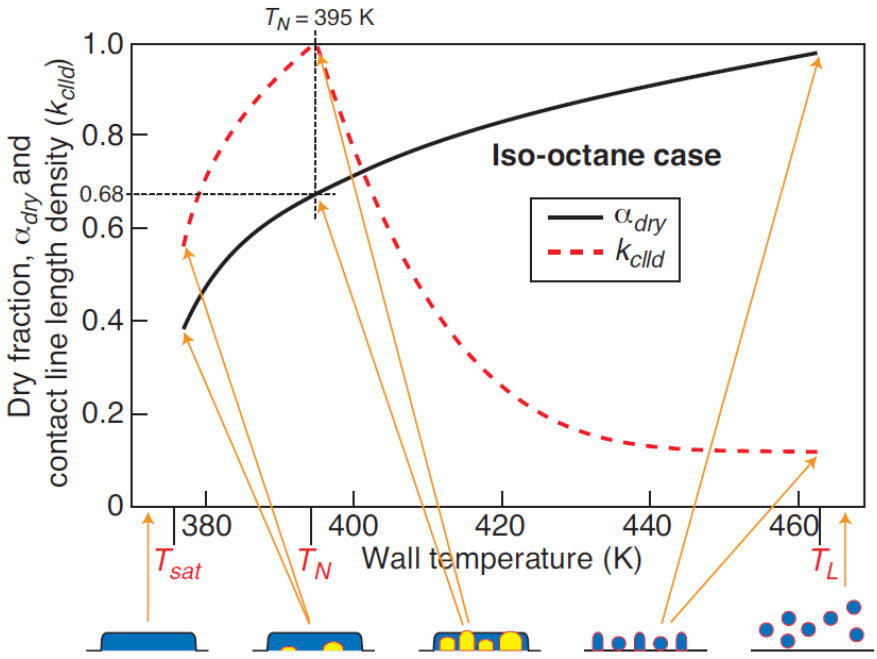

Fig. A.2.: Dry fraction and length density of contact lines over wall temperature (iso-octane at atmospheric pressure). From: Habchi [77].

A.2.3 Identification of Calibration Parameters

Available Data for Comparison

Experimental Data

The experimental results are taken from literature and include a variation of ambient pressure and temperature [96, 102, 103] (see Tab. A.1).

Tab. A.1.: Applied boundary conditions within the reference measurements [96, 102, 103].

OP	T_g [K]	p_g [bar]	T_f [K]	p_{inj} [bar]	t_{inj} [ms]
1	473	5.6	353	200	1
2	473	8.0	353	200	1
3	673	8.0	353	200	1

Engine measurement data and applied 3D-CFD model

The applied engine speed and load variation is presented in Fig. A.3). OP 2 with a moderate speed and load is chosen to be the base point for the analysis. Tab. A.2 gives an overview of the operating points

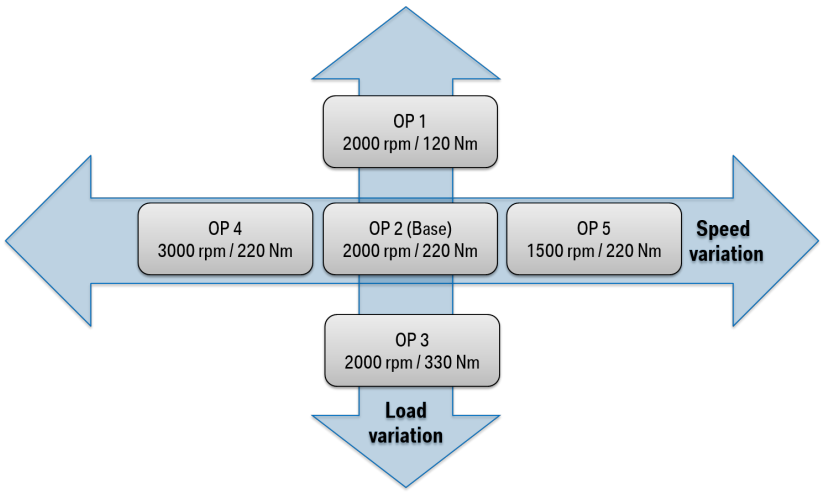

Fig. A.3.: Operating points considered in engine map variation. [81]

and related boundary conditions for the engine map variation. In Tab. A.3, the boundary conditions for the SOI variation and the coolant temperature variation are presented. An overview of the applied models in the 3D-CFD simulation is given in Tab. A.4.

Tab. A.2.: Engine map variation. Operating points and applied boundary conditions.

CFD OP	n [min^{-1}]	M_{eff} [Nm]	T_f [K]	p_{inj} [bar]	SOI [°CA]	$T_{\text{w,lin/pis}}$ [K]
1	2000	120	330	85	408	380 / 410
2	2000	220	330	140	433	390 / 420
3	2000	330	330	165	449	390 / 430
4	3000	220	330	155	434	400 / 440
5	1500	220	330	135	441	380 / 410

Tab. A.3.: SOI and coolant temperature variation. Operating points and applied boundary conditions.

	CFD OP	n [min^{-1}]	M_{eff} [Nm]	T_f [K]	p_{inj} [bar]	SOI [°CA]	$T_{\text{w,lin/pis}}$ [K]
SOI	6	2000	130	320	95	503	370 / 400
variation	7	2000	130	320	95	383	370 / 400
Coolant tempera-	8	2000	120	330	85	405	380 / 410
ture variation	9	2000	120	310	85	405	340 / 370

Tab. A.4.: Overview of the applied models in CFD simulations

Sub-module	Physical process	Applied model
Spray	Evaporation	Dukowicz
	Secondary breakup	Wave
	Turbulent dispersion	Gosman and Ioannidis
Spray-wall interaction	Splashing	Mundo/Sommerfeld
Wall film	Evaporation	Combined model
	Entrainment	Schadel-Hanratty

Comparison of spray penetration behaviour between 0D simulation and experiment for OP2:

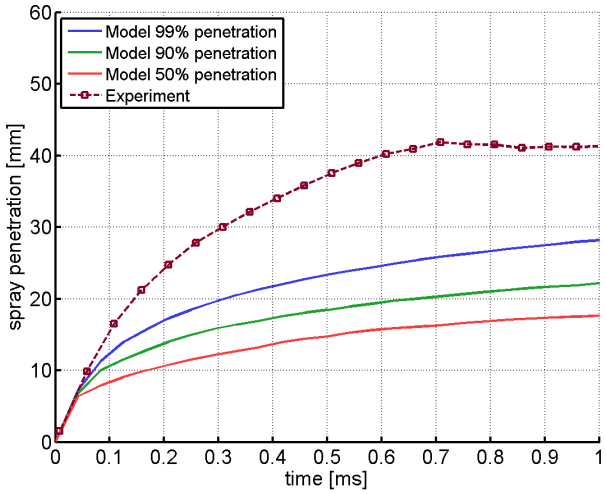

Fig. A.4.: Spray penetration at OP 2: $T_g = 473$ K, $p_g = 8.0$ bar before calibration. [81]

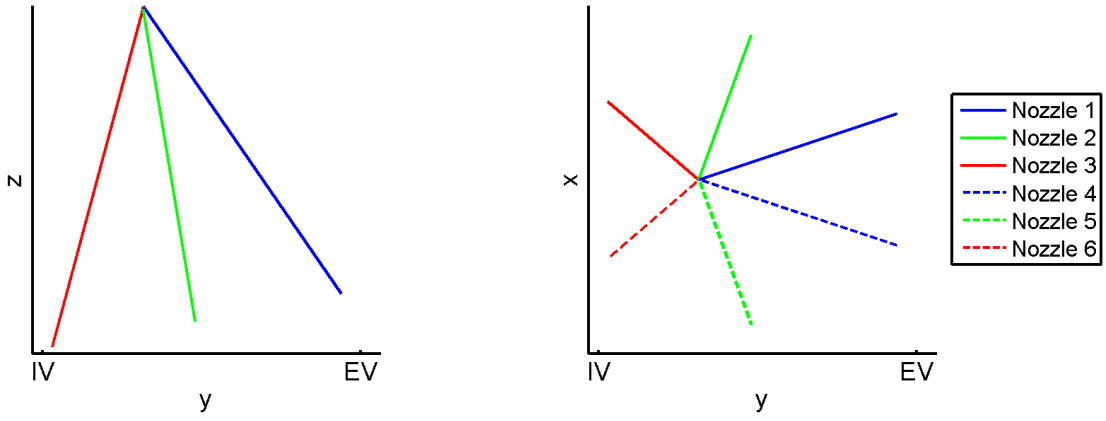

(a) side view **(b)** top view

Fig. A.5.: Spray targeting and definition of nozzle hole numbers. [81]

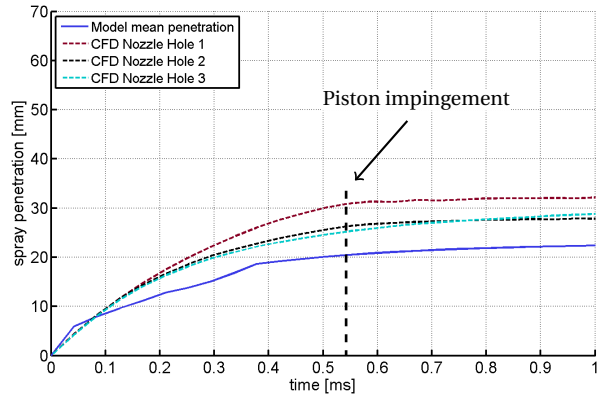

(a) CFD OP 1: 2000 rpm, 120 Nm – 50 % penetration

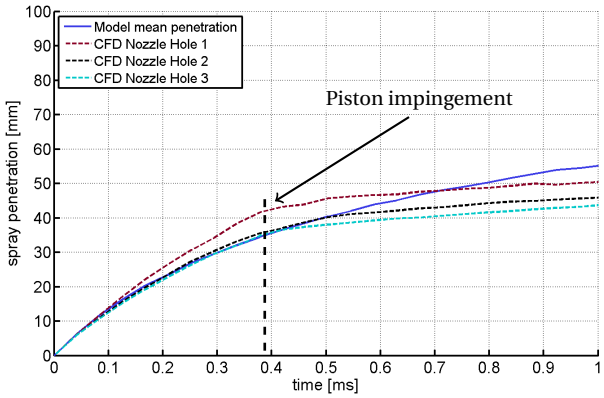

(b) CFD OP 1: 2000 rpm, 120 Nm – 99 % penetration

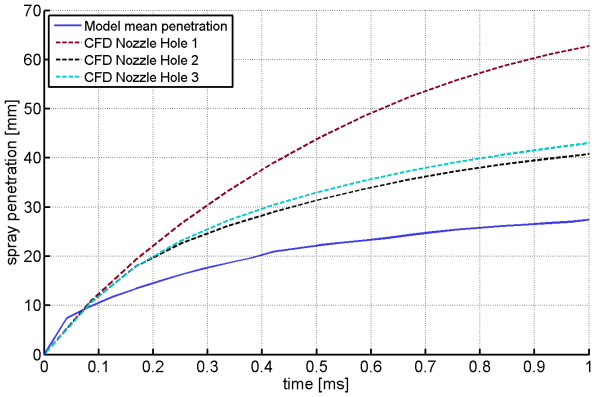

(c) CFD OP 3: 2000 rpm, 330 Nm – 50 % penetration

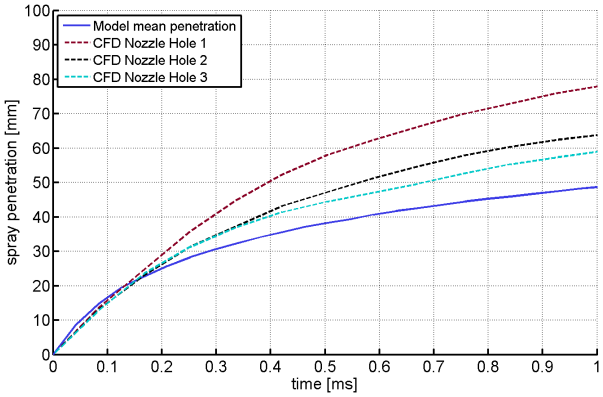

(d) CFD OP 3: 2000 rpm, 330 Nm – 99 % penetration

Fig. A.6.: Comparison of 0D model and 3D CFD before calibration. Liquid penetration over time for two operating points with load variation. [81]

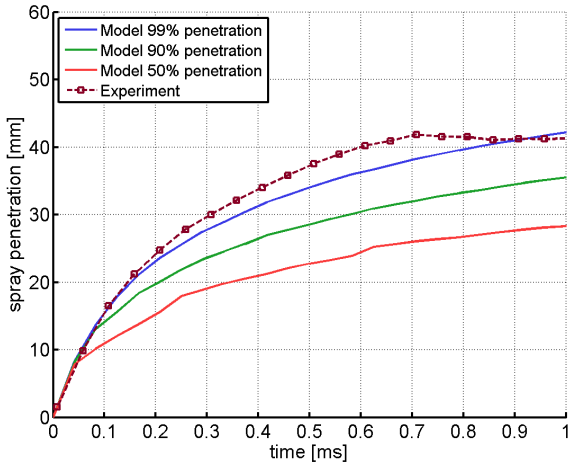

Fig. A.7.: Spray penetration at OP 2: $T_g = 473$ K, $p_g = 8.0$ bar after calibration. [81]

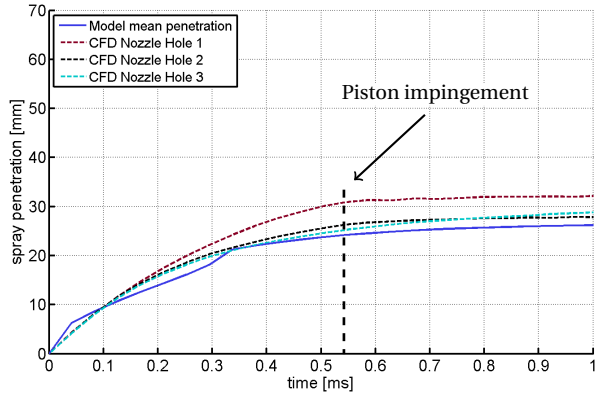

(a) OP 1: 2000 min^{-1}, 120 Nm – 50 % penetration

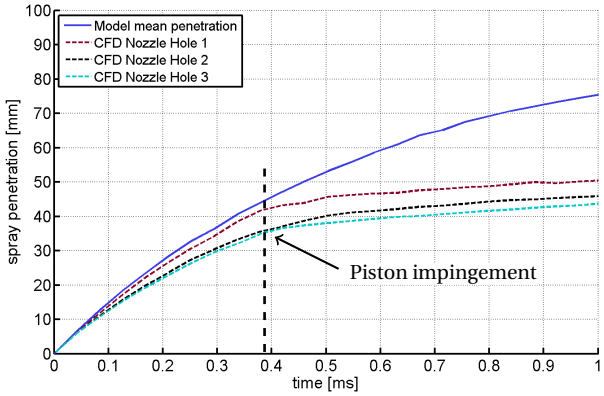

(b) OP 1: 2000 rpm, 120 Nm – 99 % penetration

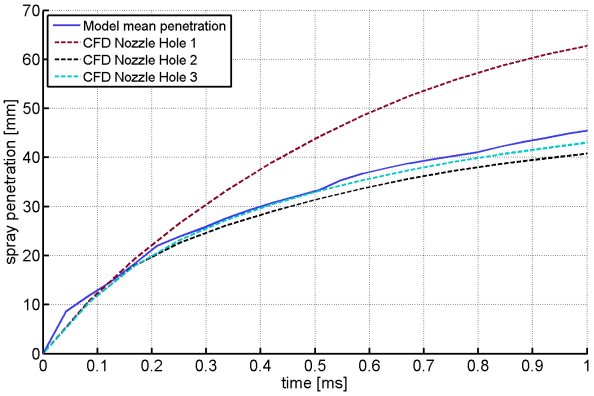

(c) OP 3: 2000 rpm, 330 Nm – 50 % penetration

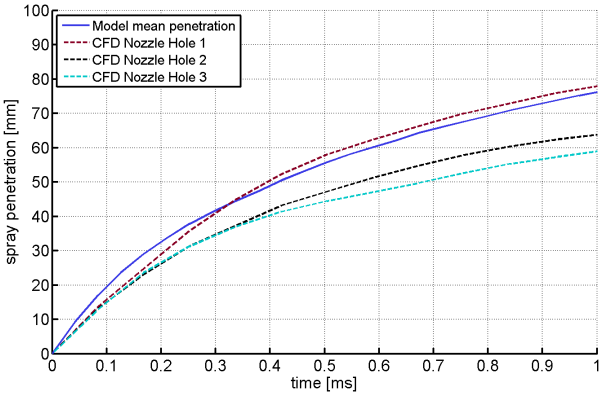

(d) OP 3: 2000 rpm, 330 Nm – 99 % penetration

Fig. A.8.: Comparison of 0D model and 3D CFD after calibration. Liquid penetration over time for three operating points with load variation. [81]

The calibration results of the evaporation module are given in Tab. A.5

Tab. A.5.: Model parameters for film thickness modifying factor (Eq. 6.37) after primary calibration.

Parameter	Piston	Liner
c_1	$4.8 \cdot 10^{-12}$	$1.061 \cdot 10^{-14}$
c_2	-3.052	-3.868
Δt_{lim}	$3 \cdot 10^{-4}$ s	$6 \cdot 10^{-4}$ s
$f_{h,\text{min}}$	0.29	0.031

Bibliography

[1] S. M. Aceves, D. L. Flowers, C. K. Westbrook, J. R. Smith, W. Pitz, R. Dibble, M. Christensen, and B. Johansson. A Multi-Zone Model for Prediction of HCCI Combustion and Emissions. In *SAE Technical Paper*, volume 2000-01-0327. SAE International, 2000.

[2] ADAC e.V. ADAC Highway Cycle, 2016. URL `https://www.adac.de/infotestrat/tests/eco-test/default.aspx`.

[3] S. K. Aggarwal and F. Peng. A Review of Droplet Dynamics and Vaporization Modeling for Engineering Calculations. *J. Eng. Gas Turbines Power*, 117(3):453, 1995.

[4] J. Aguilera-Iparraguirre and W. Klopper. Density Functional Theory Study of the Formation of Naphthalene and Phenanthrene from Reactions of Phenyl with Vinyl- and Phenylacetylene. *Journal of Chemical Theory and Computation*, 3(1):139–145, 2007.

[5] K. Aikawa, T. Sakurai, and J. J. Jetter. Development of a Predictive Model for Gasoline Vehicle Particulate Matter Emissions. *SAE Int. J. Fuels Lubr.*, 3:610–622, 2010.

[6] A. Alexiou and A. Williams. Soot formation in shock-tube pyrolysis of toluene-n-heptane and toluene-iso-octane mixtures. *Fuel*, 74(2):153–158, 1995.

[7] T. Alger, M. Hall, and R. D. Matthews. Effects of Swirl and Tumble on In-Cylinder Fuel Distribution in a Central Injected DISI Engine. In *SAE 2000 World Congress*, SAE Technical Paper Series, 2000.

[8] ANSYS, Inc. ANSYS CFX, Release 14.5.7, 2013.

[9] J. Appel, H. Bockhorn, and M. Frenklach. Kinetic Modeling of Soot Formation with Detailed Chemistry and Physics: Laminar Premixed Flames of C2 Hydrocarbons. *Combustion and Flame*, 121:122–136, 2000.

[10] N. Ashgriz, editor. *Handbook of Atomization and Sprays: Theory and Applications*. Springer Science+Business Media LLC, Boston, 2011.

[11] AVL LIST GmbH. Micro Soot Sensor, 2016. URL `https://www.avl.com/-/mssplus-avl-micro-soot-sensor`.

[12] Axel Maier, Ulrike Klaus, Andreas Dreizler, and Hermann Rottengruber. Fuel-Independent Particulate Emissions in an SIDI Engine. *SAE Int. J. Engines*, 8:1334–1341, 2015.

[13] A. Babajimopoulos, D. N. Assanis, D. L. Flowers, S. M. Aceves, and R. P. Hessel. A fully coupled computational fluid dynamics and multi-zone model with detailed chemical kinetics for the simulation of premixed charge compression ignition engines. *International Journal of Engine Research*, 6(5):497–512, 2005.

[14] C. Bai and A. D. Gosman. Development of Methodology for Spray Impingement Simulation. In *International Congress & Exposition*, SAE Technical Paper Series, 1995.

[15] C. X. Bai, H. Rusche, and A. D. Gosman. Modeling of gasoline spray impingement. *Atomization and Sprays*, 12(1-3):1–28, 2002.

[16] M. Balthasar and M. Kraft. A stochastic approach to calculate the particle size distribution function of soot particles in laminar premixed flames. *Combustion and Flame*, 133(3):289–298, 2003.

[17] M. Banholzer. Numerische Untersuchung der Wärme- und Stoffübertragung im Umströmungsbereich eines Benzininjektors: Master's Thesis, TU München, 2014.

[18] T. L. Barone, J. M. Storey, A. D. Youngquist, and J. P. Szybist. An analysis of direct-injection spark-ignition (DISI) soot morphology. *Atmospheric Environment*, 49:268–274, 2012.

[19] H. Barths, C. Felsch, and N. Peters. Mixing models for the two-way-coupling of 5CFD6 codes and zero-dimensional multi-zone codes to model 5HCCI6 combustion. *Combustion and Flame*, 156(1):130–139, 2009.

[20] A. Berndorfer, S. Breuer, W. Piock, and P. von Bacho. Diffusion Combustion Phenomena in GDi Engines caused by Injection Process. In *SAE 2013 World Congress & Exhibition*, SAE Technical Paper Series, 2013.

[21] M. Berthelot. Theorie des corps pyrogenes. *Ann. Chim. Phys*, 9:469–481, 1866.

[22] T. Blacha, M. Di Domenico, P. Gerlinger, and M. Aigner. Soot predictions in premixed and non-premixed laminar flames using a sectional approach for PAHs and soot. *Combustion and Flame*, 159(1):181–193, 2012.

[23] G. Blanquart. Chemical and Statistical Soot Modeling, Stanford University, USA, 2008.

[24] G. Blanquart, P. Pepiot-Desjardins, and H. Pitsch. Chemical mechanism for high temperature combustion of engine relevant fuels with emphasis on soot precursors. *Combustion and Flame*, 156(3):588–607, 2009.

[25] H. Bockhorn, editor. *Soot Formation in Combustion: Mechanisms and Models*, volume 59 of *Springer Series in Chemical Physics*. Springer, Berlin, Heidelberg, 1994.

[26] F. Bonatesta, E. Chiappetta, and A. La Rocca. Part-load particulate matter from a GDI engine and the connection with combustion characteristics. *Applied Energy*, 124:366–376, 2014.

[27] J. R. Brock and R. B. Bird. Surface tension and the principle of corresponding states. *AIChE Journal*, 1(2):174–177, 1955.

[28] A. Bukhvostova, E. Russo, J. Kuerten, and B. J. Geurts. DNS of turbulent droplet-laden heated channel flow with phase transition at different initial relative humidities. *International Journal of Heat and Fluid Flow*, 50:445–455, 2014.

[29] M. Burger, R. Schmehl, R. Koch, S. Wittig, and H.-J. Bauer. DNS of droplet–vortex interaction with a Karman vortex street. *International Journal of Heat and Fluid Flow*, 27(2):181–191, 2006.

[30] C. Yuan and R.O. Fox. Conditional quadrature method of moments for kinetic equations. *Journal of Computational Physics*, 230(22):8216–8246, 2011.

[31] C. Yuan, F. Laurent, and R.O. Fox. An extended quadrature method of moments for population balance equations. *Journal of Aerosol Science*, 51(0):1–23, 2012.

[32] Cambustion Limited. Cambustion DMS500, 2016. URL `http://www.cambustion.com/products/dms500`.

[33] M. Celnik, R. Patterson, M. Kraft, and W. Wagner. Coupling a stochastic soot population balance to gas-phase chemistry using operator splitting. *Combustion and Flame*, 148(3):158–176, 2007.

[34] M. S. Celnik. On the Numerical Modelling of Soot and Carbon Nanotube Formation: Ph.D. thesis, University of Cambridge, 2007.

[35] L. Chen, R. Stone, and D. Richardson. A study of mixture preparation and PM emissions using a direct injection engine fuelled with stoichiometric gasoline/ethanol blends. *Fuel*, 96:120–130, 2012.

[36] K. Choi, J. Kim, C.-L. Myung, M. Lee, S. Kwon, Y. Lee, and S. Park. Effect of the mixture preparation on the nanoparticle characteristics of gasoline direct-injection vehicles. *Proceedings of the Institution of Mechanical Engineers, Part D: Journal of Automobile Engineering*, 226(11):1514–1524, 2012.

[37] H. J. Curran, P. Gaffuri, W. J. Pitz, and C. K. Westbrook. A Comprehensive Modeling Study of n-Heptane Oxidation. *Combustion and Flame*, 114(1–2):149–177, 1998.

[38] H. J. Curran, P. Gaffuri, W. J. Pitz, and C. K. Westbrook. A comprehensive modeling study of iso-octane oxidation. *Combustion and Flame*, 129(3):253–280, 2002.

[39] H. Dageförde, H. Kubach, T. Koch, and U. Spicher. Innermotorische Ursachen für Partikelemissionen bei Ottomotoren mit Direkteinspritzung. In M. Bargende, H.-C. Reuss, and J. Wiedemann, editors, *14. Internationales Stuttgarter Symposium: Automobil- und Motorentechnik*, pages 435–459. Springer Fachmedien Wiesbaden, 2014.

[40] A. D'Alessio, G. Gambi, P. Minutolo, S. Russo, and A. D'Anna. Optical characterization of rich premixed CH4/O2 flamesacross the soot formation threshold. *Symposium (International) on Combustion*, 25(1):645–651, 1994.

[41] A. D'Anna and J. H. Kent. Aromatic formation pathways in non-premixed methane flames. *Combustion and Flame*, 132(4):715–722, 2003.

[42] A. D'Anna and J. H. Kent. A model of particulate and species formation applied to laminar, nonpremixed flames for three aliphatic-hydrocarbon fuels. *Combustion and Flame*, 152(4):573–587, 2008.

[43] S. G. Davis, A. V. Joshi, H. Wang, and F. Egolfopoulos. An optimized kinetic model of H2/CO combustion. *Proceedings of the Combustion Institute*, 30(1):1283–1292, 2005.

[44] Y. Deguchi. *Industrial applications of laser diagnostics.* CRC Press, Boca Raton, FL, 2012.

[45] J. Demuynck, D. Bosteels, M. D. Paepe, C. Favre, J. May, and S. Verhelst. Recommendations for the new WLTP cycle based on an analysis of vehicle emission measurements on NEDC and CADC. *Energy Policy*, 49:234–242, 2012.

[46] C. Disch, T. Koch, U. Spicher, and C. Donn. Engine-in-the-Loop als Entwicklungswerkzeug für die Emissionsoptimierung im Hybridkontext. *Motortechnische Zeitschrift*, 75(10):70–78, 2014.

[47] C. Disch, H. Kubach, J. Pfeil, T. Koch, U. Spicher, O. Thiele, C. Donn, and C. Schyr. Zyklusaufgelöste Verbrennungsprozessanalyse des transienten Betriebs an einem Ottomotor mit Direkteinspritzung. In *11. Internationales Symposium Verbrennungsdiagnostik*, Baden-Baden, 2014.

[48] C. Disch, J. Pfeil, H. Kubach, T. Koch, U. Spicher, and O. Thiele. Experimentelle Untersuchungen zur Entwicklung des Kurbelwinkelaufgelösten Brennraumluftverhältnisses im Transientbetrieb eines Ottomotors mit Direkteinspritzung. In *7. MTZ-Fachtagung Ladungswechsel im Verbrennungsmotor*, Stuttgart, 2014.

[49] Z. M. Djurisic. Detailed kinetic modeling of benzene and toluene oxidation at high temperatures: Master's Thesis, University of Delaware, Newark, 1999.

[50] M. Dorsch. *Detailed Modeling of SI Engines in Fuel Consumption Simulations for Functional Analysis: Ph.D. Thesis*. Logos, Berlin, 2016.

[51] M. Dorsch, J. Neumann, and C. Hasse. Detailed Modeling of SI-Engines in Driving Cycle Simulation for Fuel Consumption Analysis. In *FISITA 2014 World Automotive Congress*, volume F2014-CET-017, Maastricht, 2014.

[52] M. C. Drake, T. D. Fansler, and A. M. Lippert. Stratified-charge combustion: modeling and imaging of a spray-guided direct-injection spark-ignition engine. *Proceedings of the Combustion Institute*, 30(2):2683–2691, 2005.

[53] K. Duffy and A. Mellor. Further Developments on a Characteristic Time Model for NOx Emissions from Diesel Engines. *SAE Technical Paper*, 982460, 1998.

[54] J. K. Dukowicz. A particle-fluid numerical model for liquid sprays. *Journal of Computational Physics*, 35(2):229–253, 1980.

[55] S. B. Dworkin, Q. Zhang, M. J. Thomson, N. A. Slavinskaya, and U. Riedel. Application of an enhanced PAH growth model to soot formation in a laminar coflow ethylene/air diffusion flame. *Combustion and Flame*, 158(9):1682–1695, 2011.

[56] J. H. Dymond, N. F. Glen, and J. D. Isdale. Transport properties of nonelectrolyte liquid mixtures VII. *International Journal of Thermophysics*, 6(3):233–250, 1985.

[57] A. Eibeck and W. Wagner. An Efficient Stochastic Algorithm for Studying Coagulation Dynamics and Gelation Phenomena. *SIAM Journal on Scientific Computing*, 22(3):802–821, 2000.

[58] B. Eiteneer and M. Frenklach. Experimental and modeling study of shock-tube oxidation of acetylene. *International Journal of Chemical Kinetics*, 35(9):391–414, 2003.

[59] G. Elsaesser. Experimentelle Untersuchung und numerische Modellierung der freien Kraftstoffstrahlausbreitung und Wandinteraktion unter motorischen Randbedingungen: Ph.D. Thesis, Karlsruher Institut für Technologie, 2001.

[60] J. Etheridge, S. Mosbach, M. Kraft, H. Wu, and N. Collings. Modelling soot formation in a DISI engine. *Proceedings of the Combustion Institute*, 33(2):3159–3167, 2011.

[61] D. Fardad and N. Ladommatos. Evaporation of hydrocarbon compounds, including gasoline and diesel fuel, on heated metal surfaces. *Proceedings of the Institution of Mechanical Engineers, Part D: Journal of Automobile Engineering*, 213(6):625–645, 1999.

[62] J. H. Ferziger and M. Perić. *Computational methods for fluid dynamics*. Springer, Berlin, 3., rev. edition, 2002.

[63] W. French, D. Rose, P. Kelly-Zion, and C. Pursell. Analysis of Evaporating Fuel Films Using Shadowgraph and Schlieren Imaging Techniques. In *Powertrains, Fuels and Lubricants Meeting*, SAE Technical Paper Series, 2008.

[64] M. Frenklach. Method of moments with interpolative closure. *Chemical Engineering Science*, 57:2229–2239, 2002.

[65] M. Frenklach. Reaction mechanism of soot formation in flames. *Phys. Chem. Chem. Phys.*, 4 (11):2028–2037, 2002.

[66] M. Frenklach and H. Wang. Detailed modeling of soot particle nucleation and growth. *Symposium (International) on Combustion*, 23(1):1559–1566, 1991.

[67] S. Frommater, J. Neumann, and C. Hasse. Aufbau einer fahrzyklusfähigen Simulationsmethodik zur Modellierung der Partikelemissionen direkteinspritzender Ottomotoren. In *VPC- Simulation und Test 2015*, Hanau, 2015.

[68] S. Frommater, J. Neumann, and C. Hasse. A phenomenological mixture homogenization model for spark-ignition direct-injection engines. *International Journal of Engine Research*, page 146808741771185, 2017.

[69] Gamma Technologies Inc. GT-Suite: GT-Power, 2015.

[70] T. D. Gillespie. An Exact Method for Numerically Simulating the Stochastic Coalescence Process in a Cloud. *Journal of the Atmospheric Sciences*, 32(10):1977–1989, 1975.

[71] I. Glassman. Soot formation in combustion processes. *Symposium (International) on Combustion*, 22(1):295–311, 1989.

[72] J. Gong and C. Rutland. A Quasi-Dimensional NOx Emission Model for Spark Ignition Direct Injection (SIDI) Gasoline Engines. *SAE International*, 2013-01-1311, 2013.

[73] M. Goodson and M. Kraft. An Efficient Stochastic Algorithm for Simulating Nano-particle Dynamics. *Journal of Computational Physics*, 183(1):210–232, 2002.

[74] D. G. Goodwin, H. K. Moffat, and R. L. Speth. Cantera: An object-oriented software toolkit for chemical kinetics, thermodynamics, and transport processes. http://www.cantera.org, 2015.

[75] S. Grasreiner. Combustion modeling for virtual SI engine calibration with the help of 0D/3D methods: Ph.D. thesis, TU Bergakademie Freiberg, 2012.

[76] S. Grasreiner, J. Neumann, C. Luttermann, M. Wensing, and C. Hasse. A quasi-dimensional model of turbulence and global charge motion for spark ignition engines with fully variable valvetrains. *International Journal of Engine Research*, 15(7):805–816, 2014.

[77] C. Habchi. A comprehensive model for liquid film boiling in internal combustion engines. *Oil & Gas Science and Technology–Revue de l'Institut Français du Pétrole*, 65(2):331–343, 2010.

[78] J. Hadler, C. Lensch-Franzen, M. Gohl, and T. Mink. Emissionsreduzierung - Lösung aus Ölformulierung, Applikation und Mechanikentwicklung. *MTZ - Motortechnische Zeitschrift*, 76, 2015.

[79] M. Hageman and D. Rothamer. Sensitivity Analysis of Particle Formation in a Spark-Ignition Engine during Premixed Operation. In *8th U. S. National Combustion Meeting*, University of Utah, 2013.

[80] Z. Han, Z. Xu, and N. Trigui. Spray/wall interaction models for multidimensional engine simulation. *International Journal of Engine Research*, 1(1):127–146, 2000.

[81] T. Hanisch. Phenomenological modelling of spray-wall interaction in direct injection spark ignition engines for particle simulation: Master's Thesis, TU Bergakademie Freiberg, 2015.

[82] B. S. Haynes and H. G. Wagner. Soot formation. *Progress in Energy and Combustion Science*, 7 (4):229–273, 1981.

[83] Y. Hidaka, Y. Henmi, T. Ohonishi, T. Okuno, and T. Koike. Shock-tube and modeling study of diacetylene pyrolysis and oxidation. *Combustion and Flame*, 130(1–2):62–82, 2002.

[84] H. Hiroyasu and T. Kadota. Models for Combustion and Formation of Nitric Oxide and Soot in Direct Injection Diesel Engines. In *SAE Technical Paper*. SAE International, 1976.

[85] W. J. Imoehl. Method of optimizing direct injector tip position in a homogeneous charge engine for minimum injector deposits, US Patent US10241462, 2004.

[86] Q. Jiao and R. Reitz. Modeling of Equivalence Ratio Effects on Particulate Formation in a Spark-Ignition Engine under Premixed Conditions. *SAE International*, 2014-01-1607, 2014.

[87] Q. Jiao and R. D. Reitz. Modeling soot emissions from wall films in a direct-injection spark-ignition engine. *International Journal of Engine Research*, 16(8):994–1013, 2015.

[88] P. Jochmann, F. Köpple, A. Storch, A. Kufferath, B. Durst, B. Hußmann, M. Miklautschitsch, and E. Schünemann. Minimizing the Particulate Emissions of Gasoline Direct Injection Engines with central mounting Injector position through Innovative Injector Technologies and the Integrated Use of CFD and Engine Tests. In *10th International Symposium on Combustion Diagnostics*, Baden-Baden, 2012.

[89] D. Kalantari and C. Tropea. Spray impact onto flat and rigid walls: Empirical characterization and modelling. *International Journal of Multiphase Flow*, 33(5):525–544, 2007.

[90] N. Karwa, P. Stephan, W. Wiese, and D. Lejsek. Gasoline direct injection engine injector tip drying. In *19th Australasian Fluid Mechanics Conference*, pages 1–4, Melbourne, Australia, 2014.

[91] M. Kato and B. Launder. The Modeling of Turbulent Flow Around Stationary and Vibrating Square Cylinders. In *Proc. 9th Symposium on Turbulent Shear Flows*, pages p.pp.10.4.1–10.4.6, Kyoto, 1993.

[92] D. Kayes and S. Hochgreb. Mechanisms of Particulate Matter Formation in Spark-Ignition Engines. 1. Effect of Engine Operating Conditions. *Environmental Science & Technology*, 33(22): 3957–3967, 1999.

[93] A. Kazakov and D. E. Foster. Modeling of soot formation during DI diesel combustion using a multi-step phenomenological model. *SAE Technical Paper*, 982463, 1998.

[94] A. Kazakov, H. Wang, and M. Frenklach. Detailed modeling of soot formation in laminar premixed ethylene flames at a pressure of 10 bar. *Combustion and Flame*, 100(1-2):111–120, 1995.

[95] H. V. Kehiaian and B. J. Zwolinski, editors. *International Data Series: Selected Data on Mixtures*. Thermodynamics Research Center. Chemistry Dept.. Texas A&M University, College Station, 1973.

[96] P. Keller, T. Knorsch, M. Wensing, and C. Hasse. Experimental and numerical analysis of iso-octane/ethanol sprays under gasoline engine conditions. *International Journal of Heat and Mass Transfer*, 84:497–510, 2015.

[97] I. M. Kennedy. Models of soot formation and oxidation. *Progress in Energy and Combustion Science*, 23(2):95–132, 1997.

[98] J. E. Ketterer and W. K. Cheng. On the Nature of Particulate Emissions from DISI Engines at Cold-Fast-Idle. *SAE International*, 2014-01-1368:986–994, 2014.

[99] K.H. Homann. Carbon formation in premixed flames. *Combustion and Flame*, 11(4):265–287, 1967.

[100] I. M. Khan, G. Greeves, and D. M. Probert. Prediction of soot and nitric oxide concentrations in diesel engine exhaust. *Air Pollution Control in Transport Engines C*, 142:205–217, 1971.

[101] V. V. Kislov, A. I. Sadovnikov, and A. M. Mebel. Formation Mechanism of Polycyclic Aromatic Hydrocarbons beyond the Second Aromatic Ring. *The Journal of Physical Chemistry A*, 117(23): 4794–4816, 2013.

[102] T. Knorsch. *Untersuchungen zum Einfluss von Kraftstoffeigenschaften auf die ottomotorische Wirkkette: Ph.D. Thesis*. Berichte zur Energie- und Verfahrenstechnik. ESYTEC Energie- und Systemtechnik GmbH, Erlangen, 2015.

[103] T. Knorsch, M. Heldmann, L. Zigan, M. Wensing, and A. Leipertz. On the role of physiochemical properties on evaporation behavior of DISI biofuel sprays. *Experiments in Fluids*, 54(6), 2013.

[104] C. Krüger. Validierung eines 1D-Spraymodells zur Simulation der Gemischbildung in direkteinspritzenden Dieselmotoren: Ph.D. Thesis, RWTH Aachen, 2001.

[105] D. Kuhnke. Spray Wall Interaction Modeling by Dimensionless Data Analysis: Ph.D. Thesis, Technische Universität Darmstadt, 2004.

[106] P. Kulkarni, P. A. Baron, and K. Willeke. *Aerosol measurement: principles, techniques, and applications*. John Wiley & Sons, 2011.

[107] J. Lahaye. Mechanisms of soot formation. *Polymer Degradation and Stability*, 30(1):111–121, 1990.

[108] A. Laskin, H. Wang, and C. K. Law. Detailed kinetic modeling of 1, 3-butadiene oxidation at high temperatures. *International Journal of Chemical Kinetics*, 32(10):589–614, 2000.

[109] F. Leach, R. Stone, and D. Richardson. The Influence of Fuel Properties on Particulate Number Emissions from a Direct Injection Spark Ignition Engine. In *SAE Technical Paper*, volume 2013-01-1558. SAE International, 2013.

[110] N. Lévy, S. Amara, and J.-C. Champoussin. Simulation of a Diesel Jet Assumed Fully Atomized at the Nozzle Exit. In *International Congress & Exposition*, volume 981067 of *SAE Technical Paper Series*, 1998.

[111] L. Liang, C. V. Naik, K. V. Puduppakkam, A. U. Modak, and E. Meeks. Application of Detailed Soot-Particle Model to Simulations of Fundamental Spray Experiments and GDI Engine. In *International Multidimensional Engine Modeling User's Group Meeting*, Dtroit, Michigan, 2014.

[112] G. Liessmann, W. Schmidt, and S. Reiffarth. Data Compilation of the Sächsische Olefinwerke Böhlen Germany: Recommended Thermophysical Data, 1995.

[113] D. Linse. Modeling and Simulation of Knock and Emissions in Turbocharged Direct Injection Spark Ignition Engines. Ph.D. thesis, TU Bergakademie Freiberg, 2013.

[114] MAHA-AIP GmbH & Co. KG. Particle Counter SPC 8000, 2016. URL `http://end-of-line.info/english/spc8000.aspx`.

[115] Z. A. Mansurov. Soot Formation in Combustion Processes (Review). *Combustion, Explosion and Shock Waves*, 41(6):727, 2005.

[116] C. Marchal, J.-L. Delfau, C. Vovelle, G. Moréac, C. Mounaim-Rousselle, and F. Mauss. Modelling of aromatics and soot formation from large fuel molecules. *Proceedings of the Combustion Institute*, 32(1):753–759, 2009.

[117] D. L. Marchisio, J. T. Pikturna, R. O. Fox, R. D. Vigil, and A. A. Barresi. Quadrature method of moments for population-balance equations. *AIChE Journal*, 49(5):1266–1276, 2003.

[118] M. M. Maricq, D. H. Podsiadlik, D. D. Brehob, and M. Haghgooie. Particulate emissions from a direct-injection spark-ignition (DISI) engine. *SAE Technical Papers*, 1999-01-1530, 1999.

[119] J. S. McArragher and K. J. Tan. Soot Formation at High Pressures: A Literature Review. *Combustion Science and Technology*, 5(1):257–261, 1972.

[120] R. McGraw. Description of Aerosol Dynamics by the Quadrature Method of Moments. *Aerosol Science and Technology*, 27(2):255–265, 1997.

[121] P. S. Mehta and S. Das. A correlation for soot concentration in diesel exhaust based on fuel-air mixing parameters. *Fuel*, 71(6):689–692, 1992.

[122] G. P. Merker, C. Schwarz, and R. Teichmann. *Combustion Engines Development: Mixture Formation, Combustion, Emissions and Simulation*. Springer-Verlag, Berlin, Heidelberg, 2012.

[123] Michael Frenklach. Dynamics of Discrete Distribution for Smoluchowski Coagulation Model. *Journal of Colloid and Interface Science*, 108(1):237–242, 1985.

[124] Michael Frenklach and Stephen J. Harris. Aerosol Dynamics Modeling Using the Method of Moments. *Journal of Colloid and Interface Science*, 118(1):252–261, 1987.

[125] M. Miklautschitsch, B. Durst, S. Henrici, G. Unterweger, and A. Witt. Partikelquellenanalyse und Ableitung von PN-Reduktionsmaßnahmen am BMW TwinPower Turbo Motor. In *12. Tagung Motorische Verbrennung*, Ludwigsburg, 2015.

[126] A. L. Miller, C. B. Stipe, M. C. Habjan, and G. G. Ahlstrand. Role of Lubrication Oil in Particulate Emissions from a Hydrogen-Powered Internal Combustion Engine. *Environmental Science & Technology*, 41(19):6828–6835, 2007.

[127] D. G. Miller and G. Thodos. Correspondence. Reduced Frost-Kalkwarf Vapor Pressure Equation. *Ind. Eng. Chem. Fund.*, 2(1):78–80, 1963.

[128] J. A. Miller and S. J. Klippenstein. The Recombination of Propargyl Radicals and Other Reactions on a C6H6 Potential. *The Journal of Physical Chemistry A*, 107(39):7783–7799, 2003.

[129] A. S. Moita and A. Moreira. Drop impacts onto cold and heated rigid surfaces: Morphological comparisons, disintegration limits and secondary atomization. *International Journal of Heat and Fluid Flow*, 28(4):735–752, 2007.

[130] A. S. Moita and A. L. N. Moreira. Development of an empirical correlation to predict secondary atomization of impacting boiling droplets. In *14th Int Symp on Applications of Laser Techniques to Fluid Mechanics*, 2008.

[131] A. Moreira, A. S. Moita, and M. R. Panão. Advances and challenges in explaining fuel spray impingement: How much of single droplet impact research is useful? *Progress in Energy and Combustion Science*, 36(5):554–580, 2010.

[132] M. Mueller, G. Blanquart, and H. Pitsch. Hybrid Method of Moments for modeling soot formation and growth. *Combustion and Flame*, 156(6):1143–1155, 2009.

[133] C. Mundo, M. Sommerfeld, and C. Tropea. Droplet-wall collisions: Experimental studies of the deformation and breakup process. *International Journal of Multiphase Flow*, 21(2):151–173, 1995.

[134] M. Nagaoka, H. Kawazoe, and N. Nomura. Modeling Fuel Spray Impingement on a Hot Wall for Gasoline Engines. In *International Congress & Exposition*, volume 940525 of *SAE Technical Paper Series*, 1994.

[135] K. Narayanaswamy, G. Blanquart, and H. Pitsch. A consistent chemical mechanism for oxidation of substituted aromatic species. *Combustion and Flame*, 157(10):1879–1898, 2010.

[136] D. Y. Naziev, A. M. Aliev, and Y. M. Naziev. Study of the thermal conductivity of binary mixtures of n-heptane–isooctane with high state parameters. *Teplofiz. Vys. Temp.*, 30(2):294–298, 1992.

[137] A. Nefischer, J. Neumann, A. Stanciu, and A. Wimmer. Comparison and application of different phenomenological combustion models for turbo-charged SI engines. In *FISITA World Automotive Congress*, Budapest, Hungary, 2010.

[138] J. A. Nelder and R. Mead. A Simplex Method for Function Minimization. *The Computer Journal*, 7(4):308–313, 1965.

[139] S. Nishio and H. Tanaka. Advanced Fluid Information. Simplified Model Predicting Contact-Line-Length Density at Critical Heat Flux Based on Direct Observation of Boiling Structure. *JSME International Journal Series B*, 45(1):72–78, 2002.

[140] M. A. Oehlschlaeger, D. F. Davidson, and R. K. Hanson. Investigation of the reaction of toluene with molecular oxygen in shock-heated gases. *Combustion and Flame*, 147(3):195–208, 2006.

[141] H. Omidvarborna, A. Kumar, and D.-S. Kim. Recent studies on soot modeling for diesel combustion. *Renewable and Sustainable Energy Reviews*, 48:635–647, 2015.

[142] H. B. Palmer and C. F. Cullis. The formation of carbon from gases. *Chemistry and physics of carbon*, 1:265–325, 1965.

[143] M. R. O. Panao and A. L. N. Moreira. Experimental study of the flow regimes resulting from the impact of an intermittent gasoline spray. *Experiments in Fluids*, 37(6):834–855, 2004.

[144] R. I. Patterson and M. Celnik. Sweep2: Cambridge Soot Simulator, http://como.cheng.cam.ac.uk, 2006.

[145] R. I. Patterson, J. Singh, M. Balthasar, M. Kraft, and W. Wagner. Extending stochastic soot simulation to higher pressures. *Combustion and Flame*, 145(3):638–642, 2006.

[146] Y.-Q. Pei, J. Qin, and S.-Z. Pan. Experimental study on the particulate matter emission characteristics for a direct-injection gasoline engine. *Proceedings of the Institution of Mechanical Engineers, Part D: Journal of Automobile Engineering*, 228(6):604–616, 2014.

[147] I. Pielecha. Modeling of gasoline fuel spray penetration in SIDI engines. *International Journal of Automotive Technology*, 15(1):47–55, 2014.

[148] B. E. Poling, J. M. Prausnitz, and J. P. O'Connell. *Properties of Gases and Liquids*. Mcgraw-Hill Professional, 5th edition, 2001.

[149] K. Reavell, T. Hands, and N. Collings. A Fast Response Particulate Spectrometer for Combustion Aerosols. In *SAE Technical Paper*, volume 2002-01-2714. SAE International, 2002.

[150] M. Renksizbulut and M. C. Yuen. Numerical Study of Droplet Evaporation in a High Temperature Air Stream. *ASME Journal of Heat Transfer*, 105:387–389, 1983.

[151] K. L. Revzan, N. J. Brown, and M. Frenklach. FORTRAN Soot Subroutine, 2016. URL `http://www.me.berkeley.edu/soot`.

[152] H. Richter and J. Howard. Formation of polycyclic aromatic hydrocarbons and their growth to soot—a review of chemical reaction pathways. *Progress in Energy and Combustion Science*, 26 (4-6):565–608, 2000.

[153] H. Richter, S. Granata, W. H. Green, and J. B. Howard. Detailed modeling of PAH and soot formation in a laminar premixed benzene/oxygen/argon low-pressure flame. *Proceedings of the Combustion Institute*, 30(1):1397–1405, 2005.

[154] L. Riedel. Kritischer Koeffizient, Dichte des gesättigten Dampfes und Verdampfungswärme. Untersuchungen über eine Erweiterung des Theorems der übereinstimmenden Zustände. Teil III. *Chemie Ing. Techn.*, 26(12):679–683, 1954.

[155] R. Rioboo, C. Tropea, and M. Marengo. Outcomes from a drop impact on solid surfaces. *Atomization and Sprays*, 11(2):12, 2001.

[156] D. Sabathil, A. Koenigstein, P. Schaffner, J. Fritzsche, and A. Doehler. The influence of DISI engine operating parameters on particle number emissions. *SAE Technical Papers*, 2011-01-0143:55–66, 2011.

[157] C. Saggese, S. Ferrario, J. Camacho, A. Cuoci, A. Frassoldati, E. Ranzi, H. Wang, and T. Faravelli. Kinetic modeling of particle size distribution of soot in a premixed burner-stabilized stagnation ethylene flame. *Combustion and Flame*, 162(9):3356–3369, 2015.

[158] S. Salenbauch, A. Cuoci, A. Frassoldati, C. Saggese, T. Faravelli, and C. Hasse. Modeling soot formation in premixed flames using an Extended Conditional Quadrature Method of Moments. *Combustion and Flame*, 162:2529–2543, 2015.

[159] S. Salenbauch, M. Storch, D. Hain, S. Hartl, M. Wensing, S. Will, C. Hasse, and L. Zigan. Does ethanol always reduce the particulate emissions in gasoline engines? – A combined numerical and experimental study in a transparent engine to unravel the cause-and-effect chain for E0 to E85. In *15th Conference „The Working Process of the Internal Combustion Engine“*, Graz, 2015.

[160] W. Samenfink, A. Elsäßer, K. Dullenkopf, and S. Wittig. Droplet interaction with shear-driven liquid films: Analysis of deposition and secondary droplet characteristics. *International Journal of Heat and Fluid Flow*, 20(5):462–469, 1999.

[161] M. Sander, R. I. Patterson, A. Braumann, A. Raj, and M. Kraft. Developing the PAH-PP soot particle model using process informatics and uncertainty propagation. *Proceedings of the Combustion Institute*, 33(1):675–683, 2011.

[162] H. Sato, D. R. Tree, J. T. Hodges, and D. E. Foster. A study on the effect of temperature on soot formation in a jet stirred combustor. *Symposium (International) on Combustion*, 23(1):1469–1475, 1991.

[163] S. S. Sazhin, G. Feng, and M. R. Heikal. A model for fuel spray penetration. *Fuel*, 80(15):2171–2180, 2001.

[164] J. Singh, R. I. Patterson, M. Kraft, and H. Wang. Numerical simulation and sensitivity analysis of detailed soot particle size distribution in laminar premixed ethylene flames. *Combustion and Flame*, 145(1-2):117–127, 2006.

[165] G. P. Smith, D. M. Golden, M. Frenklach, N. W. Moriarty, B. Eiteneer, M. Goldenberg, C. T. Bowman, R. K. Hanson, S. Song, W. C. Gardiner, V. V. Lissianski, Jr., and Z. Qin. GRI-Mech 3.0, 2016. URL `http://www.me.berkeley.edu/gri_mech/`.

[166] G. W. Smith. A simple nucleation/depletion model for the spherule size of particulate carbon. *Combustion and Flame*, 48:265–272, 1982.

[167] O. I. Smith. Fundamentals of soot formation in flames with application to diesel engine particulate emissions. *Progress in Energy and Combustion Science*, 7(4):275–291, 1981.

[168] M. V. Smoluchowski. Drei Vortrage uber Diffusion, Brownsche Bewegung und Koagulation von Kolloidteilchen. *Zeitschrift fur Physik*, 17:557–585, 1916.

[169] M. Sommerfeld and S. Horender. Multiphase flows. In *Ullmann's encyclopedia of industrial chemistry*. Wiley-VCH, Chichester, 2010.

[170] R. H. Stanglmaier, C. E. Roberts, and C. A. Moses. Vaporization of Individual Fuel Drops on a Heated Surface: A Study of Fuel-Wall Interactions within Direct-Injected Gasoline (DIG) Engines. In *SAE 2002 World Congress & Exhibition*, volume 2002-01-0838 of *SAE Technical Paper Series*, Detroit, Michigan, 2002.

[171] D. W. Stanton and C. J. Rutland. Multi-dimensional modeling of thin liquid films and spray-wall interactions resulting from impinging sprays. *International Journal of Heat and Mass Transfer*, 41(20):3037–3054, 1998.

[172] J. F. Stengele. Tropfenverdunstung in Hochdruckatmosphäre: Ph.D. Thesis, Universität Karlsruhe, 1998.

[173] Stephen J. Harris and M. Matti Maricq. Signature size distributions for diesel and gasoline engine exhaust particulate matter. *Aerosol Science*, 32:749–764, 2001.

[174] E. Stevens and R. Steeper. Piston wetting in an optical DISI engine: fuel films, pool fires, and soot generation. *SAE Technical Paper*, 2001-01-1203, 2001.

[175] H. Su, A. Vikhansky, A. Bhave, F. Mauss, K.-O. Kim, M. Kraft, S. Mosbach, and T. Kobayashi. A computational study of an HCCI engine with direct injection during gas exchange. *Combustion and Flame*, 147:118–132, 2006.

[176] A. Terres. Particle Size Distribution and Counting Efficiency: Challenges of Measuring PN Emissions on the Road. In *3. Internationale Fachkonferenz: Sensoren zur Abgasreinigung und CO2-Reduktion*, Leipzig, 2016.

[177] P. A. Tesner, T. D. Smegiriova, and V. G. Knorre. Kinetics of dispersed carbon formation. *Combustion and Flame*, 17(2):253–260, 1971.

[178] The MathWorks, Inc. MATLAB Release R2015b, 2015.

[179] R. E. Thek and L. I. Stiel. A new reduced vapor pressure equation. *AIChE J*, 12(3):599–602, 1966.

[180] D. R. Tree and K. I. Svensson. Soot processes in compression ignition engines. *Progress in Energy and Combustion Science*, 33(3):272–309, 2007.

[181] A. Ueberall, R. Otte, P. Eilts, and J. Krahl. A literature research about particle emissions from engines with direct gasoline injection and the potential to reduce these emissions. *Fuel*, 147: 203–207, 2015.

[182] United Nations Economic Comission for Europe. UN Vehicle Regulations, 2011. URL `http://www.unece.org/trans/main/wp29/wp29regs81-100.html`.

[183] W. M. Van and T. F. Lin. Combined heat and mass transfer in natural convection between vertical parallel plates with film evaporation. *International Journal of Heat and Mass Transfer*, 33(3): 529–541, 1990.

[184] G. Vishwanathan and R. D. Reitz. Development of a Practical Soot Modeling Approach and Its Application to Low-Temperature Diesel Combustion. *Combustion Science and Technology*, 182 (8):1050–1082, 2010.

[185] B. Wang, S. Mosbach, S. Schmutzhard, S. Shuai, Y. Huang, and M. Kraft. Modelling soot formation from wall films in a gasoline direct injection engine using a detailed population balance model. Technical Report 157, c4e-Preprint Series, Cambridge, 2015.

[186] C. Wang, H. Xu, J. M. Herreros, J. Wang, and R. Cracknell. Impact of fuel and injection system on particle emissions from a GDI engine. *Applied Energy*, 132:178–191, 2014.

[187] H. Wang and M. Frenklach. Calculations of Rate Coefficients for the Chemically Activated Reactions of Acetylene with Vinylic and Aromatic Radicals. *The Journal of Physical Chemistry*, 98 (44):11465–11489, 1994.

[188] H. Wang, A. Laskin, N. W. Moriarty, and M. Frenklach. On unimolecular decomposition of phenyl radical. *Proceedings of the Combustion Institute*, 28(2):1545–1555, 2000.

[189] A. Warey, Y. Huang, R. Matthews, M. Hall, and H. Ng. Effects of piston wetting on size and mass of particulate matter emissions in a DISI engine. *SAE Technical Paper*, 2002-01-1140, 2002.

[190] H. Watanabe. Thermal Conductivity and Thermal Diffusivity of Sixteen Isomers of Alkanes. *Journal of Chemical & Engineering Data*, 48(1):124–136, 2003.

[191] J. R. Welty. *Fundamentals of momentum, heat, and mass transfer*. Wiley, Hoboken, NJ, 5th edition, 2008.

[192] A. Wolf. Simulation des Sprayverhaltens und der Gemischbildung im direkteinspritzenden Ottomotor: Ph.D. Thesis, Leibniz Universität Hannover, 2000.

[193] Wolfgang Schindler, Christoph Haisch, Harald A. Beck, Reinhard Niessner, Eberhard Jacob, and Dieter Rothe. A Photoacoustic Sensor System for Time Resolved Quantification of Diesel Soot Emissions. In *SAE Technical Paper*, volume 2004-01-0968. SAE International, 2004.

[194] G. Woschni. A Universally Applicable Equation for the Instantaneous Heat Transfer Coefficient in the Internal Combustion Engine. In *National Fuels and Lubricants, Powerplants, Transportation Meetings*, volume 670931 of *SAE Technical Paper Series*, 1967.

[195] T. Yamada and R. D. Gunn. Saturated liquid molar volumes. The Rackett equation. *J. Chem. Eng. Data*, 18(2):234–236, 1973.

[196] Y. Yan, H. Liu, M. Jia, M. Xie, and H. Yin. A one-dimensional unsteady wall film evaporation model. *International Journal of Heat and Mass Transfer*, 88:138–148, 2015.

[197] Y. Yoshihara, A. Kazakov, H. Wang, and M. Frenklach. Reduced mechanism of soot formation—Application to natural gas-fueled diesel combustion. *Symposium (International) on Combustion*, 25(1):941–948, 1994.

[198] F. Zhao, M.-C. Lai, and D. Harrington. Automotive spark-ignited direct-injection gasoline engines. *Progress in Energy and Combustion Science*, 25(5):437–562, 1999.

[199] A. Zschutschke, J. Neumann, D. Linse, and C. Hasse. A systematic study on the applicability and limits of detailed chemistry based NOx models for simulations of the entire engine operating map of spark-ignition engines. *Applied Thermal Engineering*, 98:910–923, 2016.